



# Study of a novel configuration of laser Assisted Bioprinting

Muhammad Ali

## ► To cite this version:

Muhammad Ali. Study of a novel configuration of laser Assisted Bioprinting. Biochemistry [q-bio.BM]. Université de Bordeaux, 2014. English. NNT : 2014BORD0070 . tel-01336839

**HAL Id: tel-01336839**

**<https://theses.hal.science/tel-01336839>**

Submitted on 24 Jun 2016

**HAL** is a multi-disciplinary open access archive for the deposit and dissemination of scientific research documents, whether they are published or not. The documents may come from teaching and research institutions in France or abroad, or from public or private research centers.

L'archive ouverte pluridisciplinaire **HAL**, est destinée au dépôt et à la diffusion de documents scientifiques de niveau recherche, publiés ou non, émanant des établissements d'enseignement et de recherche français ou étrangers, des laboratoires publics ou privés.

Année 2014



# THÈSE DE DOCTORAT DE L'UNIVERSITÉ DE BORDEAUX

ÉCOLE DOCTORALE DES SCIENCES DE LA VIE ET DE LA SANTÉ

Présentée par  
**Muhammad ALI**

Pour obtenir le grade de

**DOCTEUR de l'UNIVERSITÉ de BORDEAUX**

Spécialité : INTERFACE CHIMIE-BIOLOGIE

---

## ÉTUDE D'UN NOUVEAU DISPOSITIF DE BIOIMPRESSION PAR LASER

---

Soutenue le 23 Juin 2014

Après avis de : Stéphane PALLU

Frédéric PRIMA

Rapporteurs

Devant la commission d'examen formée de:

Eric CORMIER, Professeur, Université de Bordeaux, Bordeaux

Président

Stéphane PALLU, Maître de Conférences, Université d'Orléans, Orléans

Rapporteur

Frédéric PRIMA, Maître de Conférences, ENSC (Chimie ParisTech), Paris

Rapporteur

Fabien GUILLEMOT, Chargé de Recherche INSERM, U1026, Université de Bordeaux Directeur de Thèse

Thèse préparée à l'INSERM U 1026 « Bioingénierie Tissulaires»

-2014-



“Scientific thought and its creation is the common and shared heritage of mankind.”

**Abdus Salam**





# RÉSUMÉ DE THÈSE

Les technologies laser sont largement utilisées dans le contexte de l'impression 3D de matériaux de toute taille ainsi que pour la bioimpression des constituants de tissu biologiques. Dans ce contexte, la bioimpression par laser (LAB), basée sur le procédé LIFT, a émergé comme une technique permettant de s'affranchir des inconvénients des technologies d'impression à jet d'encre (par exemple le colmatage). La bioimpression par Laser est une technique d'écriture directe de matériaux sous forme solide ou liquide dotée d'une haute résolution spatiale. La technique permet ainsi le transfert précis de microgouttelettes (volume de l'ordre du pL) de biomatériaux et de cellules sur un substrat de réception.

Dans nos travaux de recherche, afin de mieux comprendre la dynamique du processus de transfert et d'utiliser la technique en ingénierie tissulaire, nous avons développé une approche expérimentale basée sur une méthode d'imagerie résolue en temps. Nous avons tout d'abord caractérisé les différents régimes d'éjection afin de définir des conditions appropriées à l'impression d'éléments biologiques. Nous avons également exploré la fenêtre d'éjection, afin d'étudier l'influence de l'énergie laser sur la dynamique de jet. Ensuite, nous avons étudié une nouvelle configuration bioimpression par laser pour laquelle des études paramétriques impliquant l'effet de la viscosité et de la distance d'impression sur la morphologie des gouttes imprimées ont été réalisées. Cette configuration permet d'imprimer des encres biologiques en obtenant des contours très lisses et uniformes jusqu'à une grande distance de séparation ( $\leq 10$  mm). Les paramètres d'impression de cellules ont aussi été analysés par TRI en fonction de la concentration cellulaire des encres. Nos résultats fournissent des renseignements clés sur l'optimisation et devraient permettre un meilleur contrôle du mécanisme de transfert du processus de LAB. Enfin à la lumière de ces études, nous proposons un mécanisme complet pour la bioimpression par laser.

## Mots-clés

Bioimpression, imagerie résolue en temps, formation de jet liquide par bulles de cavitation

Muhammad ALI,

Doctorat en Interface Chimie-Biologie

Composante Sciences de la Vie



# ABSTRACT

Doctor of Philosophy  
by Muhammad ALI

Laser-based approaches are among the pioneering works in cell printing. These techniques are being extensively focussed for two or three-dimensional structures of any size in transferring pattern materials including deposition of 3D biological constructs. In this context, Laser-Assisted Bioprinting (LAB), based on Laser-Induced Forward Transfer (LIFT) has emerged as a nozzleless method to surmount the drawbacks (e.g. clogging) of inkjet printing technologies. LAB is a laser direct-write technique that offers printing micropatterns with high spatial resolution from a wide range of solid or liquid materials, such as dielectrics, biomaterials and living cells. The technique enables controlled transfer of droplets onto a receiving substrate.

A typical LAB setup comprises three key components: (i) a pulsed laser source, (ii) a ribbon coated with the material to be transferred and (iii) a receiving substrate. The ribbon integrates three layers: (i) a quartz disk support transparent to laser wavelength, (ii) a thin (1–100 nm) absorbing layer (like Ti or Au), and (iii) a bioink layer (few tens of microns) incorporating the material to print. The receiving substrate is faced to the bioink and placed at 100  $\mu\text{m}$  to 1 mm distance from the ribbon. Rapid thermal expansion of metallic layer (on absorbing laser pulse) propels a small volume ( $\sim\text{pL}$ ) of the ink towards a receiving substrate. Such a metallic interlayer eliminates direct interaction between the laser beam and the bioink. Volume of deposited material depends linearly on the laser pulse energy, and that a minimum threshold energy is required for microdroplet ejection. The thickness of the absorbing layer, viscosity and thickness of the bioink, different optical parameters such as the focus spot and the laser fluence are the controlling parameters to obtain a microscopic resolution and to limit the shock inflicted on the ejected cells.

In our research works, we considered experimental approach to study the physical mechanism involved in the LAB using a time-resolved imaging method in order to gain a better insight into the dynamics of the transfer process and to use the technique for printing biomaterials. First we designed and implemented a novel configuration of LAB for upward printing. Then we characterized different ejection regimes to define suitable conditions for bioprinting. We further explored jetting window to study the influence of laser energy on jet dynamics. Ejection dynamics has been investigated by temporal evolution of the liquid jet for their potential use in cell printing. In addition parametric studies like effect of viscosity and printing distance on the morphology of the printed drops were conducted to explore jetting “window”. This configuration allows debris-free

printing of fragile bioinks with extremely smooth and uniform edges at larger separation distance (ranging from 3 to 10mm). Material criteria required for realization of the cell printing are discussed and supported by experimental observations obtained by TRI investigation of cell printing from donors with different cell concentrations. These results provide key insights into optimization and better control of transfer mechanism of LAB. Finally, in the light of these studies, a comprehensive mechanism is proposed for printing micro-drops by LAB.

#### Keywords

Bioprinting, Time-resolved imaging, Liquid jet formation by cavitation bubble

## Declaration of Authorship

This thesis work is carried out in the group TEAL (Tissue Engineering Assisted by Laser) at **Bioingénierie Tissulaire (BioTis)**, Université de Bordeaux, 146, rue Léo-Saignat Case 45 33076 BORDEAUX cedex - France. TEAL aims to provide a methodology for 3D assembly of biomaterials using different laser based methods to deal with tissue complexity and anisotropy and to apply these methods to bone and vascular tissue engineering.

I, Muhammad ALI declare that the thesis entitled, “Study of a novel configuration of Laser Assisted Bioprinting” and the work presented in it are my own. I confirm that

1. This work was done wholly while in candidature for a research degree at this University;
2. Where any part of this thesis has previously been submitted for a degree or any other qualification at this University or any other institution, this has been clearly stated;
3. Where I have consulted the published work of others, this is always clearly attributed;
4. Where I have quoted from the work of others, the source is always given. With the exception of such quotations, this thesis is entirely my own work;
5. I have acknowledged all main sources of help;
6. Where the thesis is based on work done by myself jointly with others, I have made clear exactly what was done by others and what I have contributed myself;
7. Either none of this work has been published before submission, or parts of this work have been published as [please see List of Publications]:

Signature: 

Date: 22 July 2014



## Acknowledgement

I would like to express my deepest gratitude for Fabien Guillemot for his invaluable help and support throughout the PhD. Without his suggestions, feedback and guidance this thesis would have not been possible. He tried to help in every possible way to make my stay comfortable at *Université de Bordeaux* and Laboratoire *Bioingénierie Tissulaire (BioTis) U1026*, Inserm. I won't be wrong in saying that he is the best supervisor a student can ask for. Thanks for everything.

I would like to thank Joëlle Amédée Vilamitjana and Sophie Chatelus for helping me with all the official and administrative formalities and providing me all those countless visa letters with a smiling face.

I would like to extend my special thanks to Aurélien Fontaine for teaching me all the secret tricks about LIFT and for patiently listening and answering to all my questions/doubts. I learnt a lot from you Aurélien. Thanks for all the help with the experiments and discussions that helped in understanding things better.

Bertrand Guillotin, I would like to thank you for providing the donor substrates and valuable literature. I always enjoyed never ending but heart touching discussions with you.

Thanks to Patrick Guitton for showing me how to work in the mechanical workshop, and helping me with software related stuff for manipulation of the data.

Thanks to Jérôme Kalisky for providing the biological and chemical stuff for my experiments. You helped me a lot in using profilometer.

Many thanks to Murielle Remy for helping me to work with cells and for the useful discussions and helping me to learn the cell printing. You had taught me in an exceptional way.

Thanks to Virginie Kériquel, Raphael Devillard and Emeline Pagés for their help with bioink containing cells. Thanks a lot for answering my questions.

I would like to extend my special thanks to Lila Rami, Camille Ehret and Bertrand Guillotin for helping me to learn French.

Many thanks to all my friends at Inserm U1026 for all the fun times that made my PhD journey an enjoyable and memorable one.

Especially thanks to Florent DELOISON and Hélène DESRUS for helping me to use Alphanov's facilities during my studies.



I would like to acknowledge Region Aquitaine France and Higher Education Commission of Pakistan for financial support.

I would like to thank my wife for her constant motivation and support throughout my PhD work. She believes in me more than I do myself and her unconditional love and support kept me going even during the rough phases of my PhD. Love you loads.

At last but not least, many thanks to my parents for their blessings, love and constant support.

# Table of Contents

<u>CHAPTER 1</u>	1
<u>1 INTRODUCTION</u>	3
<u>1.1 Laser</u>	3
<u>1.1.1 Laser in medicine and biology</u>	5
<u>1.2 Century of Biology</u>	6
<u>1.2.1 Organ/tissue failure</u>	6
<u>1.2.2 Tissue engineering (T.E)</u>	7
<u>1.3 Bioprinting</u>	9
<u>1.3.1 Bio-printing techniques</u>	9
<u>1.3.1.1a Inkjet printing: The technology</u>	9
<u>1.3.1.1b Bioprinting applications of inkjet technologies</u>	13
<u>1.3.1.2 Extrusion bioprinters</u>	13
<u>1.3.1.3 Related technologies</u>	14
<u>1.3.1.4 Laser assisted deposition</u>	14
<u>1.3.1.4a Laser-guided direct writing (LGDW)</u>	15
<u>1.3.1.4b Laser assisted bioprinting (LAB)</u>	15
<u>1.4 From LIFT to LAB</u>	16
<u>1.4.1 LIFT of solid materials</u>	17
<u>1.4.2 LIFT of liquids</u>	17
<u>1.4.3 Biomedical applications of LIFT</u>	18
<u>1.5 State of Art and Printing Mechanism</u>	18
<u>1.5.1 Transfer mechanism and regimes</u>	18
<u>1.5.1.1 Sub-threshold regime</u>	18
<u>1.5.1.2 Jetting regime</u>	18
<u>1.5.1.3 Plume regime</u>	19
<u>1.5.2 Different parameters for LAB</u>	20
<u>1.5.2.1 Laser energy deposition (<math>1 \text{ J/cm}^2</math>)</u>	20
<u>1.5.2.2 Vapour bubble growth and collapsing (<math>1 \mu\text{s}</math>)</u>	20
<u>1.5.2.3 Interaction of the vapour bubble with the free surface</u>	20
<u>1.5.2.4 Jetting</u>	22
<u>1.5.2.5 Deposit-landing</u>	22
<u>1.5.3 Modelling studies</u>	24
<u>1.5.3.1 Laser interaction with matter</u>	24
<u>1.5.3.2 Bubble expansion</u>	25
<u>1.5.3.3 Landing impact of droplet</u>	26
<u>1.6 Purpose of the Study</u>	28
<u>1.7 Objectives of the Thesis</u>	29
<u>CHAPTER 2</u>	31
<u>2 MATERIALS &amp; METHODS</u>	31
<u>2.1 Experimental Devices to Deposit Biomaterials</u>	33
<u>2.1.1 Choice of the laser</u>	33
<u>2.1.1.1 Wavelength</u>	33
<u>2.1.1.2 The pulse duration “<math>\tau</math>” and the repetition rate “<math>f</math>”</u>	33
<u>2.1.1.3 The beam quality</u>	33
<u>2.1.2 Transfer station</u>	33
<u>2.2 Sample Preparation</u>	35
<u>2.2.1 Choice of the absorbing layer</u>	35
<u>2.3 Preparation of the Cartridge</u>	36

2.3.1 Coating of the absorbing layer.....	36
2.3.2 Preparation of hydrogel.....	36
2.3.3 Depositing the hydrogel film.....	37
2.3.4 Bioinks containing cells.....	38
2.3.5 The printing patterns.....	39
2.4 Characterization Techniques for Post-Transfer Analysis.....	40
2.4.1 Optical microscopy.....	40
2.4.2 Optical profilometry.....	40
2.4.3 Statistical analysis.....	41
2.4.3.1 Drop volume.....	41
2.4.3.1a Volume calculations.....	41
2.4.3.1b Calculation of uncertainty in drop volume.....	42
2.5 Time-Resolved Imaging (TRI).....	43
2.5.1 The shadowgraphy.....	43
2.5.2 TRI setup for study of ejection mechanism.....	44
2.5.2.1 The optical assembly.....	45
2.5.2.2 Calibration.....	45
2.5.2.2a Energy profile.....	45
2.5.2.2b Pixel calibration.....	46
2.5.2.3 Delay.....	46
2.5.3 Printing configurations.....	47
2.5.3.1 Novel configuration.....	47
2.5.3.2 Conventional configuration.....	47
2.6 Experimental Arrangements for TRI.....	47
CHAPTER 3.....	51
3 RESULTS.....	53
3.1 Section A: Novel configuration (Upward Printing).....	53
3.1.1 Determination of the energies for transition studies.....	53
3.1.2 TRI for sub-threshold regime.....	53
3.1.3 TRI for jetting regime.....	54
3.1.4 TRI analysis.....	55
3.1.4.1 Vertex angle.....	56
3.1.4.2 Height and base-width.....	56
3.1.4.3 Volume.....	58
3.1.4.4 Velocity.....	58
3.1.5 High speed jets in jetting regime.....	59
3.2 Conventional Setup.....	61
3.2.1 TRI for sub-threshold regime.....	61
3.2.2 TRI for jetting regime.....	61
3.2.3 TRI analysis.....	62
3.2.3.1 Height and base-width.....	63
3.2.3.2 Volume.....	64
3.2.3.3 Velocity.....	64
3.2.3.4 Vertex angle.....	65
3.2.6 High speed jetting.....	66
3.3 SECTION B.....	69
3.3.1 TRI for laminar jets ejection and dynamics.....	69
3.3.2 Height of laminar jets.....	72
3.4 SECTION C: Parametric Study of Novel Configuration.....	74
3.4.1 Viscous liquids drop printing.....	74

3.4.1.1 Effect of laser energy on drop size.....	74
3.4.1.2 Effect of liquid viscosity on drop size printed at 5mm.....	75
3.4.1.3 Effect of printing distance on drop size.....	76
3.4.2 Distant printing for low viscosity solutions.....	78
3.4.2.1 Effect of printing distance on drop size of less viscous solutions.....	79
3.4.2.2 Effect of printing distance on drop height.....	80
3.4.2.3 Printing distance and drop volume.....	80
3.4.2.4 Effect of printing distance on printing position.....	81
CHAPTER 4.....	83
4 DISCUSSION.....	85
4.1 Transition between sub-threshold and jetting regimes.....	85
4.1.1.1 Sub-threshold regime.....	85
4.1.2 Vapour bubble dynamics.....	86
4.1.2.1 Interaction of the vapour bubble near rigid surface.....	87
4.1.2.2 Interaction of vapour bubble near free-surface.....	88
4.1.3 Jet Formation: A new beginning.....	88
4.1.3.1 Jetting regime.....	89
4.1.4 Jet dynamics.....	93
4.1.5 High speed jetting.....	94
4.2 Crown like structure.....	97
4.3 Temporal evolution of laminar jets.....	100
4.3.1 Laminar jets ejection and dynamics.....	100
4.4 Parametric study of the printing with novel configuration.....	102
4.5 Section B: Applications of Novel Configuration for Cell Printing.....	106
4.5.1 TRI for printing cells with slow jets.....	106
4.5.2 Cell printing.....	111
4.5.2.1 Landing impact.....	111
4.6 LAB Mechanism: Schematic representation of LAB.....	113
CHAPTER 5.....	117
5 CONCLUSIONS & PERSPECTIVES.....	117
5.1 Conclusions.....	117
5.2 Perspectives.....	120
References.....	123
APPENDIX A.....	141
APPENDIX B.....	145
ALGINATE.....	145
Structural Unit.....	145
Molecular Structure.....	145
APPENDIX C.....	147
PROCESS ASTREE.....	147
APPENDIX D.....	151
PROCEDURE ImageJ.....	151
APPENDIX E.....	153
High Speed Jets in Jetting Regime.....	153
APPENDIX F.....	157
PUBLICATIONS & COMMUNICATIONS.....	157
APPENDIX G.....	159
SCIENTIFIC PUBLICATIONS.....	159



## List of Figures

Figure 1.1: a) Stimulated absorption and stimulated emission.....	4
Figure 1.1: b) Basic operation of laser.....	4
Figure 1.2: Light modulator.....	5
Figure 1.3: Different wavelengths used in medicine.....	5
Figure 1.4: Tissue and organs to be donated.....	7
Figure 1.5: Basic principles of tissue engineering .....	7
Figure 1.6: Artificial heart valve.....	8
Figure 1.7: Continuous inkjet printing.....	10
Figure 1.8: Drop-on-demand inkjet printing.....	11
Figure 1.9: Drop formation in DOD printer .....	12
Figure 1.10: Schematic presentation of cell printing and real cell printer.....	14
Figure 1.11: Setup for acoustic picoliter droplet generation.....	14
Figure 1.12: Laser-guided-direct-writing system.....	15
Figure 1.13: A typical diagram of LIFT for bioprinting method of operation.....	17
Figure 1.14: Different regimes of LIFT.....	19
Figure 1.15: Sub-threshold, jetting and plume regime of LAB.....	21
Figure 1.16: Microscopic images of microarrays.....	22
Figure 1.17: Droplet volume as function of laser energy, film thickness and viscosity.....	23
Figure 1.18: Temperature at titanium/bioink interface vs time and penetration distance.....	24
Figure 1.19: Areas of computing and networking of the system.....	26
Figure 1.20: Simulation of landing process.....	27
Figure 2.1: High-throughput laser printer for biomaterials .....	34
Figure 2.2: Ribbon for LAB.....	36
Figure 2.3: Dynamic viscosity of bioinks versus alginate concentration.....	37
Figure 2.4: Micrometer film applicator.....	38
Figure 2.5: Optical profilometer.....	40
Figure 2.6: Spherical cap for calculation of drop volume.....	41
Figure 2.7: Principle of shadowgraphy .....	43
Figure 2.8: Schematic diagram of TRI setup.....	44
Figure 2.9: Experimental device for time-resolved imaging.....	45
Figure 2.10: a) Energy profile for laser pulse in single shot mode.....	46
Figure 2.10: b) Calibration of pixels.....	46
Figure 2.12: a) The delay generator.....	47
Figure 2.12: b) The timing of signals .....	47
Figure 2.12: a) Scheme of TRI in upward printing configuration.....	48
Figure 2.12: b) Scheme of TRI in conventional configuration.....	48
Figure 3.1: TRI for different regimes of LAB.....	54
Figure 3.2: TRI for sub-threshold and jetting regimes in upward setup.....	54
Figure 3.3: Measuring vertex angle, height, base-width and volume in novel configuration.....	55
Figure 3.4: Vertex angle in upward configuration versus time.....	56
Figure 3.5: Maximum value of height versus time (upward printing).....	57
Figure 3.6: Maximum value of base-width versus time (upward printing).....	57
Figure 3.7: Volume versus time (upward printing).....	58
Figure 3.8: Velocity versus time (upward printing).....	59
Figure 3.9: Jet velocity as function of the time .....	60
Figure 3.10: TRI of high speed penetrating jet of pure riboflavin.....	60
Figure 3.11: High speed jet velocity versus time .....	61
Figure 3.12: TRI for sub-threshold and jetting regimes in conventional configuration.....	62

Figure 3.13: Measurement of the vertex angle, height, base-width and volume.....	62
Figure 3.14: Maximum value of height versus time.....	63
Figure 3.15: Maximum value of base-width versus time.....	63
Figure 3.16: Volume versus time in conventional setup.....	64
Figure 3.17: Velocity versus time for sub-threshold and jetting regime in conventinal setup.....	65
Figure 3.18: Vertex angle versus time (conventional setup).....	65
Figure 3.19: TRI for jets with increasing energy.....	67
Figure 3.11: a) High energy jet velocity versus time.....	68
Figure 3.11: b) Printed drops from different jets.....	68
Figure 3.21: TRI of jets from different viscosities.....	69
Figure 3.22: a) TRI of jet from 27mPa s with 21 $\mu$ J.....	70
Figure 3.22: b) TRI of jet from 60mPa s with 21 $\mu$ J.....	71
Figure 3.22: c) TRI of jet from 107mPa s with 21 $\mu$ J.....	71
Figure 3.23: Height of the jet (front position) with 21 $\mu$ J versus time .....	72
Figure 3.24: Velocity of the jet (front position) form 21 $\mu$ J versus time.....	72
Figure 3.25: Diameter of the jet form 21 $\mu$ J versus time.....	73
Figure 3.26: Printed drops array from viscous alginate solution at 5mm with 55 $\mu$ J laser pulse.....	74
Figure 3.27: Printed drops at 5mm.....	75
Figure 3.28: Drop diameter versus energy.....	76
Figure 3.29: Drop diameter versus viscosity.....	76
Figure 3.30: Printed drops as observed under microscope.....	77
Figure 3.31: Drop diameter versus distance with 46 $\mu$ J.....	77
Figure 3.32:a) Drop diameter printed with 46 $\mu$ J at different distances versus viscosity.....	78
Figure 3.32:b) Drop volume printed with 46 $\mu$ J at different distances versus viscosity .....	78
Figure 3.33: Drops printed with 21 $\mu$ J laser pulse.....	79
Figure 3.34: Printed drops with 21 $\mu$ J laser pulse at different separation distances .....	79
Figure 3.35: Drop diameter and height versus separation distance.....	80
Figure 3.36: Drop volume versus separation distances .....	80
Figure 3.37: Spatial error versus separation distance .....	81
Figure 4.1: Vapour bubble radius evolution versus time.....	87
Figure 4.2: Simulation of the velocity vector and pressure contour.....	89
Figure 4.3: Vertex angle and Longuet-Higgins Model.....	90
Figure 4.4: The angle between the vertices of the free surface.....	91
Figure 4.5: Counter-jet observed in jetting regime.....	91
Figure 4.6: Stable printing in a coordinate system defined by the Reynolds and Weber numbers....	93
Figure 4.7: Schematic representation of the bubble in a liquid near free surface and jet evolution at different stand-off distances.....	95
Figure 4.8: Classification scheme for LAB regimes.....	96
Figure 4.9: Crown formation observed in TRI.....	97
Figure 4.10: Crown formation observed in TRI from 40 $\mu$ m thick layer of alginate solutions.....	98
Figure 4.11: Crown formation observed in TRI with different energies and different thicknesses....	98
Figure 4.12: Crown formation observed during TRI of cell printing.....	98
Figure 4.13: Crown formation published by Obreschkow et al. 2006.....	99
Figure 4.14: The numerical simulation and curvature scheme of the surface depression.....	99
Figure 4.15: a) Jet-contact printing, b) Breakup time versus NaAlg concentration.....	101
Figure 4.16: Drop size as a function of laser energy.....	103
Figure 4.17: A viscous jet and a thread contracting into a droplet.....	103
Figure 4.18: Microarray prepared varying the donor film–receptor substrate separation.....	104
Figure 4.19: Sessile droplets deposited at different liquid film–receptor substrate separations.....	105
Figure 4.20: a) TRI of slow jet of 1Million cells/mL & corresponding prints.....	107

Figure 4.21: a) TRI of slow jet of 5 Million cells/mL & corresponding prints.....	107
Figure 4.22: a) TRI of slow jet of 10 Million cells/mL.....	108
Figure 4.22: b) Donor of 10M/mL, c) Corresponding prints.....	108
Figure 4.23: a) TRI of slow jet of 50 Million cells/mL.....	109
Figure 4.23: b) Donor of 50 Million cells/mL, c) Corresponding prints.....	109
Figure 4.24: a) TRI of slow jet of 100 Million cells/mL.....	110
Figure 4.24: b) Donor of 100 Million cells/mL, c) Corresponding prints.....	110
Figure 4.25: Observation of the bioink donor and the substrate after printing.....	111
Figure 4.26: Viability of printed cells.....	112
Figure 4.27: Evaluation of cell velocity, acceleration and pressure.....	113
Figure: 4.28: Scheme of the bubble dynamics and jet formation for cell printing by LAB.....	114
Figure 5.1: Micromachining with laser in Polyacrylamide sheet.....	120
Figure 5.2: Blister-actuated LIFT.....	121
Figure A.1: Structural Unit of alginic acid.....	145
Figure A.2: Molecular structures of alginic acid.....	146
Figure B.1: Choice (of) donor (s) and printing distance (s) .....	147
Figure B.2: Definition of a rectangle tool.....	148
Figure B.3: Definition of the trajectory of a pattern.....	148
Figure B.4: Creating a printing process with ASTREE.....	149
Figure C.1:a) Original iImage.....	152
Figure C.1: b) Image treatemnt with ImageJ.....	152
Figure E.1: Jet speed versus time for different energies.....	153
Figure E.2: TRI of the jets from 40µm thick riboflavin.....	153
Figure E.3: Jet speed versus energy for different thicknesses.....	154
Figure E.4: TRI of jets at 7µs for a 40µm thickness of riboflavin solution diluted to 1/6.....	155
Figure E.5: TRI of the jet at 36.8µJ for a thickness of 40µm of riboflavin solution diluted to 1/3. ....	155
Figure E.6: TRI of jet at 7µs from the solution diluted to 1/3 and 40µm thickness.....	156
Figure E.7: TRI of the jet with 36.8µJ and 40µm of thickness of the solution diluted to 1/6.....	156





## **CHAPTER 1**

The first chapter of the thesis introduces the research work in the scientific context. First part is about LASER and its uses in the medical field. Second part is about the concept and developments in tissue engineering. Third part is reserved for bioprinting and the different techniques used for bioprinting along with the explanation of different laser techniques used for printing biological materials. Fourth part will provide illustration of the laser-induced forward transfer, the process which is used for laser-assisted bioprinting. Printing mechanism is discussed in the fifth section of this chapter. Finally, purpose of this research study is presented along-with objectives of the thesis.

<u>CHAPTER 1</u> .....	1
<u>1 INTRODUCTION</u> .....	3
<u>1.1 Laser</u> .....	3
<u>1.1.1 Laser in medicine and biology</u> .....	5
<u>1.2 Century of Biology</u> .....	6
<u>1.2.1 Organ/tissue failure</u> .....	6
<u>1.2.2 Tissue engineering (T.E)</u> .....	7
<u>1.3 Bioprinting</u> .....	9
<u>1.3.1 Bio-printing techniques</u> .....	9
<u>1.3.1.1a Inkjet printing: The technology</u> .....	9
<u>1.3.1.1b Bioprinting applications of inkjet technologies</u> .....	13
<u>1.3.1.2 Extrusion bioprinters</u> .....	13
<u>1.3.1.3 Related technologies</u> .....	14
<u>1.3.1.4 Laser assisted deposition</u> .....	14
<u>1.3.1.4a Laser-guided direct writing (LGDW)</u> .....	15
<u>1.3.1.4b Laser assisted bioprinting (LAB)</u> .....	15
<u>1.4 From LIFT to LAB</u> .....	16
<u>1.4.1 LIFT of solid materials</u> .....	17
<u>1.4.2 LIFT of liquids</u> .....	17
<u>1.4.3 Biomedical applications of LIFT</u> .....	18
<u>1.5 State of Art and Printing Mechanism</u> .....	18
<u>1.5.1 Transfer mechanism and regimes</u> .....	18
<u>1.5.1.1 Sub-threshold regime</u> .....	18
<u>1.5.1.2 Jetting regime</u> .....	18
<u>1.5.1.3 Plume regime</u> .....	19
<u>1.5.2 Different parameters for LAB</u> .....	20
<u>1.5.2.1 Laser energy deposition (<math>1 \text{ J/cm}^2</math>)</u> .....	20
<u>1.5.2.2 Vapour bubble growth and collapsing (<math>1 \mu\text{s}</math>)</u> .....	20
<u>1.5.2.3 Interaction of the vapour bubble with the free surface</u> .....	20
<u>1.5.2.4 Jetting</u> .....	22
<u>1.5.2.5 Deposit-landing</u> .....	22
<u>1.5.3 Modelling studies</u> .....	24
<u>1.5.3.1 Laser interaction with matter</u> .....	24
<u>1.5.3.2 Bubble expansion</u> .....	25
<u>1.5.3.3 Landing impact of droplet</u> .....	26
<u>1.6 Purpose of the Study</u> .....	28
<u>1.7 Objectives of the Thesis</u> .....	29

# 1 INTRODUCTION

Science is meticulous pursuit for veracity [1] to represent eloquent understanding of nature. Scientific advance is a succession of newer representation impelled by two main factors; technological advance and a guiding vision. The approach had led to 20<sup>th</sup> century inventions and physics-based technologies, which had eventually transformed human life. Among them, LASER is one of the most remarkable achievement of 20<sup>th</sup> century physicists.

## 1.1 Laser

The Maser phenomenon by Gordon Gould in 1954, Arthur Schawlow and Charles Townes in 1958 [2,3], paved the path for the invention of first laser by Theodore Maiman [4,5] around 1960. Einstein's idea of “wave-particle duality” of light using Plank’s law of radiation based on probability coefficients (Einstein coefficients) for absorption and emission (spontaneous and stimulated [Fig. 1.1a](#)) of electromagnetic radiation provided the bases for this research. In 1917, Albert Einstein speculated that under certain conditions atoms could absorb light and be stimulated to shed their borrowed energy which became reality with the invention of Laser. Charles Townes coined the term laser in 1951. Laser is an acronym for "light amplification by stimulated emission of radiation". Theodore Maiman investigated the glare of a flash lamp in a rod of synthetic ruby, which led to first human-made laser in 1960 [4]. The phenomenon involves exciting atoms by optical, electrical or electromagnetic energy and passing them through a medium such as crystal, gas or liquid.

Laser consists of a long cylinder of energized gas or solid. A population inversion occurs when a group of atoms exists in a state with more members in an excited state than in lower energy states ([Fig. 1.1b](#)). The concept is of fundamental importance in laser science because the production of a population inversion is a necessary step in the working of a standard laser. Normally, this energy is randomly released in random directions. The energy release, however, may be triggered by the passage of another quantum of light, synchronizing the two. In the presence of stimulating light an atom can take up or emit (if excited) a photon. The probability of both processes - stimulated absorption and stimulated emission- is the same since there is no specified time in such basic quantum mechanical processes. Fitting mirrors at the end of cylinder will accentuate the waves travelling longitudinally in the cylinder. As the cascade of photon energy sweeps through the medium, bouncing off mirrors, it is reflected back and forth, and gains energy to produce a high power light beam and when certain criteria are met, a beam of laser light is produced ([Fig. 1.2](#)). This is a monochromatic, collimated and

coherent light wave. Some types of lasers can produce extremely intense power in very short pulses; others operate continuously at more moderate power levels. The monochromaticity, collimation, high spatial, temporal coherency and power densities obtainable with lasers are above comparison.

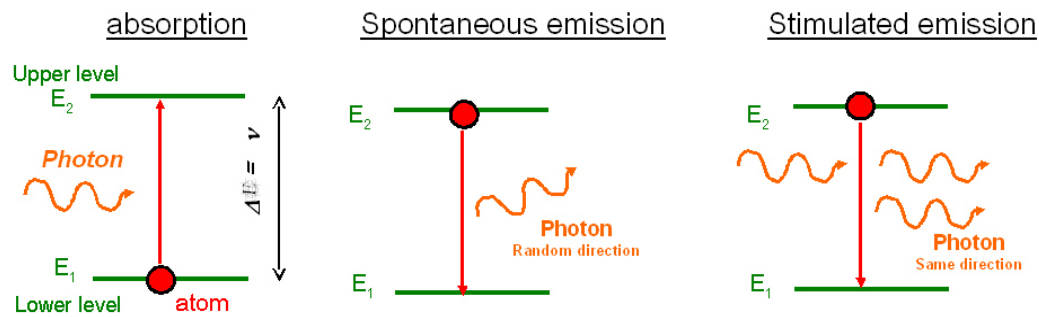


Figure 1.1: a) Stimulated absorption and stimulated emission

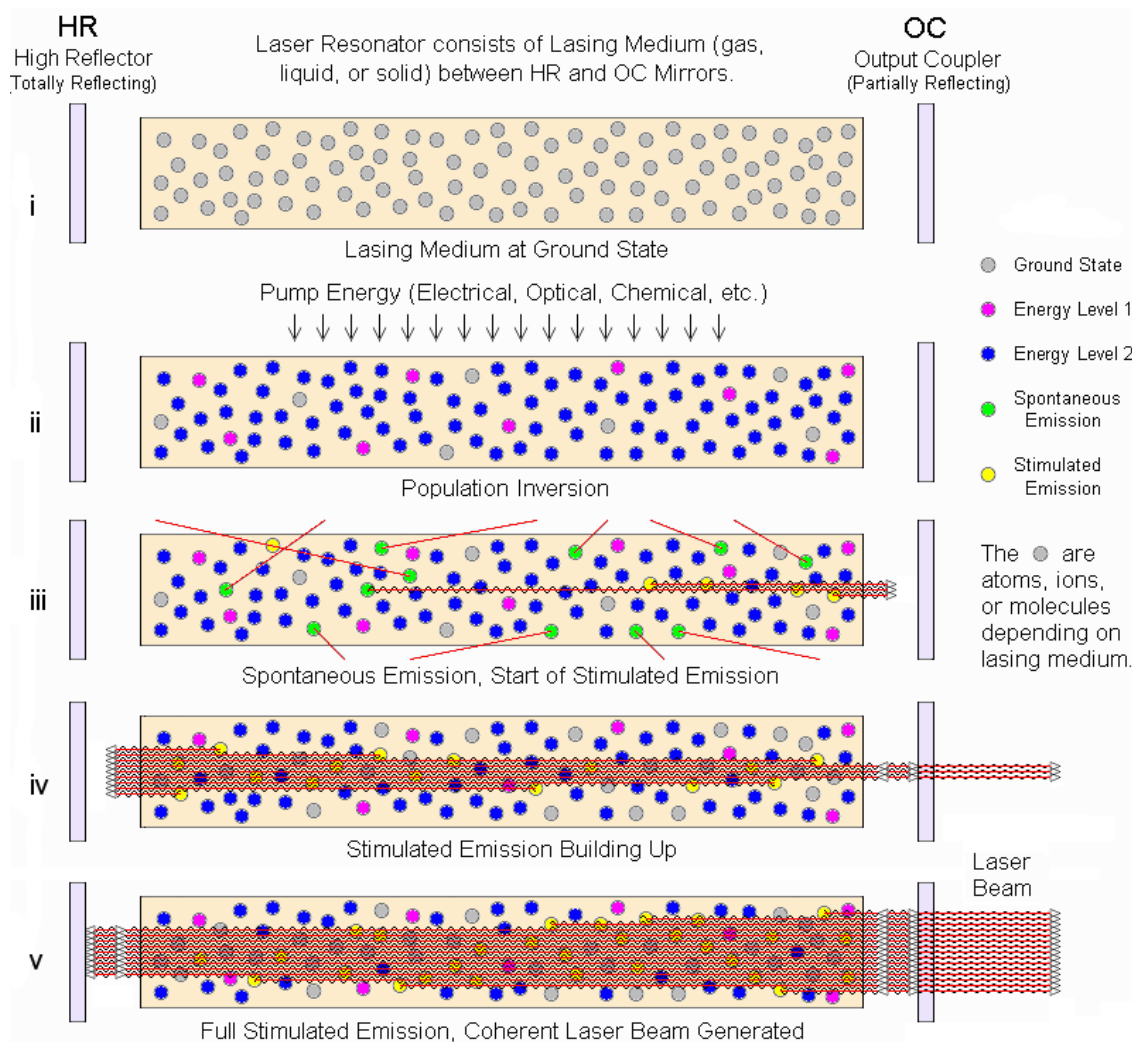


Figure 1.1: b) Basic operation of laser

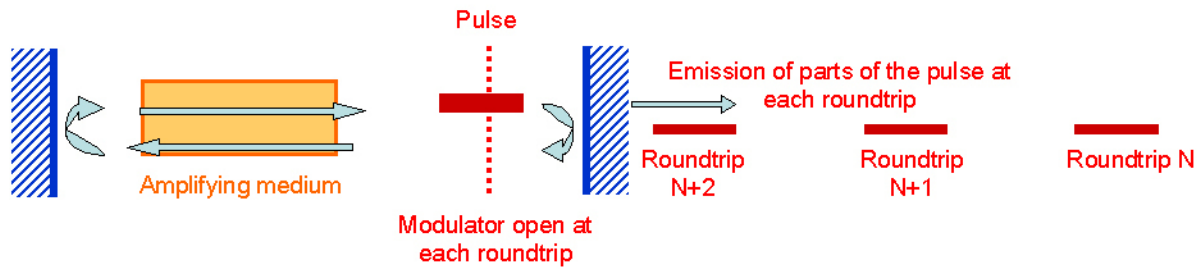


Figure 1.2: Light modulator

### 1.1.1 Laser in medicine and biology

It is hard to imagine that a narrow, one-way, coherent and amplified beam of light is powerful enough to slice through steel [6] at one hand but it could also deal with soft tissues. Today lasers are used in numerous professions, one of the most meaningful application is in medicine.

Unique properties of laser has mesmerized the masses in twentieth century. It exhorted the scientists in biology and medicine because the nature of laser light was unlike any natural or artificial light previously known. Laser was taken into clinic soon after its invention [7,8]. Although the ruby laser was the first laser developed in 1960 by Theodore Maiman [4], the Nd:YAG laser is probably the most widely used medical laser [9–13]. Today, different types of lasers are being extensively used in medical field. Figure 1.3 shows the wavelength [14] of extensively used lasers in medicine.

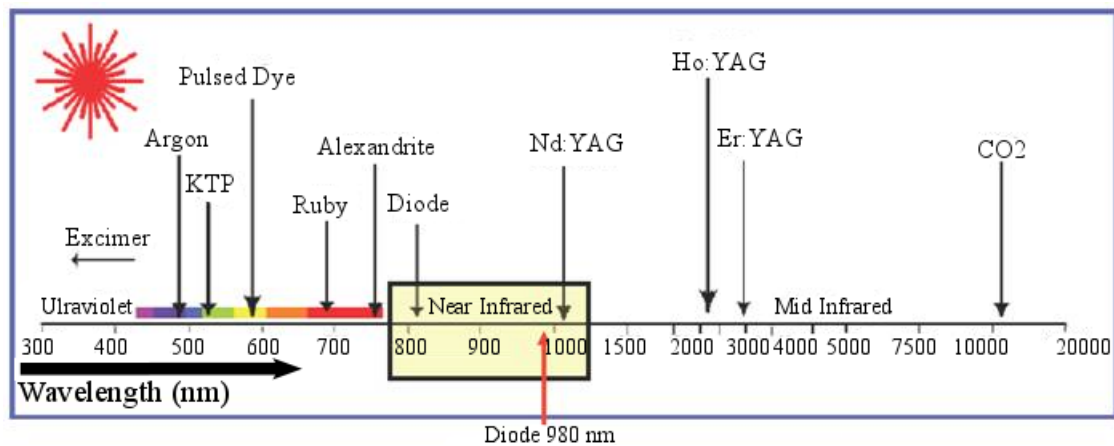


Figure 1.3: Different wavelengths used in medicine

Being faster and less invasive with a high precision, lasers have penetrated into numerous medical disciplines: dermatology [15,16], treatment of cutaneous pre-malignant and malignant lesions [17], dentistry [18–23], otolaryngology [24–27], gastroenterology [28–30], urology [31–33], gynaecology [34–36], cardiology [7,37,38], and Central Nervous System [39]. Lasers is also an indispensable tool in biological applications and being extensively used

in cell biology [40–42] apart from its diagnostic applications [43–45].

No doubt laser provides considerable benefits to both doctors and patients, however, it should be pointed out that lasers should only be used when they can offer clear advantage over conventional modalities. Successful laser treatment depends on the understanding of interactions between optical irradiation and biological tissue and on the appropriate laser energy/wavelength.

## **1.2 Century of Biology**

The technological advance and a guiding vision go hand in hand. Without technological advances the road ahead is blocked whereas absence of guiding vision inhibits the technological advance. Chemistry and physics have dominated the 19<sup>th</sup> and 20<sup>th</sup> centuries respectively. If the 20<sup>th</sup> century was the century of physics, the 21<sup>st</sup> century will be the century of biology [46]. The visionary intellect and new gadgets developed during last century could help the modern society to address the most devastating issue of today health care: organ/tissue failure.

### **1.2.1 Organ/tissue failure**

The loss or failure of an organ or tissue is one of the most frequent, devastating and costly problem of health care [47,48]. Millions of people suffer tissue loss or organ failure all over the world. Current treatment modalities include transplantation of organs, surgical reconstruction, use of mechanical devices and supplementation of metabolic products. Single organ transplants amount to 131,912 performed in five years (2007-2011) in US including 81,811 for kidney [49]. Epidemiological studies highlight tissue/organ shortage, which justifies original approaches to fulfil clinical needs [50]. As per European Union's statistics 86,304 organs were transplanted during 2000 to 2012, including 51.7% for kidney [51]. It was only possible because of the donation of tissue and organs (Fig. 1.4) from deceased donors.

The transplantation of a tissue or organ in the patient is often limited by donor scarcity along with associated risk of rejection and disease transfer. Organ shortage remains the most pressing issue. This dearth is aggravating every year and satirical prices are making the situation more devastating. The surmise, that tissue engineering/regenerative medicine is and will increasingly be the focus of biomaterials research, is justified by a very significant and well-known clinical need for the establishment of alternative therapies for the treatment of tissue loss or end-stage organ failure [52–55]. Growing large, three-dimensional organs such as a heart, liver [56] or kidney is the goal of today's biotechnology. Hence, T.E. has

become a promising choice.

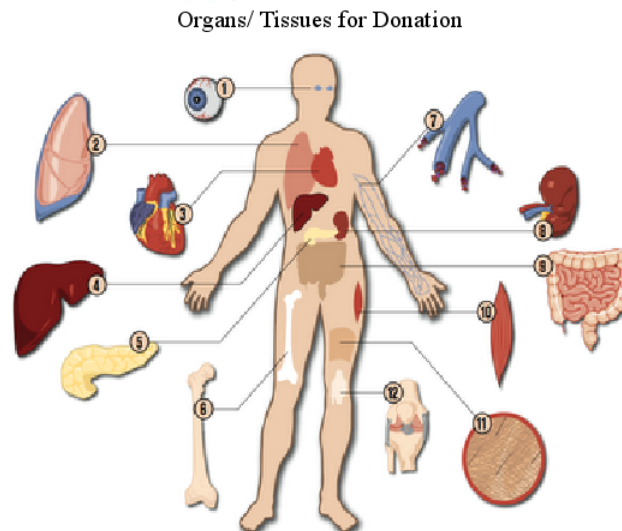


Figure 1.4: Tissue and organs as gift for donation

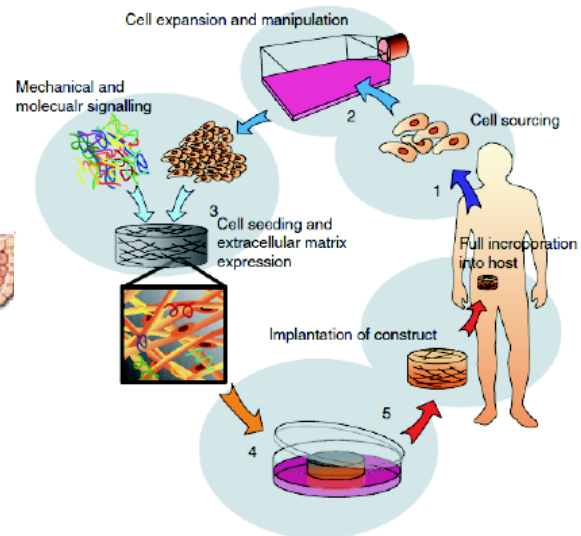


Figure 1.5: Basic principles of tissue engineering [57]

### 1.2.2 Tissue engineering (T.E)

Tissue engineering (T.E) is an emerging, interdisciplinary field promising to those in need of organ, tissue replacement and repair. To date, the commercial success of tissue engineered products is largely unfulfilled. Over the decade, biosciences are creeping to transform medicine and health care because human body is not only superbly engineered biological specimen but also the most complex phenomenon and mystery. Asking right question, to solve problems, requires an integrated biological and engineering approach. This provides the gateway to regenerative medicine: replacing ageing, diseased or injured cells or body parts with new ones. In a larger context, it is development and manipulation of laboratory-grown organs and tissues to replace or support the function of amiss or injured body parts. T.E. cannot grow whole organ. At least not yet. Growing an organ like a heart will require technical advances in number of areas, like vascularization and preparing most appropriate scaffolds.

T.E. had interwoven the biology, medicine and engineering to develop biological materials that can repair, maintain, or enhance tissue function. The comprehensive definition of tissue engineering is, “an interdisciplinary field that applies the principles of engineering and the life sciences toward the development of biological substitutes that restore, maintain, or improve tissue function”[48,53]. An other definition says, "understanding the principles of tissue growth, and applying this to produce functional replacement tissue for clinical use" [58]. Basic principles of tissue engineering are illustrated in [figure 1.5](#).

Isolated cells from the patient’s body can be expanded in a petri dish to be grown in



laboratory to create a “cell bank”. These cells are further seeded on a polymeric scaffold material, and cultured *in vitro* in a bioreactor or incubator, to form a matured construct. The process is carried out in a Tissue Culture facility to maintain a sterile environment. Cellular biochemical and physical activity can be enhanced by the addition of growth factors. After further tissue culture under the correct conditions, the resident cells of Tissue Engineered construct will dissolve the original collagen scaffold. When the construct is matured enough, then it can be implanted back into the patient from whom the cells were originally removed. Anti-rejection drugs are not required as the living tissue engineered construct has been grown from the patients own cells, and will be accepted as a natural part of the patients body. Encouraging results like tissue engineered skin [59] and liver [56] have paved the path towards the goal of T.E. The first tissue engineered heart valves (Fig. 1.6) [60] had shown promising results in function and mechanical stability. The creation of 3D tissue constructs like organs (e.g. heart or pancreas) is a big challenge.



Figure 1.6: Artificial heart valve leaflet (amniotic fluid-derived cells) after 28 days of culture[60]

Scaffold structure is one of the traditional method of T.E. adopted along with other different strategies [61–67]. A scaffold is a temporary biodegradable supporting structure which could be synthetic and naturally derived solid material [68]. Conventional scaffold fabrication techniques include fibre bonding [69,70], phase separation [71,72]. The porous structure of scaffold is designed to promote cell seeding and the establishment of vascularization [73], it may also control the diffusion of nutrients, waste products and cell-cell interactions.

Despite incredible progresses, critical limitations with present scaffold based T.E. technologies [64,74] include:

- the inability to create vascularized tissue constructs,
- limited physical and mechanical stability of scaffolds may not be suitable for some load-bearing applications,
- incomplete colonization due to less effective cell penetration and adhesion
- lack of a suitable source of functional cells that are immunologically compatible with the host

### **1.3 Bioprinting**

Precise organization of tissue components with retention of functionality is a big challenge faced by today tissue engineers. Interdisciplinary sciences have led to the development of Bioprinting [75] whereby principles of engineering and life sciences are applied for precise organisation of biomaterials and living cells into tissue constructs [76]. Bioprinting is the construction of body parts using computer-aided techniques and could be defined as, *“the use of computer-aided transfer processes for patterning and assembling living and non-living materials with a prescribed 2D or 3D organization in order to produce bio-engineered structures serving in regenerative medicine, pharmacokinetic and basic cell biology studies”* [75]. It is a technology wherein cells or other tissue components are delivered by bioprinters with high precision into biodegradable scaffolds to form three dimensional tissue constructs of specified geometry. Bioprinting techniques include:

- Contact bioprinting: (micro) extrusion
- Contactless bioprinting: ink-jet deposition, acoustic, Laser-Assisted Bioprinting

These are not competing technologies. Many applications of bioprinting cover a range of patterning length scales, depending on their biological applications. The inks can be hydrogels containing cells, proteins (collagen, growth factors) or biomaterials e.g. hydroxyapatite. There are three key technologies: ink jet [77,78], acoustic droplet ejection [79] and laser assisted [80–84] bioprinting. Information technology and rapid prototyping are also inherent in bioprinting, allowing to obtain high resolution (on cellular scale) and rapid process. Such techniques allow manipulation and organization of cells or molecules without degrading their biological function.

#### **1.3.1 Bio-printing techniques**

##### **1.3.1.1a Inkjet printing: The technology**

The concept is patented to Lord William Kelvin for steering the droplets through electrostatic forces [85]. With major advances during 1960–80, inkjet printing is now an

ubiquitous for personal printing and being extensively used in fabrication [86,87]. It deposits materials which are compatible with the print-head used and have viscosity within a specific range [88]. In fabrication, its helps in placing accurately picoliter volumes of fluid on an arbitrary substrate [89]. Versatility of the method can be imagined by its extensive use in numerous technologies, including displays [90], plastic electronics [91], solder dispensing [92], rapid prototyping [93], ceramic component [94], enzyme-based sensors [95], organic light-emitting diodes (OLEDs) [96], organic field effect transistors (OFETs) [97–99] and tissue engineering [100]. The principles of inkjet printing split into two major [101] and a few minor categories. The major division is:

- continuous inkjet (CIJ) printing and,
- drop-on-demand (DOD) inkjet printing [102]

**CIJ printing:** continuous inkjet starts by forming drops (diameter  $\sim 100\ \mu\text{m}$ ) from a continuous flowing ink which is forced out of a nozzle under pressure. Liquid column (Fig. 1.7) is ejected under pressure through a small nozzle which eventually leads to a stream of drops formed by Rayleigh instability. These drops are charged by potential applied to the nozzle. A small potential is also applied to deflection plates for steering and positioning the individual drop to the desired location. Drop diameters are typically slightly larger than the nozzle diameter. Multiple nozzles could be used simultaneously.

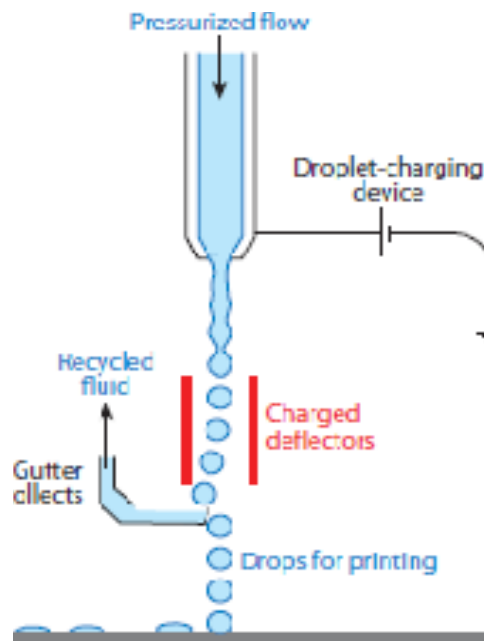


Figure 1.7: Continuous Inkjet Printing [89]

A continuous stream of liquid drops is being produced in CIJ even when no printing is required. Unused/unwanted drops are directed towards the gutter (Fig. 1.7). The unused ink is recycled for many applications in product marking and graphics. However for biomaterials,

recycling risks contamination of the ink; hence CIJ printing is a potentially wasteful process. Two possibilities to control drop positions are either by steering a drop in flight or by positioning the substrate where a deposit is required. CIJ have drop generation rates around 20–60 kHz, and drop velocity  $>10 \text{ ms}^{-1}$ . CIJ printing has been used successfully to print 3-D ceramic objects [103] and silver conducting tracks [104]. It has limited use in materials science applications. This is partly due to contamination/waste issue but also because a limited range of fluids can be deposited using CIJ printing than is possible with DOD printing. Moreover, it has lower spatial resolution than DOD printing.

**DOD printing:** DOD stands for drop-on-demand, can produce droplet with a smaller drop diameter (20–50  $\mu\text{m}$ ) at acoustic frequencies (typically 1–20 kHz) which gives it dominance in graphics and text printing. Minimum drops size of 5  $\mu\text{m}$  [105], routine resolution of 75  $\mu\text{m}$  [106] and deposition of functional materials [107] had been demonstrated with DOD inkjet printing. DOD printing is economically more efficient with ink delivery than CIJ systems because it generates individual drop only when required. For drops generation, a pressure pulse is propagated in the fluid held in a chamber behind the printing nozzle. When pressure pulse attains the required threshold at the nozzle, a drop is ejected. In the absence of a pressure pulse, liquid is held in place by surface tension at the nozzle and no drop is generated.

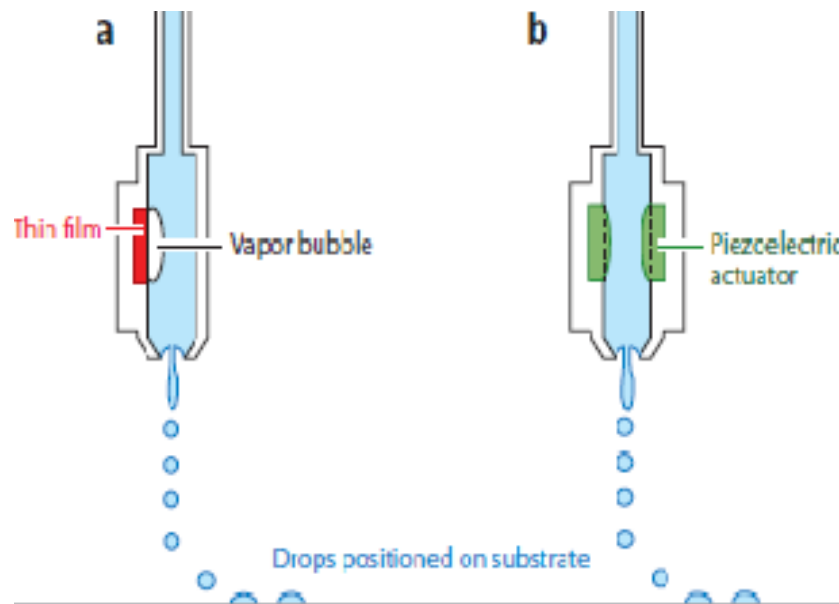


Figure 1.8: Drop-on-demand Inkjet Printing (a) Thermal, (b) Piezoelectric [89]

Two different methods are used. **Thermal DOD** printing involves heating [108] the fluid by thin-film heater. The fluid is heated to above its boiling temperature to form a small vapour pocket or bubble on passing a current through the heater (Fig. 1.8a). Heat transfer

leads to rapid bubble collapse as the current is removed. This rapid expansion and collapse of the bubble generate the required pressure pulse.

**Piezoelectric DOD** does not involve any heat. In piezoelectric DOD printing [100], the pressure pulse is generated by direct mechanical actuation with a piezoelectric transducer (Fig. 1.8b) which avoids the material to be heated.

Figure 1.9 shows the sequence of drop formation observed at a DOD printer. The long extended fluid tail is a characteristic of the DOD process. The formation of satellite drops owes to the final rupture of this elongated tail or ligament. These satellite drops can be problematic and lead to non circular impact if these drops don't catch up and merge with the leading large drop in flight, prior to impact (so-called 'infinite' satellites). Infinite satellites drops lead to a deleterious influence on deposit precision, resolution, and accuracy. Satellites are termed as forward-merging when these drop catch up and merge with leading large drop in flight, prior to impact. Presence of forward-merging satellites is irrelevant.

To facilitate drop merging in flight, it is customary to print at a stand-off distance from the substrate. For DOD printing this stand-off distance is typically 2-3 mm. The appropriate stand-off will also influence drop placement accuracy because drag from air currents in the printing environment can deviate drops from their desired trajectory. To minimize this effect, the stand-off distance is normally set at the minimum to ensure stable single drops.

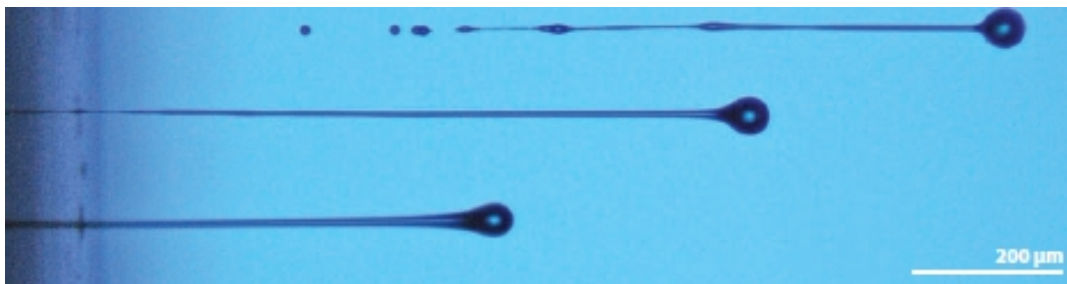


Figure 1.9: Drop formation in DOD printer [101]

Thermal DOD systems are readily miniaturized, and most desktop or domestic printers use this technology. However, for two main reasons, the majority of industrial printers use piezoelectric DOD technology. First, the need to generate a bubble in thermal DOD printing limits the fluids to those of a high vapor pressure under ambient conditions. Second, with piezoelectric DOD printing it is relatively easy to change the actuation pulse to control drop size and velocity for any fluid. DOD printing operates at acoustic frequencies (1-20 kHz). Hence, given that the fluid-filled chambers used to generate drops have dimensions of the order of  $10^{-3}$  m, significant acoustic resonances can influence drop volume and velocity

[109,110]. Thus, the shape and amplitude of the actuating pulse can strongly influence printing behaviour [101].

#### **1.3.1.1b Bioprinting applications of inkjet technologies**

Inkjet printing is among exciting and elegant biofabrication technologies. It was used for the first time by Klebe [111] for printing biological elements. It controls cell dispensing at a high level along with remarkable viability and certain functionality of printed cell patterns, as shown by Dr Thomas Boland and his followers [108,112,113]. Inkjet bioprinting *in vivo* has also been demonstrated [114]. It has the advantages like compatibility with digitalized version of cellularized solid scaffolds and hydrogels. Simultaneous usage of many print-heads and use of prestructured substrate can improve the productivity and resolution, respectively.

Inkjet bioprinting has been advanced to generate 3D biological structures through the cross linked hydrogels such as alginate. Nakamura et al. [100] published 3D constructs from cells mixed in alginate solutions which are then printed into, and crosslinked in, calcium chloride solution. Inkjet bioprinting is contributing to printing living cells and biomaterials, but the technology faces many challenges [115] like the issue of cell density and demonstration of authentic functional and structural 3D tissue organization. One of the biggest challenges is cell aggregation and sedimentation in the print cartridge reservoir. Frequent stirring can prevent sedimentation but can impair cell viability if the cells are sensitive to the shear forces and agitation. Sedimentation can also occur within the tubes connecting the reservoir to the inkjet nozzle, causing additional complications [116]. Similarly, clogging of the orifice of the nozzle also limits its flexibility. Additionally, clogging can increase the mechanical shear of ejected cells at the nozzle [117]. Droplet deposition with high cell density and high-viscosity materials faces difficulties due to frequent clogging of the nozzles. To minimize this issue, low-viscosity surfactants and humectants can be used [116] by mixing them into the 'bioink'. However, it may damage cells and induce additional challenges. Owing to the drop-wise deposition of layers, their homogeneity and resolution ( $\sim 50\ \mu\text{m}$ ) are limited. The throughput depends upon droplet dispense rate, which typically does not exceed 25 kHz.

#### **1.3.1.2 Extrusion bioprinters**

Micro-syringes have also been developed to print biological elements. In bioplotter® system, syringe whose flow is controlled by a pneumatic system is used to provide a hydrogel with or without cells. There are many variations of these bioprinters designed for either

hydrogels [78] or polymers [118]. To construct a polymer scaffold, these systems can easily print 20% poly-lactic-co-glycolic acid (PLGA) solutions and can handle viscosities up to 400 cp [78]. 3D structures comprising cell loaded hydrogel has been printed in the form of several rectangular layered scaffolds [119]. Other similar techniques and systems for printing hydrogels have capabilities to process thermal reversible hydrogels, such as a heating or cooling jacket around the syringe [118]. Researchers can mix and print cells within the hydrogel solution but will be challenged with similar sets of problems as those discussed earlier for inkjet printing.

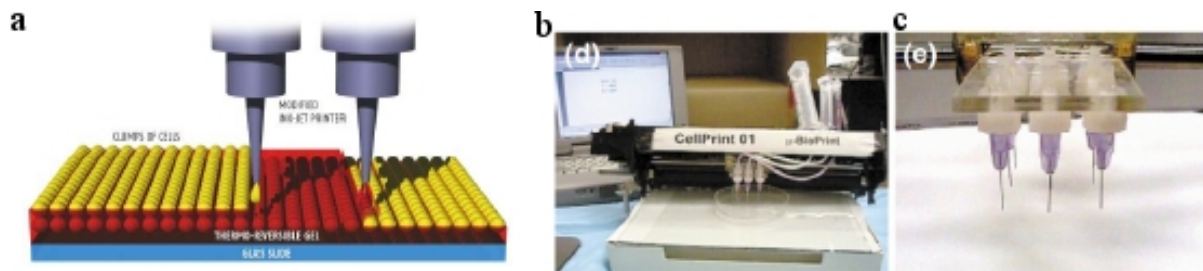


Figure 1.10: a) Schematic presentation of cell printing, b) real cell printer, c) part of the print head with nine nozzles [76]

### 1.3.1.3 Related technologies

**Acoustic or ultrasonic wave** bioprinting [79,117] is one of the developed bioprinting technologies. For single cell manipulation and analysis, the acoustic/ultrasonic bioprinting method provides picoliter precision (Fig 1.11). A piezoelectric substrate such as quartz is used to generate surface acoustic waves. The acoustic waves form an acoustic focal point and create pressure to induce placement of the picoliter droplets on demand [117].

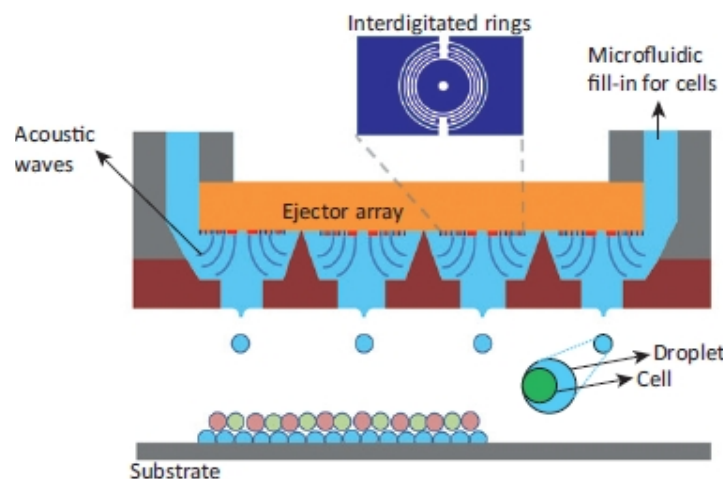


Figure 1.11: Setup for acoustic picoliter droplet generation [120]

### 1.3.1.4 Laser assisted deposition

Laser based approaches provide an alternative to above-mentioned printing techniques. The first laser bioprinting method is the laser guided direct writing (LGDW) [121] which is based on laser tweezers principles while the other laser-based technique is laser

assisted bioprinting (LAB) [122], which uses a pulsed laser source to induce vaporization of a metal film coated with cells or biological material on a ribbon of glass or quartz.

#### 1.3.1.4a Laser-guided direct writing (LGDW)

D.J. Odde and M.J. Renn for the first time [123] published the idea of using laser-induced optical forces with potential applications in 3D cell patterning for T.E. In 2000, they [124] used laser to guide living cells for viable deposition on a glass surface. They named it as "laser-guided direct writing" which can deposit cells with micrometer-scale precision (Fig. 1.12). Guiding the particle by laser radiation showed that the particles were instantaneously directed towards the centre of laser beam or more intense region of beam while continued travelling in axial direction of beam prorogation [125]. Placing a target surface in the laser path could deposit particles and continuously guide them toward the target surface. LGDW technique uses a low numerical aperture lens to focus the laser beam and to lead particles over long distances, up to 7 mm.

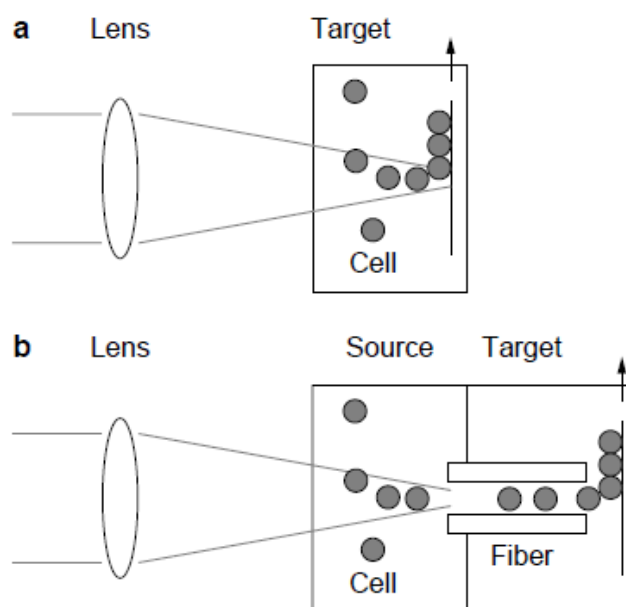


Figure 1.12: Laser-guided-direct-writing system; a) Laser light is focused weakly into a suspension of particles, b) Light is coupled into a hollow optical fiber and particles are carried through the fiber. [123]

#### 1.3.1.4b Laser assisted bioprinting (LAB)

Laser-Assisted Bioprinting (LAB) [126] based on Laser-Induced Forward Transfer (LIFT) [82–84] has emerged as nozzleless method and an alternative to overcome with the drawbacks of the conventional technologies. Numerous material has been deposited by laser-based direct writing, initially demonstrated for inorganic material [127] but since 2000, deposition of biomaterials is under extensive focus [128,129]. This technique has applications ranging from metal deposition [84] to the transfer of sensitive materials [130] like mammalian



embryonic stem cells [76,131]. It opens up new possibilities compared to conventional solvent-based deposition techniques such as screen or inkjet printing [132]. Since the LAB is one step transfer directly from donor to receiver substrate, it appears preferentially suitable for the biofabrication where sensitive and functional materials have to be arranged in a controlled manner without degrading their functional properties. Writing speed, optimum consumption of sample, post transfer viability of cells and resolution are the significant advantages.

Contrary to all bioprinting techniques [128,133,134], laser-assisted bioprinting (LAB) provides additional benefits: (i) deposition of pico to nanolitre [135] of hydrogels with different rheological properties can be carried out in a controlled and precise way [122,136–139]; (ii) different concentration of cells ranging from single [140] to dozens of cells [141] can be printed; and (iii) the printing speed (number of droplets per second) depends mainly on the pulse repetition rate of the applied laser. Printing speed of 5000 droplets per second has been demonstrated [122], which enables fast generation of large cell constructs. This represents a major prerequisite for the use of LAB in T.E.

#### **1.4 From LIFT to LAB**

LAB which is based on Laser-induced forward transfer (LIFT) is a direct-writing technique that allows depositing tiny material coated as a thin film on a transparent support to a selected target substrate by utilizing energy from a laser pulse (Fig. 1.13). A typical setup comprises three key components [141,142]: (i) a pulsed laser source, (ii) a ribbon coated with the material for transfer and (iii) a receiving substrate. The ribbon integrates three layers: (i) a support transparent to laser wavelength, (ii) a thin absorbing layer (like Ti or Au), and (iii) a bioink layer (few tens of microns). The laser pulses are focused on donor substrate which forward transfer a small fraction of donor film to the receptor substrate. The technique was initially demonstrated in vacuum [84] but now usually performed under standard laboratory condition [143].

A.D. Brisbane filed for the patent [82] of LIFT in 1967, describing the principle in detail however Levene et al. published the first work [127] on material transfer in 1970. The next application of LIFT phenomenon [84] was direct writing of 50  $\mu\text{m}$  wide copper lines on silicon and silica substrates under high vacuum condition of  $10^{-6}$  torr. Later, they demonstrated transfer of Aluminum [143] at atmospheric pressure. LIFT process can be performed in air and under room temperature without generating poisonous gases [144]. As it allows printing inorganic as well as organic material with micrometer resolution therefore, LIFT based bioprinting approach has been adapted with an aim of building 3D biological structures or

functional organs hence named as Laser Assisted Bioprinting (LAB) [122].

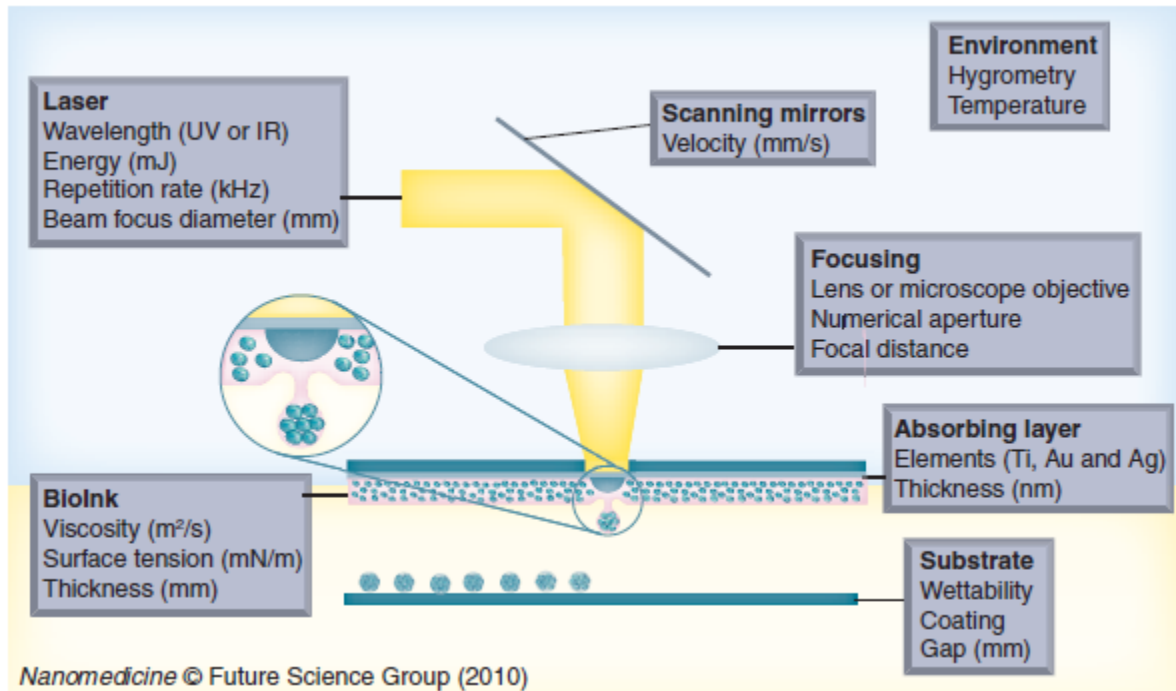


Figure 1.13: A typical diagram of LIFT for bioprinting method of operation [145]

#### 1.4.1 LIFT of solid materials

In context of transfer of solids, LIFT process can be categorized into two ways [144]. *One* is the ablation where thin film is ablated by laser irradiation for transfer. *The other* way of LIFT transfer is solid phase process. After successful demonstration of transfer of copper and aluminium by Bohandy group, the technique gained acceptance for depositing solid materials. Few examples of thin film transfer include gold [146], aluminium [147], titanium [148], germanium/selenium [149], tungsten [150–152] chromium [153], platinum [154] and nickel [155] where as metallic oxides include  $\text{In}_2\text{O}_3$  [153,156] and  $\text{V}_2\text{O}_5$  [157]. Vacuum deposition and other expensive techniques for solid film preparation make LIFT bit unfavourable. Moreover phase changes occurring during the transfer may cause serious and irreversible damages due to ablation from direct laser heating. Phase transformation and post transfer re-solidification of the material undergoing laser transfer, are also among major problems which inhibit deposition of sensitive materials by LIFT.

#### 1.4.2 LIFT of liquids

Transfer of functional materials needs to be carried out such a way that their desired properties should remain intact. Therefore studies of the LIFT for liquid are oriented to demonstrate its feasibility to transfer different functional materials while their properties remains preserved. Studies include liquid ink on paste for fabrication of ultracapacitors [158],

batteries [159–162] chemical sensors [163] thin-film transistor [164,165].

### 1.4.3 Biomedical applications of LIFT

Creating a precise and complex tissue comprising several cell types arranged in a specific 3D pattern remains a challenge in T.E. LAB could be the solution [166]. It can produce high resolution 2 and 3D patterns, incorporating different cell types which includes: human osteoprogenitor cells [167], human endothelial cells [122] and human adipose derived mesenchymal stem cells which can subsequently be differentiated to fat [168]. Skin substitute [166] has also been reported and 3D tissue constructs *in vitro* [169] had shown tissue formation and functional cell-cell contacts. LAB has gained tremendous focus during last decade. Already published applications of LAB for biological molecules or cells are listed in [Appendix A](#).

## 1.5 State of Art and Printing Mechanism

Physical parameters contributing to the transfer process via LAB mainly include: laser energy e.g. beam diameter (laser fluence), composition of bioink in context of rheological properties (viscosity, elasticity etc). LAB in experimental context can be explained as follows:

### 1.5.1 Transfer mechanism and regimes

Laser pulse is focused through the donor-slide onto the interface between support and bioink which is evaporated locally. This rapid energy deposition leads to the generation of vapour pocket that expands and propels the material to the receiver. Depending on the temperature of the vapour/plasma pocket, there are three types of behaviours: sub-threshold (sub-threshold regime), jetting (jetting regime) and plume (plume regime). First study to demonstrate these regimes was conducted by Young et al. [170]:

#### 1.5.1.1 Sub-threshold regime

At sub-threshold fluence the expansion of vapour pocket is not energetic enough to detach any material from the donor. Cooling and condensation processes will dominate the thermal expansion of vapour pocket, ink layer will collapse back to its original form. [Figure 1.14a](#) indicates this sub-threshold regime. The value of threshold fluence will depends on properties of the material being used as absorption layer.

#### 1.5.1.2 Jetting regime

Once the threshold limit is crossed, it's a new beginning i.e. jetting. The area of the

vapour pocket increases with increasing energy. Interaction between vapour pocket and fluid nature of ink layer will control this behaviour. Theoretically elasticity and viscosity are considered as controlling parameters. At intermediate fluences, the jetting regime takes place, characterized by development of an irregular and turbulent jet which broke up into multiple parts after travelling a very short distance (Fig. 1.14b).

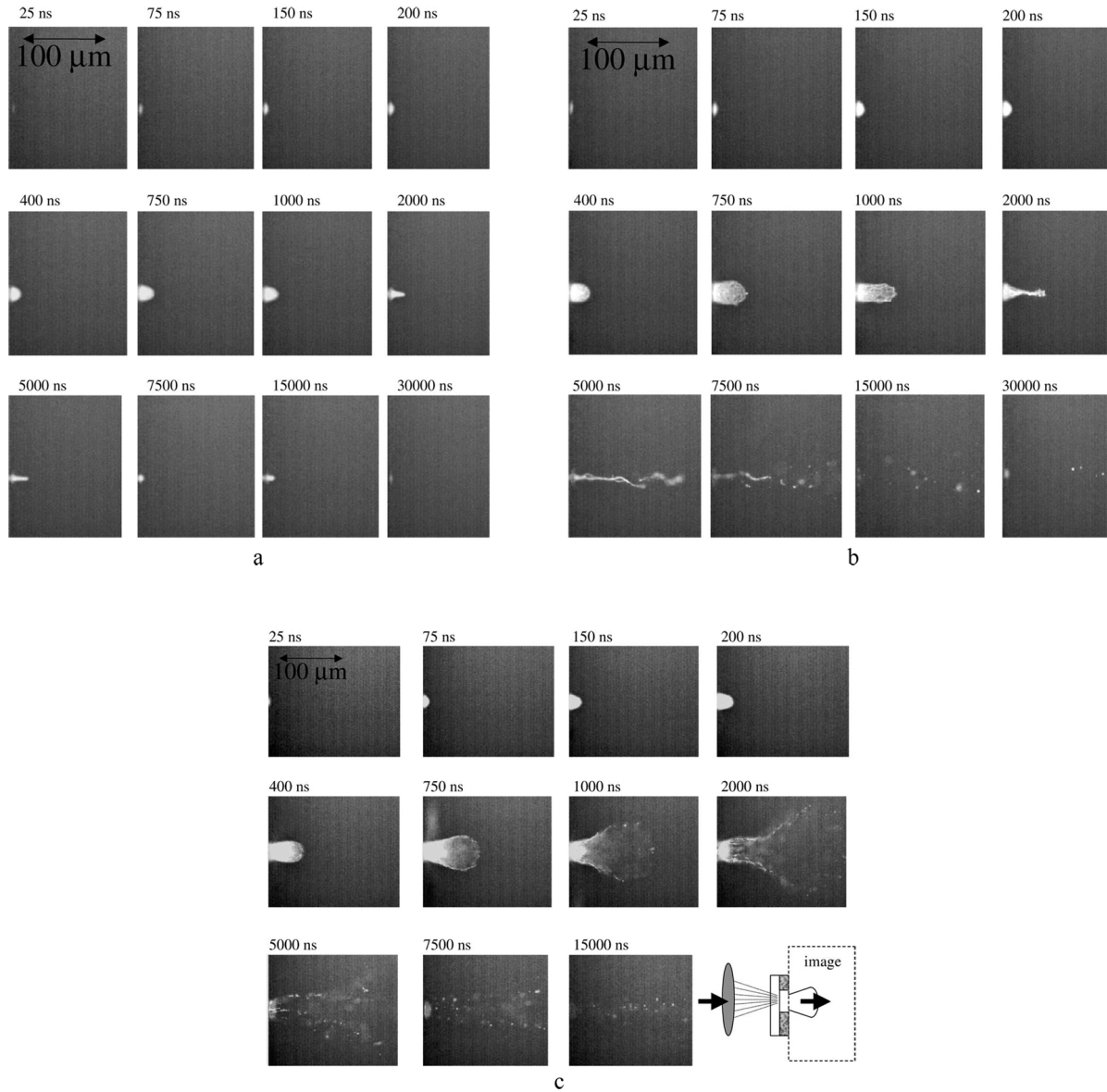


Figure 1.14: Different regimes observed during transfer, a) Fluence lower than  $0.026 \text{ J/cm}^2$  was observed as threshold, for 5-10 $\mu\text{m}$  thick  $\text{BaTiO}_3$  layer, while using 355 nm frequency tripled Nd:YAG ablation laser, b) jetting regime for fluences ranging from  $0.026$  to  $0.039 \text{ J/cm}^2$ , c) plume regime for fluences ranging from  $0.065$  to  $0.65 \text{ J/cm}^2$ . [170]

### 1.5.1.3 Plume regime

At higher fluences, vigorous protrusion occurs (Fig. 1.14c). The vapour pocket bursts with violent ejection of material hence termed as plume regime [170]. A lucid scheme (Fig. 1.15) of this mechanism [145] was published by Guillemot group.

## 1.5.2 Different parameters for LAB

LAB mechanism depends on many parameters (Fig. 1.13). A new insight [145] to above mentioned three regimes has been provided in light of (i) experimental approaches involving post-mortem observations and/or time-resolved imaging and (ii) numerical modelling of laser-induced hydrodynamics. LAB can be described in sequence of the events as follows:

### 1.5.2.1 Laser energy deposition (1 J/cm<sup>2</sup>)

Pulsed energy (ns lasers with UV wavelength or with near IR wavelength of 1064 nm) deposition leads to evaporation of the absorbing layer onto the bioink-support interface. This evaporation leads to a vapour bubble which expands towards the free surface.

### 1.5.2.2 Vapour bubble growth and collapsing (1 µs)

Growth and collapse of bubble are primary controlling phenomena of the printing regime (Fig 1.15). Moreover time-resolved imaging, which furnished time scale and morphological information [170,171], analytical (using Rayleigh-Plesset equation 1.1) and numerical modelling (37,38) incorporating the effect of different medium material properties (viscosity, surface tension) have been reported for bubble dynamics.

$$R \ddot{R} + \frac{3}{2} \dot{R}^2 = \frac{\kappa P_l}{\rho_l} \left( \frac{R_o}{R} \right)^{3\gamma} - \frac{(P_l - P_v)}{\rho_l} - 4\eta \frac{\dot{R}}{R} - \frac{2\sigma_l}{R\rho_l} \quad (1.1)$$

The modelling showed that compressibility of bioink controls the bubble dynamics. Bubble front reaches rapidly its maximum velocity (up to 100 m/s, 100 ns after plasma-induced generation) while the maximum bubble radius  $R_{\max}$  (i.e. when collapsing starts) is reached later (1.2 µs) [172].

### 1.5.2.3 Interaction of the vapour bubble with the free surface

Surface tension has to be taken into account for bubble interaction with the free surface due to significant size of the vapour bubble as compared to bioink thickness. In this regard, Pearson et al. [173] and Robinson et al. [174] have demonstrated the standoff conditions (i) bubble starts collapsing due to high pressure region generated in the bubble apex soon after it had attained its maximum radius ( $R_{\max}$ ) which may lead to a jet according to the dimensionless distance  $I = h/R_{\max}$  (where  $h$  represents the distance between the initial vapour bubble centroid and the free surface) [173,174].

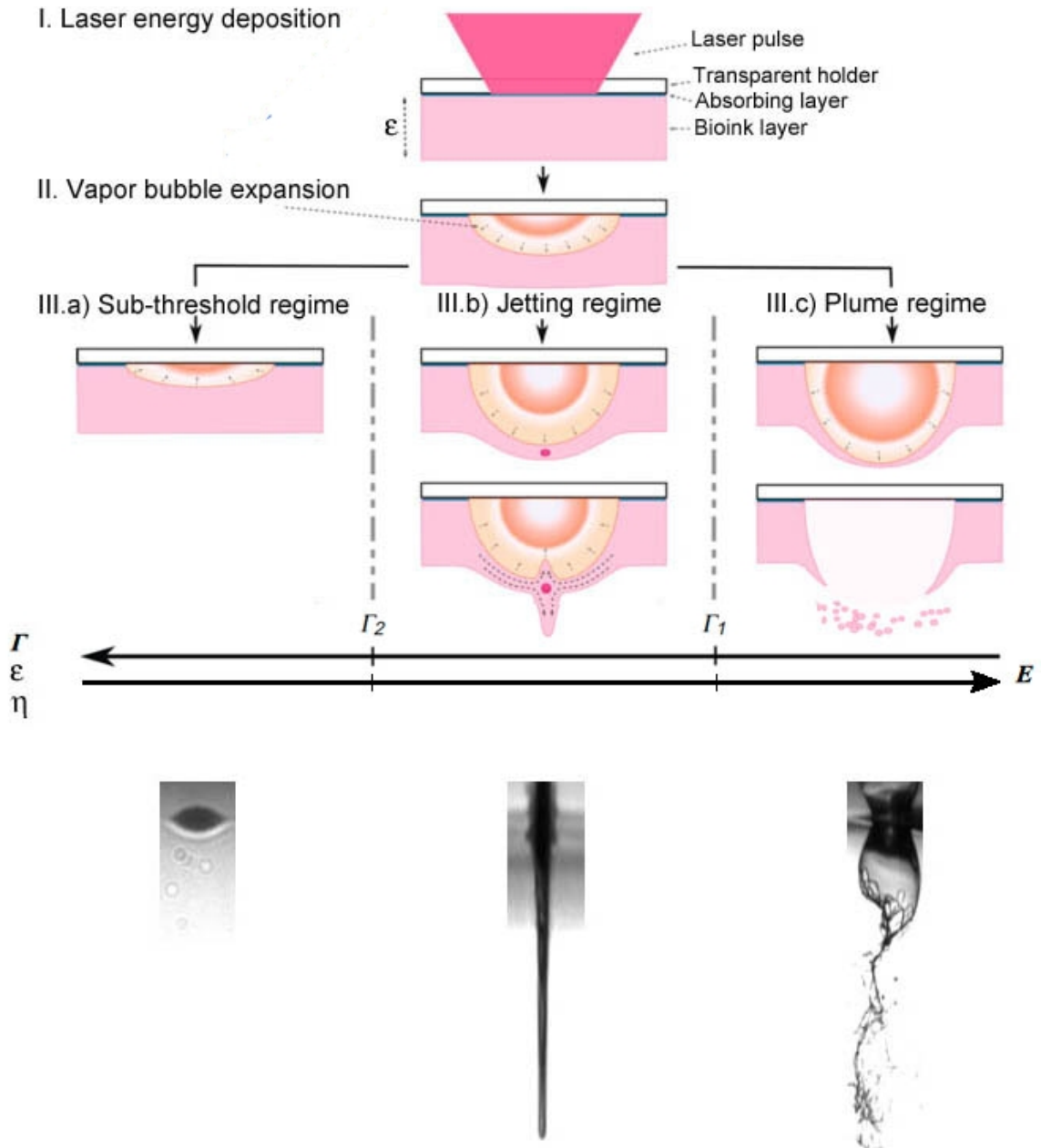


Figure 1.15: Sub-threshold, jetting and plume regime of LAB

- If  $\Gamma > \Gamma_2$  (threshold value): the droplet ejection cannot occur (Fig. 1.15 III.a), so called Sub-threshold regime.
- When  $\Gamma < \Gamma_1$ : the violent bubble expansion leads to bubble burst (Fig. 1.15 III.c). It is the plume regime.
- If  $\Gamma_2 < \Gamma < \Gamma_1$ : bubble collapse leads to jetting (Fig. 1.15 III.b). This is the jetting regime.

The sub-threshold regime is unable to deposit any material at all; the jetting material may be considered as operating regime for deposition of droplet but it suffers from multiple and disperse droplets; whereas the plume region is completely splashing and can't be favoured.



#### 1.5.2.4 Jetting

Duocastella et al. had demonstrated that a long and uniform jet is developed, which advances at a constant velocity (between 20 to 150 m/s, depending on experimental conditions) until it reaches the receptor substrate [139]. Jet produced with lowest fluences (e.g.  $I \rightarrow I_2$ ), may recoil before reaching substrate. However, reduction of the gap could be a choice for material deposition. Whereas jets caused by higher fluences ( $I \rightarrow I_1$ ), have inertia high enough to suppress the recoiling forces (surface tension and elasticity) of bioink. After attaining a certain length, jet becomes unstable and finally breaks due to so-called Rayleigh-Plateau instability.

#### 1.5.2.5 Deposit-landing

Printed droplets may exhibit different morphologies (splashing and spreading phenomena) depending on substrate surface properties, kinetic energy of the droplet/jet as well as bioink viscosity. Basically, for moderate initial energies, the surface tension will be able to absorb the initial kinetic energy while for higher energies, the surface tension couldn't overcome outward motion as the drop spreads upon impact, which induces formation of small satellites droplets (Fig. 1.16). Experimentally, droplets as small as 8  $\mu\text{m}$  were produced by reducing the air gap distance i.e. conditions close to the sub-threshold regime ( $I \rightarrow I_2$ .) [175].

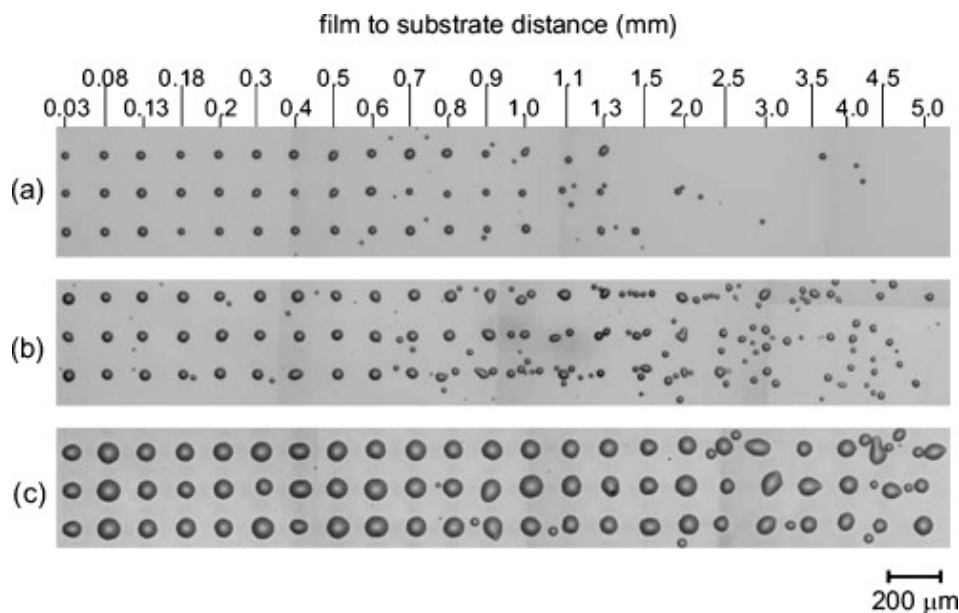


Figure 1.16: Optical microscopy images of three microarrays obtained varying the film to substrate distance, prepared with three different energies: (a) 170 nJ, (b) 360 nJ, and (c) 630 nJ. [172]

- Droplet volume shows a linear dependence on the laser pulse energy. High energy pulses lead to irregular droplets, satellites and/or splash (Fig. 1.16) [172].
- The laser spot size, laser fluence, bioink viscosity and film thickness [176] are controlling parameters for quantity of items transferred (Fig. 1.17). Duocastella et al.

had demonstrated that drop size can be controlled by varying the spot size of the laser pulse [172]. Minimum achieved diameter reported so far is 30 microns and transferred volumes are in the range of few hundred pL to nL ([140,172].

- The transfer material undergoes an average acceleration of  $10 \times 10^6 g$  and deceleration of an average  $10^6 g$  [137].

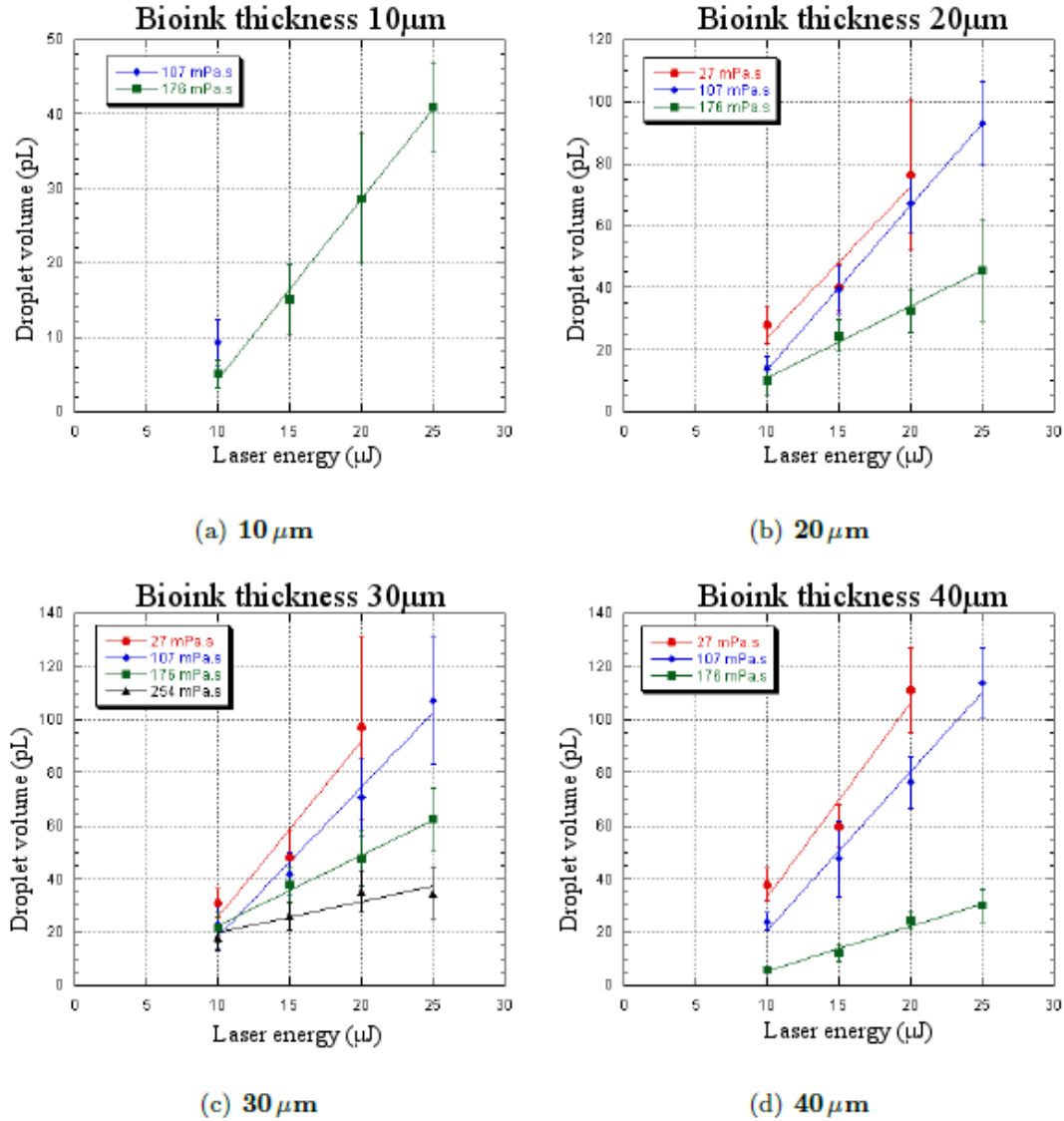


Figure 1.17: Droplet volume as function of laser energy, film thickness and viscosity [176]

In a comprehensive scenario, Sub-Threshold, Jetting and Plume regimes do not solely result from laser energy ( $E$ ) intensity but, also, of rheological properties of the bioink (viscosity ( $\nu$ ), surface tension ( $\sigma$ ) and film thickness ( $\epsilon$ )). In other words, jetting is not simply occurring on the basis of an energy threshold mechanism but rather on the basis of a complex  $\Gamma(E, \nu, \sigma, \epsilon)$  threshold mechanism. Over a given laser energy for which a vapour bubble is formed, the whole mechanism can be shown as Figure 1.15.



This clearly indicates that LAB mechanism needs further research based on such parameters for better controlled printing with cellular resolution especially for cell printing. The transition from sub-threshold to jetting and juvenescence of the jetting regime should further be investigated. Moreover receiver substrate needs to be placed very close to the donor-slide (Fig. 1.16), as demonstrated by Duocastella et al. [172], printing at distances larger than 5 mm leads to loss of control on the printing mechanism. Apart from satellites droplets, resolution is deteriorating the printing process which could not be afforded in LAB with an aim of proper cell positioning with cellular resolution. Studies involving time-resolved imaging [139,177–181] could provide a better insight to the printing mechanism.

### 1.5.3 Modelling studies

Different numerical modelling studies has been performed based on laser interaction with matter, bubble dynamic and landing impact on substrate.

#### 1.5.3.1 Laser interaction with matter

The interaction of the laser pulse with the target (based on the transmission of the light energy to the donor) has been studied by Barron et al. [182,183]. Absorption of laser energy (rapid heating and cooling of the absorbing layer) leads to the photomechanical and/or thermal shocks. The penetration depth of laser is far less than thickness of the absorbing layer. Even the temperature of absorbing layer can vary from  $10^2$  to more than  $10^3$  K but less than 5% of the transferred material is exposed to the temperatures higher than room temperature. The temperature evolution of the interface absorbing layer/bioink is shown in Figure 1.18 (a) as a function of time after the laser pulse.

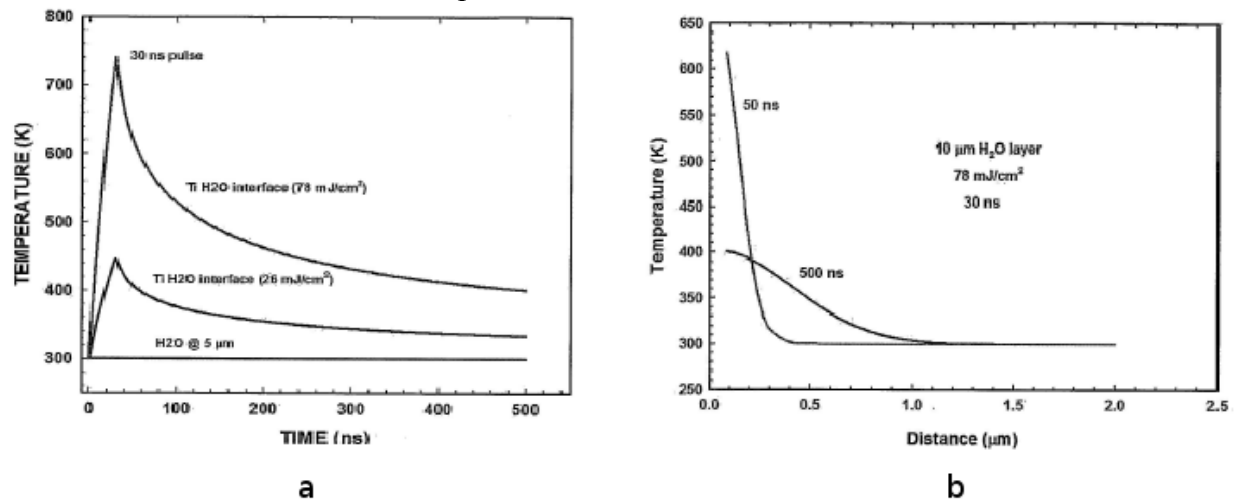


Figure 1.18: a) Temperature at titanium/bioink interface vs time for a pulse of 30 ns and fluences of 26 and 78 mJ/cm<sup>2</sup>, b) Thermal penetration into the bioink at 10 microns of absorbing layer after 50 and 500 ns of the pulse [182]

The energy absorbed by the absorbing layer is quickly converted into thermal energy

[183]. Overheating of the absorbent layer leads to ejection of the bioink. This method of ejection of material is restricted to less fragile biological elements because the energy transferred to the bioink is high which may cause damage to biological properties. But in all cases, the absorbing layer converts the incident laser light energy into thermal energy by absorption and heat conduction and propagates it to bioink. Heat transfer depends on the nature (reflectivity, thermal conductivity) and the thickness of this layer. For long pulses, the temperature of the absorbing layer rises to the boiling temperature of bioink, whereas for short pulses mechanical forces (shock waves) are responsible for the ejection of material.

Energy conversion is very rapid in the absorbing layer but thermal penetration into the hydrogel is negligible. [Figure 1.18b](#) illustrates the thermal penetration as function of distance, 50 and 500 ns after the laser pulse. After 50 ns, the thermal penetration inside the bioink is less than 400 nm and is only 1.2 microns after 500 ns. The summary of this interaction is:

- i. heating the material through laser absorption till partial or complete volatilization
- ii. through thermo-acoustic mechanism generated by the photo-ablation due to incident laser energy,
- iii. a combination of (i & ii)

### **1.5.3.2 Bubble expansion**

Bubble expansion leads to formation of a droplet containing cells. The proposed modelling approach is also applicable to other methods based on sacrificial layer energy absorption (DRL) assuming that the thickness used for conversion of energy (usually <100 nm) is negligible.

Wang et al. included four materials: bubble of vaporized gas, air, bioink and cells [184,185] for computational modelling of expansion and the formation of the bubble. Cell taken as a solid material, a Lagrangian mesh was used for its simplicity and fast implementation, while the bubble, the bioink and air were modelled by an Eulerian mesh to prevent its distortion during ejection of material ([Fig. 1.19](#)). The cells/bioink interface was modelled using the Euler/Lagrange coupling option to incorporate the viscosity effect in the interface layer (cell/bioink), and interactions between bioink, the gas bubble and air were modelled by defining these materials in multi-material groups. Cell centre velocity, cell centre acceleration, and pressure were evaluated to determine cell mechanical profile during ejection. The estimates predicted that the cell first experienced very high pressure (221 MPa) and acceleration ( $10^9 \text{ m/s}^2$ ) at the beginning period of bubble expansion. After a very short

period ( $\sim 0.1 \mu\text{s}$ ), both pressure and acceleration reduced significantly. The cell top surface region (Fig. 1.19b Element 1) usually experienced the highest pressure level, followed by the bottom surface (Fig. 1.19b Element 3) and the middle regions (Fig. 1.19b Element 2). The cell viability affected adversely by large initial pressures. This modelling study helped to optimize the cell direct writing process by better estimating the landing velocity for given operating conditions.

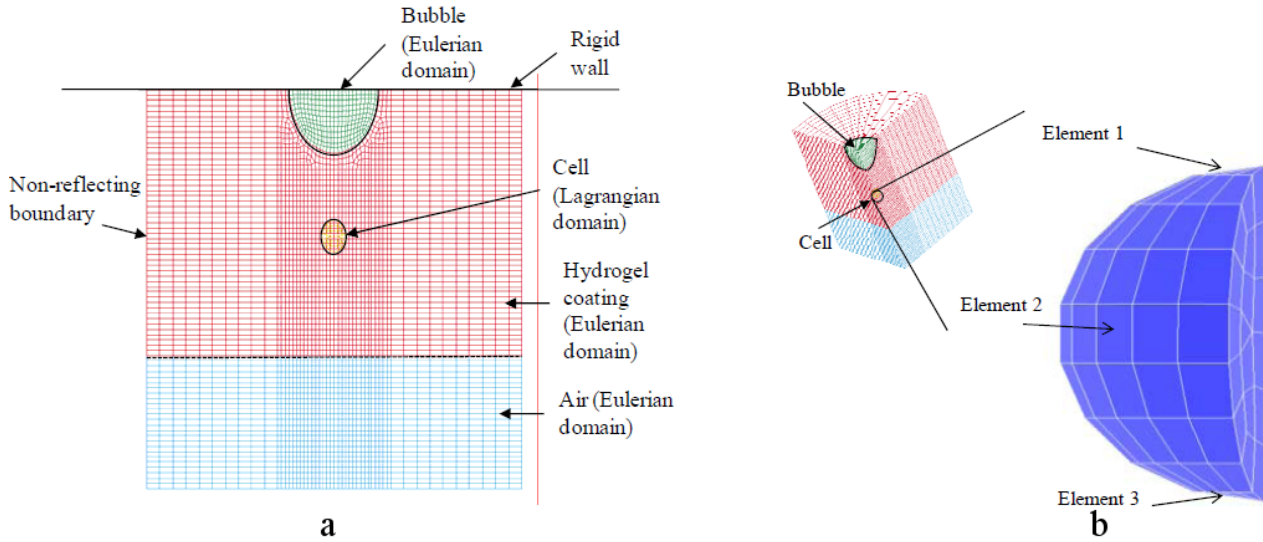


Figure 1.19: Areas of computing and networking of the system. (a) Areas of calculation Lagrangian and Eulerian coupled and (b) distribution of elements of the cells [185]

### 1.5.3.3 Landing impact of droplet

Upon landing, the droplet undergoes a significant deceleration and one or more impacts on the receiver substrate which can be cushioned by a hydrogel layer to absorb shocks. However, cells survive much higher external force than they are able to afford in equilibrium conditions. Wange et al. [184] argues that landing process and stress induced by the impact can be modelled using the equations of conservation of mass, momentum and energy. The constitutive model defines the dependence of the stress on strain, strain rate and temperature. Usually a model for material also includes a fracture criterion to determine whether the material loses its ability to withstand stress/strain.

From these modelling studies [184,185], a result presented in Fig. 1.20, we see that :

- peripheral regions of cells especially the lower region experience higher stress than the centre (Fig. 1.20a) i.e. cell membrane is easily affected by the impact
- the profile of mechanical loading and cell post-transfer viability depend on the initial velocity of the droplet and the thickness of the hydrogel of the receiver substrate
- two important impact processes can occur during the landing process, the first interaction between droplet and the hydrogel and the second between the cell and the substrate (Fig. 1.20a & d).

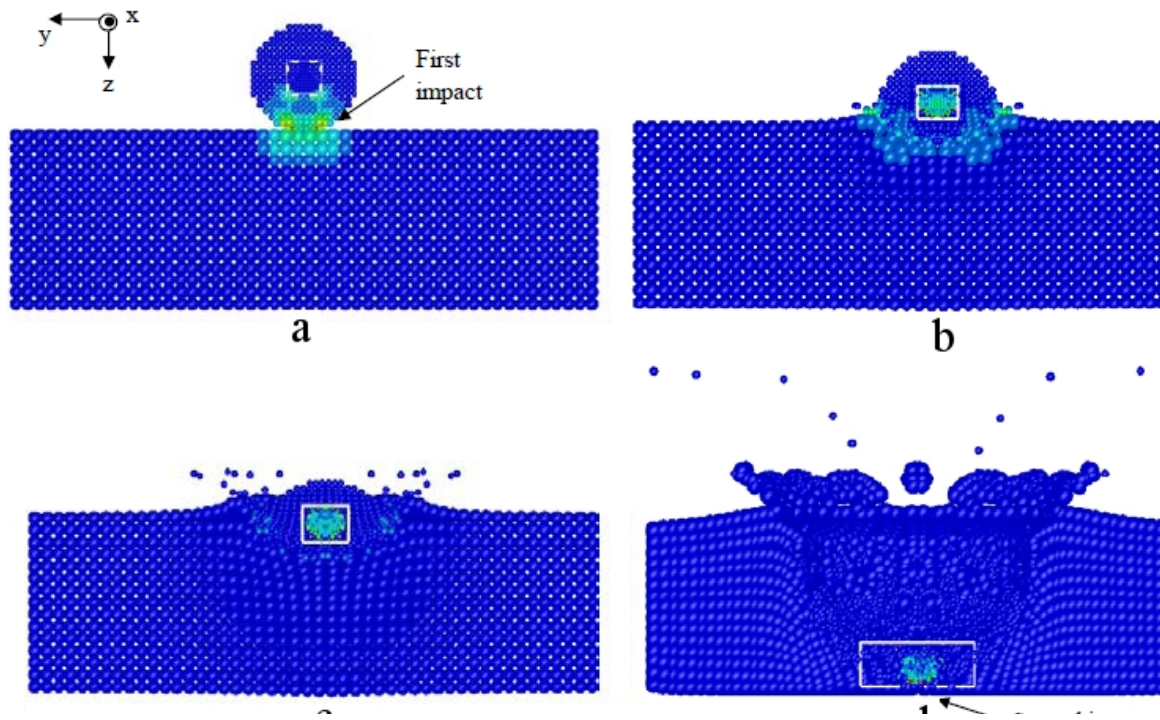


Figure 1.20: Simulation of Landing process at (a) 5.9322 ns (b) 0.1359  $\mu$ s (c) 0.2725  $\mu$ s and (d) 2.4865  $\mu$ s [184].

It shows that cell damage induced by the impact depends on the magnitude of stress, acceleration and/or shear deformation. Three different processes are involved in mechanical stress induced by the printing process: droplet formation (acceleration), shear stress of cells in the jet and the landing of droplets on the receiver substrate (deceleration). During jet formation, the rapid expansion of the high pressure bubble accelerates the jet. This acceleration can be as high as  $10^5$ - $10^9$  times of g. Higher the laser fluence, greater the pressure is, which leads to a higher acceleration/speed. Cell viability found to be closely related to the thickness of hydrogel on the receiver substrate. Cell viability was 95% when the receiver substrate is a layer of plaited Matrigel™ 40  $\mu$ m thick [182]. Endothelial cell viability study, by Catros et al. [186], demonstrates that high cell viability can be maintained for thinner Matrigel™ film (e.g. for 20  $\mu$ m thick Matrigel™ film) when laser energy is reduced (e.g. 8  $\mu$ J), and/or by using a viscous bioink. Indeed increasing the bioink viscosity improved the viability of cells. Since an increase of the bioink viscosity reduces jet velocity, it tends to minimize impacts intensity, thus improving cell viability after printing. In most of the cases, dependence of cell viability on laser fluence indicated the existence of mechanical damage. Indeed greater laser fluence results in a higher cell acceleration (or deceleration) and a higher speed, which results in a lower cell viability.

## 1.6 Purpose of the Study

In conventional setup of the LAB (Figure 1.13) donor is fixed in an inverted position and has following inherited limitations.

- This setup faces a major drawback of inhomogeneity of the liquid film (bioink). A uniform thickness with micron level accuracy all over the surface of the donor could not be possible in conventional setup because donor needs to be fixed in inverted position. Inhomogeneity of the liquid films results into formation of local areas with different thickness which seriously compromises the LAB process and leads to irreproducibility.
- Gap between the donor and receiver is very small usually between 500 to 1500  $\mu\text{m}$ . Such small distances may lead to contact transfer and contamination. Moreover, printing at distances larger than 2 mm leads to loss of control on the printing mechanism and formation of satellite droplets. This deteriorates the resolution of the printing process which could not be affordable in LAB.
- High-speed jetting has not been explored, currently potential applications of high-speed jetting are unknown.

It is very much clear from section 1.4 and 1.5 that LAB mechanism needs further research based on parameters like energy, viscosity and film thickness for better controlled printing with cellular resolution especially for cell printing. The transition from sub-threshold to jetting and juvenescence of the jetting regime should further be investigated. Studies involving time-resolved imaging could provide a better insight to the printing mechanism.

## **1.7 Objectives of the Thesis**

The overall objective of the thesis is to study the physical mechanisms (droplet ejection mechanism in relation with the laser conditions and the rheological properties of the bioink) involved in the printing of biological materials by laser. To carry out this project secondary objectives were proposed:

- to study a novel configuration of LAB and to study the effects of upward printing on jet dynamics and transfer process
- defining transition from sub-threshold to jetting regime in geometrical context by Time Resolved Imaging
- study the influence of printing distance (larger than conventional separation distances i.e. ~2mm) on the printing and morphology of the printed droplets
- TRI study for influence of cell concentration on jet dynamics and evaluate the novel configuration for cell printing
- propose a comprehensive mechanism of LAB for upward printing



## **CHAPTER 2**

### **2 MATERIALS & METHODS**

This chapter focuses on the materials and methods used to carry out different experiments of laser printing to perform transfers and to characterize the deposited materials. The first part is devoted to the different experimental systems used. The second part explores the composition of the bioink followed by the preparation of the target described in the third part. The fourth part describes the different characterization techniques for post-transfer analysis of transferred biomaterials. The fifth part is dedicated to the time resolve imaging technique used to study the LAB mechanism by shadowgraphy. Finally, experimental arrangements are described in the sixth part.



<u>CHAPTER 2</u> .....	31
<u>2 MATERIALS &amp; METHODS</u> .....	31
<u>2.1 Experimental Devices to Deposit Biomaterials</u> .....	33
<u>2.1.1 Choice of the laser</u> .....	33
<u>2.1.1.1 Wavelength</u> .....	33
<u>2.1.1.2 The pulse duration “<math>\tau</math>” and the repetition rate “<math>f</math>”</u> .....	33
<u>2.1.1.3 The beam quality</u> .....	33
<u>2.1.2 Transfer station</u> .....	33
<u>2.2 Sample Preparation</u> .....	35
<u>2.2.1 Choice of the absorbing layer</u> .....	35
<u>2.3 Preparation of the Cartridge</u> .....	36
<u>2.3.1 Coating of the absorbing layer</u> .....	36
<u>2.3.2 Preparation of hydrogel</u> .....	36
<u>2.3.3 Depositing the hydrogel film</u> .....	37
<u>2.3.4 Bioinks containing cells</u> .....	38
<u>2.3.5 The printing patterns</u> .....	39
<u>2.4 Characterization Techniques for Post-Transfer Analysis</u> .....	40
<u>2.4.1 Optical microscopy</u> .....	40
<u>2.4.2 Optical profilometry</u> .....	40
<u>2.4.3 Statistical analysis</u> .....	41
<u>2.4.3.1 Drop volume</u> .....	41
<u>2.4.3.1a Volume calculations</u> .....	41
<u>2.4.3.1b Calculation of uncertainty in drop volume</u> .....	42
<u>2.5 Time-Resolved Imaging (TRI)</u> .....	43
<u>2.5.1 The shadowgraphy</u> .....	43
<u>2.5.2 TRI setup for study of ejection mechanism</u> .....	44
<u>2.5.2.1 The optical assembly</u> .....	45
<u>2.5.2.2 Calibration</u> .....	45
<u>2.5.2.2a Energy profile</u> .....	45
<u>2.5.2.2b Pixel calibration</u> .....	46
<u>2.5.2.3 Delay</u> .....	46
<u>2.5.3 Printing configurations</u> .....	47
<u>2.5.3.1 Novel configuration</u> .....	47
<u>2.5.3.2 Conventional configuration</u> .....	47
<u>2.6 Experimental Arrangements for TRI</u> .....	47

## **2.1 Experimental Devices to Deposit Biomaterials**

This section details the prototype experimental machine, installed at Inserm U1026 University of Bordeaux Segalen, which was used for these studies. The INSERM prototype transfer station was developed in 2007.

### **2.1.1 Choice of the laser**

Laser characteristics play vital role and have special importance in designing laser printer for biology which include: first to determine its suitability to work with biomaterials or living cells and secondly to perform rapid prototyping applications. In this context following laser characteristics need to be considered:

#### **2.1.1.1 Wavelength**

The prime objective of bioprinting is to print biomaterials with post transfer retention of functional properties. To avoid alteration in biological properties due to potential distortion of DNA by ultraviolet (UV) radiation, near infra-red (IR) lasers are preferred over UV lasers.

#### **2.1.1.2 The pulse duration “ $\tau$ ” and the repetition rate “ $f$ ”**

Higher frequency laser with short pulse duration is required to develop high speed processes. So it is necessary to have a high frequency ( $\sim$ kHz) laser with a short pulse duration ( $\sim$ ns).

#### **2.1.1.3 The beam quality**

The divergence  $q$ , the spatial mode TEM and peak to peak (ptp) stability of laser pulses must be taken into account to ensure reproducibility, stability and high resolution of the system. A laser transfer station dedicated to T.E. applications should be versatile and have a designed flexibility of performing procedures beyond the simple biological impression. So, the average laser power  $P$  must be high enough to perform additional processes such as micro-machining, sintering etc. Keeping in view these criteria, a laser crystal Neodymium-doped Yttrium Aluminium Garnet; Nd:YAG (Navigator I, Newport Spectra Physics, United States) is used in our transfer station with the following specific properties:

$$\lambda = 1064\text{nm}, \tau = 30 \text{ ns}, f = 1\text{-}100\text{kHz}, q = 3.4 \text{ mrad}, \text{TEM}_{00}, \text{ptp} < 1.5\% \text{ rms}, P = 7\text{W}$$

### **2.1.2 Transfer station**

In order to print multi-type patterns and to build three-dimensional (3D biostructures) biological structures, a workstation (Novalase SA Canéjan, France) (Fig. 2.1a) integrated with a sophisticated positioning system for 5 donors (Fig. 2.1b) was used.

The substrate is held on a motorized micrometric translation stage (x,y,z) having a resolution of  $1\mu\text{m}$  in horizontal axes (x,y) and  $5\mu\text{m}$  along vertical axis (z). Five different targets (Fig. 2.1b) can be simultaneously loaded for multi-color printing with motorized carousel of high resolution ( $1^\circ$  angular resolution). The positioning system of the substrate and the carousel are held on the same vertical axis with different focusing conditions keeping a constant gap (distance between donor and receiver substrate). Droplets are generated from donor target by deflecting the laser beam through a system consisting of two high speed scanning galvanometric mirrors (SCANgine 14 Scanlab, France), scanning speed up to 2000 mm/s, and a large optical field F-theta lens (S4LFT, Sill Optics, France) of focal length 58mm.

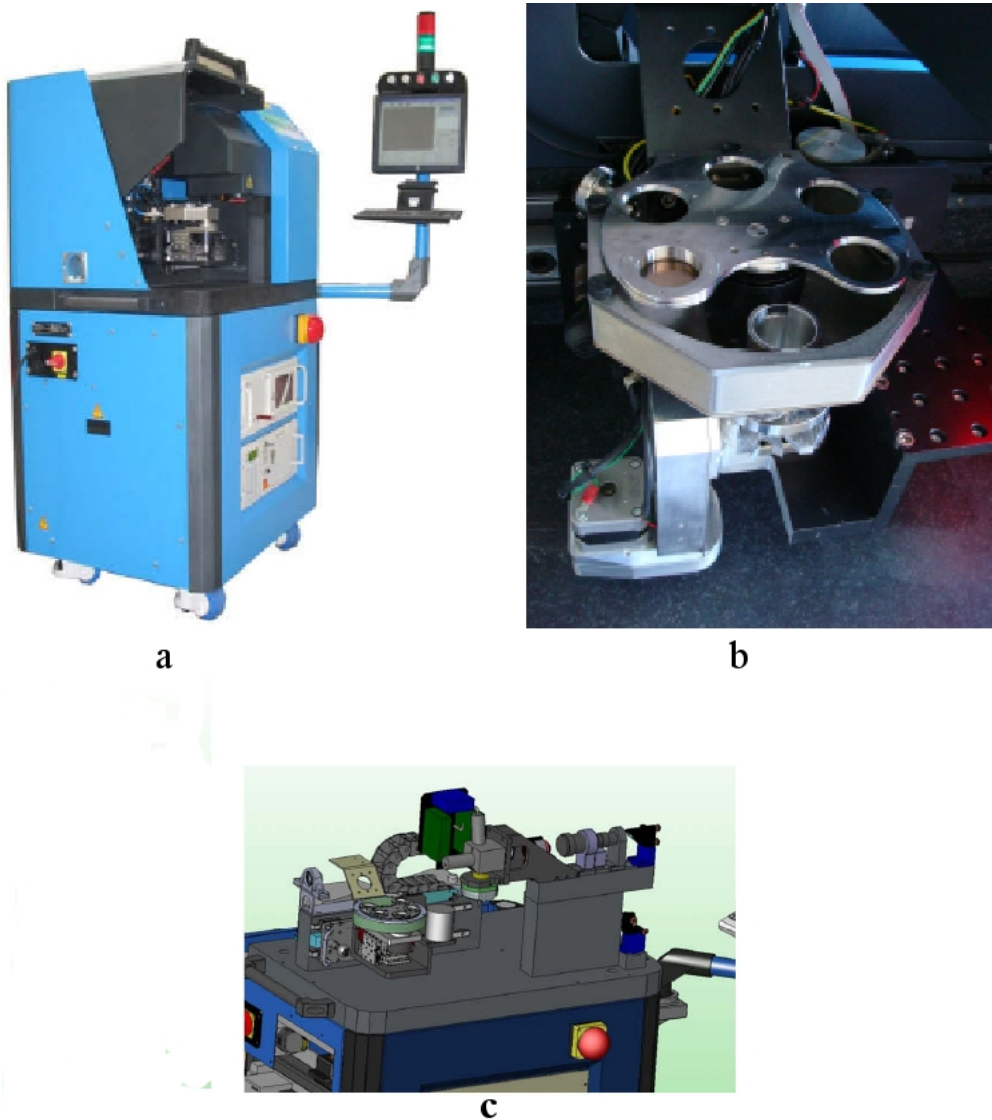


Figure 2.1: a) High-throughput laser printer for biomaterial, b) high resolution positioning system placed below the carousel holder with a loading capacity of five different ribbons, c) opto-mechanical setup

A beam expander (1x to 3x) and a diaphragm (opening range from 3 to 18mm) are placed in the optical path of laser output and galvanometric mirrors. And the edges of the

beam can be more or less removed depending on beam expander and aperture. A CCD camera is used to focus the target and the position (x,y,z) of the substrate through an optical system. Figure 2.1c illustrates the internal schematic diagram of the transfer station. The integration of laser and all the elements mentioned above was carried out with the help of Solidworks software. The positioning of the substrate, the steering carousel, video observation and design patterns are controlled by dedicated software developed by Delphi , ASTRÉE.

Table 2.1: Different conditions used for experimental printing

Printing Conditions	Laser Station	Time Resolved Imaging Setup
Laser	Nd:YAG	Nd:YAG
$\lambda$	1064nm	1064nm
$\tau$	30ns	30ns
$f$	1-100kHz	single-shot
$E$	5-25 $\mu$ J	9-160 $\mu$ J
$R_{focal}$	15 $\mu$ m	35-40 $\mu$ m
Ablator	Au (30nm)	Au (30-50nm)
Focalisation	Lens F-Thea 58mm	Microscopic objective (10x, NA 0.25)
Target positioning	Mechanical	Mechanical
Moving element	Laser	Target

## 2.2 Sample Preparation

### 2.2.1 Choice of the absorbing layer

As discussed in the introduction (Chapter 1), the donor is composed of three layers i.e. so-called ribbon (Fig. 2.2) in this thesis. The ribbon is a multilayer component made of a transparent glass slide onto which a thin layer of liquid (bioink) with an embedded heat sensitive biological material (e.g. biomaterials, cells, biomolecules) is spread. It integrates three layers: *i*) a support transparent to laser wavelength, *ii*) an absorbent layer (like Ti or Au) to allow conversion of the laser energy, and *iii*) a bioink layer (few tens of microns) incorporating the printing material. The transparent support is, in our case, a 1.5mm thick quartz disk of 30mm diameter. The absorbent layer (gold) must absorb the laser energy, that's why a thin metallic film (50nm) is used. The absorption coefficient  $A$  of this layer is defined by the Fresnel relations [187] with the wavelength  $\lambda$ , the reflection coefficient  $R$  of the metal,  $n$  is the real part of the complex refractive index of the metal,  $\kappa$  is its imaginary part.

$$A(\lambda) = 1 - R = \frac{4n}{[(n+1)^2 + \kappa^2]} \quad (2.1)$$

The skin depth  $\delta$ , or penetration depth, that is the length over which the laser wave is absorbed, depends on  $\lambda$  and  $\kappa$  according to the relation:

$$\delta = \frac{\lambda}{2\pi\kappa} \quad (2.2)$$

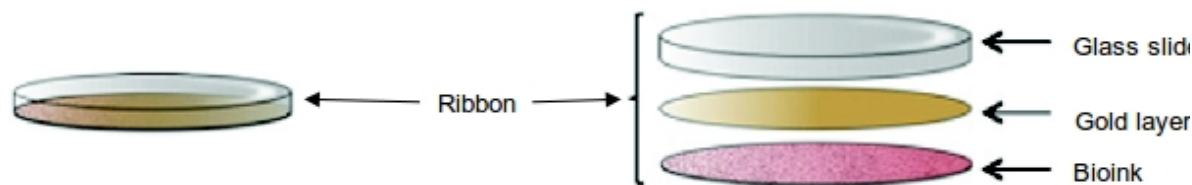


Figure 2.2: Ribbon

Energy absorption varies according to characterise of the absorbent metal used. Table 2.2 gives the optical properties of gold for the IR wavelength of the laser transfer station (1064nm). It is noted that in the near IR gold absorbs less than 1% of the laser energy. The thickness of the absorbent layer should be equal to or greater than the skin depth, namely, at least 25nm for gold for 1064nm laser pulse. Hence the liquid film is not directly heated by the laser pulse.

Table 2.2: Optical properties of gold for 1064 nm

$\lambda(\text{nm})$	Element	n	$\kappa$	A (%)	R(%)	$\delta(\text{nm})$
1064	Au	0.1	6.54	0.91	99.09	25

## 2.3 Preparation of the Cartridge

### 2.3.1 Coating of the absorbing layer

The quality and cleanness of the donor glass slide determines printing accuracy because scratches and impurities disturb the laser light absorption and hence the jet formation. First of all, the slides were cleaned with detergent, rinsed with distilled water and then dried with paper towel. Once cleaned, they are placed in a gold cathode spray (Emscope SC500, Elexience) to be coated for 2 minutes to obtain a gold layer about 50nm thick.

### 2.3.2 Preparation of hydrogel

The hydrogels used for the experiments are solutions of sodium alginate (Protanal 10/60, FMC Biopolymer, Norway) (see Appendix B) prepared with different concentrations i.e. 0.5% to 1% in weight to volume ratio (w/v) with deionized water. Glycerol (glycerol RP, Normapur, Prolabo, France) with 30% volume/volume ratio(v/v) and bovine serum albumin (BSA fraction V, Eurobio, France) 15 mg/ml were also added. The use of glycerol increases the evaporation temperature of the solution and the BSA with its surfactant properties,

improves the spreading of the film on the gold coated glass slide and thus limits the hydrophobicity. The viscosities of organic inks used in the experiments were determined by using applied stress rheometer (AR1000, TA Instruments). The graph in (Fig. 2.3) shows the evolution of the viscosity of organic inks containing 30%(w/v) glycerol and 15mg/mL BSA as a function of alginate concentration (w/v) for an applied stress of 5Pa. Exponential growth is observed; the evolution of the dynamic viscosity of the bioink follows the following law:

$$\nu(mPa)=10.3\times e^{2.27\times C} \quad (2.3)$$

where C represents percentage concentration of alginate

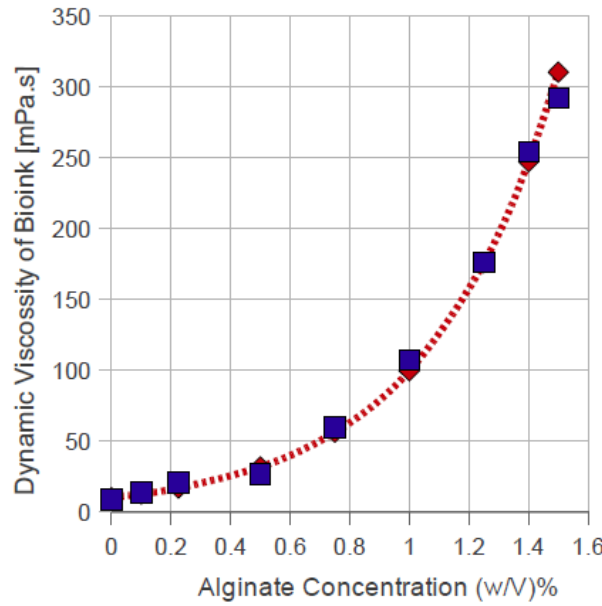


Figure 2.3: Dynamic viscosity [mPa.s] of bioinks (30% (v/v) glycerol and 15 mg/mL BSA for different concentrations of alginate (w/v)%

Other viscous liquid solutions used in the experiments of the thesis are water based and (10 v/v%) glycerol solutions with 2, 4 and 6 (w/v)% alginate. First, alginate is dissolved in 90 v/v% water. Later 10 v/v% glycerol is added to these solutions resulting in 2, 4 and 6 (w/v)% alginate concentration.

### 2.3.3 Depositing the hydrogel film

The hydrogel is then deposited as a thin film on the gold coated glass slide by micrometer film applicator (3570, Elcometer, France) (Fig. 2.4). To ensure that the thickness deposited on the slide with the applicator, the necessary volume (V) to obtain a thickness ( $\epsilon$ ) is deposited on the glass slide and the applicator is set (Fig. 2.4b) to desired thickness ( $\epsilon$ ). Indeed  $V=S\times\epsilon$  where S is the area of gold coated glass slide, which is a disk of radius 15mm. The hydrogel film becomes as:

$$V_{[\mu L]} \approx 0.7 \times \varepsilon_{[\mu m]} \quad (2.4)$$

hence for a standard microscope glass slide (25mmx75mm) we get:

$$V_{[\mu L]} \approx 2 \times \varepsilon_{[\mu m]} \quad (2.5)$$

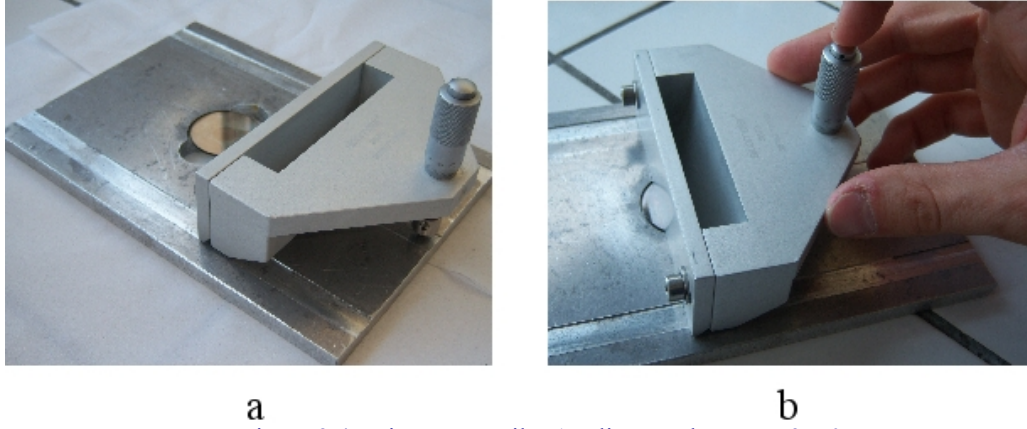


Figure 2.4: Micrometer Film Applicator Elcometer 3570

Table 2.3 is an example of volumes matching to thicknesses studied in U1026. For example, for a thickness of 40 $\mu$ m, it will require 28 $\mu$ L of solution and the applicator is adjusted to 40 microns.

Table 2.3 Volume to thickness correspondence

Thickness ( $\mu$ m)	10	20	30	40	50
Volume ( $\mu$ L)	7	14	21	28	35

$$1 \mu L = 1 \text{ mm}^3$$

### 2.3.4 Bioinks containing cells

D1 ORL UVA (D1) cell line is purchased from ATCC (LGC Standards, Molsheim, France). D1 are grown on plastic dishes in DMEM Low Glucose (GIBCO, Life Technologies) supplemented with 10% foetal bovine serum (Lonza), in a controlled atmosphere (5% CO<sub>2</sub>, 100% humidity, 37°C). For cell printing experiments, the bioink is composed of a concentrated cell suspension (10<sup>6</sup>-10<sup>8</sup> cells/mL), and the receiver substrate of a glass slide covered by a layer of collagen type 1 (2 mg/mL, BD Biosciences, Pont de Claix, France). Briefly, when cells reach 80% confluency, they are detached and prepared as a suspension. For the experiments, a suspension of concentrated cells was prepared extemporaneously (called the bioink). For that purpose detached cells were collected by centrifugation, washed once by PBS 0.1M, and the pellet was put in DMEM at a final concentration of 1, 5, 10, 50 or 100 million cells/mL. After the printing process, the receiver is incubated with few medium for 45 minutes to allow cell to adhere to the underlying collagen, before being completely



covered with medium and incubated for cell culture (5% CO<sub>2</sub>, 100% humidity, 37°C). For cell viability analysis, 24 hours after printing, cells are stained using Live/Dead assay kit (Invitrogen) according to manufacturer's instructions. Briefly, the samples are incubated in 2µM calcein-AM and 4µM ethidium homodimer (EthD-1) in PBS for 20 minutes in controlled atmosphere (5% CO<sub>2</sub>, 100% humidity, 37°C) and samples are observed using a fluorescent microscope (Axiovert 25, Zeiss).

The bioinks with different concentrations of cells are spread on clean and sterilized transparent gold (50nm thickness) coated glass slides. Clean and scratchless glass slides are used to avoid defects in laser light aberration and to maintain printing accuracy. The cell ink suspension is first dropped onto the gold-coated side of the glass slide before being spread using the blade coater to obtain a uniform film thickness. The donor is checked under the microscope to confirm that the cell concentration is sufficient to cover all the slide and that cells are uniformly distributed. It is then positioned on a metal holder in TRI setup. In order to maintain stable viscoelastic bioink properties and to avoid its dehydration, donor and the holder are maintained on ice.

### **2.3.5 The printing patterns**

Once the ribbon is ready, then the transfer can take place either for a post-mortem study or for a time-resolved study to tune different parameters like influence of laser energy, film thickness and/or the viscosity of bioink on printed drops etc.

To conduct a post-mortem study for characterization, different processes can be made for printing with different conditions on same recipient glass slide. Micro-arrays of the drops can be created either by using transfer station with programmed patterns (the creation process is detailed in [Appendix C](#)) or manually by 3D translational stage with TRI setup. Micro-array (5x7) of drops separated by 500 and 1000µm are printed with different laser energies at different separation distances larger than 1mm (the conventional separation distance).

Here it must be noted that the same transfer station is used for time resolve imaging. In the case of a time-resolved study, the laser (1064nm) of the transfer station is switched to single-shot mode using a locally fabricated connector. The translation stages of the sample for TRI are not motorized that's the reason of using single-shot mode as it is impossible to translate manually for distinct laser shots on the same sample if the laser is set to the minimum i.e. 1 kHz rate.



## 2.4 Characterization Techniques for Post-Transfer Analysis

### 2.4.1 Optical microscopy

The first post-transfer observation of the printed droplet is done under microscope. Once the biomaterial has been transferred by laser, donor and recipient slides are observed under inverted optical microscope Nikon Optiphot-2 equipped with a colour video camera Sony Power HAD 3CCD driven by the software “Matrox Intellicam”, later, to measure the diameter of the droplets transferred by ImageJ software (see [Appendix D](#)).

### 2.4.2 Optical profilometry

The height of the droplets is determined by profilometry with an optical interferometer (Wyko NT1100, Veeco Instruments SAS, France) used in Vertical Scanning Interferometry (VSI) mode ([Fig. 2.5a](#)). The principle of profilometry with an optical interferometer is described below.

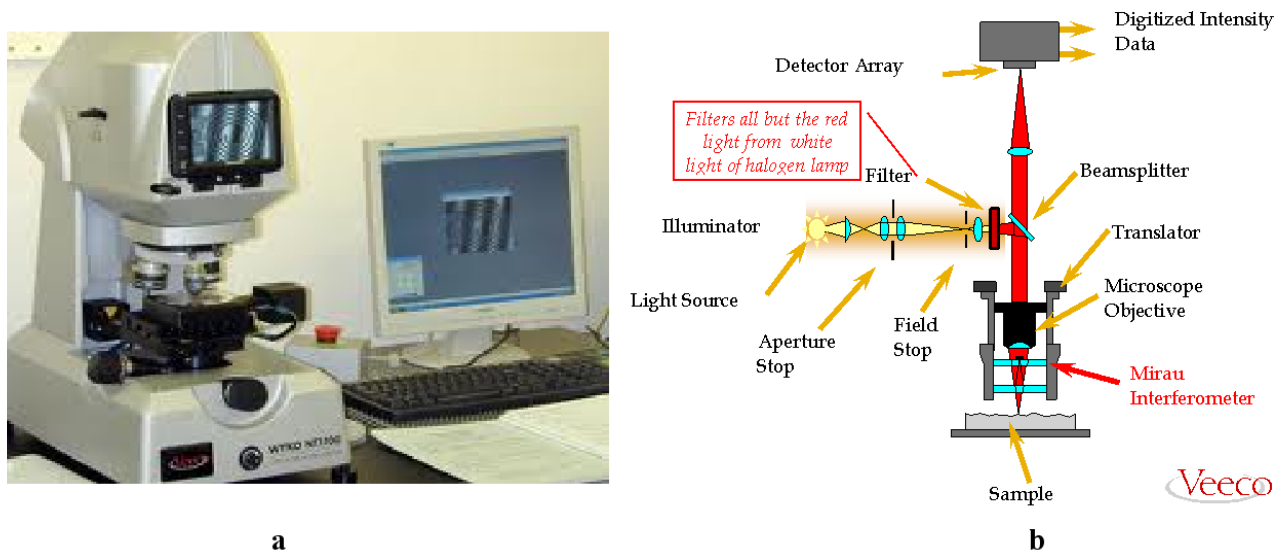


Figure 2.5: Interferometric optical profilometer Wyko NT1100, a) Optical interferometric profilometer Wyko NT1100, b) Principle of Optical interferometric profilometer Wyko NT1100

Optical profilometry is a non-contact method for 3D measurement. The device is based on the interference caused by two different beams of white light. A beam of white light is focused through a filter and an interferometric microscope lens on the surface of the sample. A beam splitter reflects half of the incident beam to a reference surface within the interferometer. The two reflected beams, one from the sample and the other from reference surface recombine to form interference fringes ([Fig. 2.5b](#)). The best contrast is obtained at the focusing point.

In VSI mode, the white light is filtered by an orange neutral density filter and

maintaining the coherence length ( $L_c$ ) of the white light. White light has a very short  $L_c$ , interference is produced only when the optical path difference between the two light beams is less than  $L_c$ . The interferometric objective scans the surface at different heights while moving in vertical direction. The movement is precisely controlled with a motor. During translation of the microscope objective, interference is produced only when the path difference between the reflected optical beam from the object and the reference is approximately  $L_c$ . With simultaneous recording of the interference produced by different parts of the object and position of the microscope objective, 2D and 3D profiles of the object can be reconstructed.

## 2.4.3 Statistical analysis

### 2.4.3.1 Drop volume

#### 2.4.3.1a Volume calculations

For calculation purpose, printed drop is considered as a spherical cap of diameter “ $\phi$ ” and height “ $h$ ” (Fig. 2.6). To calculate drop volume we must integrate a disk surface of variable radius  $r(z)$  over  $z$  for height of  $z = R-h$ , where  $R$  is the radius of sphere. The variable radius can be defined as function of  $z$ :

$$r(z) = \sqrt{R^2 - (R - z)^2} \quad (2.6)$$

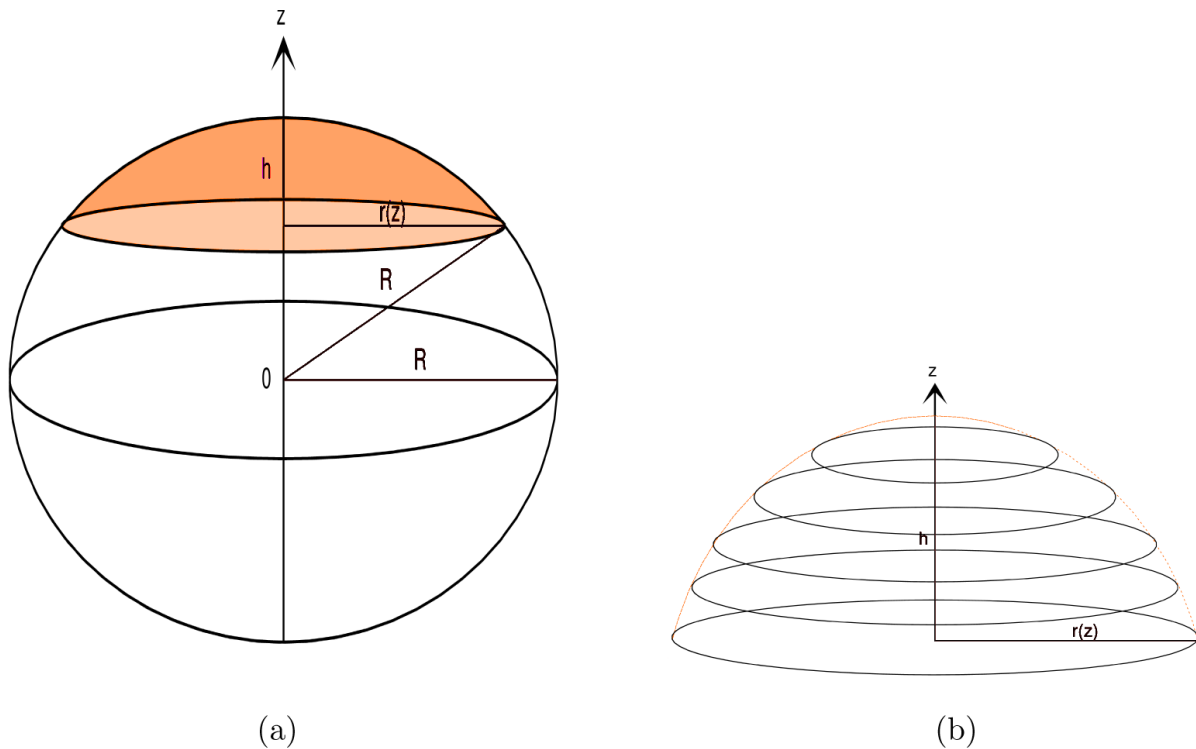


Figure 2.6: Spherical cap for calculation of volume

The triple integral of Equation 2.7 gives the volume of the spherical cap.

$$V_c = \int_{R-h}^R \int_0^{2\pi} \int_0^{\sqrt{R^2-z^2}} r dr d\theta dz \quad (2.7)$$

$$\begin{aligned} V_c &= 2\pi \int_{R-h}^R \left[ \frac{r^2}{2} \right]_0^{\sqrt{R^2-z^2}} dz \\ V_c &= 2\pi \int_{R-h}^R \left( \frac{R^2-z^2}{2} \right) dz \\ V_c &= 2\pi \left[ \frac{R^2 z}{2} - \frac{z^3}{6} \right]_{R-h}^R \\ V_c &= 2\pi \left[ \frac{R^3}{3} - R^2 \frac{(R-h)}{2} + \frac{(R-h)^3}{6} \right] \\ V_c &= 2\pi \left[ \frac{(3Rh^2-h^3)}{6} \right] \\ V_c &= \frac{\pi}{3} h^2 (3R-h) \end{aligned} \quad (2.8)$$

To express this expression (equation 2.8) in term of diameter “ $\phi$ ” of the drop. We use:

$$R^2 = (R-h)^2 + \frac{\phi^2}{4} \quad (2.9)$$

$$\begin{aligned} R^2 &= R^2 + h^2 - 2Rh + \frac{\phi^2}{4} \\ 2Rh &= h^2 + \frac{\phi^2}{4} \\ R &= \frac{h}{2} + \frac{\phi^2}{8h} \end{aligned} \quad (2.10)$$

Substituting value of R from equation 2.10 into equation 2.8, we get

$$V_c = \frac{1}{6} \pi h \left[ \frac{3}{4} \phi^2 + h^2 \right] \quad (2.11)$$

#### 2.4.3.1b Calculation of uncertainty in drop volume

As drop volume is a function of variables “h” and “ $\phi$ ”. The error  $\Delta V$  in the volume  $V(h, \phi)$  of the drop depends upon errors in h and  $\phi$  i.e. the standard deviations of h and  $\phi$ ,  $\Delta h$  and  $\Delta \phi$  respectively, is determined by partial differential of V (h,  $\phi$ ),  $dV(h, \phi)$ .

$$dV(h, \phi) = \frac{dV(h, \phi)}{\partial h} dh + \frac{dV(h, \phi)}{\partial \phi} d\phi \quad (2.12)$$

We can determine the maximum for  $dV$ :

$$|dV(h, \varphi)| \leq \left| \frac{dV(h, \varphi)}{\partial h} \right| |dh| + \left| \frac{dV(h, \varphi)}{\partial \varphi} \right| |d\varphi| \quad (2.13)$$

As,  $\Delta\varphi = |d\varphi|$ ,  $\Delta V = |dV|$  and  $\Delta h = |dh|$ , we obtain the following relation:

$$\Delta V(h, \varphi) = \left| \frac{\partial V}{\partial h} \right| \Delta h + \left| \frac{\partial V}{\partial \varphi} \right| \Delta \varphi \quad (2.14)$$

It gives:

$$\Delta V(h, \varphi) = \frac{1}{2} \pi \left[ \left( h^2 + \frac{\varphi^2}{4} \right) \Delta h + \frac{1}{2} h \varphi \Delta \varphi \right] \quad (2.15)$$

## 2.5 Time-Resolved Imaging (TRI)

To better understand the mechanisms of droplets formation printed on the substrate, time-resolved imaging (TRI), a technique based on the principle of shadowgraphy was used. Principle of shadowgraphy is presented here and then experimental device is explained.

### 2.5.1 The shadowgraphy

The shadowgraphy is one of the simplest visualization techniques. It is an optical method that reveals non-uniformities in the transparent object. In this method, a transparent object is illuminated and its shadow is observed on a screen. In principle, we cannot directly see a difference in temperature, a different gas, or a shock wave in the transparent air. However, all these disturbances refract light rays, so they can cast shadows. This is an optical method to reveal local changes in the refractive index of the most transparent media such as gas (e.g. air), liquid (e.g. water) and solid (e.g. the glass). These gradients can be static for instance irregularities in the glass, or dynamic such as those induced by the pressure, density, composition or temperature gradients in fluids.

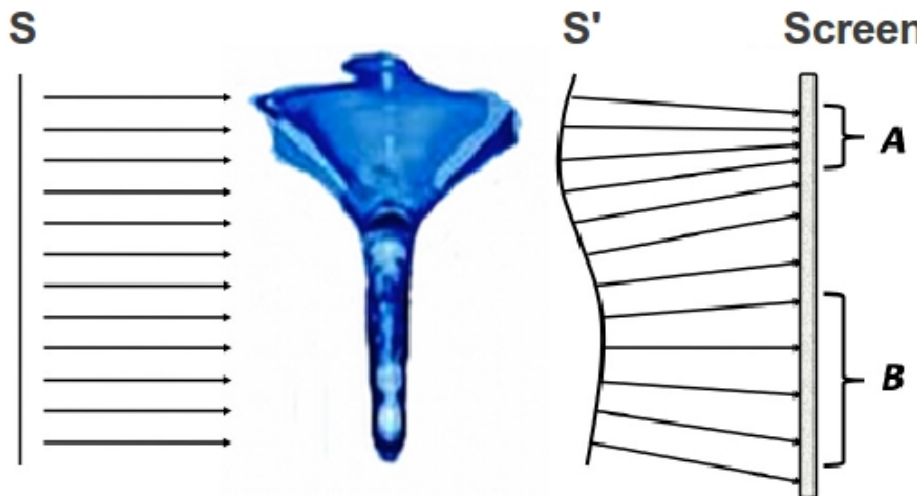


Figure 2.7: Principle of shadowgraphy

If a point source of the light is focussed on an object with variable refractive index (variations caused by density, pressure or temperature gradients), local illumination changes will be visible on the screen. This could be explained as: the lateral index gradients distort the wave leaving the object (Fig. 2.7). At the position where curvature of the wave is directed towards the source, the diverging light rays will occupy a larger area on the screen as compared to the object and this spread reduces the brightness (zone B in Fig 2.7). On the other hand, if the curvature of the wave is facing downstream, the rays come together and, if the screen is not too far away, there will be a more brighter area (zone A in Fig 2.7). The directed rays from the point source uniformly illuminate the screen. Variations in brightness on the screen not only depend on the local curvature of the emerging wave, but also the remoteness of screen. In our case we use a pulsed laser as a light source and a camera as a display. The camera is connected to a computer and image is displayed on the computer screen and saved for further studies.

In figure 2.7 S and S' are the surfaces of incoming and outgoing wave respectively. The beams of light for source consists of parallels rays of light which are deviated after passing through the object. As the curvature of the wave is directed toward the source, the rays diverge producing brighter areas (A) and they converge, if it is bent downstream leading to the darker areas (B).

### 2.5.2 TRI setup for study of ejection mechanism

This section presents TRI experimental setup, used during this PhD, to study laser-induced jetting mechanism of bioinks.

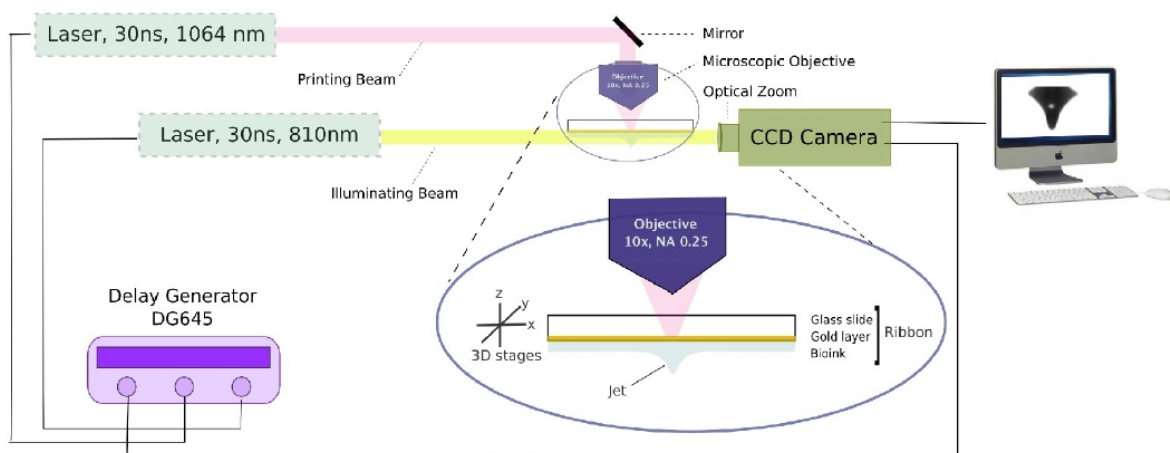


Figure 2.8: Schematic diagram of TRI setup

To understand the phenomena of droplets formation, it is necessary to observe the ejection of the bioink which lasts for few microseconds. Good temporal resolution of this

ejection could be achieved by observing this ejection with a time resolution of the order of nanoseconds. To observe such a fast phenomenon, time-resolved imaging microscopy or time-resolved Imaging (TRI) based on the principle of the shadowgraph was used. This principle is already described in [section 2.5.1](#). The system consists of two pulsed lasers. The first (1064nm) produces the ejection and the second (810nm probe laser) illuminates the region at a given time after the first pulse. The time difference between the two pulses is adjusted by a delay generator. An example of this system is illustrated in [Figure 2.8](#). Subsequent details are mentioned below.

### 2.5.2.1 The optical assembly

The transfer station is compact and rigid. Its structure can not accommodate optical elements due to congestion, therefore laser beam from the laser output is collected out of the station ([2.9a](#)) in order to recreate a setup on an optical table for laser-assisted bioprinting. Using sets of mirrors, the laser beam is guided and focused on the target through a microscopic objective of magnification 10x and numerical aperture (NA) of 0.25 (LMH-10x 1064 OFR, Thorlabs, Great Britain).

As shown in schematic diagram the sample is illuminated by a near IR laser of wavelength 810nm, 30ns pulse duration (Cavitar, R&D Vision, France). A CCD camera having resolution 1038x1388 pixels (Stringray, AVT, R&D Vision, France) and coupled with the optical zoom, Zoom 6000 (Zoom Macro Navitar, R&D Vision, France) is facing the illuminating laser with a working distance of 36mm and magnification can range from 4.9x to 31.5x ([Fig. 2.9 b&c](#)). In the experiments described hereinafter, the optical zoom is set at 4.9x.

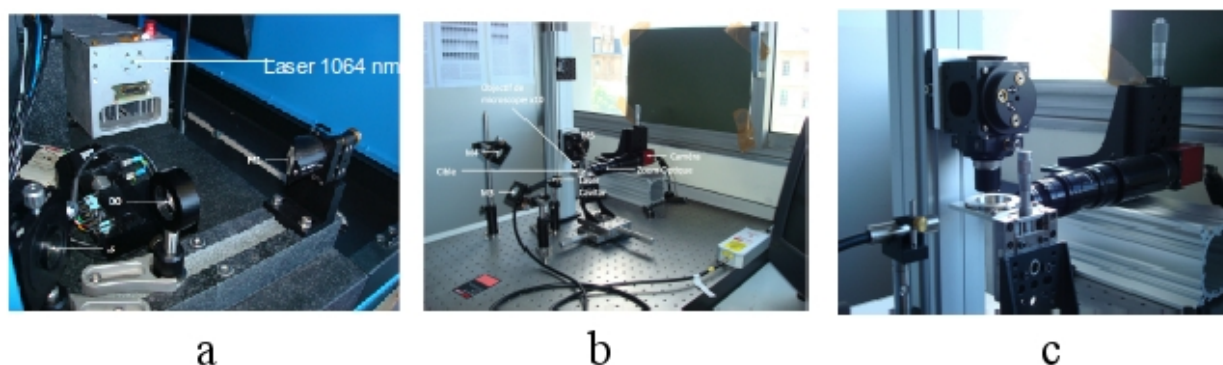


Figure 2.9: Experimental device for Time-Resolved Imaging, a) Laser beam output of the transfer station, M: mirror - OD: optical density – LS: light beam splitter, b) General view of the optical arrangement of the TRI, c) Detailed view of the optical system of shadowgraphy

### 2.5.2.2 Calibration

#### 2.5.2.2a Energy profile

The energy of the laser pulse is selected by adjusting the diode current which is a

controlling parameter for the pulse energy. The calibration is done in order to obtain exact energy required for the experimental studies. Graphs (Fig. 2.10a) shows the energy calibration for different values of the current.

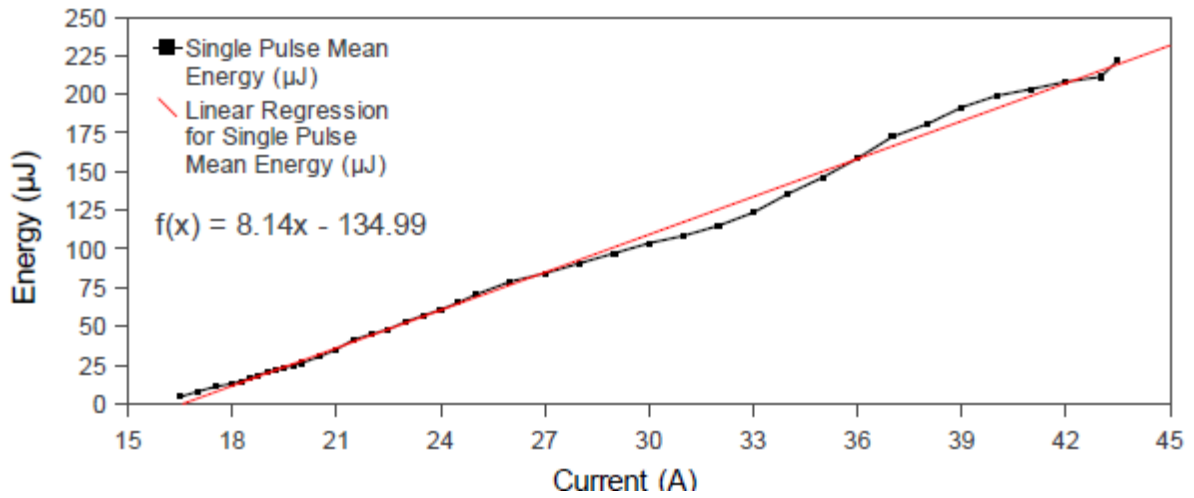


Figure 2.10: a) The energy profile for laser pulse in single shot mode

#### 2.5.2.2b Pixel calibration

To calibrate the pixels of the image obtained, a needle of 810 microns in diameter was placed in path of illuminating laser beam at the focal point of the camera, the image of this needle was taken i.e. instead of the jet to be imaged. In this picture (Fig. 2.10b), 810 microns occupy 810 pixels both in horizontal and vertical axes. Hence it provides the following relationship for calibration of TRI images: 1 px ↔ 1 μm, a spatial resolution of 1 μm for a field 1.3mmx1.0mm (H x V) (maximum field observed).

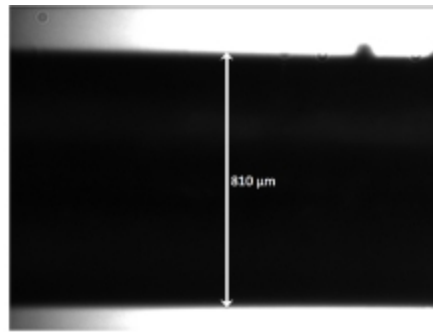


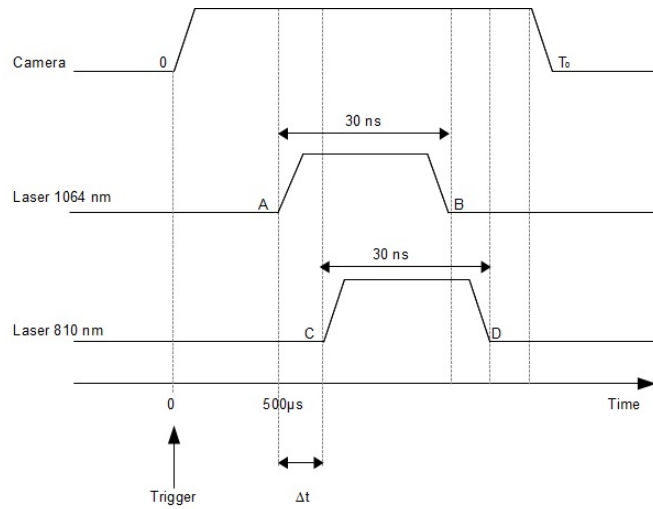
Figure 2.10: b) Calibration of pixels in the image for a magnification of 4.9x

#### 2.5.2.3 Delay

The delay  $\Delta t$  between the laser pulse to induce ejection process and the other which illuminates the region of ejection is controlled by a delay generator (DG645, Stanford Research Systems, Optoprism, France) (Fig. 2.11a) and can make a temporal resolution of the order of nanoseconds. Each acquired image corresponds to a laser shot. The trigger sequence of signals is illustrated by the diagram (Fig. 2.11b). The camera is triggered at  $t = 0$ , then the



laser with 1064nm at  $t = 500\mu\text{s}$ . Finally at  $t = 500\mu\text{s} + \Delta t$ , the 810nm laser illuminates the sample and the camera captures the image.



(a) The delay generator DG645

(b) Timing of signals for acquisition of an image (lengths are not scaled)

Figure 2.11: a) The delay generator and b) the timing of signals

## 2.5.3 Printing configurations

Two different setups were used for study of ejection mechanism by TRI.

### 2.5.3.1 Novel configuration

First a novel **bottom to top setup** (Fig. 2.12a) was used. Laser pulse was fired from downside to upward. Subsequent emanation of bioink was upward. For temporal evaluation of jet formation and dynamics, same TRI setup was used.

### 2.5.3.2 Conventional configuration

Secondly, conventional **top to bottom setup** (Fig. 2.12b) was used for TRI of the ejection mechanism. Laser pulse was fired from top which led bioink ejection in downward direction.

## 2.6 Experimental Arrangements for TRI

As described in § 2.1, the laser of LAB setup is composed of a pulsed Nd:YAG laser (1064nm wavelength, 30ns pulse duration), a microscopic objective (10x, NA 0.25) to focus laser pulses on ribbon and an XYZ stage for 3D translation of ribbon. Temporal profiles from lateral view are obtained by ombroscopy using a dedicated system. Basically, the jet optical scene is illuminated by a near-IR pulse laser (810nm, 30ns, Cavitar, R&D Vision, France) and captured by a CCD camera (resolution 1038x1388 pixels, Stringray, AVT, R&D Vision,



France) through an optical zoom (magnification  $M= 4.9 - 31.5$ , Zoom Macro Navitar, R&D Vision, France) and using a dedicated software (HIRIS, R&D Vision, France). Time delay between the initial Nd:YAG pulse and image capture is monitored by a trigger (DG645, Stanford Research Systems, Optoprim, France). Images obtained had a  $1 \text{ px}/\mu\text{m}$  resolution (at  $M = 4.9$ ) and a  $30\text{ns}$  time resolution, that is high enough as compared to the size and duration of the complete jet process (about  $10\mu\text{s}$ ), respectively.

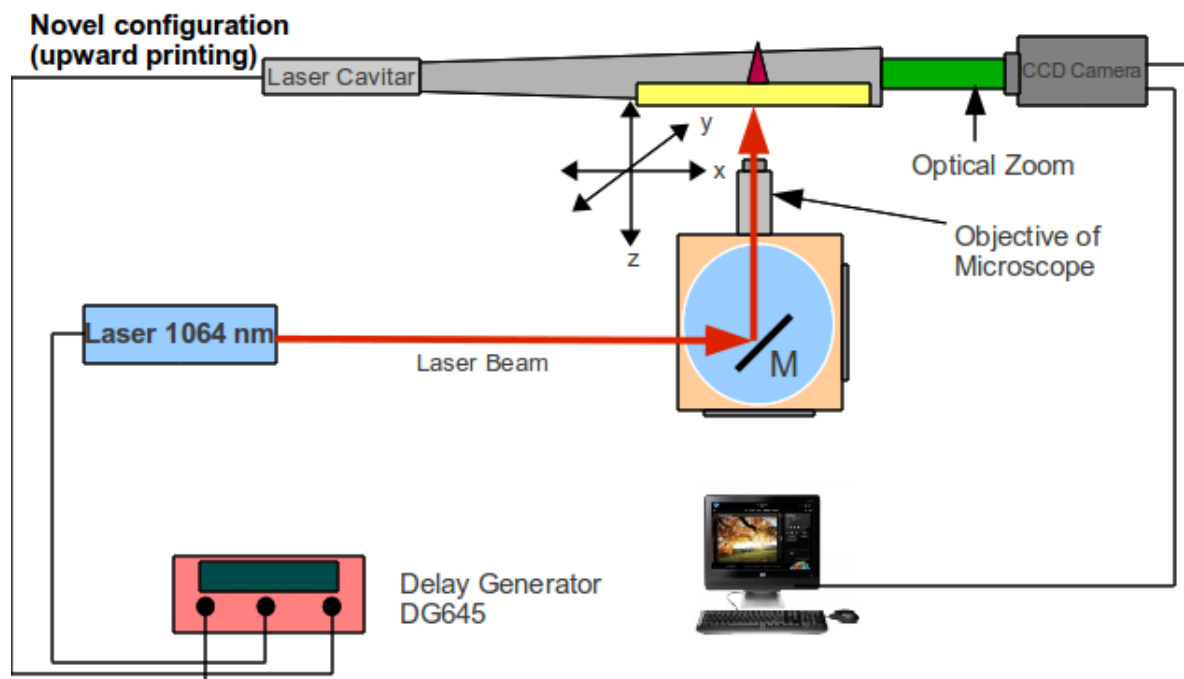
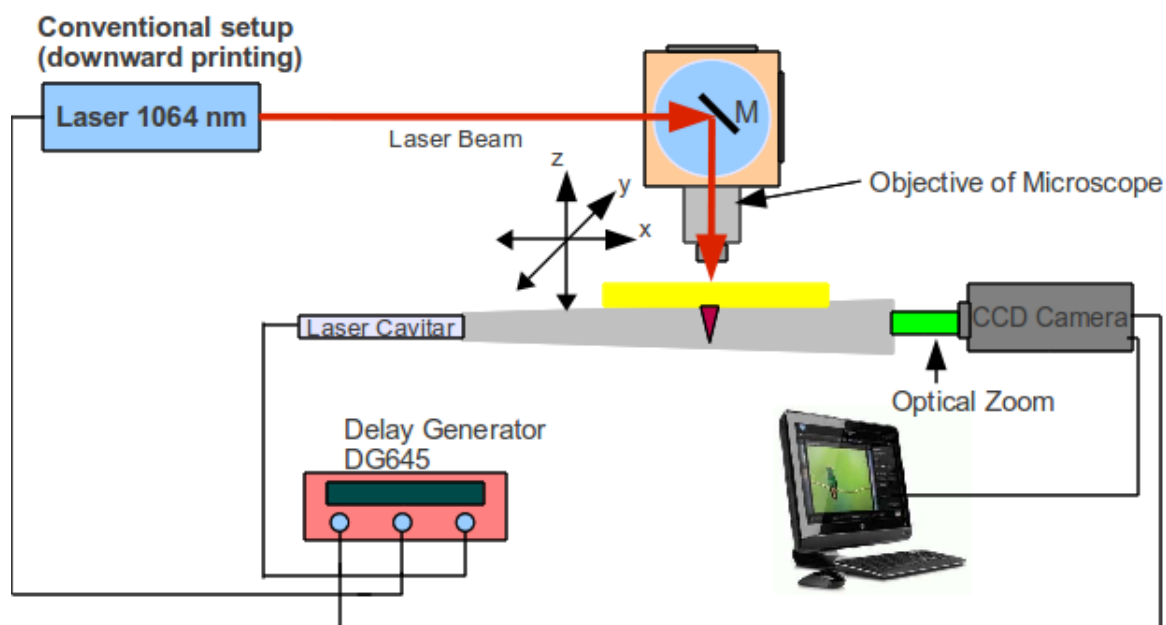


Figure 2.12 a) Scheme of TRI in upward printing setup



b) Scheme of TRI in conventional setup

Figure 2.12: Schematically representation of TRI setups

The ribbon is prepared by depositing a sacrificial absorbing layer of gold (50nm) by Emscope SC500 sputter coating unit onto a transparent quartz glass. The bioinks used in these experiments are described in § 2.3. Unless otherwise mentioned, 28 $\mu$ L of bioink is spread on the gold layer by a micrometric blade coater (3570, Elcometer) to make 40 $\mu$ m thick film and controlled by weight measurements. The energy of the laser pulse is selected by adjusting the diode current.



## **CHAPTER 3**

This chapter presents experimental results in three sections. The first section “A” is devoted to the regime transition studies by using novel configuration (upward printing setup), which is further extended to explore high speed jets. A comparison of the transition between different regimes of LAB with conventional configuration (downward printing setup) which is further extended to explore high speed jets is also presented. The second section “B” presents TRI studies of jet dynamics for laminar jets which seems more suitable for cell printing. The third section “C” describes distant printing, in which the novel configuration is used to produce drops at increasing distances between donor and receiver.

<u>CHAPTER 3</u>	51
<u>3 RESULTS</u>	53
<u>3.1 Section A: Novel configuration (Upward Printing)</u>	53
<u>3.1.1 Determination of the energies for transition studies</u>	53
<u>3.1.2 TRI for sub-threshold regime</u>	53
<u>3.1.3 TRI for jetting regime</u>	54
<u>3.1.4 TRI analysis</u>	55
<u>3.1.4.1 Vertex angle</u>	56
<u>3.1.4.2 Height and base-width</u>	56
<u>3.1.4.3 Volume</u>	58
<u>3.1.4.4 Velocity</u>	58
<u>3.1.5 High speed jets in jetting regime</u>	59
<u>3.2 Conventional Setup</u>	61
<u>3.2.1 TRI for sub-threshold regime</u>	61
<u>3.2.2 TRI for jetting regime</u>	61
<u>3.2.3 TRI analysis</u>	62
<u>3.2.3.1 Height and base-width</u>	63
<u>3.2.3.2 Volume</u>	64
<u>3.2.3.3 Velocity</u>	64
<u>3.2.3.4 Vertex angle</u>	65
<u>3.2.6 High speed jetting</u>	66
<u>3.3 SECTION B</u>	69
<u>3.3.1 TRI for laminar jets ejection and dynamics</u>	69
<u>3.3.2 Height of laminar jets</u>	72
<u>3.4 SECTION C: Parametric Study of Novel Configuration</u>	74
<u>3.4.1 Viscous liquids drop printing</u>	74
<u>3.4.1.1 Effect of laser energy on drop size</u>	74
<u>3.4.1.2 Effect of liquid viscosity on drop size printed at 5mm</u>	75
<u>3.4.1.3 Effect of printing distance on drop size</u>	76
<u>3.4.2 Distant printing for low viscosity solutions</u>	78
<u>3.4.2.1 Effect of printing distance on drop size of less viscous solutions</u>	79
<u>3.4.2.2 Effect of printing distance on drop height</u>	80
<u>3.4.2.3 Printing distance and drop volume</u>	80
<u>3.4.2.4 Effect of printing distance on printing position</u>	81

### 3 RESULTS

A detailed analysis of the different regimes which affect the LAB process is carried out. Results of the experiments presented in this chapter are interpreted by analogy with cavitation studies near free surface [173,174,188,189].

#### 3.1 Section A: Novel configuration (Upward Printing)

In this section, experimental study conducted with novel configuration used for TRI of the ejection mechanism, is presented. Laser pulse is fired from bottom which led bioink ejection in upward direction. Experimental arrangements are described in § 2.6. A novel configuration of LAB (Fig. 2.12a) for upward printing is initiated. It aims at depositing and printing liquid droplets with reproducible results and accuracy as well.

##### 3.1.1 Determination of the energies for transition studies

As mention in first chapter the sub-threshold, jetting and plume regimes do not solely result from laser energy ( $E$ ) but, also depend on rheological properties (viscosity ( $\nu$ ), surface tension ( $\sigma$ ) and film thickness ( $\varepsilon$ )) of the bioink. To keep all other parameters ( $\nu$ ,  $\sigma$  and  $\varepsilon$ ) constant, the ribbon is prepared with 40 $\mu$ m thick layer of alginate solution (1%(w/v) NaAlg, 70%(v/v) water, 30% (v/v) glycerol, and 15 mg/mL).

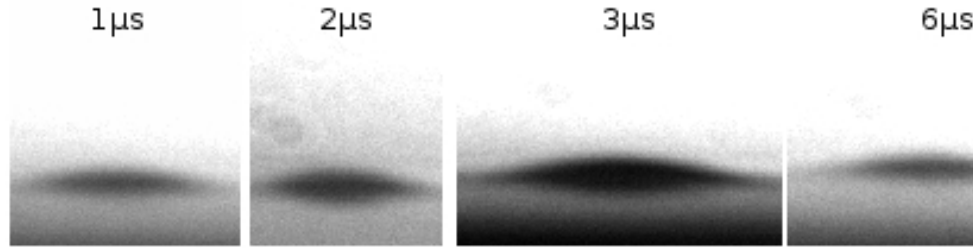
After energy calibration, TRI is conducted in order to determine the energies required for study of transition between sub-threshold and jetting. Series of lateral view images are acquired using TRI system (see § 2.6). Figure 3.1 shows the temporal profiles for different energies. Each series is representative of different laser energy with stipulated time delay. Very low energy of 7.8 $\mu$ J leads to the sub-threshold regime (Fig. 3.1a), and 25 $\mu$ J leads to jetting (Fig. 3.1b), whereas very high energy of 45 $\mu$ J produces the plume regime (Fig. 3.1c). For distinct characterization between sub-threshold and jetting energies the gap between the two energies is gradually decreased and eventually reached to 9.1 $\mu$ J as the energy for sub-threshold and 11.2 $\mu$ J for jetting in our experimental conditions. The corresponding fluences (J/cm<sup>2</sup> or energy per surface area) are: for sub-threshold (Fig. 3.2a) 1.06J/cm<sup>2</sup> and 1.3J/cm<sup>2</sup> for jetting (Fig. 3.2b). The darker portion (Fig. 3.2) corresponds to bioink and bright part is the air. The reflection of flowing fluids from gold coating (which acts as a mirror) is also visible in the darker portion, therefore only the brightest front is analysed.

##### 3.1.2 TRI for sub-threshold regime

Figure 3.2a represents temporal profiles for the sub-threshold regime with 9.1 $\mu$ J

(1.06J/cm<sup>2</sup>). The laser energy ( $E_L$ ) is less than the threshold value ( $E_{Th}$ ) i.e. ( $E_L < E_{Th}$ ). The induced deformation is expanding during 0-4 $\mu$ s and then receding from 5 $\mu$ s onward. This recession is gradually continued but at a slower rate after 7 $\mu$ s and onward. Finally, the bubble reduces to a small protrusion and is relaxing over longer time.

#### a TRI with 7.8 $\mu$ J



#### b TRI with 25 $\mu$ J

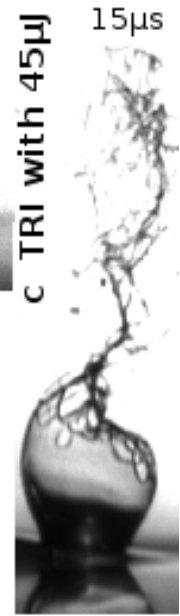
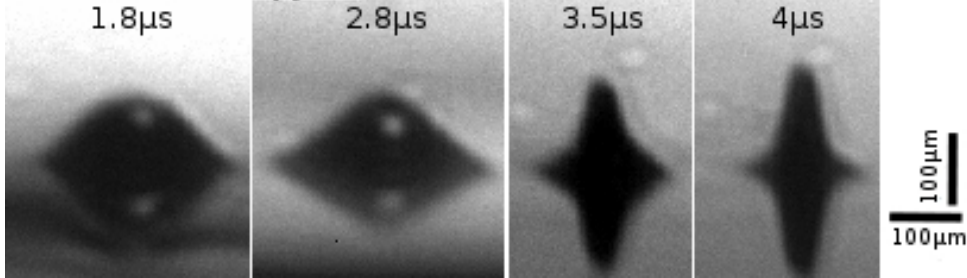


Figure 3.1: TRI for different regimes a) sub-threshold regime, b) jetting regime and c) plume regime

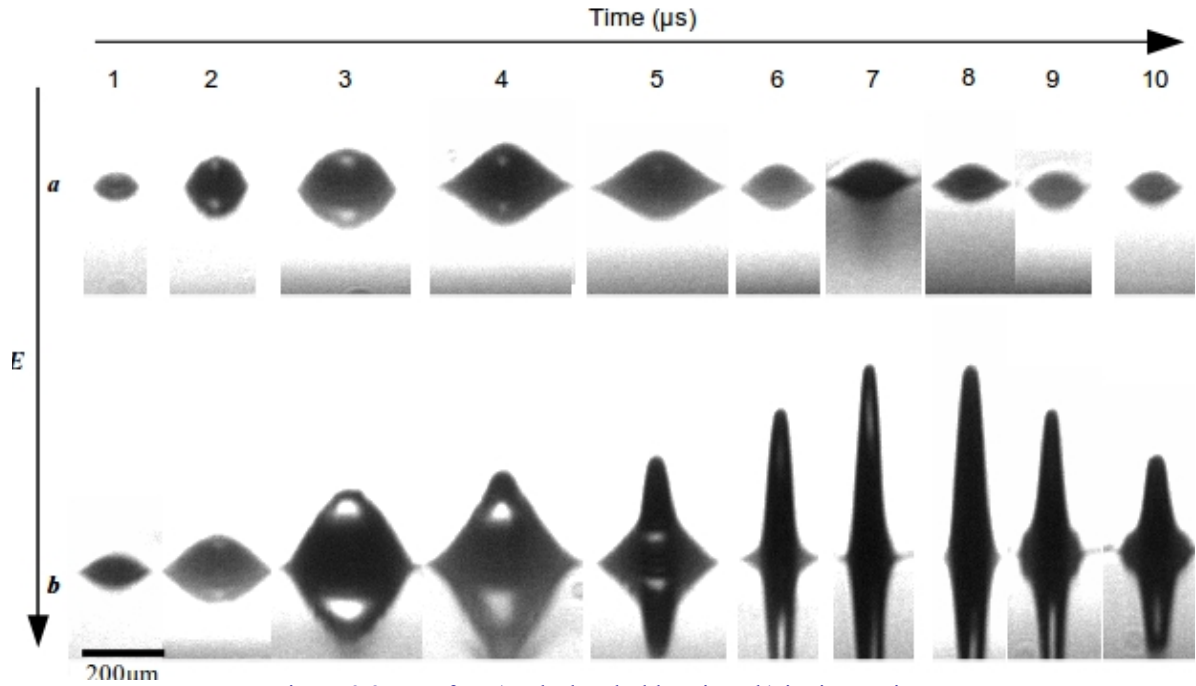


Figure 3.2: TRI for, a) sub-threshold regime, b) jetting regime

### 3.1.3 TRI for jetting regime

A laser pulse of 11.2 $\mu$ J is used for jetting conditions (Fig. 3.2b). The laser energy corresponds to jetting regime (it ranges between the threshold energy and the plume energy ( $E_P$ ) i.e.  $E_{Th} < E_L < E_P$ ): the bubble expands and collapses, resulting in a jet.

The energy deposition produces a protrusion which is expanding rapidly. Initial expansion rate is high during first  $3\mu\text{s}$  and pushes the bioink forward. At  $5\mu\text{s}$ , jet is fully developed (5<sup>th</sup> frame in Fig 3.2b) and starts onward progression. After  $6\mu\text{s}$  of the laser pulse, the jet diameter is rapidly decreasing as it progresses upward. The longest jet is observed at  $7\mu\text{s}$ . The crown formation is also visible (9<sup>th</sup> frame in 3.2b). During 6-9 $\mu\text{s}$ , the advancing front is more self focused. Slender and stable jets are produced in jetting conditions.

### 3.1.4 TRI analysis

After acquisition of temporal images, ImageJ software is used for analysis of the images and measurement of vertex angle, height and basis-width (Fig. 3.3a&b) to discern the sub-threshold and jetting regime. Vertex angle is defined as the angle between the local tangents to the surface of the bubble or jet. Every value corresponds to the mean values of thirty images. Finally the vertex angle, height and basis-width are plotted against the time.

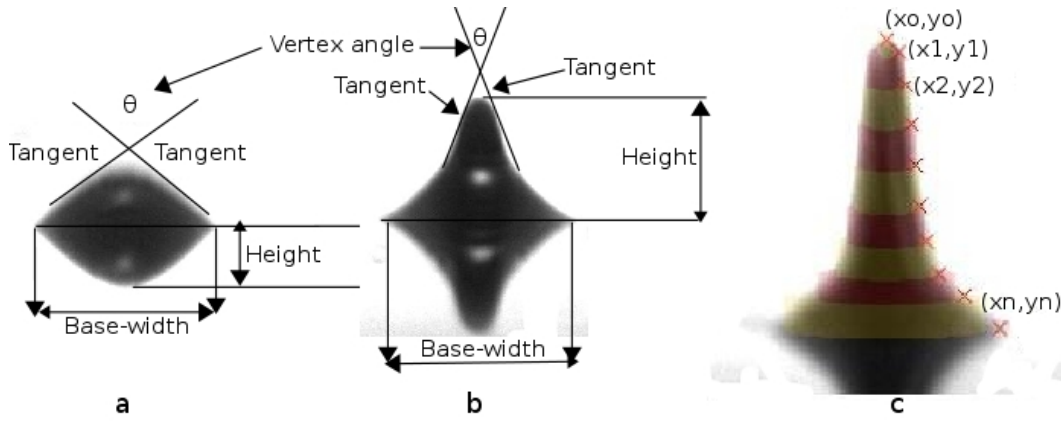


Figure 3.3: Measurement of vertex angle, height base-width and volume a) sub-threshold, b) jetting, c) Estimating the volume of a jet with cylindrical elements

To estimate the jet volume, we assumed it a solids of revolution. The approximations are carried out by method of disk integration. After pinpointing a relatively large number of points (over 30) at the edge of the shape in the 2-D pictures, we have estimated the volume as the sum of the volumes of the corresponding “elemental” cylinders as shown in Figure 3.3c. To be more accurate, the radius of each cylinder is taken from mean value of the x-coordinates of two successive points that define its height same as in the method of Riemann middle sums for estimating integrals.

$$V \approx \sum_{i=0}^{n-1} \pi \left( \frac{r_i + r_{i+1}}{2} \right)^2 (y_i - y_{i+1}) \quad (3.1)$$

Where

$$r_i = x_i - x_0 \quad (3.2)$$



### 3.1.4.1 Vertex angle

In sub-threshold regime, vertex angle of the protrusion decreases gradually (Fig. 3.4) from  $180^\circ$  to  $140^\circ \pm 8$  in  $1\mu\text{s}$  after the laser pulse and keeps on decreasing further. During 1-3  $\mu\text{s}$ , vertex angle decreases from  $131^\circ \pm 6$  to  $107^\circ \pm 3$ . At 4  $\mu\text{s}$ , minimum vertex angle is  $105^\circ \pm 3$  (4<sup>th</sup> frame in Fig. 3.2a). The vertex angle increases again from 5  $\mu\text{s}$  onward and jet does not emerge. It is  $110^\circ \pm 4$  at 5  $\mu\text{s}$ . During 5-9  $\mu\text{s}$ , vertex angle increases slowly (Fig. 3.4). Slope ( $\sim 18$  degree/ $\mu\text{s}$ ) of the graph is higher from 0-4  $\mu\text{s}$  than 5-10  $\mu\text{s}$  ( $\sim 3$  degree/ $\mu\text{s}$ ). From 6-10  $\mu\text{s}$ , oscillations are observed. After 10  $\mu\text{s}$  of energy deposition the vertex angle increases to  $123^\circ \pm 7$ .

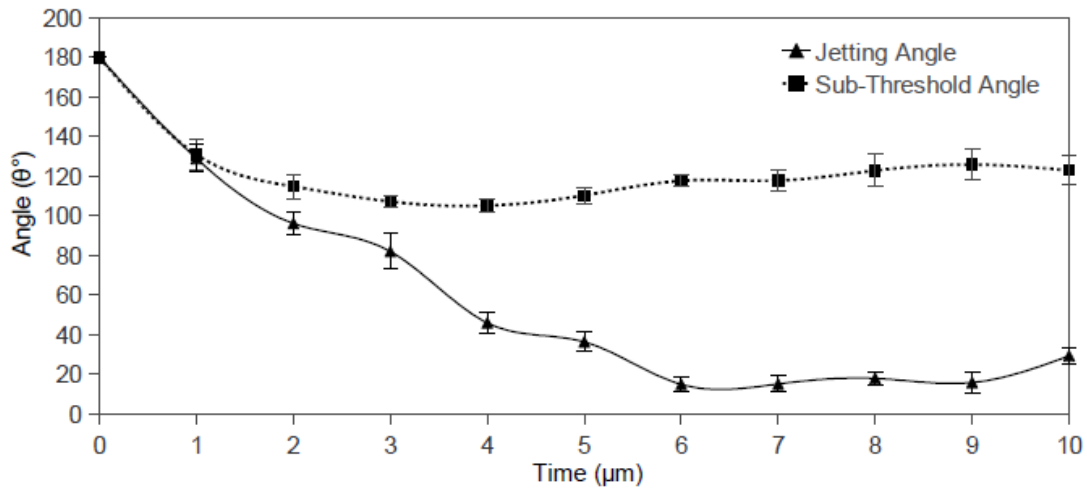


Figure 3. 4: Vertex angle versus time. Fine dots denote sub-threshold regime and solid line denotes jetting regime

In case of jetting, vertex angle of the front of the jet decreases quickly from  $180^\circ$  to  $129^\circ \pm 7$  at  $1\mu\text{s}$ . The vertex angle crosses critical limit of  $105^\circ$  by dropping to  $96^\circ \pm 6$  at  $2\mu\text{s}$ . It keeps on decreasing further to  $82^\circ \pm 9$  at  $3\mu\text{s}$ . Subsequent decrease in vertex angle is bit slow, it is  $18^\circ \pm 3$  at  $8\mu\text{s}$ . The slope ( $\sim 27$  degree/ $\mu\text{s}$ ) of the graph in Figure 3.4 is higher between 0-6  $\mu\text{s}$  than during 6-10  $\mu\text{s}$  ( $\sim 1.5$  degree/ $\mu\text{s}$ ). However, at 10  $\mu\text{s}$  the vertex angle again increases to  $29^\circ \pm 4$ . This vertex angle is shown (Fig. 3.4) as function of time.

### 3.1.4.2 Height and base-width

In sub-threshold regime, the height (front of the induced protrusion) is  $15 \pm 3\mu\text{m}$  after  $1\mu\text{s}$ . It triples to  $\sim 42 \pm 8\mu\text{m}$  during 1-3  $\mu\text{s}$  and attains its maximum  $49 \pm 9\mu\text{m}$  at 4  $\mu\text{s}$  (Fig. 3.5), when the minimum vertex angle of  $105^\circ$  is observed at this stage. From 5  $\mu\text{s}$ , height decreases gradually. A decrease of  $\sim 30\mu\text{m}$  is observed during 4-6  $\mu\text{s}$  where it is  $18 \pm 3\mu\text{m}$  at 6  $\mu\text{s}$ . Subsequent decrease is bit slower and finally  $17 \pm 4\mu\text{m}$  at 10  $\mu\text{s}$ .

The base-width of deformation is  $54 \pm 4\mu\text{m}$  after  $1\mu\text{s}$  which reaches to  $111 \pm 15\mu\text{m}$  at 4  $\mu\text{s}$ . Hence it doubles during 1-4  $\mu\text{s}$ . It is the maximum base-width, and is decreasing

subsequently during 7-9 $\mu$ s and reaches to  $56\pm 7\mu$ m at 9 $\mu$ s. Finally it is  $50\pm 9\mu$ m at 10 $\mu$ s. The height (Fig. 3.5) and base-width (Fig. 3.6) drop slowly from 6-8 $\mu$ s and recoil with few fluctuations at later stages.

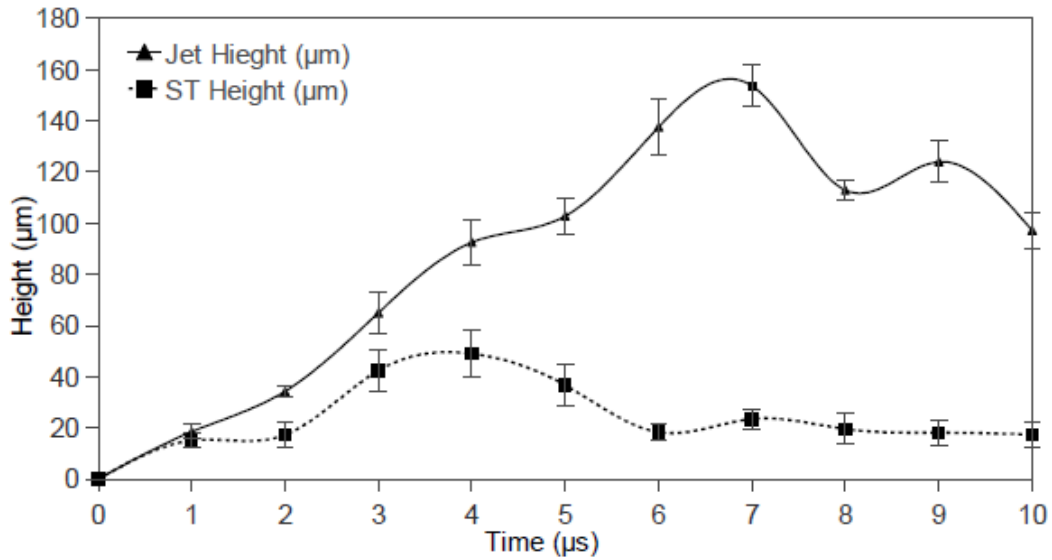


Figure 3.5: Maximum height versus time, sub-threshold regime (fine dot curve) and jetting regime (solid curve)

In case of the jetting regime, the height is  $19\pm 3\mu$ m at 1 $\mu$ s, which quickly reaches to  $34\pm 2\mu$ m at 2 $\mu$ s. Generally, height (Fig. 3.5) increases. Its augmentation rate is high ( $\sim 6$ ) till 4 $\mu$ s when height reaches to  $93\pm 9\mu$ m. Height increases at a lower pace till 7 $\mu$ s where it attains its maximum i.e.  $153\pm 8\mu$ m. Afterwards the height is fluctuating, and declines to  $97\pm 7\mu$ m at 10 $\mu$ s.

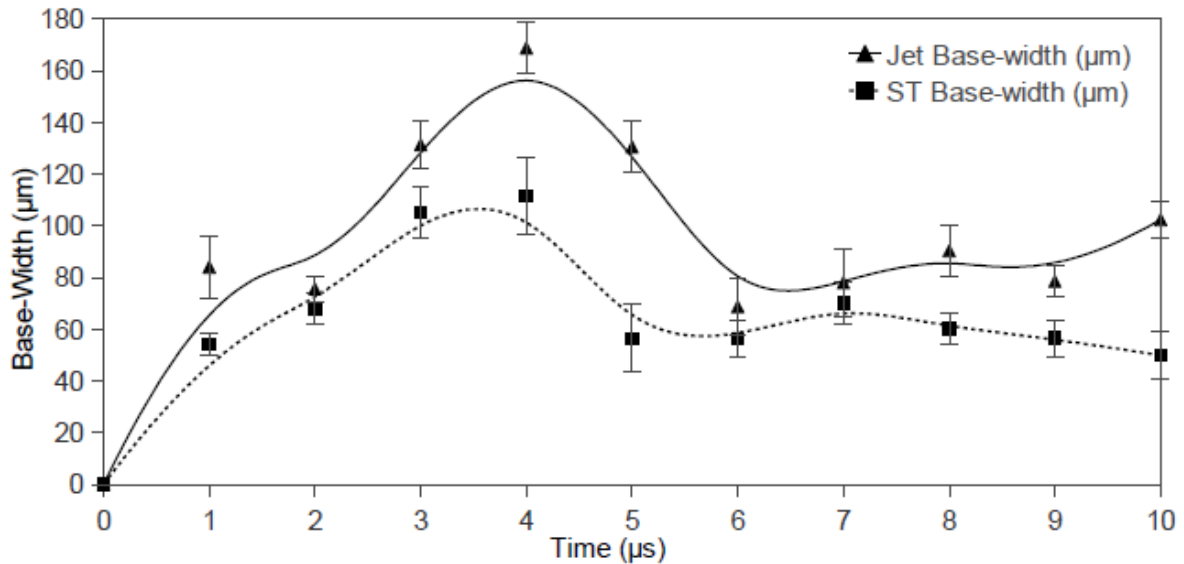


Figure 3.6: Maximum base-width versus time, sub-threshold regime (fine dot curve) and jetting regime (solid curve)

Base-width (Fig 3.6) in jetting conditions increases rapidly to  $84\pm 12\mu$ m at 1 $\mu$ s and reaches to  $131\pm 9\mu$ m at 3 $\mu$ s. The expansion continues till its maximum  $169\pm 10\mu$ m at 4 $\mu$ s. At

this stage the jet is fully developed and base-width declines as jet progresses further. The base-width shrinks to  $78 \pm 6 \mu\text{m}$  at  $9 \mu\text{s}$  after few fluctuations during  $6-8 \mu\text{s}$ . Finally, it is  $102 \pm 7 \mu\text{m}$  at  $10 \mu\text{s}$ .

### 3.1.4.3 Volume

Volume increases to  $18 \pm 4 \text{ pL}$  after  $1 \mu\text{s}$  in sub-threshold regime. It further increases to its maximum  $215 \pm 32 \text{ pL}$  at  $4 \mu\text{s}$ . A plateau is observed during  $3-5 \mu\text{s}$ . Subsequently, it starts decreasing rapidly to  $58 \pm 9 \text{ pL}$  at  $7 \mu\text{s}$ . It decreases further to  $40 \pm 20 \text{ pL}$  at  $9 \mu\text{s}$  before finally reducing to  $17 \pm 10 \text{ pL}$  at  $10 \mu\text{s}$  (Fig. 3.7).

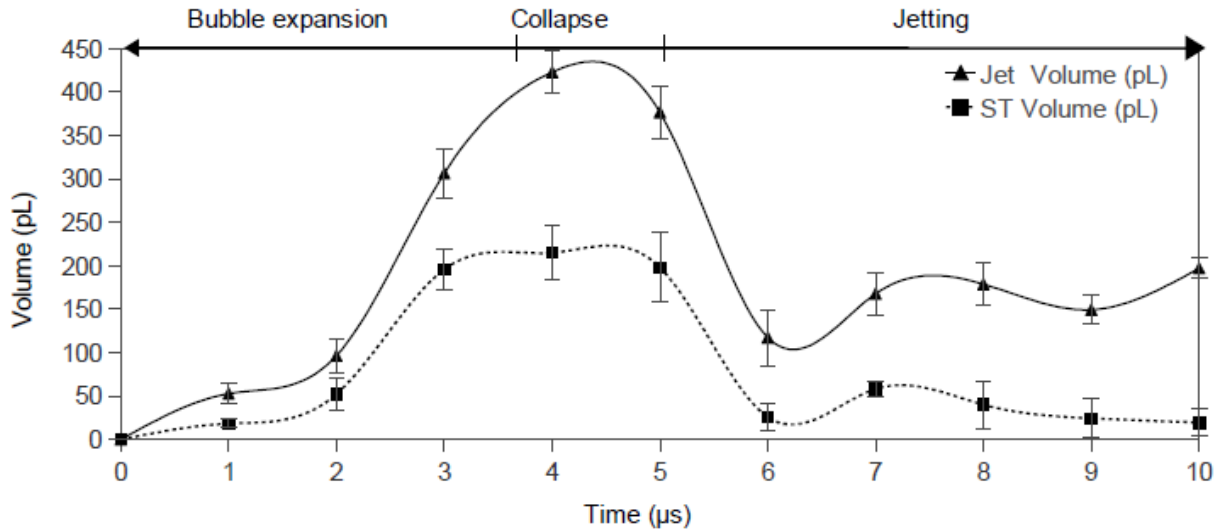


Figure 3.7: Volume versus time; sub-threshold regime (fine dot curve) and jetting regime (solid curve)

In jetting regime, volume (Fig. 3.7) increases apace during first few micro seconds. The volume increases from 0 to  $306 \pm 29 \text{ pL}$  during first  $3 \mu\text{s}$  and it reaches to  $423 \pm 24 \text{ pL}$  at  $4 \mu\text{s}$  which is the maximum volume of the flowing fluid. Afterwards, volume decreases and remains close to  $\sim 150 \pm 30 \text{ pL}$  during  $7-9 \mu\text{s}$ . The final value is  $197 \pm 12 \text{ pL}$  as estimated from temporal profiles at  $10 \mu\text{s}$ .

### 3.1.4.4 Velocity

Instantaneous velocity has been calculated from temporal images by  $v_{inst} = (H_2 - H_1) / (t_2 - t_1)$ , where  $H$  and  $t$  represent height and time respectively. The protrusion of sub-threshold regime emerges with a velocity (Fig. 3.8) of  $15 \pm 3 \text{ m/s}$ . Its velocity decreases to  $9 \pm 5 \text{ m/s}$  at  $2 \mu\text{s}$ . It fluctuates and increases to  $25 \pm 6 \text{ m/s}$  at  $3 \mu\text{s}$ . After  $4 \mu\text{s}$ , it starts decreasing. The forward progression is ceased and its velocity reduces to  $-18 \pm 3 \text{ m/s}$  at  $6 \mu\text{s}$ . Finally it reduces to  $-0.71 \text{ m/s}$  at  $10 \mu\text{s}$ .

In jetting regime, velocity (Fig. 3.8) increases gradually. It starts with  $19 \pm 3 \text{ m/s}$  at  $1 \mu\text{s}$ . In contrast to sub-threshold it increases to  $16 \pm 2 \text{ m/s}$  at  $2 \mu\text{s}$ . The maximum value for  $v_{inst}$

is  $35 \pm 8 \text{ m/s}$  at  $6 \mu\text{s}$ . The jet is fully developed at this stage and progressing further. The velocity greater than  $16 \text{ m/s}$  is maintained during jet progression till  $7 \mu\text{s}$  when it is  $16 \pm 4 \text{ m/s}$ . Afterwards it fluctuates and finally decreases to  $-26 \pm 7 \text{ m/s}$  at  $10 \mu\text{s}$ .

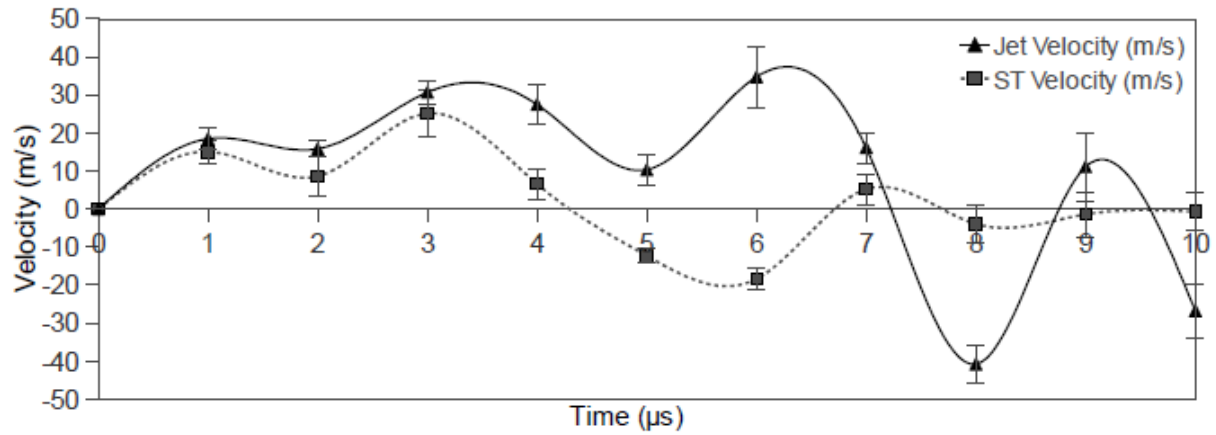


Figure 3.8: Instantaneous velocity versus time; sub-threshold regime (fine dots curve) and jetting regime (solid curve)

These experiments are conducted for the characterisation of the sub-threshold and jetting regime which led to the fact that protrusion has an initial velocity of  $19 \text{ m/s}$  which increases to  $35 \text{ m/s}$  as jet fully develops hence so-called slow jets.

After characterization of sub-threshold and jetting regime, we further explored jetting regime to analyse jet dynamics. For quantitative study of jet speed, we evaluated LAB for creating high speed and stable jet to study its capacity - as a powerful tool for therapeutic delivery. We selected riboflavin for its frequent application in several clinical and therapeutic situations. For over 30 years, riboflavin supplements have been used as part of the phototherapy treatment of neonatal jaundice. In this context our manipulations are carried out by using 20, 30, 40,  $50 \mu\text{m}$  thick layer of the riboflavin as bioink and laser energy from 11.2 to  $56.7 \mu\text{J}$  are used to produce jets. Temporal profiles of the jets are acquired from 1 to  $10 \mu\text{s}$  with step-index of  $1 \mu\text{s}$ . Images acquired by TRI were analysed with imageJ to calculate the instantaneous velocity.

### 3.1.5 High speed jets in jetting regime

This work was done in collaboration with **Joy TELLOUCK** and **Antoine Rrobinet PERRIN** in the frame work of their master training (for details please see [Appendix E](#)). [Figure 3.9](#) shows jet velocity versus time for 30 microns thick layer of riboflavin with increasing energies ranging from 30 to  $69.2 \mu\text{J}$ . The velocity increases rapidly till  $2 \mu\text{s}$  before reaching the maximum for a given energy and finally it decreases. Growth phase of the bubble is dominant till  $2 \mu\text{s}$  later jetting starts. The speeds are ranging from 60 to  $200 \text{ m/s}$ .

Jet speed increases with increasing energy. Whereas speed is adversely affected by

increasing viscosity and thickness of the bioink. A 40 $\mu\text{m}$  thick layer of pure riboflavin is used to study penetration power of jets produced with 51 $\mu\text{J}$ .

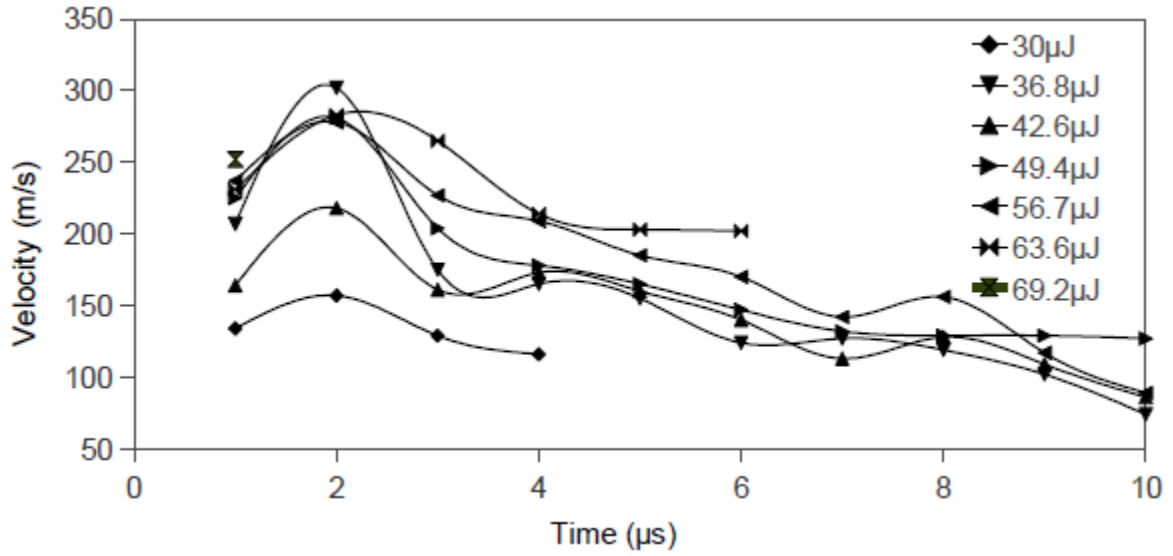


Figure 3.9: Jet velocity as function of the time

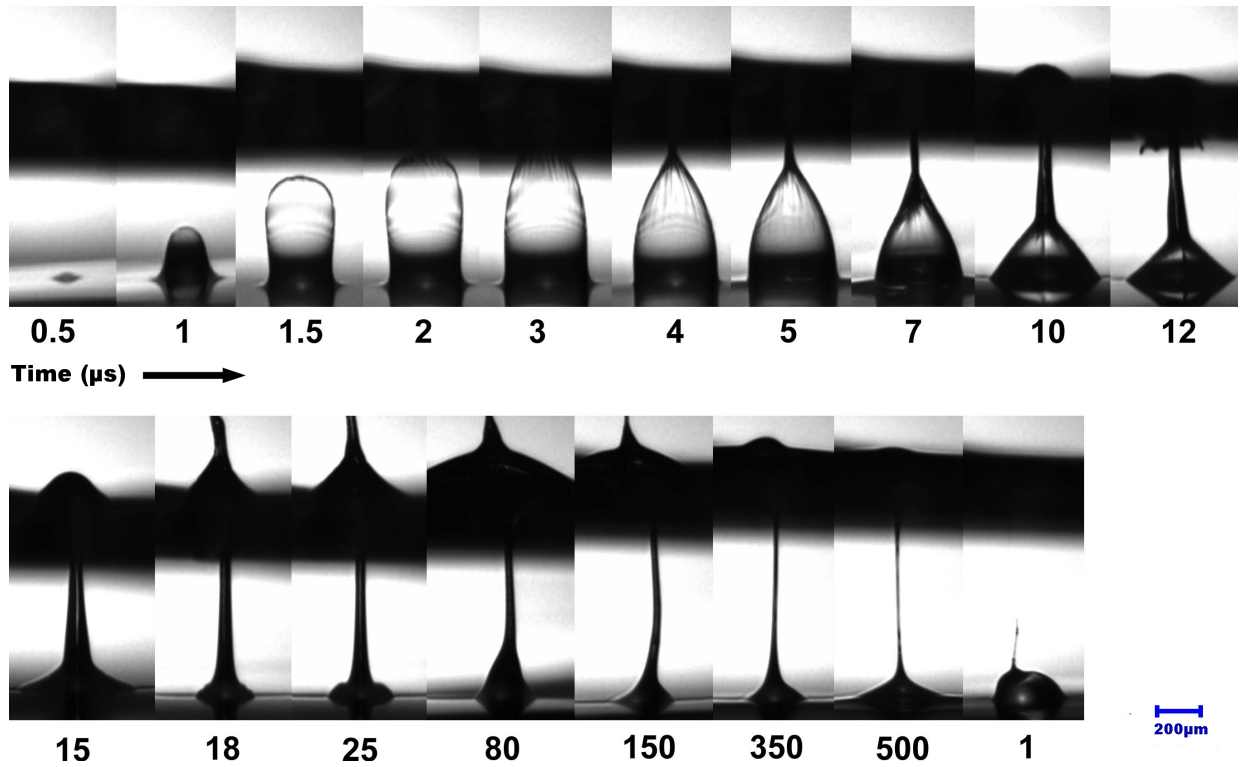


Figure 3.10: TRI of high speed jet produced from 51 $\mu\text{J}$  laser pulse 40 $\mu\text{m}$  thick riboflavin and penetrating through 150 $\mu\text{m}$  collagen membrane

Temporal images (Fig. 3.10) demonstrates that jet penetrates through the target (150 $\mu\text{m}$  thick collagen membrane). Corresponding instantaneous velocity for penetrating jets (Fig. 3.11) is determined from temporal images. The initial expansion of the bubble is rapid and more prominent and expanding with 52m/s at 0.5 $\mu\text{s}$ . It further accelerates to 527m/s at 1.5 $\mu\text{s}$ . Its  $v_{\text{inst}}$  decreases to 352m/s at 3 $\mu\text{s}$  when bubble reaches the collagen membrane (Fig.

3.10) at its apex. Jet emerges at 4 $\mu$ s (Fig. 3.10). The jet is fully developed and progressing upward whereas elongated bubble is still there. At 10 $\mu$ s it penetrates through the collagen membrane thereby protrusion rate of collagen membrane is 12m/s. Later elongation and thinning of jet lead to considerable reduction in base-width. Deformation rate of collagen membrane reduces to 6.3m/s at 15 $\mu$ s eventually jet penetrates through from collagen membrane at 18 $\mu$ s with a velocity of 84.8m/s which diminishes later at 1s.

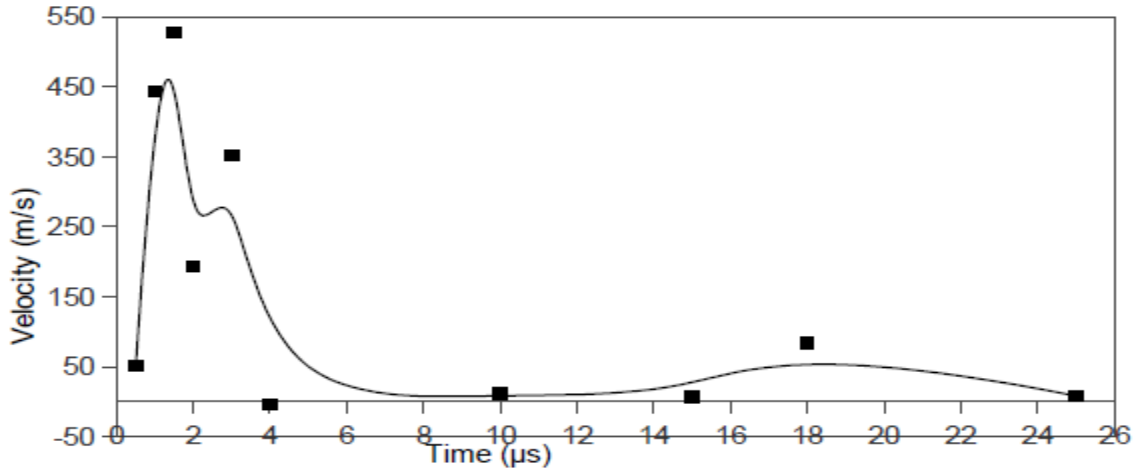


Figure 3.11: Velocity versus time for penetrating jet wit 51 $\mu$ J, 40 $\mu$ m thick riboflavin and 150 $\mu$ m collagen membrane

### 3.2 Conventional Setup

In the last section, the experiments were conducted with the novel configuration of LAB for upward printing. This section provides a comparison study conducted with conventional setup (Fig. 2.12a) for TRI of the ejection mechanism. Laser pulse is fired from top which led bioink ejection in downward direction. Experimental arrangements are described in § 2.6.

#### 3.2.1 TRI for sub-threshold regime

Figure 3.12a represents TRI for the sub-threshold regime with 9.1 $\mu$ J laser energy ( $E_L$ ). Pulse energy is less than threshold value ( $E_{Th}$ ) (minimum energy required to produce a jet i.e. ( $E_L < E_{Th}$ )): so that jetting can not occur. The energy deposition produces a protrusion which expands gradually. The expansion continues till 5 $\mu$ s and then starts receding. This recession is gradually continued but at a slower rate after 7 $\mu$ s. Finally, the bubble reduces to a small protrusion and is relaxing over longer time.

#### 3.2.2 TRI for jetting regime

A 11.2 $\mu$ J pulse energy was selected for jetting (Fig. 3.12b). The laser energy corresponds to jetting regime ( $E_{Th} < E_L < E_P$ ). The energy deposition produces a protrusion which is expanding rapidly. Initial expansion rate is high during first 3 $\mu$ s and pushes the

bioink forward. At  $6\mu\text{s}$  jet is fully developed (6<sup>th</sup> frame in Fig. 3.12b) and starts onward progression. The initial expansion is more prominent, whereas after formation of jet, it attains needle-like shape during the whole progression. From  $6\mu\text{s}$  onward the jet diameter is rapidly decreasing during its downward progression. The crown formation is also visible in the 9<sup>th</sup> frame of the figure 3.12b but more profound as compared to figure 3.2b. At  $10\mu\text{s}$ , the advancing front is more self focused. Slender and stable jets are observed in jetting conditions whereas vertex angle endures rapid decrease.

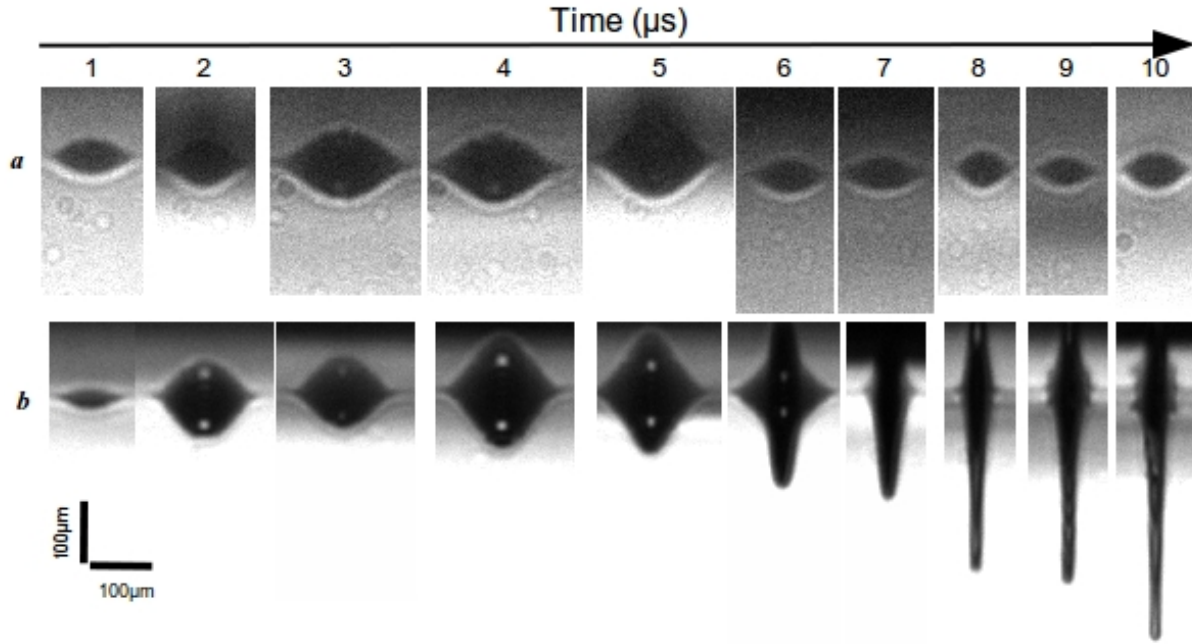


Figure 3.12: TRI in conventional configuration for, a) sub-threshold regime, b) jetting regime

### 3.2.3 TRI analysis

After acquisition, images are analysed with ImageJ software as explained in § 3.1.4 to estimate the volume in the similar way as described earlier. This time the jet is inverted so lower front is taken into account as shown in figure 3.13.

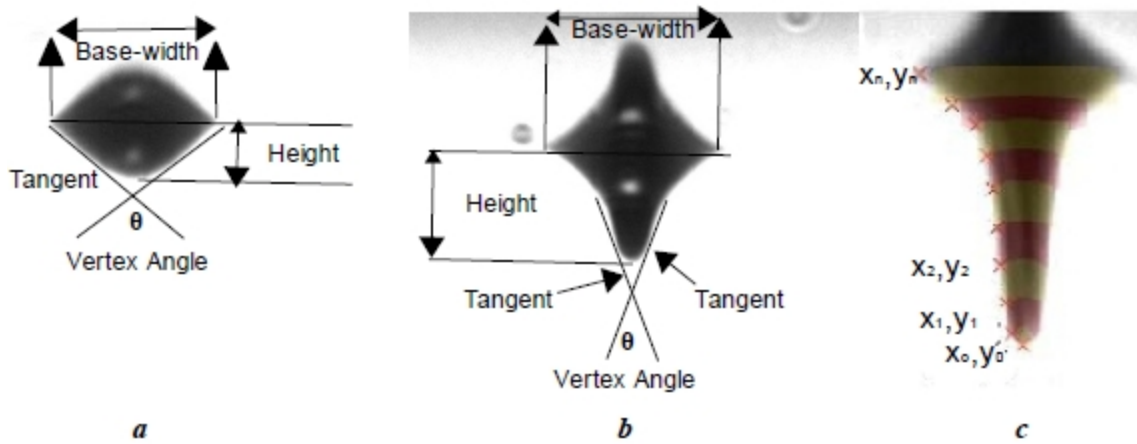


Figure 3.13: Measurement of the vertex angle, height, base-width and volume in conventional setup a) Sub-Threshold regime, b) Jetting regime, c) Estimating the volume with cylindrical elements



### 3.2.3.1 Height and base-width

In the sub-threshold regime, the height (front of the induced protrusion) increases gradually. It is  $9 \pm 4 \mu\text{m}$  after  $1 \mu\text{s}$  which almost doubles to  $21 \pm 7 \mu\text{m}$  at  $2 \mu\text{s}$ . During  $3\text{-}5 \mu\text{s}$  a plateau is observed where it is approximately  $34 \pm 5 \mu\text{m}$  at  $5 \mu\text{s}$ . From  $6 \mu\text{s}$  it decreases and reduces to  $18 \pm 6 \mu\text{m}$  at  $10 \mu\text{s}$ .

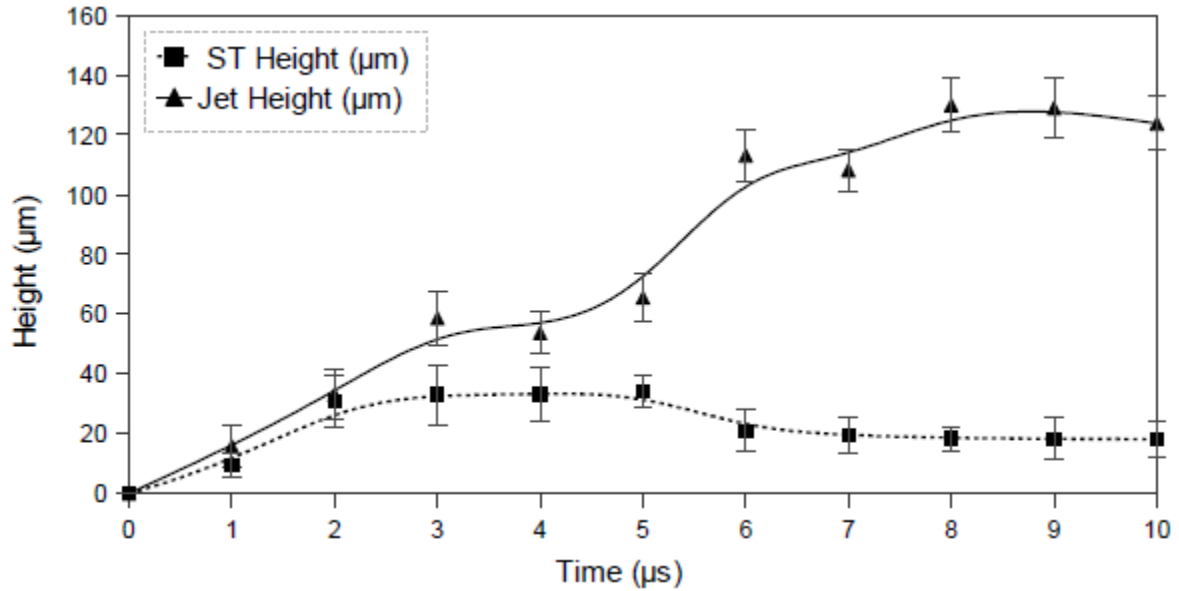


Figure 3.14: Maximum height versus time; sub-threshold (fine dots), solid curve for jetting regime

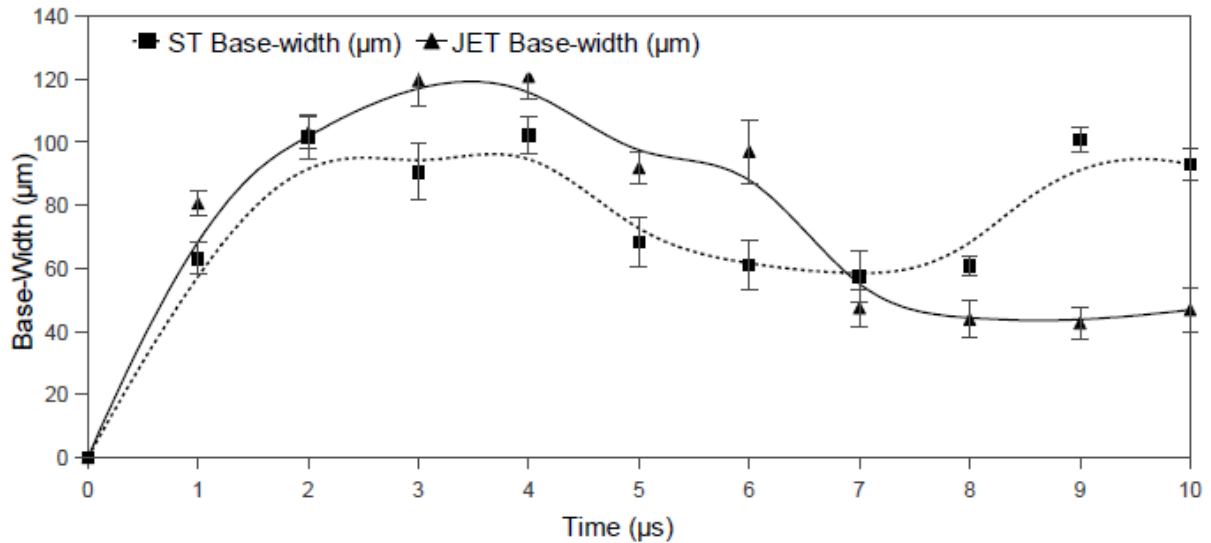


Figure 3.15: Maximum base-width versus time; sub-threshold (fine dots), solid curve for jetting regime

The base-width (Fig. 3.15) of deformation increases rapidly in the sub-threshold regime. It is  $63 \pm 5 \mu\text{m}$  after  $1 \mu\text{s}$  and reaches to  $101 \pm 7 \mu\text{m}$  at  $2 \mu\text{s}$ . It attains its maximum  $102 \pm 6 \mu\text{m}$  at  $4 \mu\text{s}$  later it decreases. At  $5 \mu\text{s}$ , the base-width is  $68 \pm 8 \mu\text{m}$  and decreases gradually to  $61 \pm 3 \mu\text{m}$  at  $8 \mu\text{s}$ . It increases again to approximately  $101 \pm 4 \mu\text{m}$  at  $9 \mu\text{s}$  and finally it is  $93 \pm 5 \mu\text{m}$  at  $10 \mu\text{s}$ . The height (Fig. 3.14) and base-width (Fig. 3.15) drop slowly from  $6\text{-}8 \mu\text{s}$  and recoil with few fluctuations at later stages.



In case of the jetting regime, the height (Fig. 3.14) increases apace during first few micro seconds. At  $1\mu\text{s}$ , height is  $16\pm 7\mu\text{m}$  and doubles to  $33\pm 8\mu\text{m}$  at  $2\mu\text{s}$ . The rapid expansion leads it to  $58\pm 9\mu\text{m}$  at  $3\mu\text{s}$ . A plateau is observed during 3-4 $\mu\text{s}$  in height. Afterwards it increases gradually as jet proceeds downward. The maximum height is  $\sim 130\pm 9\mu\text{m}$  at  $8\mu\text{s}$ .

Base-width (Fig 3.15) for jetting conditions also increases at a rapid pace. It is  $80\pm 5$  and  $103\pm 5\mu\text{m}$  after 1 and  $2\mu\text{s}$  respectively and attains its maximum value  $\simeq 120\pm 8\mu\text{m}$  at  $4\mu\text{s}$ . From  $5\mu\text{s}$  onward the base-width starts shrinking as the jet progresses. It is  $97\pm 10\mu\text{m}$  at  $6\mu\text{s}$  and shrinks quickly to  $47\pm 6\mu\text{m}$  at  $7\mu\text{s}$  afterwards it attains the final value  $46\pm 7\mu\text{m}$  at  $10\mu\text{s}$ .

### 3.2.5.2 Volume

In the sub-threshold regime, the volume of deformation is  $24\pm 3\text{pL}$  after  $1\mu\text{s}$ . During 1-3 $\mu\text{s}$  volume increases rapidly from  $24\pm 3$  to  $174\pm 9\text{pL}$ , which is its maximum value. At  $5\mu\text{s}$ , it is  $139\pm 3\text{pL}$  and further decreases to  $94\pm 4\text{pL}$  at  $6\mu\text{s}$ . Afterwards it is continuously decreasing and finally reduces to  $24\pm 10\text{pL}$  at  $10\mu\text{s}$  (Fig. 3.16).

In jetting conditions, volume (Fig. 3.16) increases from 0 to its maximum value of  $308\pm 26\text{pL}$  during first 3 $\mu\text{s}$ . Afterwards, it decreases. It attains approximate values of  $252\pm 14$ ,  $202\pm 18$ ,  $82\pm 11\text{pL}$  at 4, 6 and  $8\mu\text{s}$  respectively. It fluctuates to  $80\pm 8$  and  $88\pm 4\text{pL}$  at 9 and  $10\mu\text{s}$ .

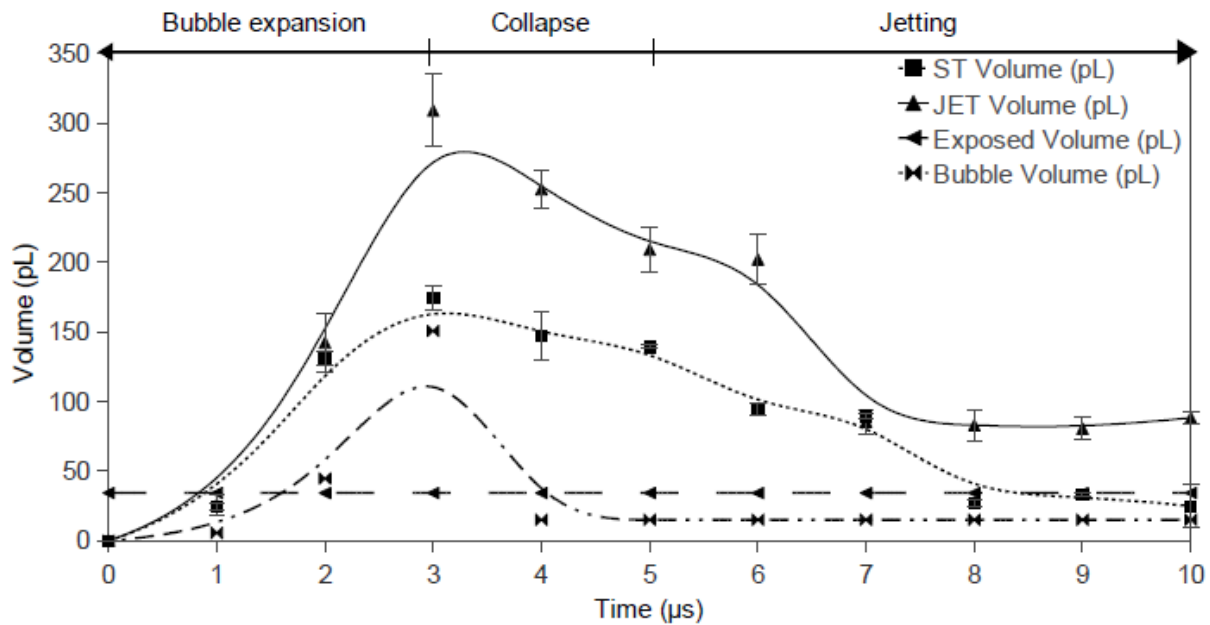


Figure 3.16: Volume versus time, sub-threshold (fine dots), solid curve for jetting regime volume, dashed and dotted curve denotes estimated bubble volume and dashed line denotes estimated volume exposed to laser pulse

### 3.2.5.3 Velocity

Height difference as measured from temporal images are divided by corresponding times interval to determine instantaneous velocity (Fig. 3.17). The protrusion of sub-threshold regime makes a debut with  $9\pm 4\text{m/s}$ . However, the velocity more than  $11\pm 4\text{m/s}$  is maintained

only for  $2\mu\text{s}$ . Later a profound decrease is observed as  $v_{\text{inst}}$  reduces to 0 at  $4\mu\text{s}$ . It keeps on decreasing to its minimum  $-13\pm 2\text{m/s}$  at  $6\mu\text{s}$ . The forward progression is ceased and it is also evident from zero acceleration during  $8\text{--}10\mu\text{s}$ .

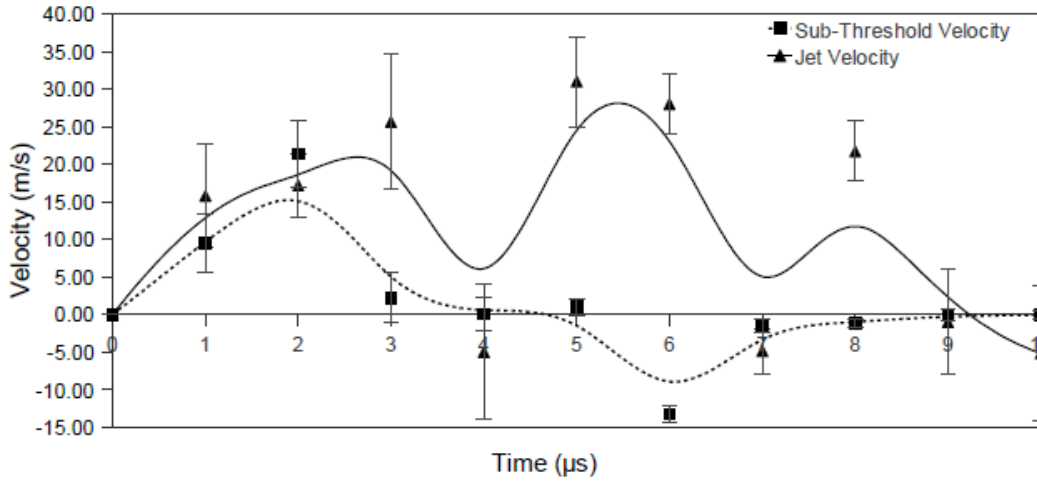


Figure 3.17: Velocity versus time for Sub-Threshold regime (fine dots) and curve (solid line) for Jetting regime

In jetting conditions, initial velocity of the protrusion is  $16\pm 7\text{m/s}$  and reaches to  $17\pm 4\text{m/s}$  at  $2\mu\text{s}$ . It further increases to  $25\pm 9\text{m/s}$  at  $3\mu\text{s}$  and attains the maximum ( $\sim 31\pm 6\text{m/s}$ ) at  $5\mu\text{s}$ . At  $6\mu\text{s}$  as the jet is fully developed and progressing forward with  $28\pm 4\text{m/s}$ . Afterwards its velocity decreases and finally reduces to  $-5\pm 5\text{m/s}$  at  $10\mu\text{s}$ .

#### 3.2.5.4 Vertex angle

In sub-threshold regime, the vertex angle of deformation decreases rapidly from  $180^\circ$  to  $140\pm 8^\circ$  at  $1\mu\text{s}$  and further decreases to  $113\pm 5^\circ$  at  $2\mu\text{s}$  and  $111\pm 4^\circ$  during  $3\text{--}4\mu\text{s}$ . It attains the minimum value of  $105\pm 5^\circ$  (5<sup>th</sup> frame of Fig. 3.12a) at  $5\mu\text{s}$ . From  $6\mu\text{s}$ , the vertex angle increases again. It is  $118\pm 7^\circ$  at  $6\mu\text{s}$  and reaches to  $124\pm 5^\circ$  at  $10\mu\text{s}$ .

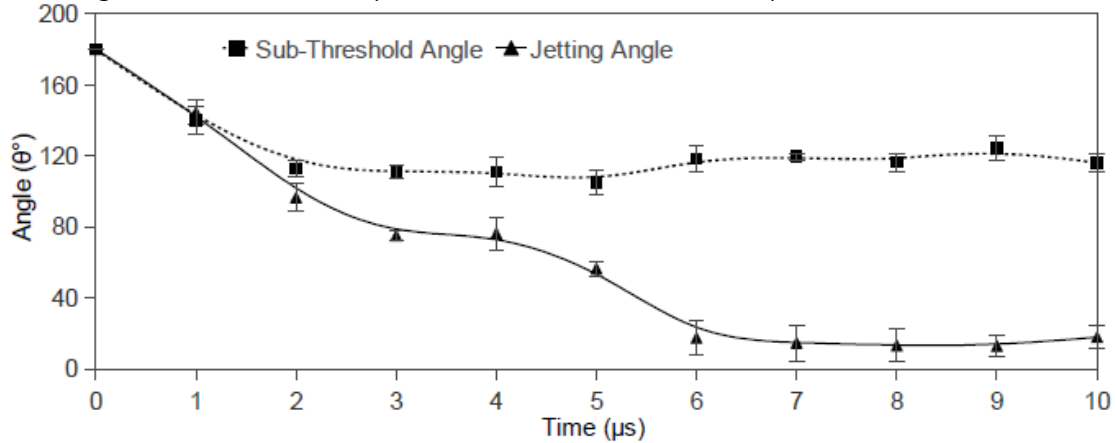


Figure 3.18: Vertex angle versus time; sub-threshold regime (fine dots) and jetting regime (solid line).

In case of the jetting-regime, vertex angle of the front of the jet decreases apace as compared to sub-threshold regime. It drops from  $180^\circ$  to  $144\pm 7^\circ$  at  $1\mu\text{s}$ . Quickly expanding bubble crosses critical limit of  $105^\circ$  and vertex angle drops to  $96\pm 7^\circ$  at  $2\mu\text{s}$  and keeps on

decreasing further to  $75\pm3^\circ$  at  $3\mu\text{s}$ . The plateau appears during  $3\text{--}4\mu\text{s}$  (Fig. 3.18). The further decrease in vertex angle is bit slow,  $12\pm6^\circ$  at  $9\mu\text{s}$ . The slope ( $\sim 27^\circ/\mu\text{s}$ ) of the graph in Figure 3.18) is higher between  $0\text{--}6\mu\text{s}$  than that during  $6\text{--}10\mu\text{s}$  ( $\sim 1.5^\circ/\mu\text{s}$ ). However, at  $10\mu\text{s}$  the vertex angle again increases to  $18\pm7^\circ$ .

### 3.2.6 High speed jetting

After characterization of transition between sub-threshold and jetting regimes, we explored jetting regime to analyse jet dynamics. For quantitative study of velocity in jetting condition, we evaluated LAB for high speed and stable jet to study its capacity - as a powerful tool for high speed printing. The time-resolved profiles of the jets were acquired, from 1 to  $10\mu\text{s}$  with step-index of  $1\mu\text{s}$ , for temporal evaluation of jet stability and jet speed. In this context our manipulations were carried out by altering energy from 21 to  $43\mu\text{J}$  and using  $40\mu\text{m}$  thick layer of the bioink (1%NaAlg, 30% glycerol, 70% water and 15mg/mL BSA).

We also analysed jetting regime (Fig. 3.19) to study the influence of laser energy on jet velocity, jet turbulence and resulting prints. Temporal images (Fig. 3.19) of jets, corresponding velocities (Fig. 3.20a) and respective printed drops (Fig. 3.20b) are shown.

The initial expansion of the bubble is significant which leads to jetting. For jets produced with  $21\mu\text{J}$  ( $2.5\text{J}/\text{cm}^2$ ), bubble expands quickly and reaches to its maximum size at  $3\mu\text{s}$  and a jet arises at  $4\mu\text{s}$  (Fig. 3.19a). The jet is fully developed and progressing forward at  $5\mu\text{s}$  whereas collapsing bubble is also visible till  $6\mu\text{s}$  where a counter jet can also be observed (6<sup>th</sup> frame of Fig. 3.19a). From  $7\mu\text{s}$  and later, elongation and thinning of jet cause considerable reduction in base-width. Crown-like formation around the base of the jet appears at  $9\mu\text{s}$  and becomes more prominent at  $10\mu\text{s}$ . Jet (Fig. 3.19b) produced with  $35\mu\text{J}$  ( $4.1\text{J}/\text{cm}^2$ ) shows similar profiles and jet emerges at  $3\mu\text{s}$ . The fully developed jet is progressing forward at  $4\mu\text{s}$  whereas collapsing bubble is also visible till  $6\mu\text{s}$ . Later, an elongating and thinning jet is observed with reducing base-width. Jet becomes more thinner at  $10\mu\text{s}$ . For jets (Fig. 3.19c) produced with  $40\mu\text{J}$  ( $4.7\text{J}/\text{cm}^2$ ), the initial expansion of the bubble is violent. Bubble expands to its maximum size in  $2\mu\text{s}$  and jet emerges at  $3\mu\text{s}$ . The jet is fully developed at  $3\mu\text{s}$  and becomes turbulent at  $5\mu\text{s}$ . Its forward perturbed progression contains enclosed vapour cavity till  $10\mu\text{s}$ . Temporal profiles produced with  $43\mu\text{J}$  ( $5\text{J}/\text{cm}^2$ ) present the plume (Fig. 3.19d) in which violent explosion of bubble leads to liquid spray.

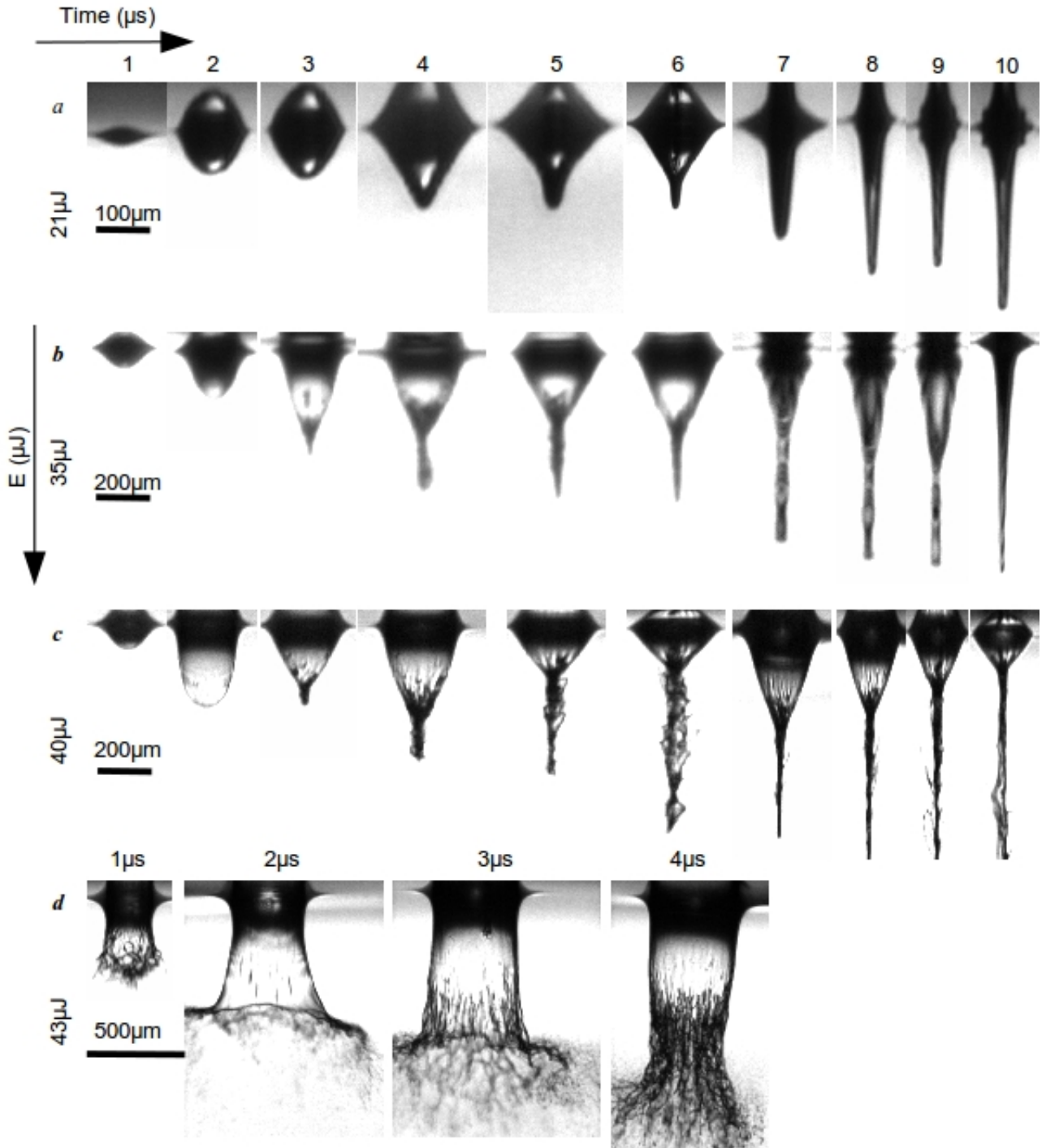


Figure 3.19: TRI for jets with increasing energy a) 21μJ, b) 35μJ, c) 40μJ, d) 43μJ

Figure 3.20a shows jet velocity profiles. The maximum instantaneous velocity ( $v_{\text{inst}}$ ) are ranging from 97m/s to 626m/s: namely 97, 534 and 626m/s for jets produced with 21, 35 and 40μJ energies respectively. Jet shown in Figure 3.19a has maximum  $v_{\text{inst}}$  of 97m/s which reduces to -2.7m/s at 10μs. The jet produced with 35μJ (Fig. 3.19b) emerges with 188m/s and attains maximum  $v_{\text{inst}} \sim 534\text{m/s}$  and is moving with 352m/s at 10μs. In case of turbulent jet produced with 40μJ, initial  $v_{\text{inst}}$  of the jet is 240m/s which reaches to its maximum value of

626m/s. These supersonic jets have turbulent profile (Fig. 3.19c). The jet crosses field of view (FOV) of the camera at  $8\mu\text{s}$ , therefore, velocity at later stages can't be determined. The fastest jet has velocity of 626m/s and plume regime is obtained with  $43\mu\text{J}$ .

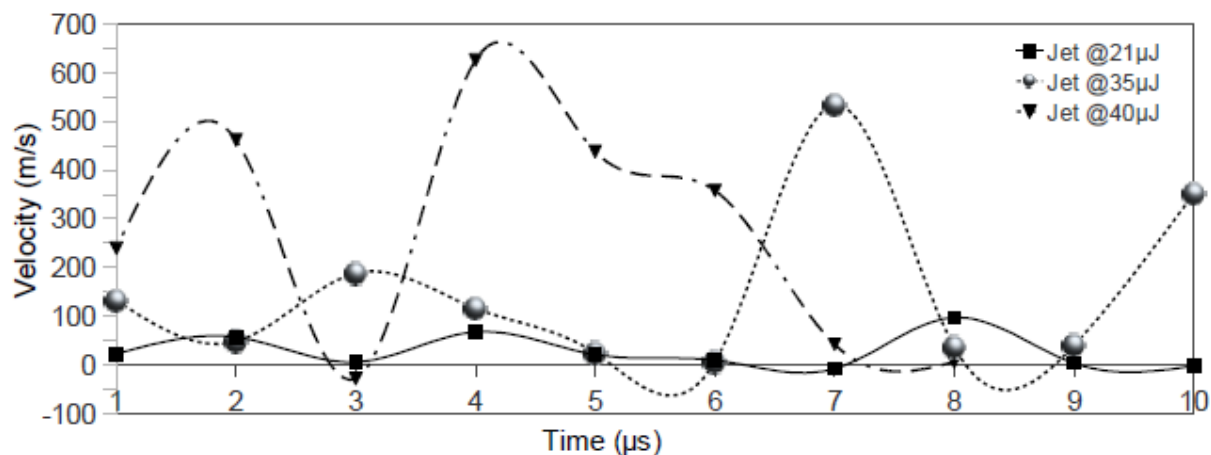


Figure 3.20a: High energy jet velocity versus time

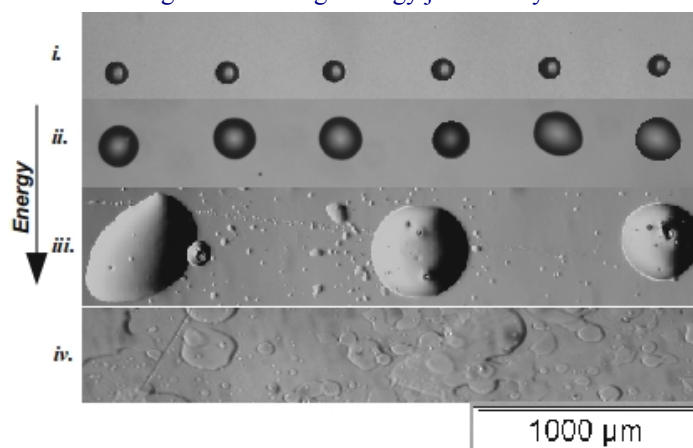


Figure 3.20b: Printing bioink from different jets, i) laminar jet, ii) high speed jet iii) turbulent jet and iv) plume

Printed drops from jets of different velocities are shown in figure 3.20b. Fine and perfectly spherical drops result from jets of  $21\mu\text{J}$ . High speed jet of  $35\mu\text{J}$  produces spherical drops of larger size with few satellite drops. The turbulent jet of  $40\mu\text{J}$  not only produces bigger drops but also deteriorates their spherical shape. Moreover satellite drops are also observed. In case of very high energy ( $43\mu\text{J}$ ) leading to plume regime, no perfect drop is obtained on receiver substrate and uncouth spray of the bioink is observed.

This part (§3.2) was devoted to the experiments conducted in the conventional LAB setup. In these experiments, it is observed that the setup faces a major drawback of inhomogeneity of the liquid film (bioink). Moreover it seriously compromises the LAB process and leads to irreproducibility. The energy used for the jetting is slightly above threshold, sometimes it does not produce jet at one position of the donor slide and it works well for another position on the same donor slide.

### 3.3 SECTION B

This section presents detailed results of laminar jets close to the threshold. An experimental study of laser-induced jet formation from thin films of different viscosities is designed to extend previous results for a comprehensive picture of the LAB. This section emphasize the effect of viscosity on jet formation.

#### 3.3.1 TRI for laminar jets ejection and dynamics

TRI study is conducted for laminar jets produced with 21 $\mu$ J energy and 40 $\mu$ m thick layer of three different bioinks having different viscosities 27, 60 and 107mPa s respectively. Temporal images (Figs. 3.21-3.22) of the transfer process from lateral view are acquired with different time delay to analyse the mechanism of LAB.

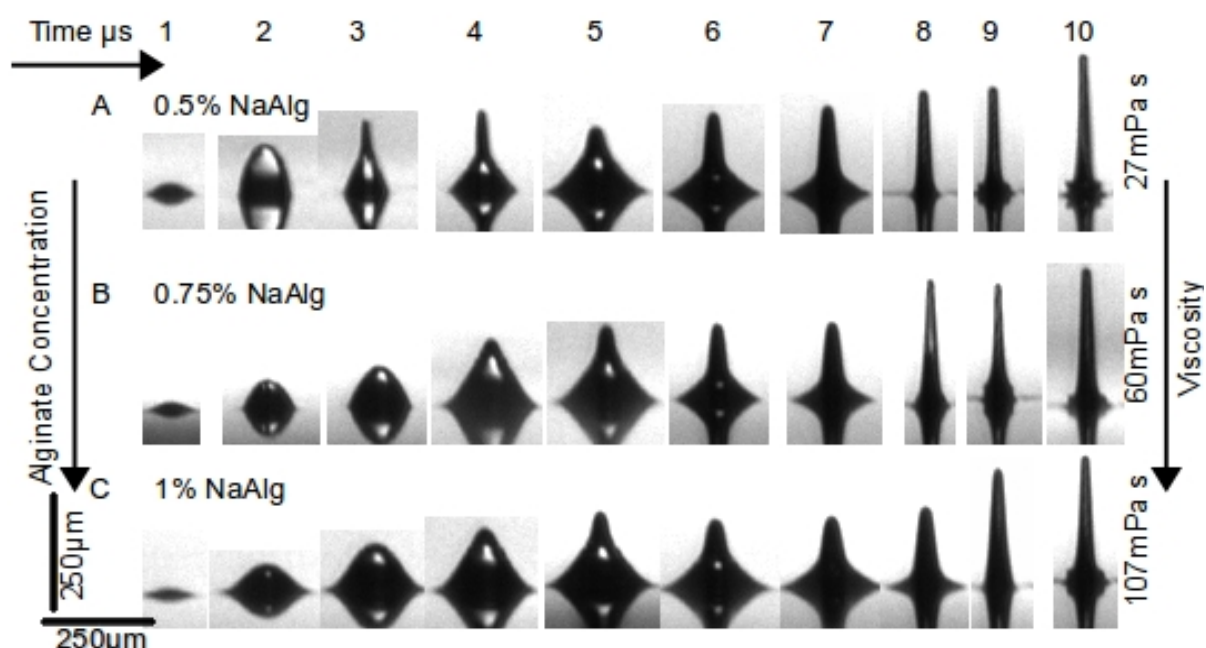


Figure 3.21: TRI for jet formation with 21 $\mu$ J from solutions of different viscosities

The initial expansion of the bubble further leads to jet formation after the bubble collapse. For all three bioinks, initial expansion is more prominent (Fig. 3.21), whereas after bubble collapse and formation of jet, its elongation and thinning is dominant with needle-like shape during the whole progression.

Bubble expansion is more rapid and prominent in case of 27mPa s solution (Fig. 3.21a) as compared to more viscous solutions. It expands quickly and reaches to its maximum size at 2 $\mu$ s where it collapses and jet emerges at 3 $\mu$ s. The jet is fully developed and progressing forward at 3 $\mu$ s whereas collapsing bubble is also visible till 5 $\mu$ s. Later the jet elongates with considerable reduction in base-width till 8 $\mu$ s. Crown-like structure around its



base appears at  $9\mu\text{s}$  which becomes more prominent at  $10\mu\text{s}$ . Rapid expansion of bubble can also be observed for other two solutions of alginate (Fig. 3.21b&c). Unlike  $27\text{mPa s}$  solution, the expansion is round till  $3\mu\text{s}$  and jet emerges at  $5\mu\text{s}$ . Later jet moves forward elongating and thinning with reducing base-width till  $8\mu\text{s}$ . For  $60\text{mPa s}$  solution (Fig. 3.21b), the crown-like structure appears at  $9\mu\text{s}$  and become prominent at  $10\mu\text{s}$  in contrast to  $107\text{mPa s}$  solution where the base-width of the jet is less reduced till  $8\mu\text{s}$  and crown-like structure appears at  $10\mu\text{s}$ .

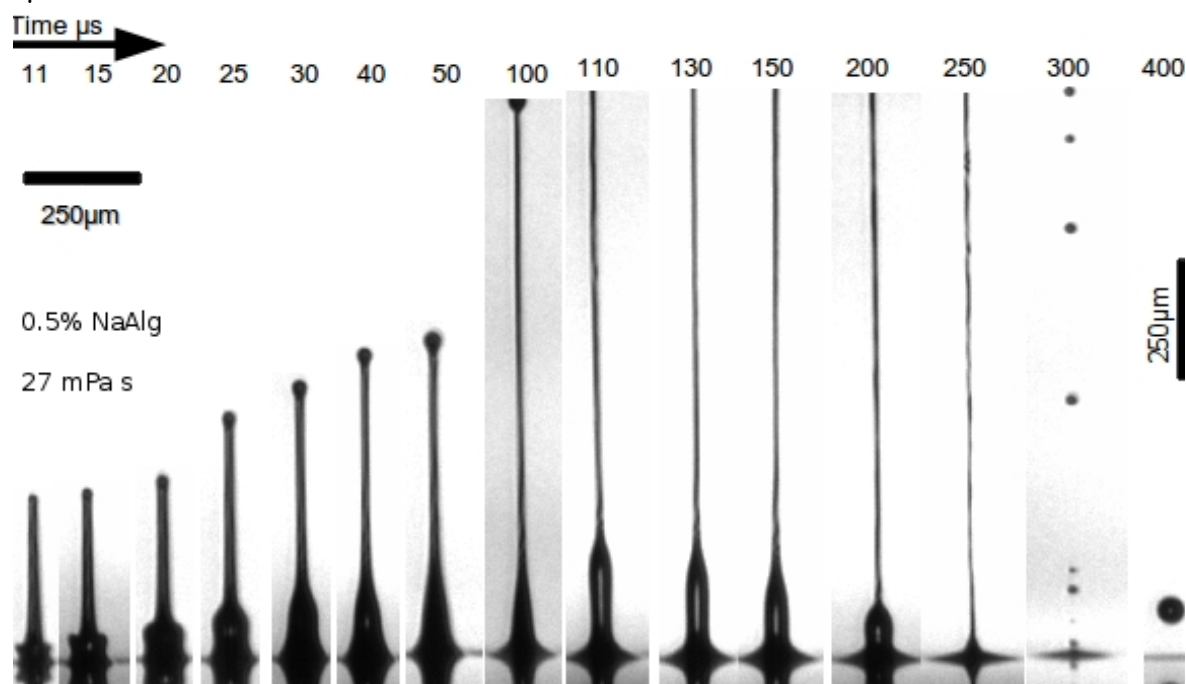


Figure 3.22a: TRI of jet progression from  $27\text{mPa s}$  (0.5% NaAlg) with  $21\mu\text{J}$

Further investigation of jet dynamics by TRI (Fig. 3.22) shows that jet from  $27\text{mPa s}$  solution has very clear crown around its base at  $11\mu\text{s}$  (Fig. 3.22a) which persists till  $15\mu\text{s}$  and later converges to shoulder like structure at  $20\mu\text{s}$  remaining persistent till  $25\mu\text{s}$ . At this stage, tip of the jet has grown into an almost spherical mass i.e. formation of drops at the top of the jet can be seen with is fully developed at  $50\mu\text{s}$ . At  $100\mu\text{s}$  the jet containing drop at its head is crossing the FOV of the camera. Afterwards drop can't be seen. Slender jet with clear shoulder structure is present till  $200\mu\text{s}$ . At  $250\mu\text{s}$  jet is converted into thread like structure which is fragmented into drops at  $300\mu\text{s}$ . Finally at  $400\mu\text{s}$  the last drop is observed which is moving downward.

TRI investigation of jet produced with  $60\text{mPa s}$  solution is presented in Figure 3.22b. The jet has a crown around its base at  $11\mu\text{s}$ . The crown persists till  $15\mu\text{s}$  and converges into shoulder like structure at  $20\mu\text{s}$ . Formation of drops at the top of the jet appears at  $25\mu\text{s}$  which is fully developed at  $100\mu\text{s}$ . At  $110\mu\text{s}$ , the jet carrying drop at its head is crossing the FOV of

the camera. Afterwards thin jet is present till 200 $\mu$ s. At 250 $\mu$ s jet has thread like structure which converts into drops connected by thread at 300 $\mu$ s. Finally at 400 $\mu$ s the last drop moving downward is observed.

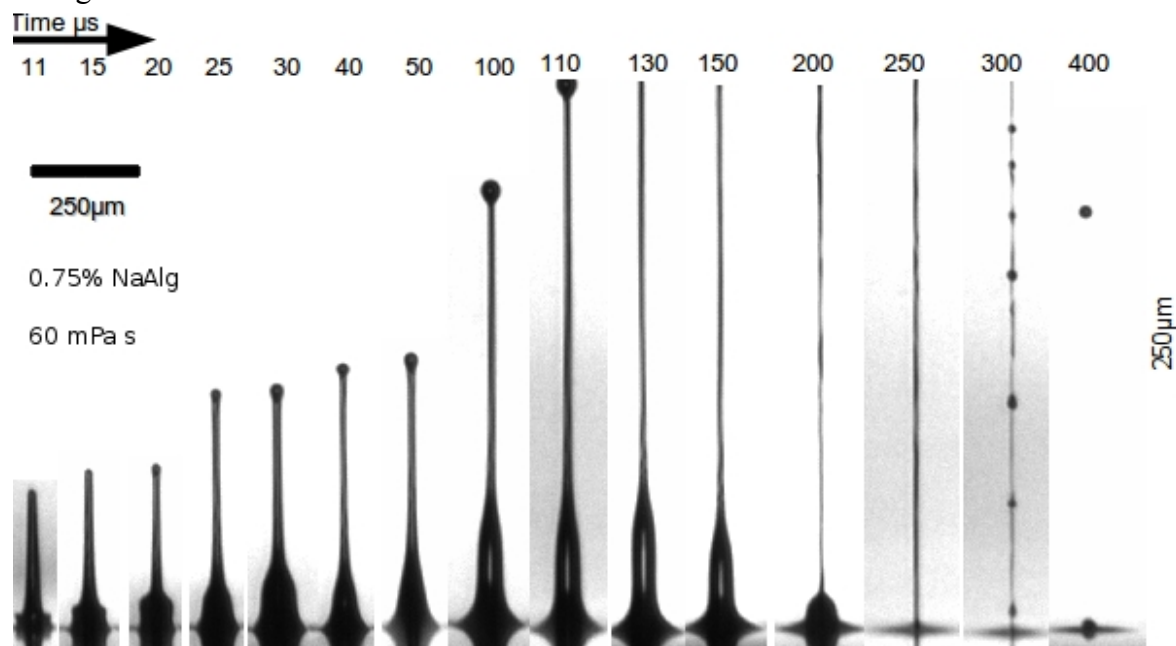


Figure 3.22b: TRI of jet progression from 60mPa s (0.75% NaAlg) with 21 $\mu$ J

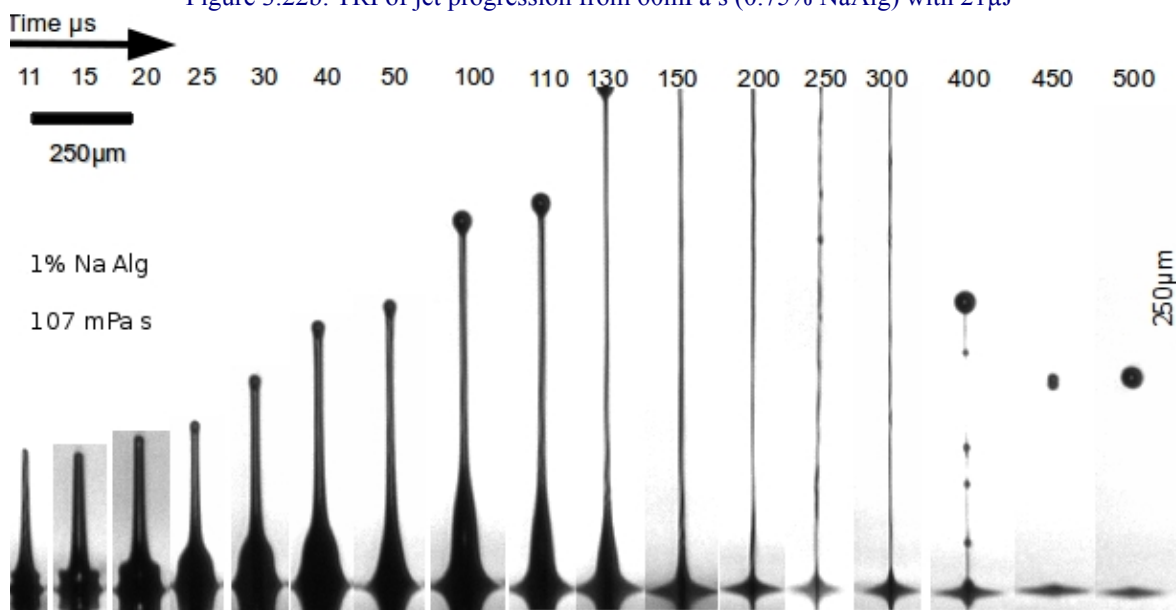


Figure 3.22c: TRI of jet progression from 107mPa s (1% NaAlg) with 21 $\mu$ J

Figure 3.22c is meant for the jet produced by 107mPa s solution. The crown-like structure makes its first appearance at 10 $\mu$ s (Fig. 3.22c) and becomes more profound and prominent at 15 $\mu$ s. As the jet elongates, shoulder structure appears at 20 $\mu$ s with gradual reduction in its width while increasing height. Drop formation starts at 25 $\mu$ s and becomes prominent at 100 $\mu$ s. Jet carrying drop at its head is crossing the FOV of the camera at 130 $\mu$ s. Unlike 27mPa s and 60mPa s solutions, the height of the shoulder is reducing quickly in this case and jet converted into thread at 150 $\mu$ s. The fragmentation of the jet into drops connected



with thread appears late with a difference of  $100\mu\text{s}$  at  $400\mu\text{s}$  instead of  $300\mu\text{s}$  as observed for other two solutions. From  $400\mu\text{s}$  drops are observed moving downward which persists till  $500\mu\text{s}$ .

### 3.3.2 Height of laminar jets

Plot of jet height versus time (Fig. 3.23) provides a direct relation between height and time. Height of the jet of 27mPa s solution is higher than solutions of 60 and 107mPa s. The velocity profiles (Fig. 3.24) show that ejection velocity ( $25\text{m/s}$  at  $1\mu\text{s}$ ) is higher for 27mPa s solution in comparison to 60 ( $21\text{m/s}$ ) and 107 mPa s solutions ( $19\text{m/s}$ ). It increases at first stage ( $1\text{-}3\mu\text{s}$ ) due to bubble expansion. It drops once the jets are formed. It is gradually decreasing as jets progress upward until they cross FOV, having front velocities  $12\text{m/s}$  ( $0.5\%$  at  $100\mu\text{s}$ ),  $10\text{m/s}$  ( $0.75\%$  at  $110\mu\text{s}$ ) and  $8\text{m/s}$  ( $1\%$  at  $130\mu\text{s}$ ). Jets become thinner (Fig. 3.25) with the increasing viscosity.

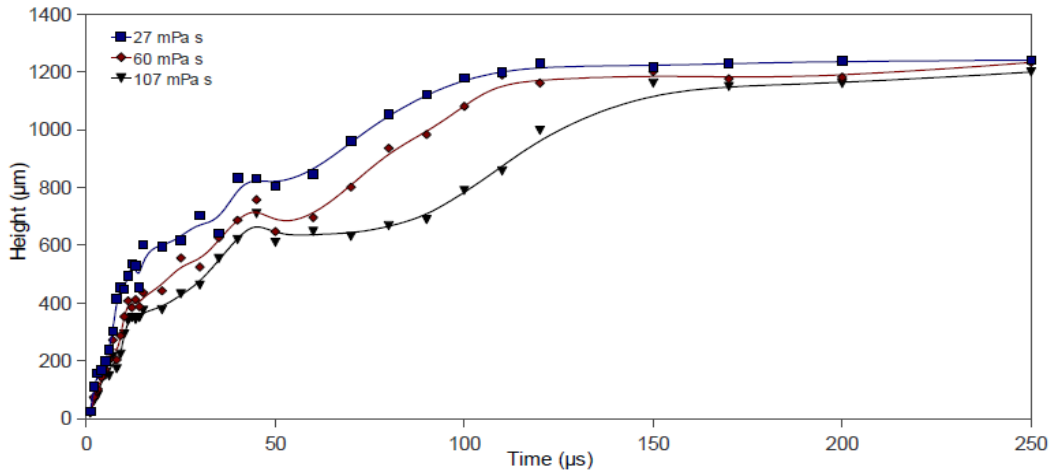


Figure 3.23: Height of the jet (front position) with  $21\mu\text{J}$  versus time

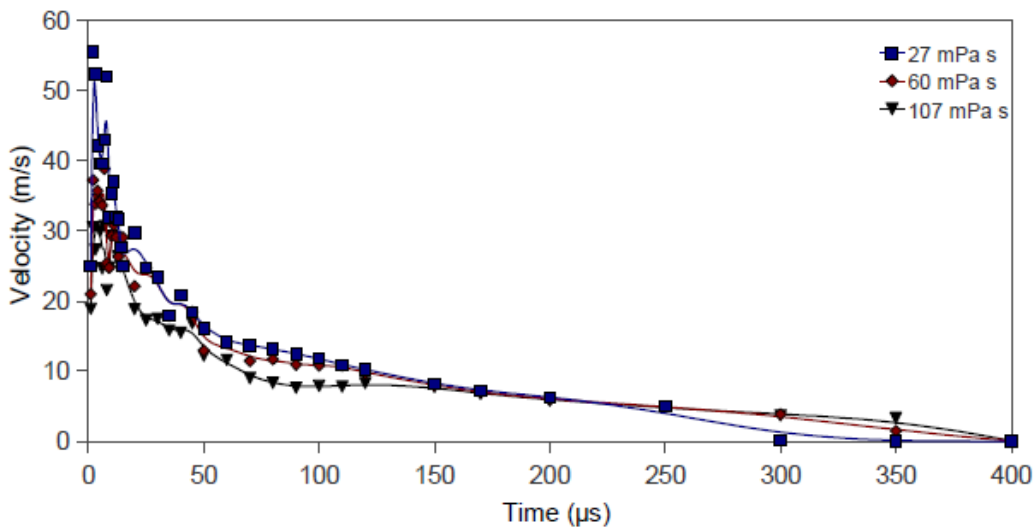


Figure 3.24: Velocity of the jet (front position) from  $21\mu\text{J}$  versus time

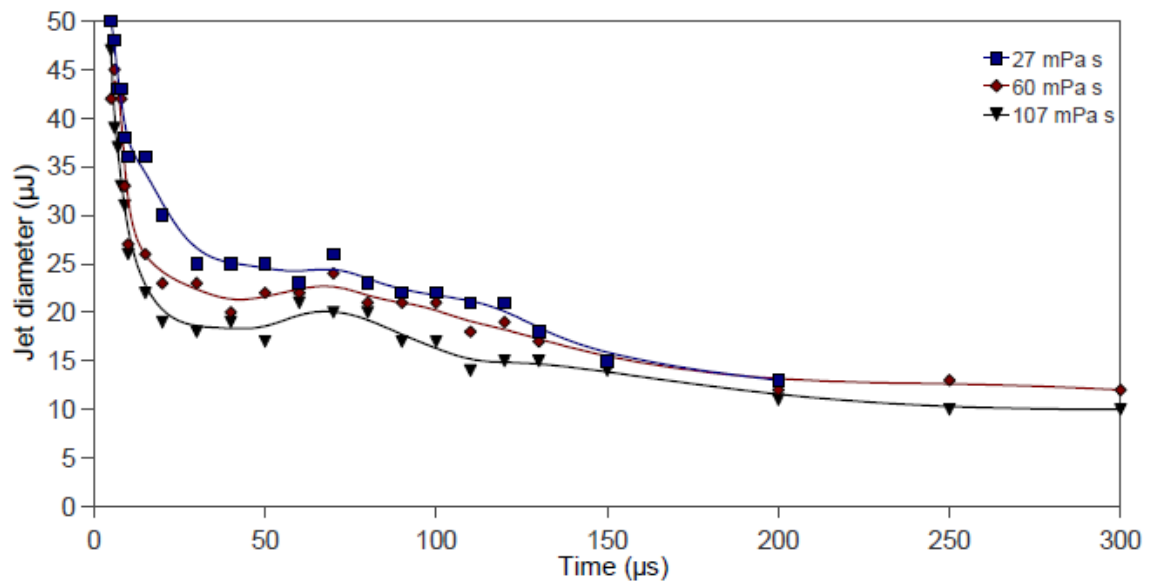


Figure 3.25: Diameter of the jet from 21  $\mu$ J versus time

### 3.4 SECTION C: Parametric Study of Novel Configuration

This section presents detailed results of parametric studies of LAB. Although some of the effects of some parameters on the printed droplets have already been described [122,142,145,190,191], an experimental study of droplet printing from thin films of viscous bioinks is designed to extend previous results. The capacity to print at large distance is investigated for the first time with wide range of viscosity as well as energy.

#### 3.4.1 Viscous liquids drop printing

In order to study the relation between laser pulse energy and size of printed drops and its dependence on the viscosity of the bioinks, experiments were conducted for distant printing of viscous liquid solutions having 2, 4 and 6(w/v%) of NaAlg, 10 (v/v)% glycerol and 90(v/v)% water. Corresponding viscosities are 94, 694 and 2618mPa s. Micro-array (5x7) separated by 1000 $\mu$ m are prepared. The thickness of the liquid film is maintained at 40 $\mu$ m. The optical microscopy of the printed array of droplet is shown in Figures 3.26-3.27. The laser energies used are 37.2, 47, 55,78.5, 111.4,147.2, 159.7 $\mu$ J.

##### 3.4.1.1 Effect of laser energy on drop size

To study the influence of laser energy and viscosities on size of the printed droplets, separation distance is kept constant by keeping the collector substrate at 5mm. Printed drops are tails free with almost no satellite droplets. At higher laser energies satellites droplets are observed where as for 2% NaAlg solution, high energy leads to splashes. Shape of the drop is deteriorated with high energy (Fig. 3.27c).

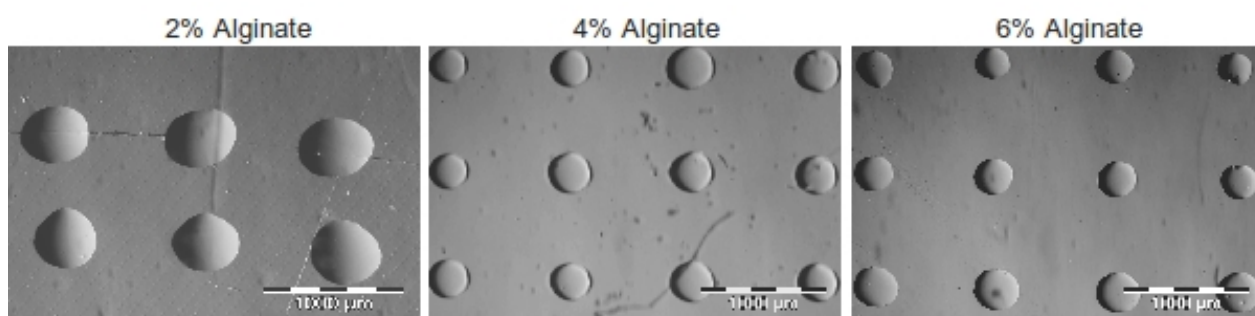


Figure 3.26: Printed drops array from viscous alginate solution at 5mm with 55 $\mu$ J laser pulse

Drops diameter increases with the energy for a given viscosity. The smallest drops are obtained with the  $E_{\min}$ =37.2 $\mu$ J for each solution. The minimum drop size is ~217 $\mu$ m for 6% NaAlg solution at  $E_{\min}$ . For qualitative analysis of the present results the drop diameter is measured from the optical microscopic images of the printed arrays with the help of ImageJ. The results are plotted against energy (Fig 3.28). The graph provides an upward trend showing a linear dependence between drop size and laser energy.

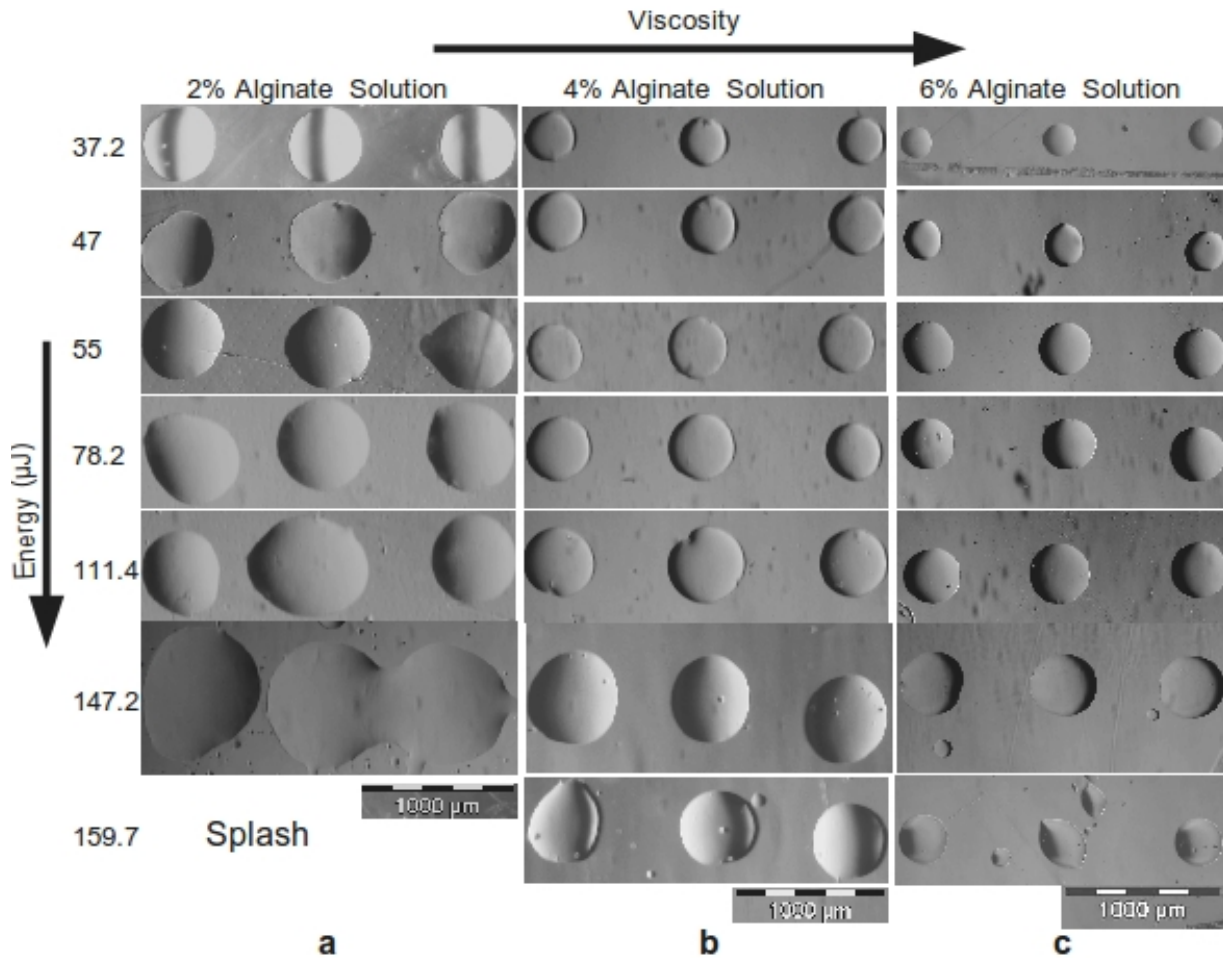


Figure 3.27: Printed drops at 5mm

We can conclude that circular and well define drops are successfully printed at 5mm distance in upward printing configuration. The printed drops are almost satellite free, however satellite droplets are observed for higher energies. It is observed that drop diameter is directly proportional to the laser energy.

#### 3.4.1.2 Effect of liquid viscosity on drop size printed at 5mm

The viscosities of the solutions are also different (i.e. 94, 694 and 2618mPas respectively as mentioned by Lin et al. [192]). Such high concentration of alginate and significant viscosity differences, led to profound difference among the diameter of the drops for a given energy (Fig. 3.28).

It is also interesting to note that the slope difference (Fig. 3.29) between 2% and 4% is larger than that between 4% and 6% solutions. Drop size linearly increases with energy and decreases with viscosity (i.e. NaAlg concentration). The decrease in the drop size with increasing viscosity is also visible in printed arrays (Fig. 3.26-3.27). Satellite droplets are observed at higher energies. Numbers of the satellite drops are increasing with increasing

viscosity. However with less viscous solution increasing energy leads to splashes and printed drops are not perfectly round. Smaller drops are obtained for high alginate concentration which mean high viscosity has reduced drop diameter. Hence an inverse relationship between drop diameter and viscosity is observed for a given laser energy.

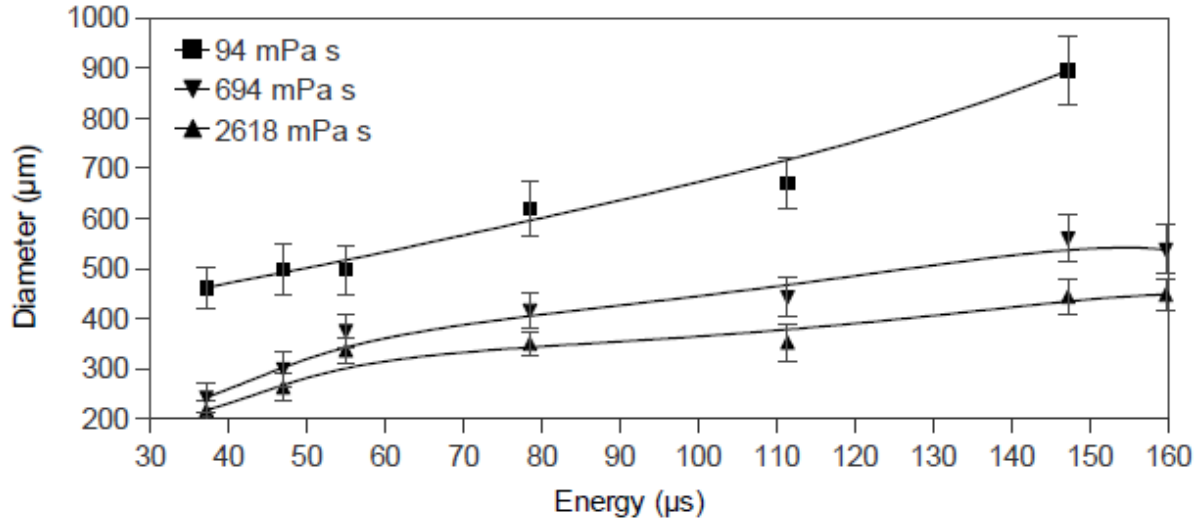


Figure 3.28: Drop diameter versus Energy

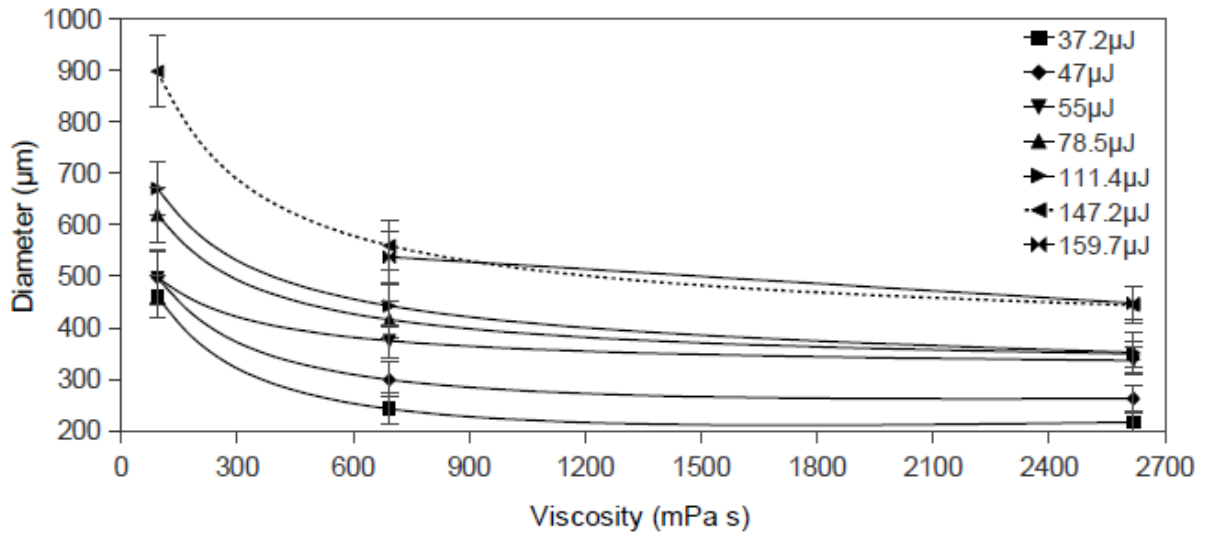


Figure 3.29: Drops diameter versus viscosity

### 3.4.1.3 Effect of printing distance on drop size

The separation distance (liquid film-receiver substrate separation) is one of the most important and relevant parameter apart from the laser energy used for printing purposes. The research further extends to determine the range of the separation distance which could be used to print circular drops. Separation distance are 3, 6, 8 and 10mm. Laser energy is fixed to 46μJ and film thickness is 40μm. The printed drops are observed under microscope and the corresponding images are recorded (Fig. 3.30).

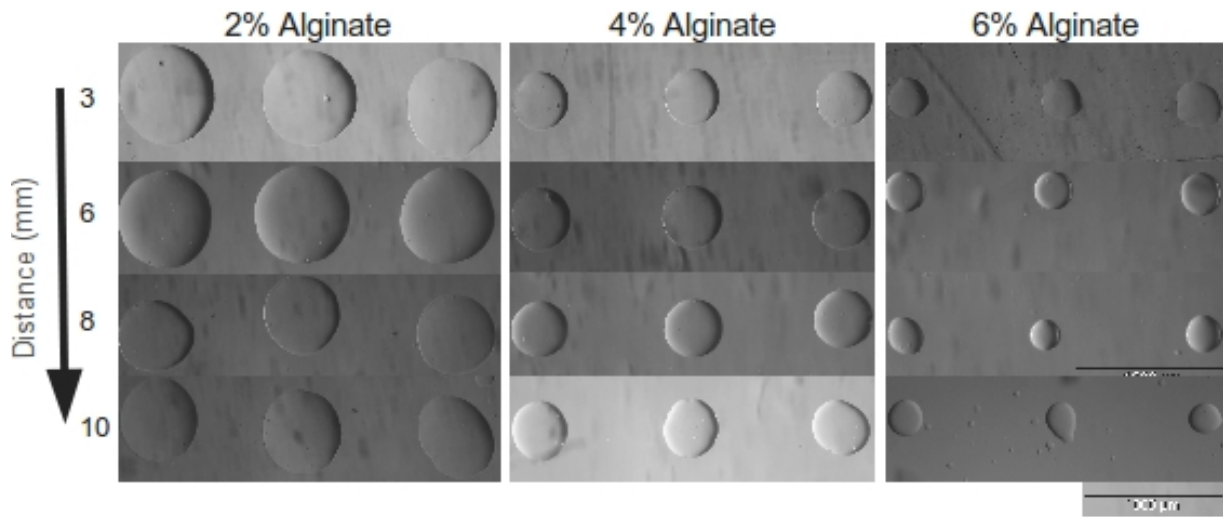


Figure 3.30: The printed drops as observed under microscope, scale bar is 1000 $\mu$ m

Circular and well-defined drops are printed. From 8 to 10mm satellite droplets appear, and in larger number for 6% alginate solution. Drop diameter is measured by imageJ and plotted versus distance and viscosity as shown in the figures 3.31-3.32.

Drop size decreases from  $510 \pm 38$  to  $430 \pm 24$  for solution of 94mPa s viscosity as distance increases from 3 to 10mm. For 694 mPa s viscosity, drop size  $310 \pm 33\mu$ m at 3mm. Increasing distance to 10mm, drop size drops to  $260 \pm 21\mu$ m for the same viscosity. In case of the most viscous ink 2618mPa s, drop diameter decrease from  $290 \pm 17\mu$ m to  $208 \pm 21\mu$ m as separation distance changes from 3 to 10mm.

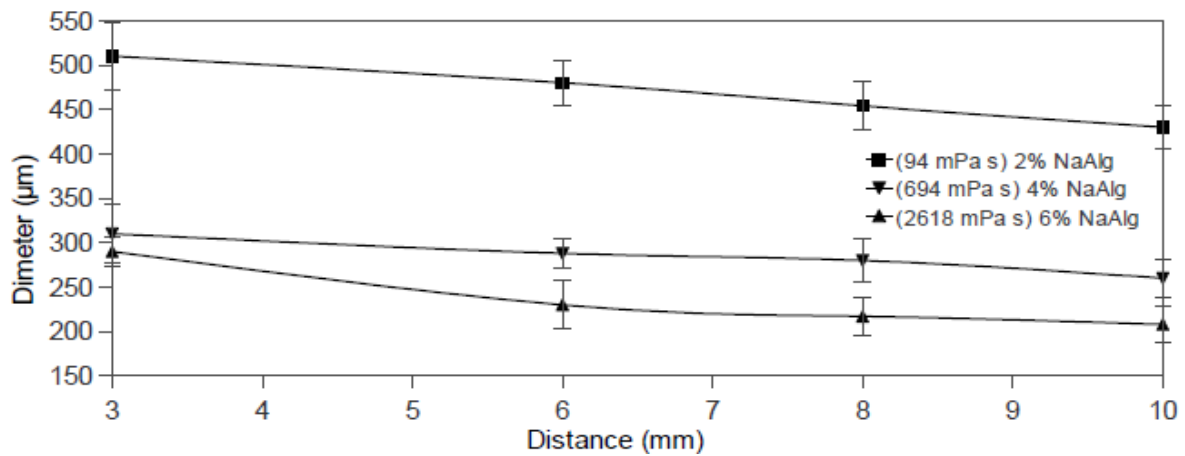


Figure 3.31: Drop diameter versus distance at 46 $\mu$ J

Drop diameter decreases with the increasing distance and viscosity. The minimum diameter  $\sim 208\mu$ m is observed for the drops from 6%NaAlg solution printed at 10mm. Slope of the curve is higher for 6%NaAlg as compared to other solutions (Fig. 3.31). Drop diameter decreases significantly for 3mm distance as compared to other distances (Fig. 3.32a). After measuring diameter and height of the drop, we estimated volume of the drops (cf. § 2.4.3). Drop volume (Fig. 3.32b) decreases with the increasing distance and viscosity. The minimum

volume  $\sim 326\text{pL}$  is observed for the drops from 6%NaAlg solution printed at 10mm.

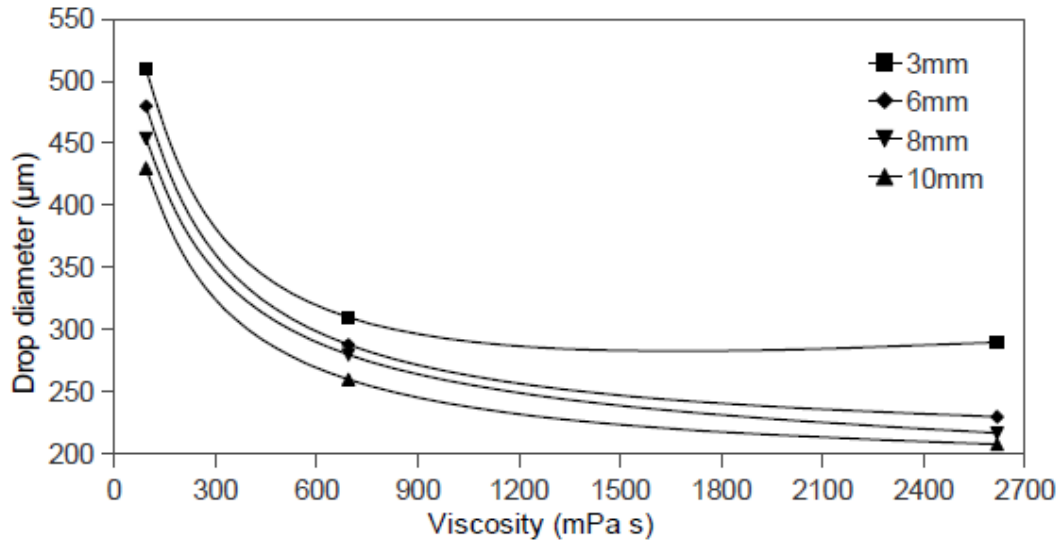


Figure 3.32a: Drop diameter printed with  $46\mu\text{J}$  at different distances versus viscosity

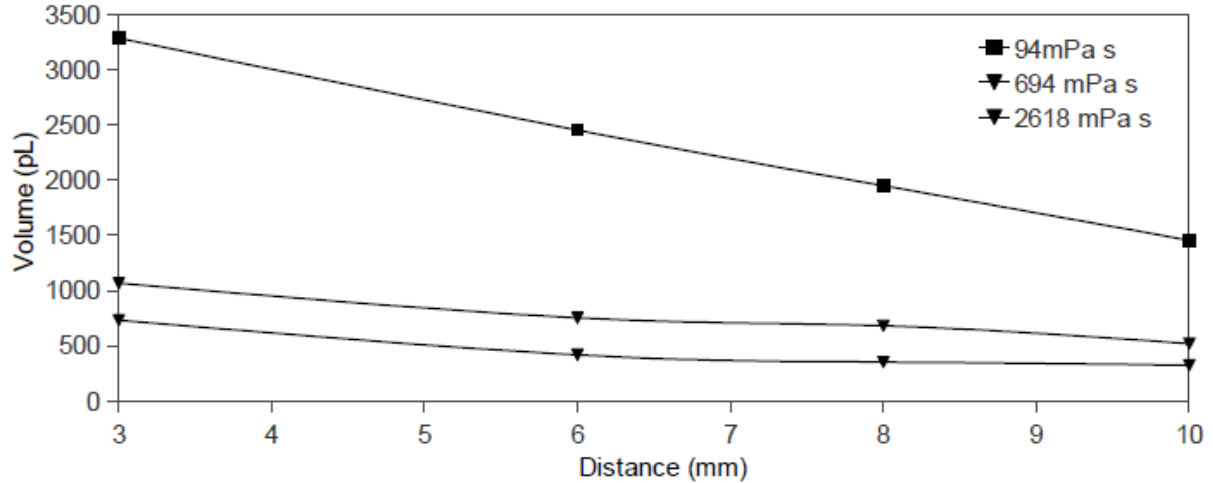


Figure 3.32b: Drop volume printed with  $46\mu\text{J}$  at different distances versus viscosity

From these experiments, it has been demonstrated that circular drops with well-defined contours can be printed by LAB for a wide range of viscous solution at considerably larger separation distances upto 10mm with very few satellites droplets. The spatial resolution is deteriorated with increasing distance however it is in the range of 10 to  $60\mu\text{m}$ . An inverse relationship between drop diameter and separation distance is found for a given energy and viscosity. This shows the high degree of flexibility of the configuration as the solutions viscosity has been changed almost 28 times.

### 3.4.2 Distant printing for low viscosity solutions

In last § 3.4.1, the solutions used are viscous and without BSA (biomolecule). As cell viability is function of laser energy, for its application in bioprinting it must be investigated with low energy. Therefore, a new set of experiments is designed to print less viscous solutions with BSA (15mg/mL) as biomolecule, 0.5 and 1(w/v%) of NaAlg concentration,



30(v/v)% glycerol and 70(v/v)% water. Corresponding viscosities are 60 and 107mPa s. Arrays (5x7) of the drops are printed (Fig. 3.33) with 21 $\mu$ J energy.

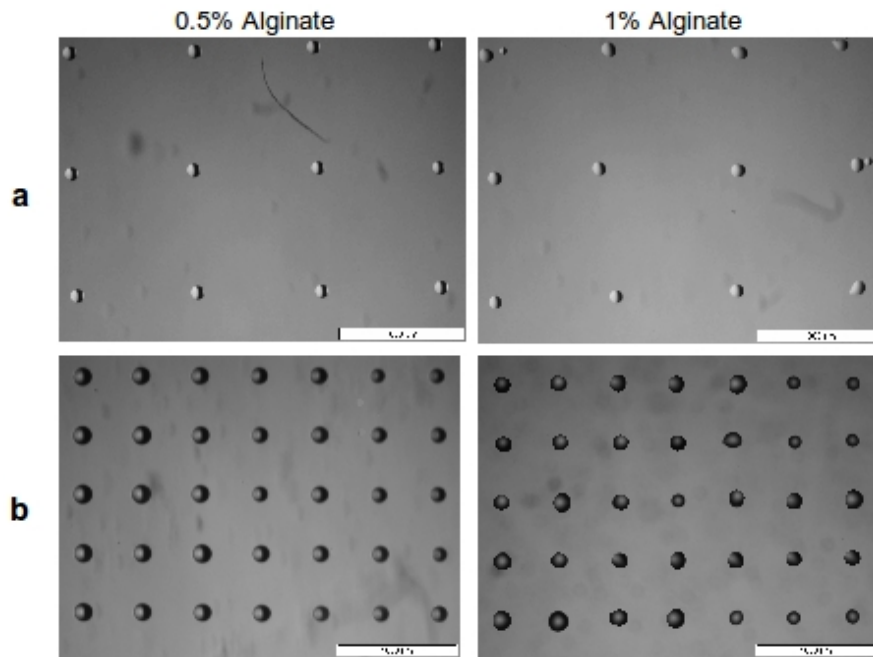


Figure 3.33: Prints with 21 $\mu$ J laser pulse, a) 1000 $\mu$ m apart at 6mm, b) 500 $\mu$ m apart at 5mm, scale bar 1000 $\mu$ m

#### 3.4.2.1 Effect of printing distance on drop size of less viscous solutions

The printed drops are observed under microscope (Fig. 3.34). Circular and well-defined drops are printed at larger separation distance upto 10mm. In this case satellite droplets appear at 6mm (Fig. 3.34). The shape of the drops remains regular at larger distance. The drops size is considerably decreased with increasing distance. Drop diameter is measured by ImageJ and plotted against distance (Fig. 3.35). The diameter decreases more than half for both solutions. In case of 0.5%NaAlg solution, it varies from 212 to 81 $\mu$ m where as for 1% alginate solution it goes from 194 to 77 $\mu$ m as separation distance has changed from 3 to 10mm. This provides an inverse relationship between drop size and printing distance.

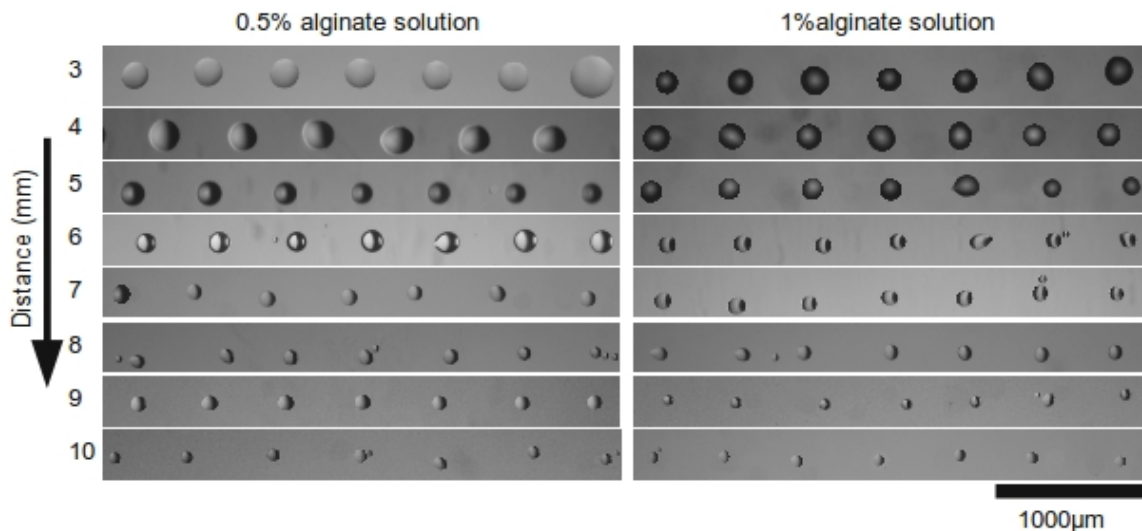


Figure 3.34: Printed drops with 21 $\mu$ J laser pulse at different separation distances



### 3.4.2.2 Effect of printing distance on drop height

The height of the drops is determined by profilometry with an optical interferometer used in VSI mode (Wyko NT1100, Veeco Instruments SAS, France) as described in [section 2.4.2](#). The height is plotted against printing distance ([Fig. 3.35](#)). The height of the drop decreases with the increasing distance for both solutions. Hence an inverse relation exists between height and printing distance.

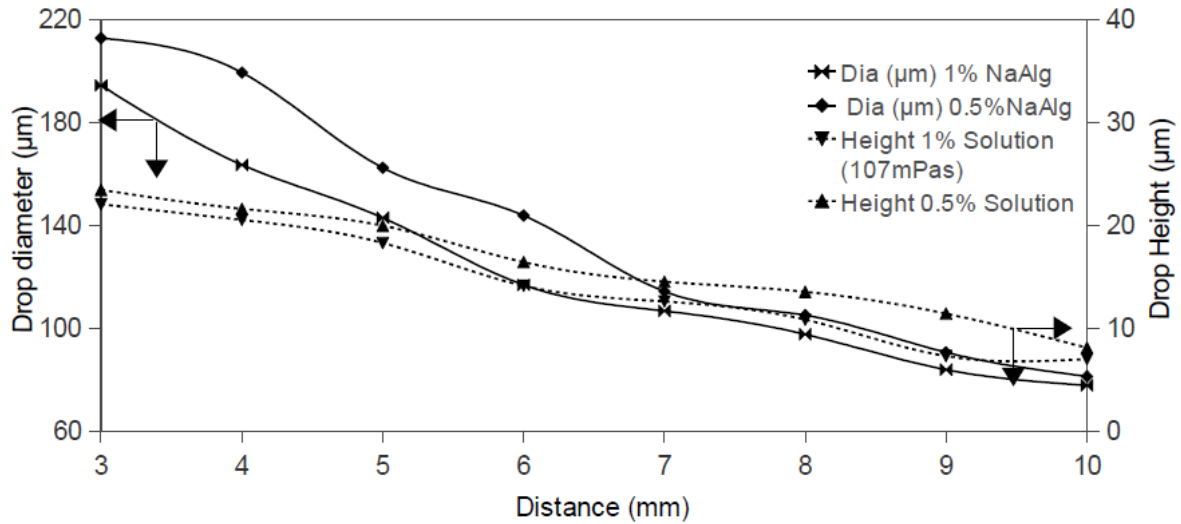


Figure 3.35: Drop diameter and height versus separation distances

### 3.4.2.3 Printing distance and drop volume

After measuring diameter and height of the drop, we estimated volume of the drops by supposing the drops as spherical caps ([cf. § 2.4.3](#)).

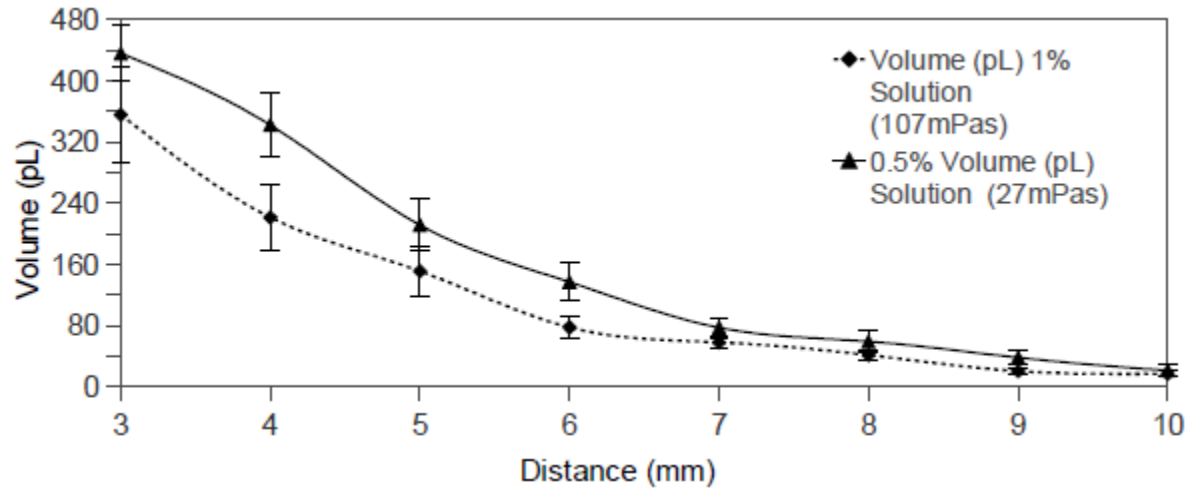


Figure 3.36: Drop volume versus separation distances

The volume of the circular and well-defined drops printed at larger separation distance upto 10mm is plotted against distance ([Fig. 3.36](#)). It decreases significantly with increasing distance. The volume has dropped more than 1/20 times for both solutions as distance has increased from 3 to 10mm. For 0.5% NaAlg solution, it decreases from 436 to

21pL where as for 1% alginate solution it dropped from 355 to 16.7pL. This establishes an inverse relationship between volume of the printed drop and separation distance.

#### 3.4.2.4 Effect of printing distance on printing position

Upward configuration prints at desired position with considerable accuracy. The arrays are designed to print drops 500 and 1000 $\mu$ m apart (Fig. 3.33). The maximum error measured is 10 $\mu$ m which is just 2% of the 500 $\mu$ m and 1% of 1000 $\mu$ m. The spatial error has been plotted against the printing distance (Fig. 3.37). However in comparison to the the spot position on the donor slides no significant error is observed in position. These results indicate that this configuration can be used efficiently for printing with significant accuracy at larger separation distances upto 10mm.

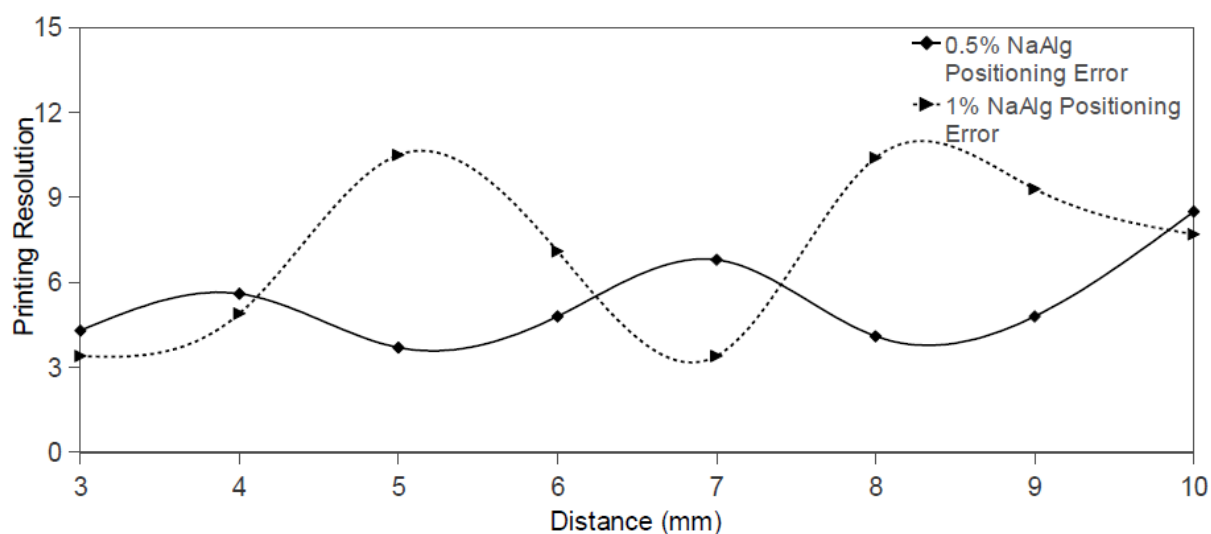


Figure 3.37: Spatial error versus separation distance



## **CHAPTER 4**

This chapter provides discussion on results mentioned in chapter 3 obtained by temporal profiles of ejection mechanism, jet dynamics and post-printing analysis of the printed drops. It deals with the ejection mechanism and subsequent jet dynamics leading to transfer of biomaterial. This provides a synthesis of proposed ejection mechanism, jet formation and effect of diverse controlling parameters on printing process of Laser Assisted Bioprinting. It also demonstrates application of upward configuration for cell printing.

<u>CHAPTER 4</u> .....	83
<u>4 DISCUSSION</u> .....	85
<u>4.1 Transition between sub-threshold and jetting regimes</u> .....	85
<u>4.1.1.1 Sub-threshold regime</u> .....	85
<u>4.1.2 Vapour bubble dynamics</u> .....	86
<u>4.1.2.1 Interaction of the vapour bubble near rigid surface</u> .....	87
<u>4.1.2.2 Interaction of vapour bubble near free-surface</u> .....	88
<u>4.1.3 Jet Formation: A new beginning</u> .....	88
<u>4.1.3.1 Jetting regime</u> .....	89
<u>4.1.4 Jet dynamics</u> .....	93
<u>4.1.5 High speed jetting</u> .....	94
<u>4.2 Crown like structure</u> .....	97
<u>4.3 Temporal evolution of laminar jets</u> .....	100
<u>4.3.1 Laminar jets ejection and dynamics</u> .....	100
<u>4.4 Parametric study of the printing with novel configuration</u> .....	102
<u>4.5 Section B: Applications of Novel Configuration for Cell Printing</u> .....	106
<u>4.5.1 TRI for printing cells with slow jets</u> .....	106
<u>4.5.2 Cell printing</u> .....	111
<u>4.5.2.1 Landing impact</u> .....	111
<u>4.6 LAB Mechanism: Schematic representation of LAB</u> .....	113

## 4 DISCUSSION

Experimental studies of the LAB mechanism by TRI and post transfer analysis reveal that resultant transfer depends not only on the applied laser energy but also the film thickness [176] and rheological properties of the bioink. The first phase of this discussion focusses transition between different regimes followed by the subsequent jetting dynamics. The second phase explains the application of upward configuration as a novel cell printing setup. Finally a synthesis of whole mechanism depending on different physical parameters is deduced.

### 4.1 Transition between sub-threshold and jetting regimes

Following consecutive steps [170–172,179,193] describe the generation of microdrops by LAB: (i) deposition of the laser energy into the skin depth of the absorbing layer (ii) conversion of the absorbed energy into the heat (iii) generation of vapour bubble (iv) expansion of vapour bubble (v) deformation of the bioink-air interface (vi) genesis of jet due to bubble collapse at  $R_{\max}$  (vii) jet progression with constant thinning (in absence of receiving substrate jet breaks due to the Rayleigh–Plateau instability) (viii) drop formation as jet impinges on the substrate (a. fast spreading of drops, b. growth of drop due to jet feeding c. slow relaxation of drop as jet breaks due to Rayleigh–Plateau instability). Depending on process parameters, it is observed that deformation caused by expansion of vapour bubble could lead to three different regimes [170,194]. As jet speed is also critical to minimise cell damage [195], generating jet close to the sub-threshold may improve cell viability and slacken the applied stress to the materials (e.g. cells). Our results provide an insight to LAB mechanism with an aim to elucidate different parameters associated with the transition of sub-threshold to jetting conditions in a geometrical context i.e. vertex angle of hyperboloid equal to  $2\arctan 2^{1/2}$ , or  $109.5^\circ$  which corresponds to jet initiation as proposed by M.S. Longuet-Higgins [189] and Blake & Gibson [50].

#### 4.1.1.1 Sub-threshold regime

Absorption of laser pulse generates expanding vapour bubble formed by laser ablation [170,180]. This expansion increases height (Fig. 3.5, 3.14), base-width (Fig. 3.6, 3.15) and volume (Fig. 3.7, 3.16). The pressure enclosed in the bubble surpasses the atmospheric pressure and surface energy. This rapid expansion of the bubble accelerates the bioink at high rate, causing a rapid decrease in vertex angle (Figs. 3.4, 3.18). The constant height during 3-5 $\mu$ s (Fig. 3.5, 3.14) suggests a transient equilibrium due to surface energy and viscoelastic properties.

During first 5 $\mu$ s, expanding bubble protrudes the bioink by stretching it forward [139]. At 4 $\mu$ s (Fig. 3.2a), the vertex angle is 105°, the same is observed at 5 $\mu$ s (Fig. 3.12a). The bubble expansion builds up the stresses in projected liquid which leads to a decrease in the internal pressure due to increasing bubble volume and collision of particles with walls of the vapour pocket. Due to this energy dissipation, external pressure overcomes the internal pressure, hence ceasing down the accelerating veneer. At this stage, deformation has reached to its maximum expansion with uniformly rounded shape which suggests the influence of surface tension (5<sup>th</sup> frame of Fig. 3.2a, 3.12a). Later fluctuations are fully damped which could be attributed to viscosity (Fig. 4.1a) and it could not emerge as jet [142,191]. Velocity profiles (Fig. 3.8, 3.17) indicate zero velocity during 8-10 $\mu$ s which also show that forward progression could not be maintained. As the viscoelastic properties and surface tension dominate the laser induced pressure, it increases the vertex angle (Figs. 3.2a, 3.12a, 3.4 & 3.18) and causes a decrease in height (Fig. 3.5, 3.14), base-width (Fig. 3.6, 3.15), volume (Fig. 3.7, 3.16), and velocity (Fig. 3.8, 3.17). Induced protrusion faces higher deceleration in upward configuration as compared to conventional setup which can be attributed to gravity as it is moving in upward direction in the former case. Due to the suppression and recoil, bubble retreats without producing a jet which is also evident from diminishing velocities (Figs. 3.8, 3.17). Bubble dynamics has primary importance as liquid ejection is basically mediated by formation of cavitation bubble. We discuss it here in detail.

#### 4.1.2 Vapour bubble dynamics

Temporal profile of the LAB process has shown that vapour bubble (for instance Fig. 3.10b, 3.11b & 3.19) is formed as a result of laser energy deposition. Liquid ejection is basically mediated by formation of cavitation bubble. Depending on experimental parameters (energy ( $E$ ), viscosity ( $\nu$ ), surface tension ( $\sigma$ ), thickness ( $\epsilon$ ) of bioink), this leads to different scenarios. It has been shown that bubble dynamics could be described by the Rayleigh-Plesset equation, which states [196,197]:

$$R \ddot{R} + \frac{3}{2} \dot{R}^2 = \frac{\kappa P_l}{\rho_l} \left( \frac{R_o}{R} \right)^{3\gamma} - \frac{(P_l - P_v)}{\rho_l} - 4\nu \frac{\dot{R}}{R} - \frac{2\sigma_l}{R\rho_l} \quad (4.1)$$

where  $R$  is the vapour bubble radius,  $\rho_l$  the liquid density,  $P_l$  the liquid pressure,  $\nu$  the kinematic viscosity,  $\sigma_l$  the surface tension,  $\gamma$  the ratio of specific heats,  $P_v$  the saturated pressure in the bubble and  $\kappa$  the ratio of gas pressure in the bubble  $P_g$  to the liquid pressure  $P_l$ . This equation is the expression of the bubble radius evolution. It provides temporal evolution of the bubble radius and mainly depends on the liquid kinematic viscosity and surface tension.

The evolution of a water bubble radius versus time (Fig. 4.1a) shows that higher the kinematic viscosity of the liquid, the lesser the oscillation of bubble radius, the smaller the maximum vapour bubble radius, and the faster the maximum radius is reached and vice-versa [142,198]. Surface tension has no influence on the bubble radius as decreasing surface tension of the hydrogel from 72 to 65 mN/m by adding a surfactant (Sodium Dodecyl Sulphate) makes no significant difference in evolution of bubble radius (Fig. 4.1b).

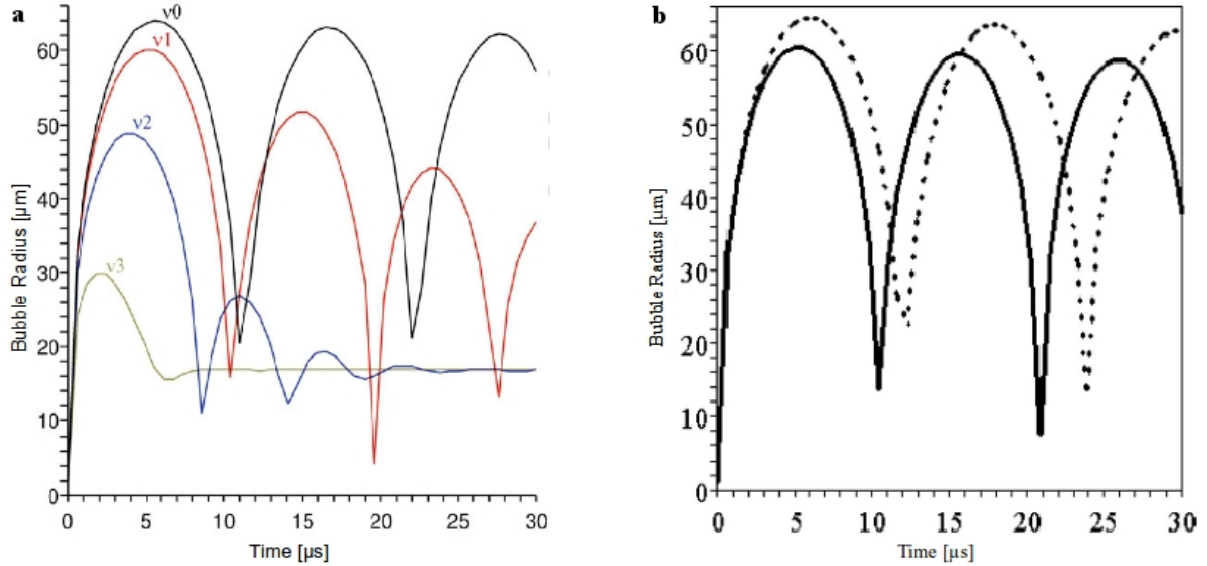


Figure 4.1: a) Vapour bubble radius evolution versus time for different viscosities ( $v_0 = 1 \times 10^{-6} \text{ m}^2/\text{s}$ ,  $v_1 = 10 \times 10^{-6} \text{ m}^2/\text{s}$ ,  $v_2 = 40 \times 10^{-6} \text{ m}^2/\text{s}$ ,  $v_3 = 108 \times 10^{-6} \text{ m}^2/\text{s}$ ). Evaluation parameters used:  $\rho = 1,000 \text{ kg m}^{-3}$ ,  $v = v_0 = 1.05 \times 10^{-6} \text{ m}^2/\text{s}$ ,  $\sigma_l = 72 \text{ mN.m}^{-1}$ ,  $k = 50,000$ ,  $R_0 = 1.26 \mu\text{m}$ ,  $\gamma = 1.4$ ,  $P_l = 1 \times 10^5 \text{ Pa}$  and  $P_v = 2,330 \text{ Pa}$  (for more details see [142]) and for kinematic viscosity values corresponding to different hydrogel solutions (at  $10^\circ\text{C}$ )

b) Effects of surface tension on the radius in micrometer evolution on time microsecond of a water vapour pocket  $v = 1.05 \times 10^{-6} \text{ m}^2/\text{s}$ . Variations of the surface tension,  $\sigma = 0.2\sigma_l$  dotted line and  $\sigma = 6\sigma_l$  solid line do not change significantly the pocket radius and behaviour in time.

Temporal profile of the LAB process has shown that vapour bubble (for instance Fig. 3.10b, 3.12b & 3.19) is formed as a result of laser energy deposition. The dynamics of a free standing cavitation bubble generated into a liquid and near a free surface has been previously studied [188]. It is bit different from LAB setup because the bubble is not a free standing bubble in our case, this bubble is trapped between donor slide (rigid boundary) and air (free surface). Bubble has expansion and collapsing phases whereby collapse leads to different behaviours depending on the nature of surrounding boundary (surface). Bubble interaction with two different (Rigid and Free) surfaces is presented.

#### 4.1.2.1 Interaction of the vapour bubble near rigid surface

Expanding bubble near a rigid boundary migrates away from the surface and the



bubble oblates in the side close to the rigid boundary due to non-uniform flow field between the bubble and the boundary. The rigid boundary can be considered as infinite-inertial limit. The expanding bubble repels the boundary and the collapsing bubble approaches it respectively. In the collapsing phase, the moving bubble front reverses direction compared to the expanding phase.

#### **4.1.2.2 Interaction of vapour bubble near free-surface**

As compared to bubble migration near a rigid boundary, bubble migration near a free surface is exactly opposite. Because the free surface is considered as a zero-inertial limit boundary, the expanding bubble moves toward the free surface (Fig. 4.2b) and the collapsing bubble repels the free surface (Fig. 4.2c). The bubble expands under the liquid surface thereby the liquid surface protrudes upward associated with a pointed pole of the expanding bubble. Then the nonlinear surface instability makes the liquid surface grow into a spike subsequently. The high pressure between the upward spike of liquid surface and the protruding bubble surface generates a small tip of the downward liquid jet whereby the bubble starts to collapse. The upward spike and downward liquid jet penetrating through the bubble keep growing. In this context, dynamics of cavitation bubble (in infinite liquid) created close to free surface has been modelled by Blake et al. [188] and Pearson et al. [173].

#### **4.1.3 Jet Formation: A new beginning**

For jet formation the bubble must be generated very close to free surface [173,199]. In the case of cavitation bubbles, a high pressure area between the bubble and the free surface is generated. This pressure gradient (Fig. 4.2) presents the theoretical calculations of Pearson et al. They used boundary integral method for highly non-linear motion of bubble beneath a free surface: the pressure beneath the bubble is higher (white colour) than that of the bubble pole (black colour). The bubble becomes elongated with a high pressure zone at its pole. Bubble internal pressure decreases due to its expansion [199] which leads to bubble collapse. The overpressure at bubble pole displaces the fluid along the symmetry axis towards lower pressures. This results into formation of two jets (jet and counter jet) directed in opposite directions (Fig. 4.2).

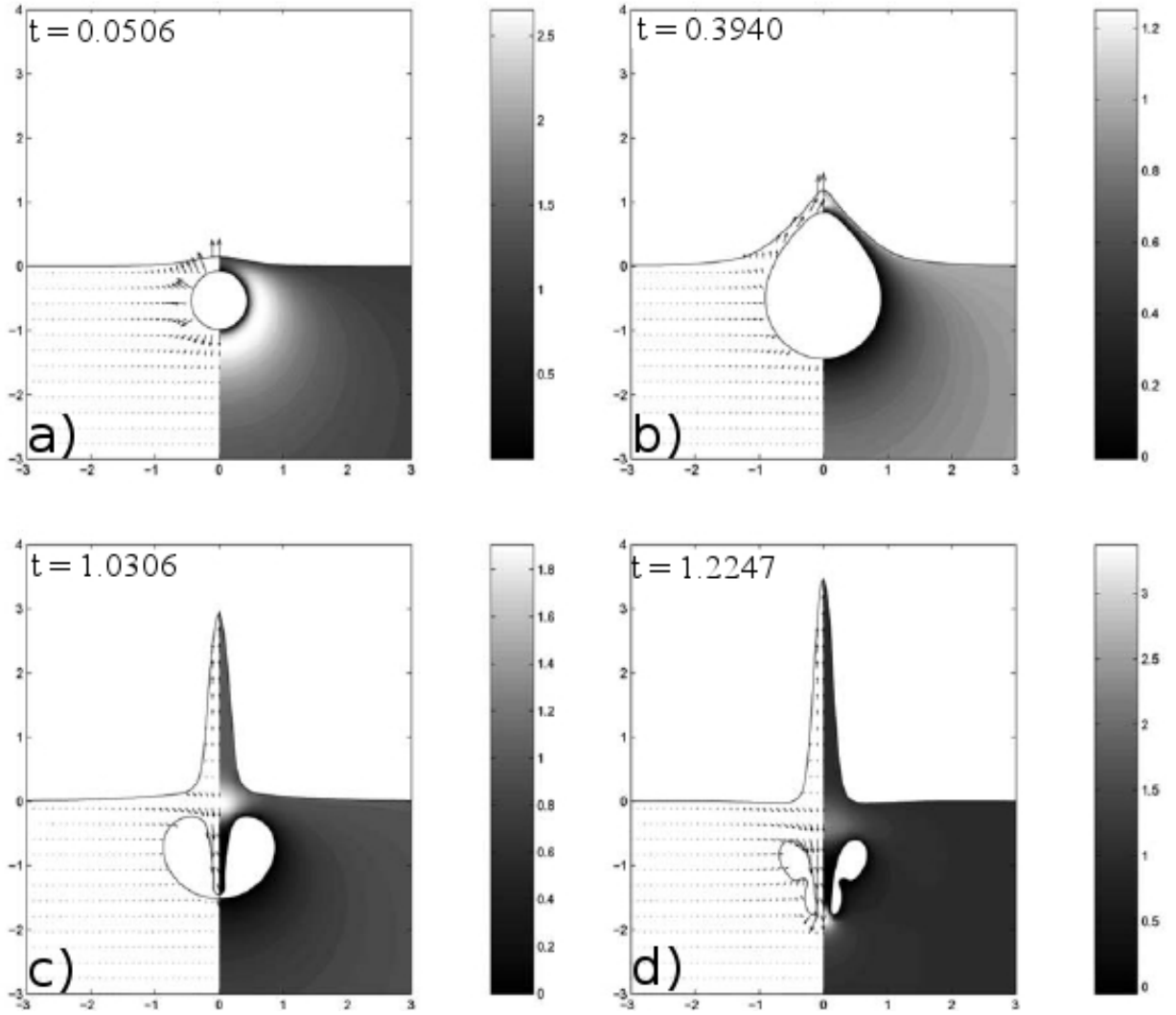


Figure 4.2: Simulation of the velocity vector and pressure contour with temporal dynamics of the vapour bubble near free surface. Arrow size is scaled with respect to the maximum instantaneous velocity in each frame. The pressure scales are shown to the right of each image. Times are 0.0506, 0.3940, 1.0306 and 1.2247 from left to right and from top to bottom respectively. [173]

#### 4.1.3.1 Jetting regime

In jetting regime (Figs. 3.2b, 3.12b), initial expansion of bubble, rapid decrease in vertex angle (Fig. 4.3) and the increasing height (Fig. 3.5, 3.14), velocity (Figs. 3.8, 3.17), base-width (Fig. 3.6, 3.15) and volume (Fig. 3.7, 3.16) indicate that the initial expulsion due to the ablation of gold layer accelerates the bioink in forward direction at a high rate. This acceleration helps it to cross the limiting critical angle of  $105^\circ$  to rise as a jet. Vertex angle is shown as function of time (Fig. 4.3) and compared with the model given by equation (4.2) proposed by M.S. Longuet-Higgins [189] based on dirichlet hyperboloid.

$$2\theta \approx 2 \arctan \left( \frac{2^{\frac{1}{2}}}{(\tau - \tau_0)^{\frac{3}{2}}} \left[ 1 + \frac{3}{8} (\tau - \tau_0)^{-3} \right] \right) \quad (4.2)$$

where  $\tau_0 = -1.2936$  is the fitting parameter and  $\theta$  is the vertex angle.

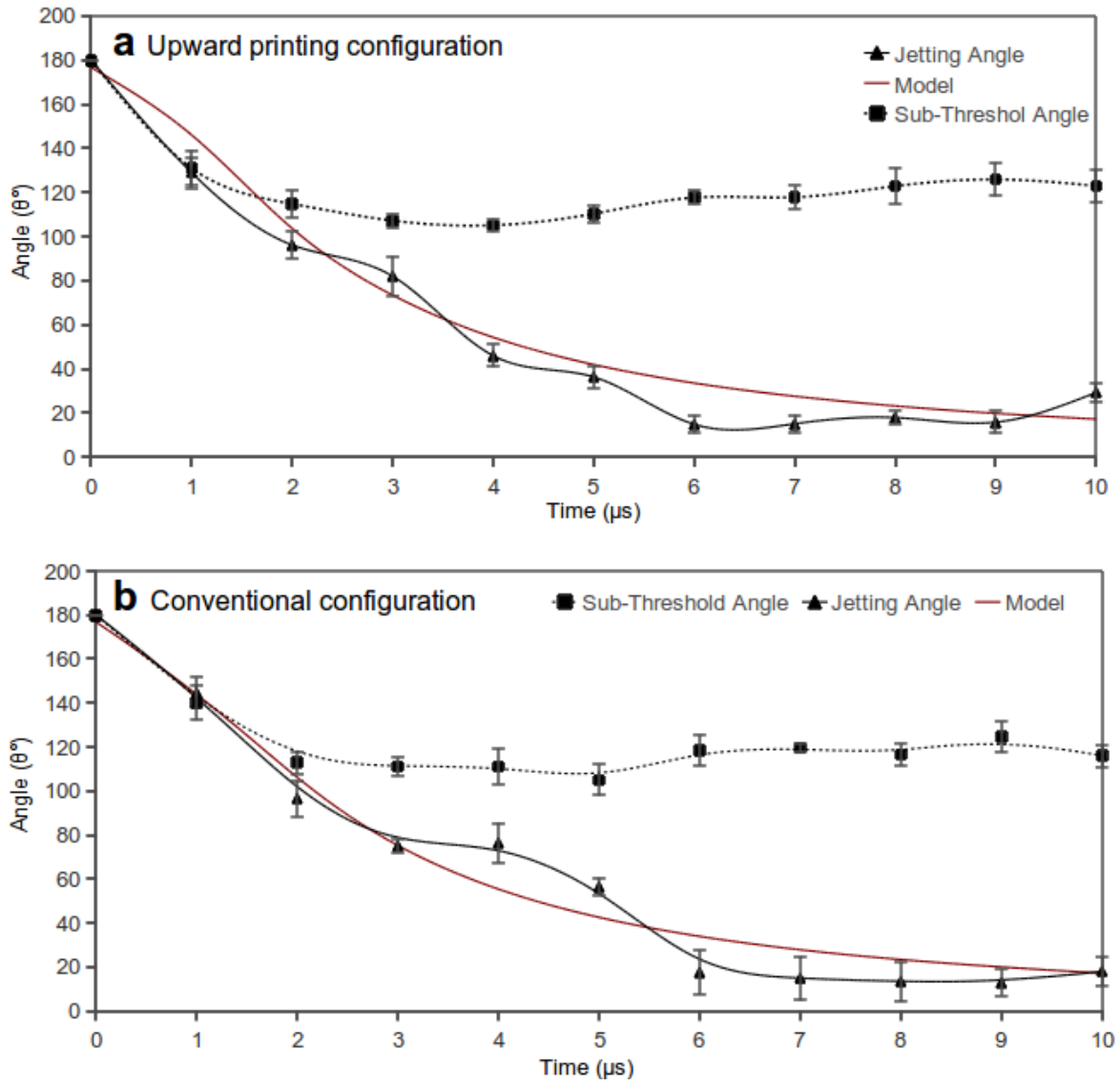


Figure 4.3: Vertex angle versus time; fine dots denote Sub-Threshold regime and solid line denotes jetting regime experimental data and red curve denotes M.S. Longuet-Higgins Model [189].

Vertex angle drops in accordance with the analytical model, but an abrupt change at  $4\mu\text{s}$  (Fig. 4.3) indicates deviation from model curve. This deviation indicates that bioink is engaged in sustaining the pressure enclosed inside the liquid through viscoelastic effect. However it can't sustain it, as its viscoelastic properties and external pressure are unable to overcome the enclosed pressure. Similar studies on cavitation by Robinson et al. [174] and Patrascioiu et al. [200] show abrupt change in vertex angle (Fig. 4.4), where it was shown that the vapour pocket formation near a free surface could be controlled to form a fast free-surface spike during the collapse, due to the acceleration of the liquid in the symmetry axis of the pocket i.e. in the laser wave propagation path.

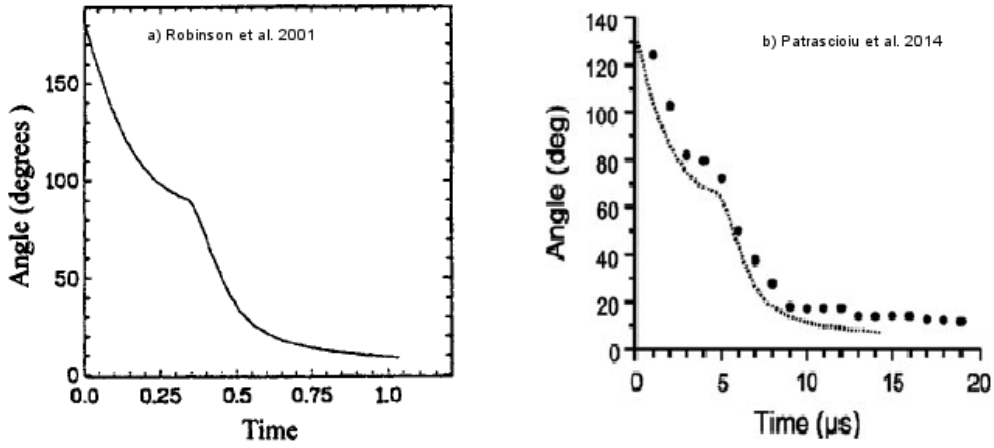


Figure 4.4: The angle between the vertices of the free surface a) Robinson et al. [174] b) Patrascioiu et al. [200]

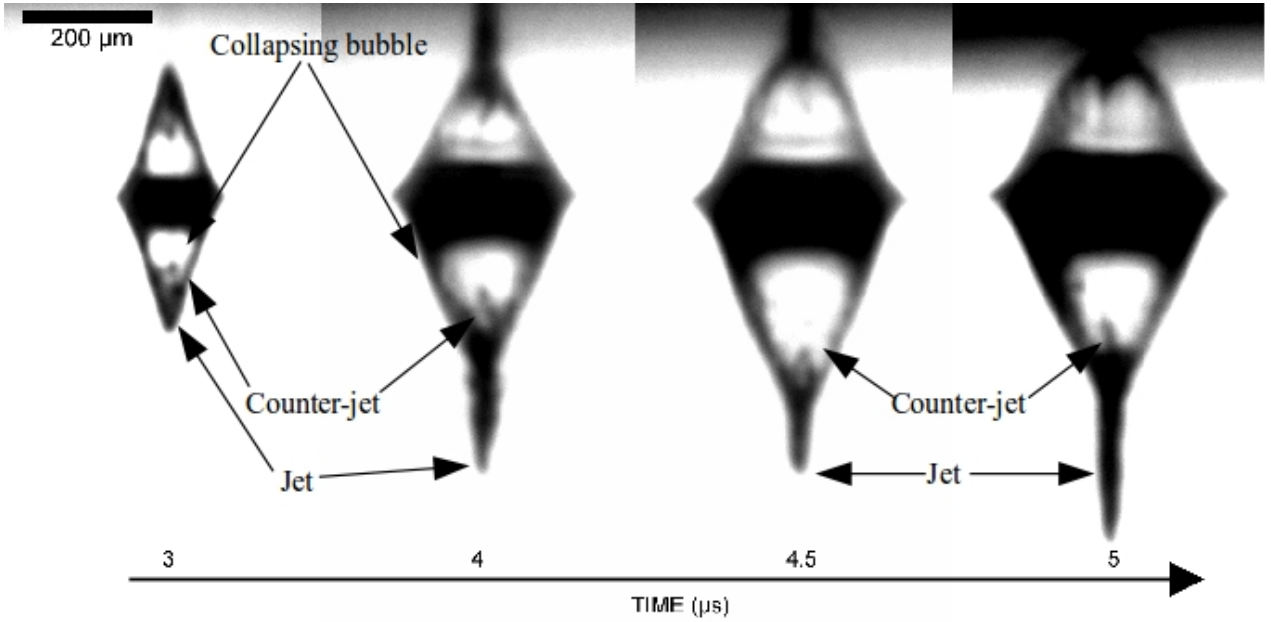


Figure 4.5: Counter-jet observed in jetting regime using 35μJ laser energy. Observation of the counter-jet is difficult however at 3μs it is also evident in reflection.

At 4μs (Fig. 3.2b) the formation of a spike on the axis is possibly related to a concentration of hydrodynamic pressure [142] at the singular point on the axis at the rear surface. Slower increase in height after 4-5μs (Fig. 3.5, 3.14) indicates a transient equilibrium (due to surface tension) before spike formation. Since the bubble internal pressure decreases during bubble expansion [199], the balance between internal and external forces favours to the later, after which the bubble collapse starts. It leads to the development of needle like jets [201]. In fact, two jets are usually produced: [201,202] one directed away the free surface (Figs. 3.2b, 3.12b), and another inside the bubble called counter-jet, which is very difficult to observe in TRI and have only been reported at couple of occasions [180,203]. However figure 4.5 with high energy provides an evidence to the fact. The formation of such jets can be understood considering the two streams of the fluid across the bubble boundaries flowing

toward the symmetry axis. Their collision at the pole of the liquid sheet lead to formation of jet and counter-jet [202]. At 6 $\mu$ s, jet is fully developed. Once jet emerges, subsequent progression is maintained by the momentum [181] of jet by pulling additional fluid from the surrounding film. This induction of fluid increases the jet inertia which suppresses the recoiling process (caused by surface tension). It had already been demonstrated in studies on cavitation bubbles [188,189]. Slender jets can be observed after 7-9 $\mu$ s (Fig. 3.2b, 3.12b) which is attributed to self focussing [204] which further decays the vertex angle (Fig. 4.3).

In conventional configuration, the increase in vertex angle at 10 $\mu$ s is caused by the fact that more fluid being injected in the jet; also evident from the height (Fig. 3.14), volume (Fig. 3.16) and base-width (Fig. 3.15) curves. In upward configuration (Fig. 3.2b), it is more plausible to account gravity being responsible for the increase in vertex angle at 10 $\mu$ s as the fluid is unable to maintain upward flow against the gravity. Velocity profile (Fig. 3.8) also indicates that jet is decelerating as velocity decreases from 16 $\pm$ 4 to -26 $\pm$ 7m/s during 7-10 $\mu$ s. It is also evident from increasing base-width (Fig. 3.6) and decreasing height (Fig. 3.5). The jet becomes more thicker due to downward settling of flowing liquid.

The volume profiles (Fig. 3.7, 3.16) indicate three dominant regions. First during the bubble expansion, volume increases rapidly and reaches to its maximum at 3 $\mu$ s after laser irradiation. Second from 3-5 $\mu$ s, a significant reduction is evident during collapsing phase of bubble. Finally, jet emerges and proceeds forward without significant change in volume. The volume (Fig. 3.7, 3.16) of the emanated fluid is plotted with the volume exposed to the laser pulse and bubble volume estimated from the relation between bubble's collapse time ( $T_c$ ) and maximum bubble radius ( $R_{max}$ ) [205,206]

$$T_c = 0.915 R_{max} \sqrt{(\rho / P_o)} \quad (4.3)$$

where  $\rho$  is density = 10<sup>3</sup> kg/m<sup>3</sup> and  $P_o$  = 1 atm. The initial increase in volume of the jet is due to expanding bubble and emanating fluid till 3 $\mu$ s, bubble observation by TRI is difficult particularly for small deformation (low fluences). However its logical to assume that the maximum bubble radius is reached at 3 $\mu$ s. Immediate drop in the volume of the jetting regime from 4 $\mu$ s (Fig. 3.7, 3.16) assists the argument that collapse starts before 4 $\mu$ s which is corroborating (Fig. 4.1) to previous modelling studies [142,191,198]. Such collapse [207] leads to jet formation which is also evident from TRI (Fig. 3.2b, 3.12b, 3.19). The later decrease in volume during 7-10 $\mu$ s is attributed to jet elongation and thinning during its forward progression.

#### 4.1.4 Jet dynamics

Once jet is formed, its subsequent dynamics could be analysed on rheological parameters. Liquid jets involve complex fluid mechanics and dimensionless numbers like Reynolds (Re), Weber (We) and Ohnesorge (Oh) are most useful tool to characterize jet behaviour. These dimensionless numbers are given as:

$$R_e = \frac{v\rho a}{\mu} \quad (4.4)$$

$$W_e = \frac{v^2 \rho a}{\sigma} \quad (4.5)$$

$$Oh = \sqrt{\left(\frac{W_e}{R_e}\right)} \quad (4.6)$$

Or

$$Oh = \frac{\mu}{\sqrt{\sigma \rho a}} \quad (4.7)$$

where “ $\rho$ ”, “ $\mu$ ”, and “ $\sigma$ ” are the density, viscosity, and surface tension of the fluid respectively, “ $v$ ” is the velocity, and “ $a$ ” is a diameter of the jet. A flow is considered laminar when  $Re < 2000$  and turbulent for  $Re > 4000$ . The analyses of slow jetting data, based on Re and We and Oh numbers, also show that the produced jets are in laminar flow domain and may print materials without formation of satellite droplets. This is confirmed by calculating dimensionless numbers where Re is  $\sim 9$ , We is  $\sim 333$  and Oh is equal to 2. Interestingly, this is corroborating with printable domain (Fig. 4.6) for inkjet printing by Derby [89].

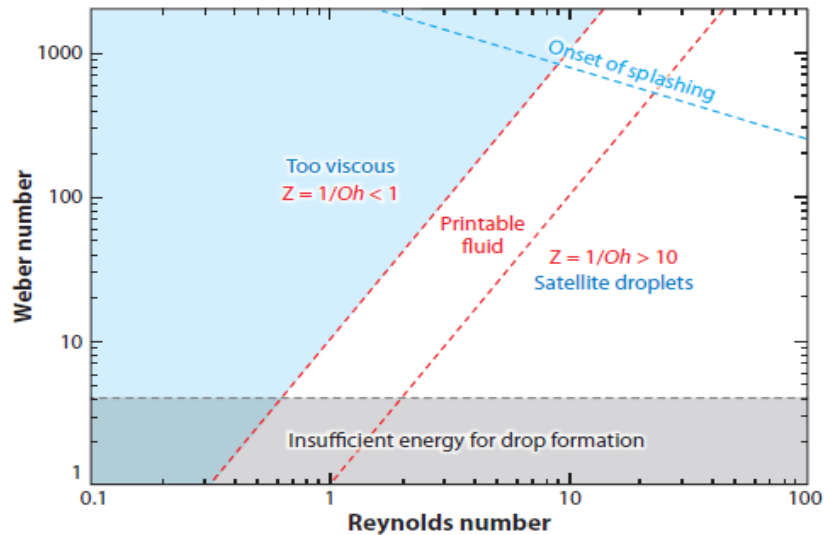


Figure 4.6: Stable printing in a coordinate system defined by the Reynolds and Weber numbers to illustrate the regime of fluid properties where DOD inkjet printing is possible. [89]

Perfect spherical drops (Fig. 3.20bi) are due to low velocity which reduces landing impact [184]. Analysis of high speed jets produced from 21 $\mu$ J (Fig. 3.19a) yields  $Re=12$  in

the printable domain of inkjet printing whereas  $We$  corresponds to 346, both of them are in printable domain as shown by Derby [89]. In case of jets produced from 35  $\mu$ J (Fig. 3.19b), high laser energy increases jet velocity which eventually leads to higher landing impact. This leads to large size drops (Fig. 3.20bii), where few satellites are attributed to high  $We=4037$  which falls into onset of splashing domain. Corresponding  $Re$  is 28, which also falls into onset of splashing. Further increase in laser energy produces supersonic but turbulent jets (Fig. 3.19c). Such dynamics leads to distorted drops as well satellite droplets (Fig. 3.20biii).  $Re$  and  $We$  correspond to 122 and 87152, both are in splashing domain. Moreover higher landing impact may also introduce splash leading to satellite droplets formation. The plume produced from the highest laser energy used in these experiments has resulted into uncouth spray (Fig. 3.20biv) of the bioink which has also been observed in temporal profiles (3.19d).

#### 4.1.5 High speed jetting

The quantitative study of jet speed in jetting condition are conducted in collaboration with **Joy TELLOUCK** and **Antoine Rrobinet PERRIN** in the frame work of their master project aiming to improve the penetration of riboflavin in the corneal stroma for therapeutic efficacy. Riboflavin is selected for its frequent application in several clinical and therapeutic situations and its supplements have been used as part of the phototherapy treatment of neonatal jaundice. All the jets (produced form riboflavin) have similar velocity profiles (Fig. 3.9): they are composed of three distinct parts with an increasing phase till 2  $\mu$ s subsequently a maximum speed is reached for a given energy and finally a decreasing phase. The increasing phase is due to rapid growth of the bubble which remains dominant till 3  $\mu$ s and once jet emerges, a maximum speed is achieved due to larger K.E. The final decreasing phase is attributed to loss of kinetic energy in moving against gravity.

Turbulence observed in high speed jets (see Appendix E) is attributed to rheological properties of riboflavin (e.g. low viscosity  $\sim 50$  mPa s) and high laser energy which produces high pressure vapour bubble. Speed (Fig. 3.9) is directly proportional to the energy for a given thickness of the ink. For a given energy, jet speed increases with decreasing thickness of riboflavin and vice versa which indicates an inverse relation between jet velocity and thickness of the bioink. Reducing viscosity of the bioink also leads to turbulence. This has been observed by dilution of the riboflavin by 1/3 and 1/6 times. This led us to use 40  $\mu$ m thick layer of riboflavin and 51  $\mu$ J energy to study penetrating jet through 150  $\mu$ m collagen membrane (Fig. 3.10). Corresponding velocity profile (Fig. 3.11) indicates an acceleration of  $10^6$  g at contact with collagen membrane. It suggests that jet has enough inertia to penetrate



through the target therefore it protrudes through the collagen membrane. This perforation leads to jet penetration through surface of collagen. This indicates potential particularly attractive application of the present supersonic jets as needle-free drug injectors [208,209]. For this application, in which a liquid solution containing a drug is forced to penetrate human or animal tissue through the skin, ultra-high velocities (greater than 200 m/s), fine scales (down to 30 m), and good reproducibility and controllability are essential.

For higher energies, the jet tends to become turbulent which is evident from temporal images of jetting regime with higher energies (Fig. 3.19). Counter jet (Fig. 3.19a) appears at  $6\mu\text{s}$  to conserve momentum [181]. Crown-like structure at  $10\mu\text{s}$  is explained in § 4.2. Presence of the vapour cavity (Fig. 3.19c) is attributed to high-pressure induced by plasma generated due to laser energy. Such high energy could produce supersonic jets but also introduces turbulence in subsequent jet dynamics.

For jetting, bubble must be generated very close to free surface to produce larger jet. This is due to the relative ease with which the bubble displaces the free surface compared with the fluid below. Pearson et al. [173] evaluated dimensionless height (Fig. 4.7) based on a critical parameter i.e. the stand-off distance  $\Gamma$  (the dimensionless distance between bubble and boundary scaled with respect to the maximum radius ( $R_{\text{max}}$ ) the bubble would attain in an infinite fluid). Smaller the  $\Gamma$ , higher will be the jet height and vice-versa.

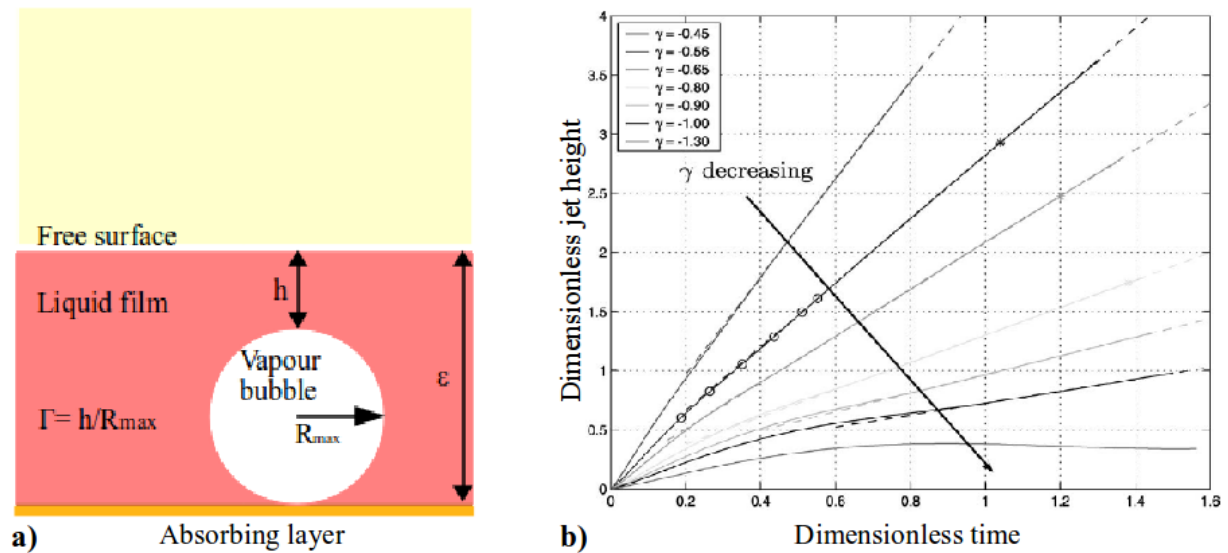


Figure 4.7: a) Schematic representation of the bubble in a liquid near free surface with representation of  $\Gamma$ .

b) evolution of the jet height caused by the motion of a single vapour bubble beneath the free surface for a range of stand-off distances [173]

Depending upon value of “ $\Gamma$ ” ranging from less than 1 to larger than 1, bubble interaction with free surface leads to quite different results.

- If  $\Gamma > \Gamma_2$  (threshold value): jet cannot emerge as the bubble expansion is not energetic



enough to reach the free surface (Fig. 4.8-III.a). It is termed as Sub-threshold regime.

- When  $\Gamma < \Gamma_1$ : the violent bubble expansion overcomes surface tension resulting in bubble bursting, and hence results into liquid spray onto the substrate (Fig. 4.8-III.c). This regime is therefore so called the plume regime.
- If  $\Gamma_2 < \Gamma < \Gamma_1$ : the bubble expands and collapses, finally a jet emerges (Fig. 4.8-IIIb). It is the jetting regime.

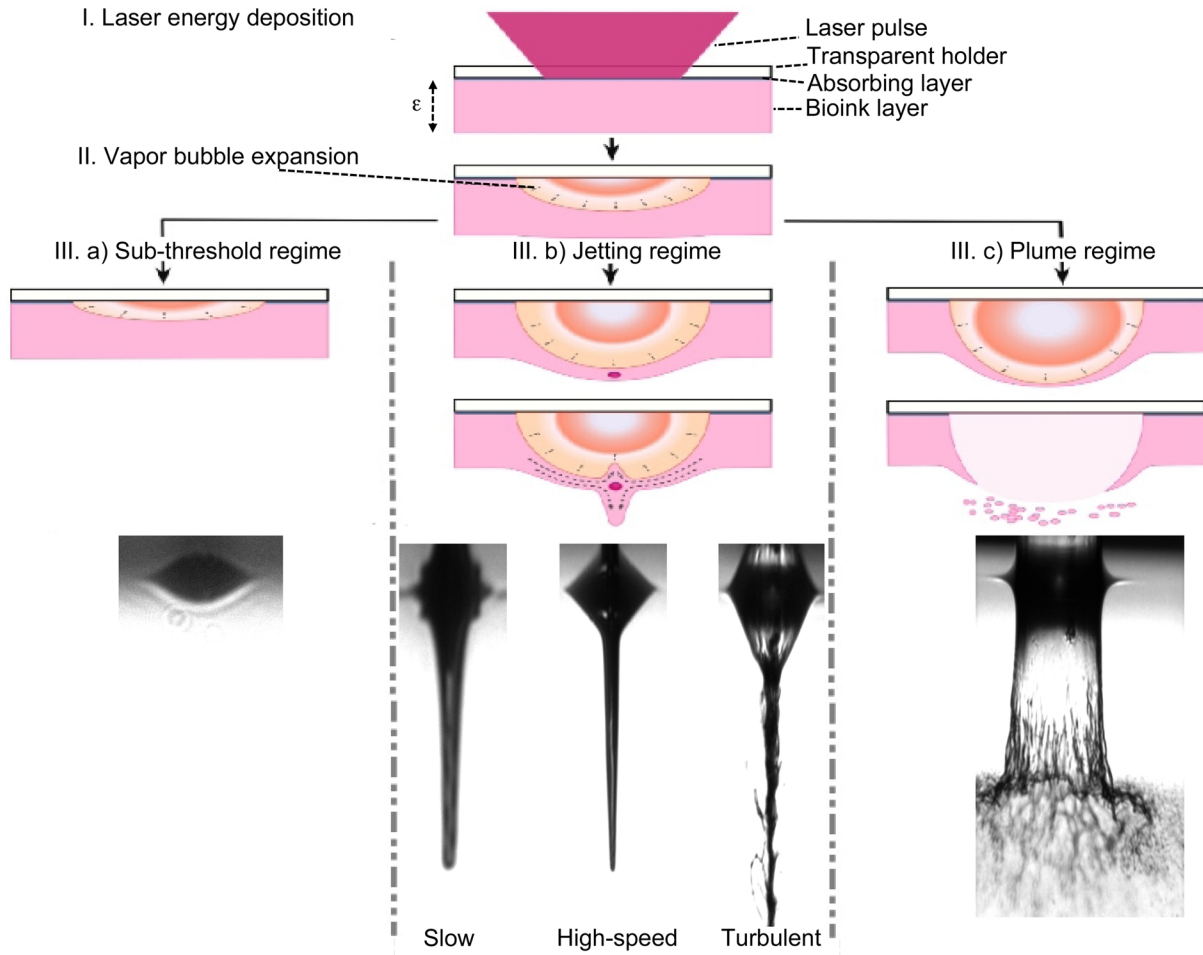


Figure 4.8: Classification scheme for LAB regimes by TRI of the jets captured at 10μs

This section provides a detailed analysis of the different results obtained aiming to study different parameters which affect LAB. It is observed that there exists a minimum vertex angle of  $105^\circ$  (so called critical angle) regardless of setup. This is corroborating to the findings of Blake & Gibson as  $104^\circ$  which is in qualitative agreement with  $109.5^\circ$  as modelled by M.S. Longuet-Higgins. Hence it is proposed that the vertex angle is the geometrical parameter which could be controlling parameter in jet formation. Accordingly it can be assumed that any protrusion remains in Sub-Threshold regime till its vertex angle  $> \sim 105^\circ$  (critical angle), once vertex angle drops below this critical value, deformation emerges

as a jet (Jetting regime).

Study of jet dynamics leads to conclude that jetting regime could be further classified as *slow jetting*, *high-speed jetting* and *turbulent jetting*. In this context, classification of LAB regimes is presented in Figure 4.8 as Sub-threshold, Jetting (slow, high-speed and turbulent) and Plume regime. Quantitative analysis of the jetting regime demonstrates a direct relation between energy and jet speed and fascinating features of the jets. On one hand, the remarkable potential of high speed jets is the penetration through thick membrane of collagen. And on the other hand, slow jets are unperturbed, more stable, causing reduced landing impact on substrate and can produce perfect prints, hence printing with jetting close to the sub-threshold is very much recommended for cell printing, where as turbulent jets could not be an optimum choice for bioprinting.

## 4.2 Crown like structure

Once jet has emerged, further exploration of the its dynamics reveals formation of the crown like structure around its base. Crown-like structure [210–213] at the base of the jet (9th & 10th frames of Fig. 3.2b, 3.12b, 3.19a) is attributed to sinking surface previously referred as surface depression [214]. Such crown-like structure can also be observed in temporal profiles (Fig. 4.9) reported by Unger et al. [179].

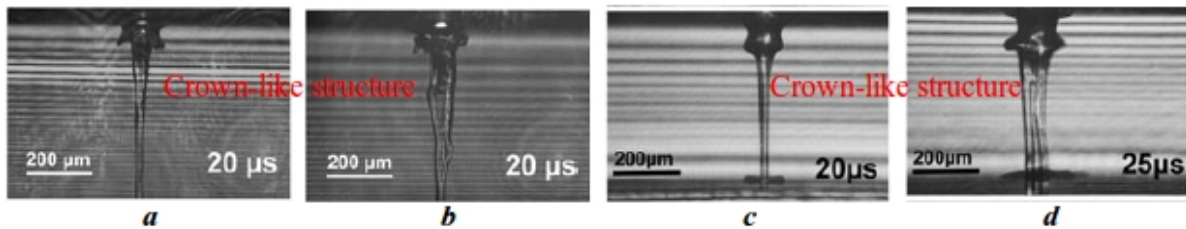


Figure 4.9: Crown formation in TRI of the hydrogel jet formation, (a & b) without collector slide and (c & d) with collector slide with different fluences  $1.6 \text{ J/cm}^2$  (a & c) and  $2.7 \text{ J/cm}^2$  (b & d). [179]

This feature has also been observed in our research with different viscosities (Fig. 4.10), energies, bioink thickness (Fig. 4.11) and cell concentration (Fig. 4.12). It becomes more prominent with higher laser intensity, lesser thickness and lower viscosity of the bioink due to high pressure bubble resulting from such energetic laser pulses. Previously, it has been named as circular ring-shaped crater [210], crown formation [215] and collar formation [211] etc. We refer it as crown like structure.

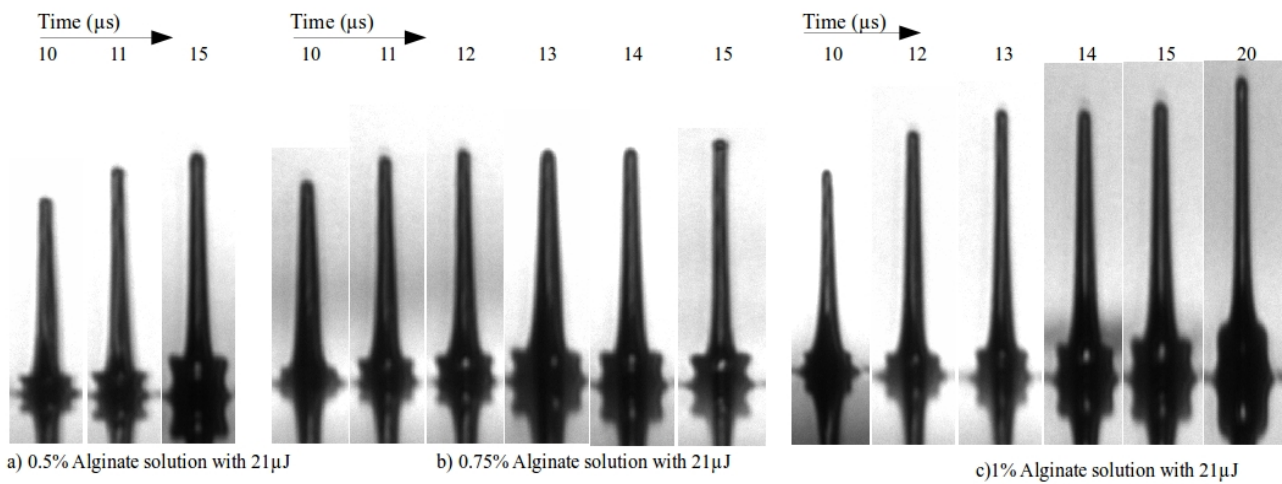


Figure 4.10: Crown formation observed in TRI from 40μm thick layer of NaAlg solutions

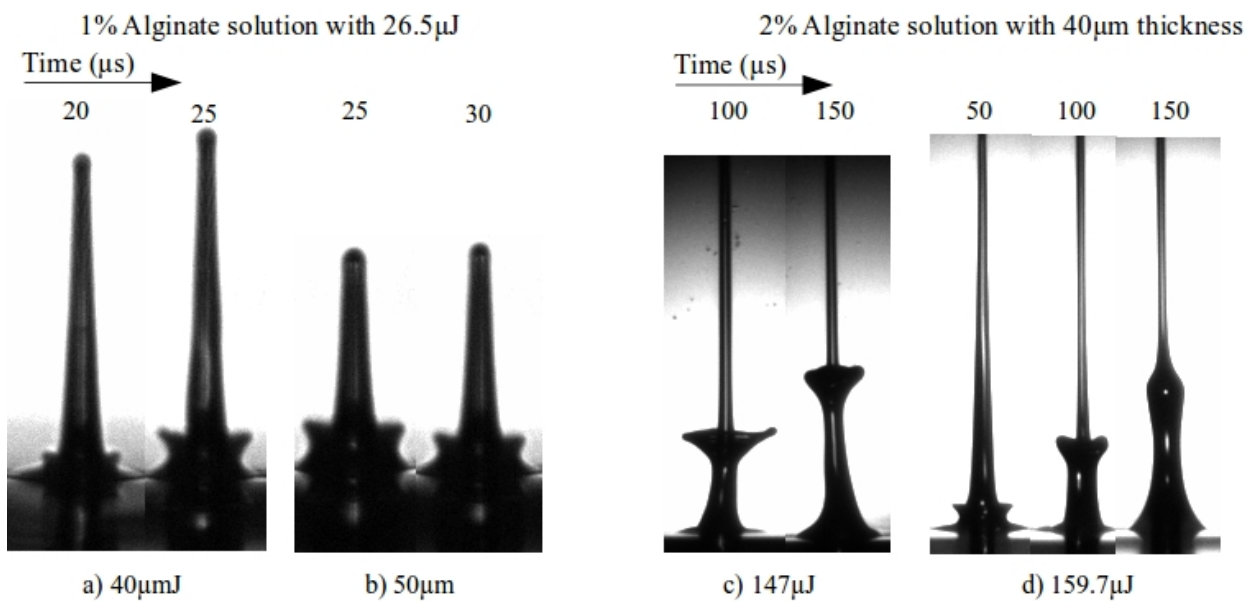


Figure 4.11: Crown formation observed from solutions of different viscosities with energies and thicknesses

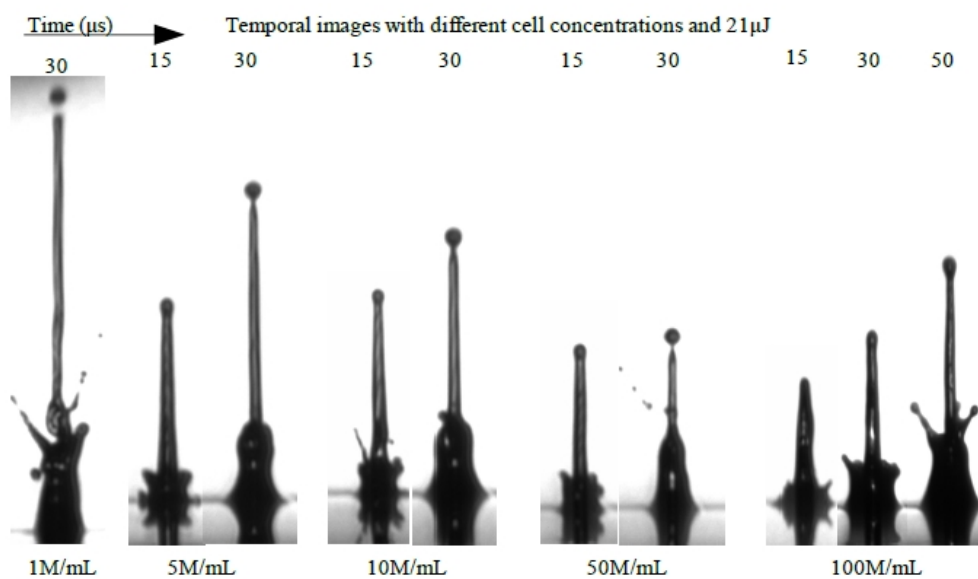


Figure 4.12: Crown formation observed during TRI of cell printing with different cell concentrations, where M/mL =  $10^6$  cells/mL

Thoroddsen et al. 2009 [211] reports it as collar formation and argue that the generated bubble is entirely confined inside liquid bioink. It expands and becomes progressively larger. Hence the bubble grows and collapses without entraining outside air. The pressure wave generated at the end of this internal bubble collapse produces a collar around the base of this protrusion, to form a characteristic jet-and-collar shape. The same (Fig. 4.13) has been observed by Obreschkow et al. 2006 [215] in so-called crown formation.

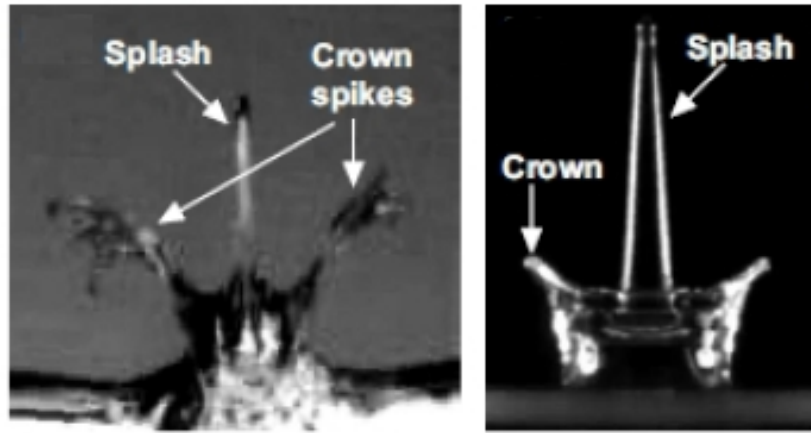


Figure 4.13: Crown formation published by Obreschkow et al. 2006 [215]

Chen et al. 2013 [210] argue that the crown formation is caused by the collapse of a circular ring-shaped crater which is due to a thin jet on the centre of the surface depression. By using boundary integral method they provide simulated dynamics of the bubble and free surface along with the detailed schematic curvature of the surface depression (Fig. 4.14).

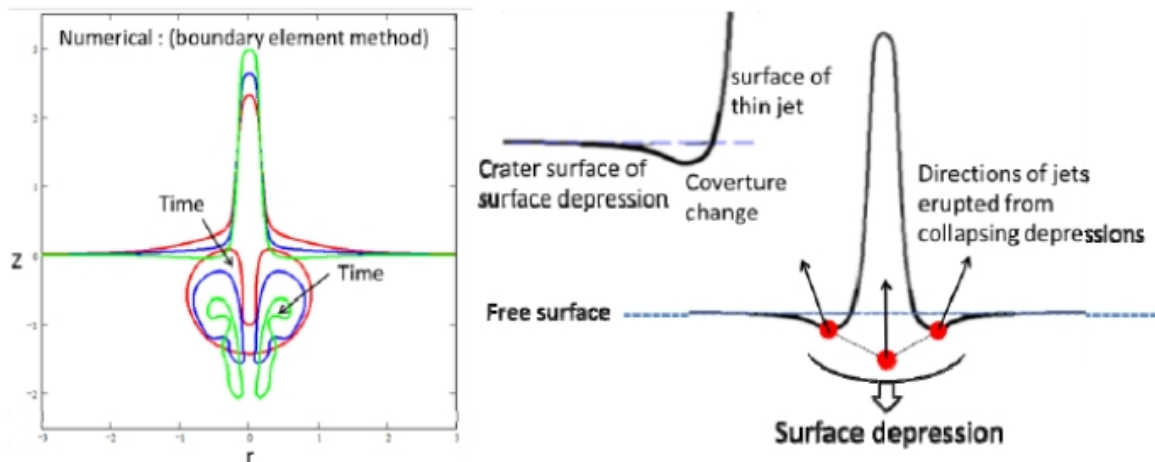


Figure 4.14: The numerical simulation and curvature scheme of the surface depression by Chen et al. 2013 [210]

This schematic diagram is helpful in explanation of the crown like structure observed during our studies. The vapour bubble expands in its first phase ( $P_{in} > P_{external} = P_{hydro} + P_{atm}$ ). At the end of the expansion phase, the bubble starts to collapse due to the pressure decrease inside the bubble ( $P_{in} < P_{ext}$ ) and moves downward, leading to the sinking around the surface

on the bottom of the jet. This sinking surface was previously referred as surface depression [214]. When the sinking surface reaches its maximum depth, the surrounding water flows toward the crater of the sinking surface. Generally in cases of surface depression, a crater appears on the free surface by inserting an external force [216–218] or a burst cavity just below the surface [219]. In fluid systems, a surface depression usually causes a singularity or near singularity of certain physical observables (divergences of velocity, surface curvatures, or pressure gradients) at the minimum depth or pinch-off point [216]. The collapse of a surface singularity or near singularity leads to a jet formation. As shown in Figure 4.14, the cross-sectional schematic image shows three singularities or near singularities denoted by three dots. The central dot, obtained by linearly extrapolating the symmetric curves of the free surface without the thin jet, results in a thick jet as observed in collapsing depression [214]. The surface connected from the crater to the thin jet contributes to a curvature change (singularity or near singularity depended on the change of surface topology [216]) which can induce two off-axis jets during the collapse of surface depression as indicated by the two arrows in figure 4.14. From the top view, this curvature change encircles around the thin jet, therefore so called circular ring-shaped crater by Chen et al. 2013 [210].

This could be summarize with, as jet moves forward, its elongation and thinning during its forward progression causes sinking of the surface around the base of the jet. When this sinking surface reaches its maximum depth, the surrounding liquid flows toward the crater of the sinking surface, resulting in formation of the crown around the base of the jet. This is in accordance to the general case of surface depression in which a crater appears on the free surface by a burst cavity just below the surface [207]. Crown-like structure at the base of the jet is attributed to sinking surface so-called surface depression [214].

### 4.3 Temporal evolution of laminar jets

This section is dedicated to the formation and dynamics of the laminar jet from three solutions of different viscosities (27, 60, 107mPa s respectively) obtained by dissolving 0.5, 0.75 and 1(w/v)% alginate in 70(v/v)% water, 30 (v/v)% glycerol and 15 mg/mL of BSA. Temporal images (Fig. 3.21-3.22) of the transfer process from lateral view are acquired. Here we discuss the results mentioned in § 3.3 Section B.

#### 4.3.1 Laminar jets ejection and dynamics

21μJ energy used in these experiment corresponds to jetting regime ( $E_{Th} < E_L < E_P$ ). Bubble expansion is more rapid and prominent in case of 0.5 % alginate solution (Fig. 3.21a) because it is less viscous as compared to the other two solutions (Fig. 3.21b,c). So less energy

is used in bubble formation and more energy is available as K.E. (Fig. 4.12) for expansion. Rapid expansion reduces the internal pressure which leads to earlier collapse as compared to other two bioinks. That's why jet is fully developed at  $3\mu\text{s}$  (Fig. 3.21a) whereas it is at  $5\mu\text{s}$  for 0.75 and 1% NaAlg solutions (Fig. 3.21b,c). Later elongation and thinning of jets (Fig. 3.21) reduce the base-width consequently crown-like formation around the base of the jet appears due to surface depression [214]. Temporal images of these jets indicate that crown-like structure persists for few microsecond (Fig. 3.22) but could not evolve as a second jet due to low energy. It converges to a shoulder like structure as the fluid of the crown is settling down.

Height of the jet from less concentrated solution is higher than that with more concentration. The velocity profiles (Fig. 3.24) show that velocity increases at first stage (1- $3\mu\text{s}$ ) due to bubble expansion. It drops once the jets are formed. It is gradually decreasing as jets progress upward until they cross FOV. Liquid flow in the jets is laminar due to small lateral dimension of bubble and jets, which prevents the turbulence in the flow.

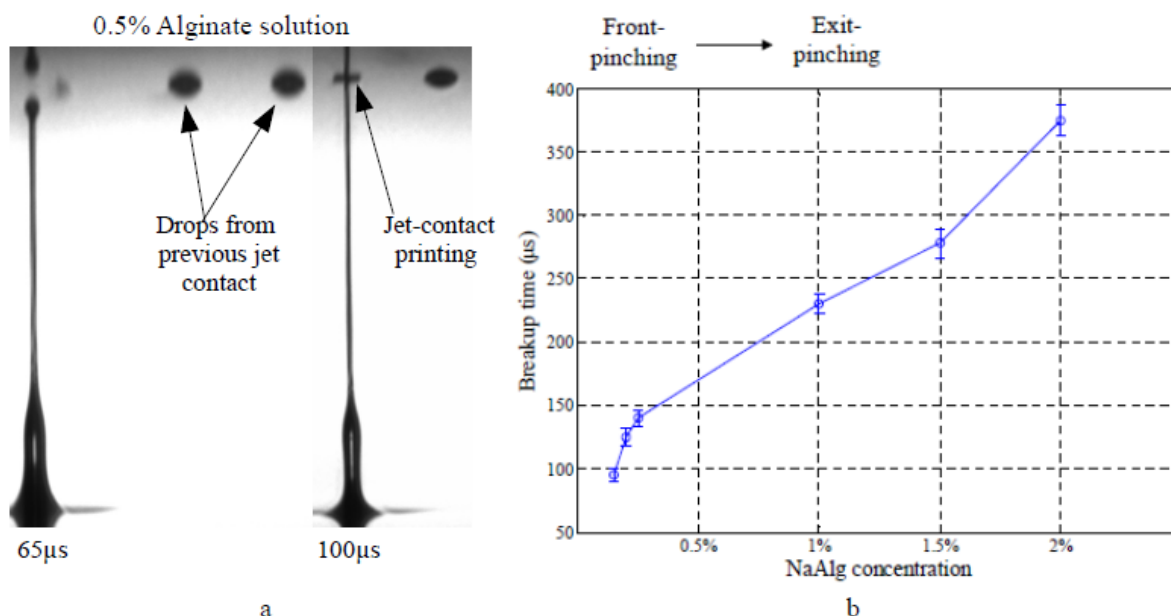


Figure 4.15: a) Jet-contact printing at 1mm from  $21\mu\text{J}$ , b) Breakup time as a function of NaAlg concentration [220]

Reynolds numbers calculated from the velocities and diameters of jets at  $6\mu\text{s}$  are 66, 21 and 15 for 0.5, 0.75 and 1% NaAlg solution respectively. Formation of drops observed at the the top of the jets is due to surface tension during the jet growth. Due to limited FOV ( $\sim 1.3\text{mm}$ ) of the camera first pinch off (flying drop) can't be observe. Therefore printing at this distance will be jet contact printing (Fig. 4.15a) which negates the generally assumed idea of signal drop deposition [106,221]. Jets become thinner (Figs. 3.22, 3.25) with the increasing viscosity (NaAlg concentration). It is also possible that the higher viscosity of the alginate



solution reduces the flow of liquid limiting the quantity of liquid in flowing jet. These long liquid jets are unstable and undergo breakup into multiple droplets due to so-called Rayleigh-Plateau (surface tension) instability. The breakup length and time (Fig. 4.15b) are increasing with increasing alginate concentration [220] which is attributed to the viscosity [222]. This is the reason we observe droplet formation without threads in jets from 0.5% NaAlg at 300 $\mu$ s. Whereas, threads has been observed in jets form 0.75% and 1% NaAlg solutions. Same has also been reported for 1% NaAlg by Kuznetsov et al. (Fig. 8 of [223]).

#### 4.4 Parametric study of the printing with novel configuration

Upward printing helps in reducing the non uniformities of the bioink thickness, parametric study was carried out in order to study effect of energy, viscosity and separation distance on the morphology of the printed drops. The printed drops at 5mm with different energies were analysed with ImageJ to study the effects of printing parameters.

The viscosities of 2, 4, and 6% NaAlg solutions used here are 94, 694 and 2618mPas respectively as mentioned by Lin et al. [192]. Drop dimensions (Fig. 3.27) displays a linear dependence [221] on energy for a given viscosity (NaAlg concentration). Same trend (Fig. 4.16) has been reported in previous studies by Kattamis et al. and Dinca et al. [130,224]. The difference in drop size is very much clear in figures 3.26-3.27. High energy pulse produces larger bubble which activates more liquid flow. Three viscous solutions used in these experiments have different NaAlg concentration which leads to significant difference between viscosities. Less energy is dissipated during jet formation from solution with low viscosity therefore resulting jet has higher K.E. (higher landing impact) as compared to jet produced with higher viscosity. Splashes observed for 2% NaAlg with 159.7 $\mu$ J energy are attributed to the high landing impact [184]. As so, more energy is dissipated during jet ejection and drop formation while using a more viscous solution, it leads to lower velocity. Therefore landing impact is reduced due to low K.E. in case of 4 and 6% solutions. Hence landing impact is less likely to introduce satellite droplets but it could be attributed to high viscosity which causes long and thin threads formation between droplets before breakup (Fig. 4.17) that's why satellite droplets are observed instead of splashes for 4% and 6% solution in figure 3.27. Increasing numbers of the satellite drops with 6% solution are attributed to the higher viscosity, the larger elasticity, and/or the longer relaxation time of high-concentration viscoelastic NaAlg solutions. This has been reported for inkjets that breakup time increases with increasing alginate concentration (Fig. 4.15b) regardless of the type of pinch-off behaviour [220]. As viscosities of the solutions are 94, 694 and 2618mPas, such significant

viscosity differences among these solutions, led to pronounced difference among the diameter of the printed drops under a given energy (Figs. 3.26-3.27). The slope difference (Fig. 3.29) between 2% and 4% is larger than that between 4% and 6% due to their viscosity difference as viscosity (694mPa s) of 4% is almost 7 times than that (94mPa s) of 2% where as viscosity (2618mPa s) of 6% solution is  $\sim 4$  times than that of 4% solution. Smaller drop diameter from high alginate concentration indicates that high viscosity reduces drop's diameter. Hence an inverse relationship between drop's diameter and viscosity exists for a given laser pulse energy. Drop diameter linearly increases with the energy and decreases with the NaAlg concentration (i.e. viscosity).

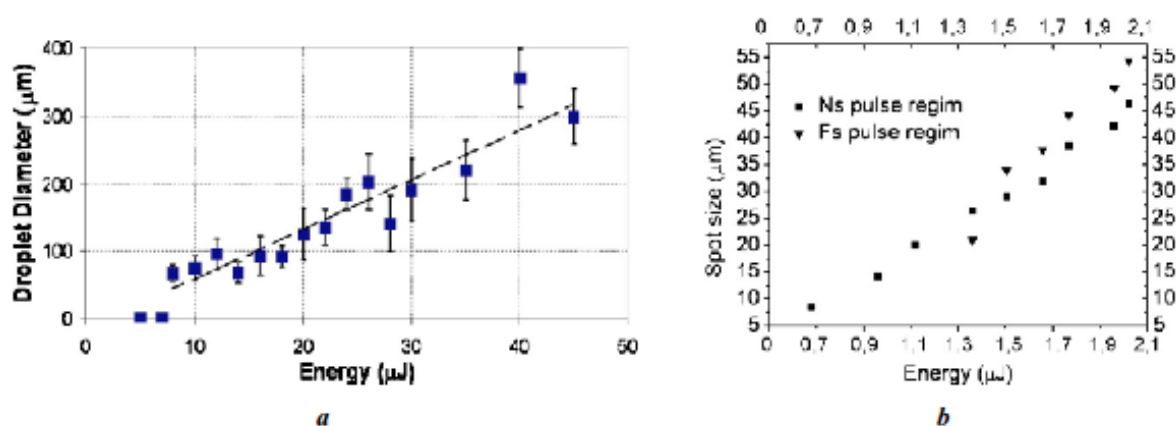


Figure 4.16: Drop size as a function of laser energy, a) (Kattamis et al. 2007 [130]) (b) Dinca et al. 2008 [222])

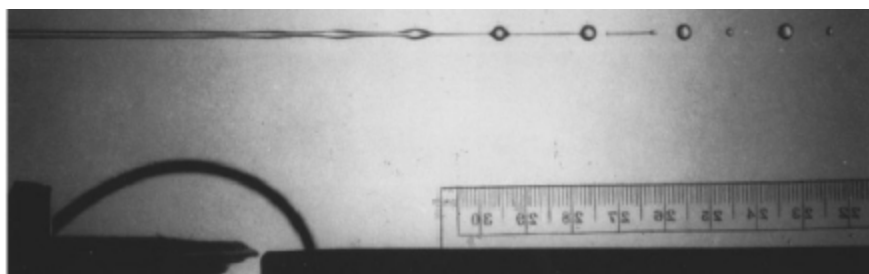


Figure 4.17: A photograph of a viscous jet (Fig. 13 from Eggers et al. 2008 [222]). A thread has just broken at the ends and is contracting into a droplet.

In conventional LAB setup, receiving substrate is placed in proximity of donor (normally  $\leq 1000\mu\text{m}$  [122,179,221,225,226]). Such a small distance could lead to contact transfer and be the source of contamination also. Moreover it limits the industrial applications. In context of implementations many external factors like vibration could serious modify the printing process. Hence we further extended our research of LAB to determine the range of the separation distance which could be used to print circular droplets with high spatial resolution. In this context, printing viscous liquids at larger distance reveals that the drop dimensions are decreasing with increasing separation distance for a given viscosity and energy (Figs. 3.30-3.32). Higher viscosity could help in printing more uniform drops with



well-defined contours. Larger separation distances also cause formation of satellite droplets; such droplets are increasing in number with increasing viscosity. This could be attributed to viscosity as long and thin threads are formed between droplets before breakup for viscous solutions as observed by Eggers et al. (figure 13 of Eggers et al. [222]). These threads may be potential cause of satellite droplets.

Printing viscous solutions requires high energy. As cell viability is function of laser energy, for its application in bioprinting it must be investigated with low energy. Therefore, our study further extend to printing with low energy from less viscous solutions (with 0.5 and 1% NaAlg concentrations having viscosities 27 and 107mPa s respectively). Significant reduction in diameters of the printed drops with increasing distance (Figs. 3.34-3.35) is attributed to low energy, 21μJ in this case. Low energy causes low intensity laser-induced stress wave which subsequently leads to laminar flow during the transfer process. Perfect contours and precise deposition (Figs. 3.33-3.34) of the printed drops are attributed to the low landing impact [184]. The diameter has dropped more than ½ times for both solutions. It indicates that drop size has an inverse relationship with the printing distance (Figs. 3.35). Similar profile for height with increasing septation distance confirms that lesser amount of the liquid reaches to the receiving substrate. Hence an inverse relation exists between drop's dimensions and separation distance. This inverse relation indicates that reduced amount of the liquid will be printed which is also confirmed from volume profile (Fig. 3.36). Moreover gravity could also be taken into account in case of upward printing. Less fluid can reach the receiving substrate due to dissipation of K.E. in upward motion.

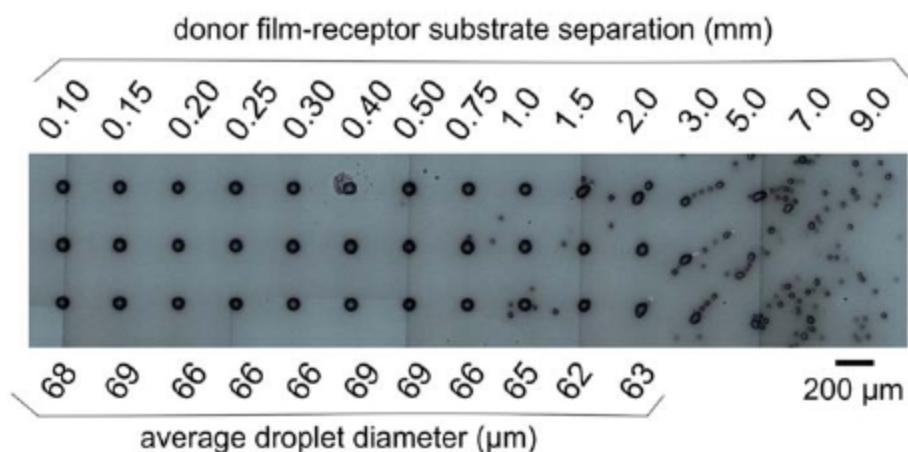


Figure 4.18: Microarray prepared varying the donor film–receptor substrate separation (Duocastella et al. [214])

In case of printing resolution, the maximum error in position is ~10μm which is just 2% of the 500μm and 1% of 1000μm (Fig. 3.37). Such error may arise form air current as

printing has been performed without vacuum. Moreover donor position has been changed manually by 3D micrometric translational stage. These results indicate that this configuration can efficiently be used to print drop with significant accuracy at larger separation distances upto 10mm which was previous recommend  $\sim 0.5\text{-}0.75\text{mm}$  [214]. The optical images (Figs. 3.26, 3.27, 3.30, 3.33, 3.34) of the printed drops contain less satellites as compared to Duocastella et al. (Fig 4.18). Previously, Dinca et al. [224] has demonstrated uniform transfer of drops at 1mm separation distance whereas it was 1.5mm (Fig. 4.19) in case bubble contact printing [227].

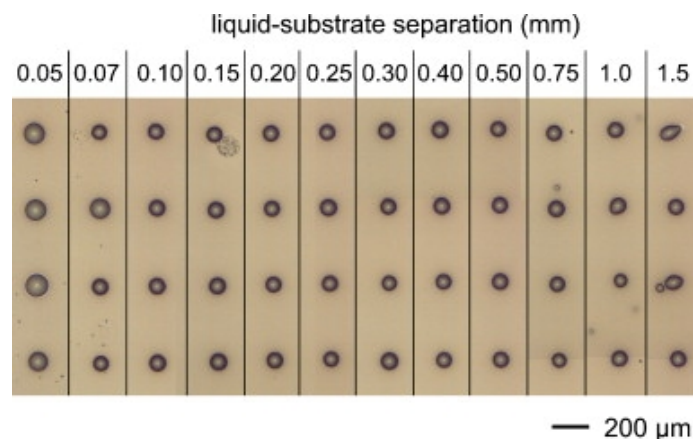


Figure 4.19: Sessile droplets deposited at different separations distances (Duocastella et al. [227])

This concludes that circular drops with well defined contours are successfully printed with significant accuracy at larger separation distances ranging from 3 to 10mm distance with upward configuration of LAB. The printed drops are almost satellite free, however satellite droplets are observed at higher energies. It shows high degree of flexibility of the LAB as the solutions with wide range of viscosity (27 to 2618mPas) has been successfully printed. The diameter of microdrops linearly increases with energy and decreases with the NaAlg concentration (i.e. viscosity) and separation distance.

## 4.5 Section B: Applications of Novel Configuration for Cell Printing

After extensive study of the LAB novel configuration it was used for cell printing. As it is learnt that printing could be through jet contact, multiple drops or single drop depending on experimental conditions. Due to limited FOV of the camera single flying drops deposition is difficult to be observed with large separation distance. In distance printing wide range of viscosity (27-2618mPa s) was used and it was noticed that increase in viscosity led to increase in breakup length. Moreover viscous solutions require higher laser energy for jet formation which may be damaging to cells in case of cell printing.

As it is already established that different regimes are function of the laser fluence. Same is the case for cell printing for given viscosity and film thickness. For cell printing, jetting regime allows a precise bioink transfer with moderate laser fluences. Viscoelastic properties of bioink are strongly dependent on cell concentration, cell type (diameter) and extracellular matrix (ECM) content (composition and quantity). Therefore different cell concentrations could modify the printing process. Consequently, LAB conditions suitable for a dedicated bioink must be set for each condition. To define these parameters, the jet formation, jet dynamics and cell landing on substrate are observed with TRI.

### 4.5.1 TRI for printing cells with slow jets

For cell printing, bioinks of different cell concentrations ranging from  $10^6$ - $10^8$  cells/mL are prepared as described in § 2.3.4. Arrays (5x7) of cells separated by 500 $\mu$ m and 1000 $\mu$ m are created as cell patterns using 3D translational stage of TRI setup to observe jet dynamics simultaneously. We used 50 $\mu$ m thickness of bioink and 21 $\mu$ J energy to evaluate LAB capacity- as a powerful tool for printing cells with slow jets.

Temporal images (Fig. 4.20) from  $10^6$  cells/mL show that a laminar jet is moving upward. Jet maintains its an axisymmetric shape with a sharp tip. Tip of jet has grown into an almost spherical mass and first pinch off occurs at 30 $\mu$ s. The jet gets thinner as it moves and prints cells by contact at 50 $\mu$ s with a velocity of approximately 20m/s. It fragments into droplets at 100 $\mu$ s and is moving backward. The reciever has very few cells and lot of corresponding prints (Fig. 4.20c) are without cells.

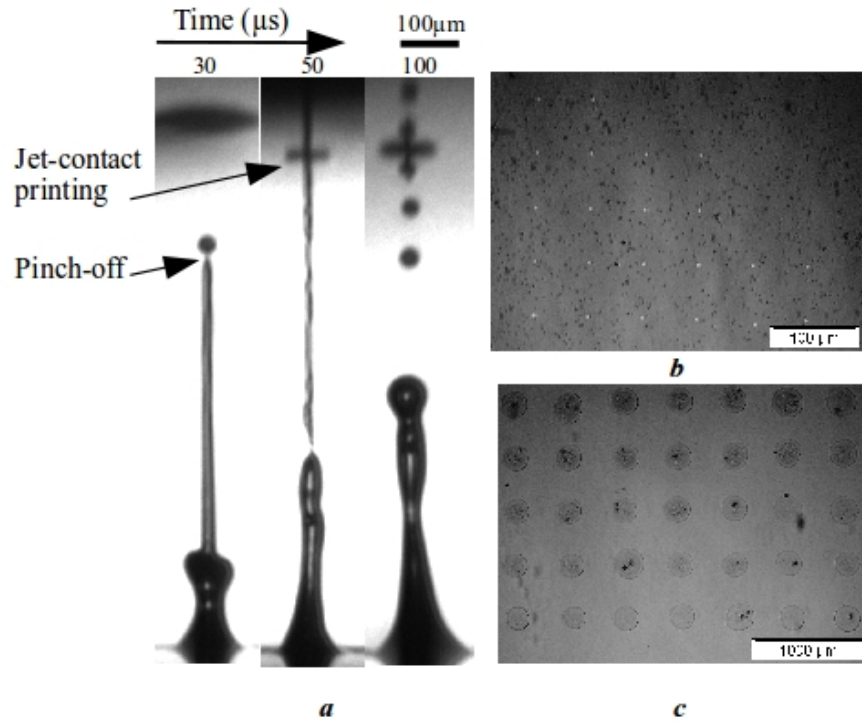


Figure 4.20: a) TRI of slow jet of  $10^6$  cells/mL with  $21 \mu\text{J}$ , b) Donor, c) Droplets obtained on receiver

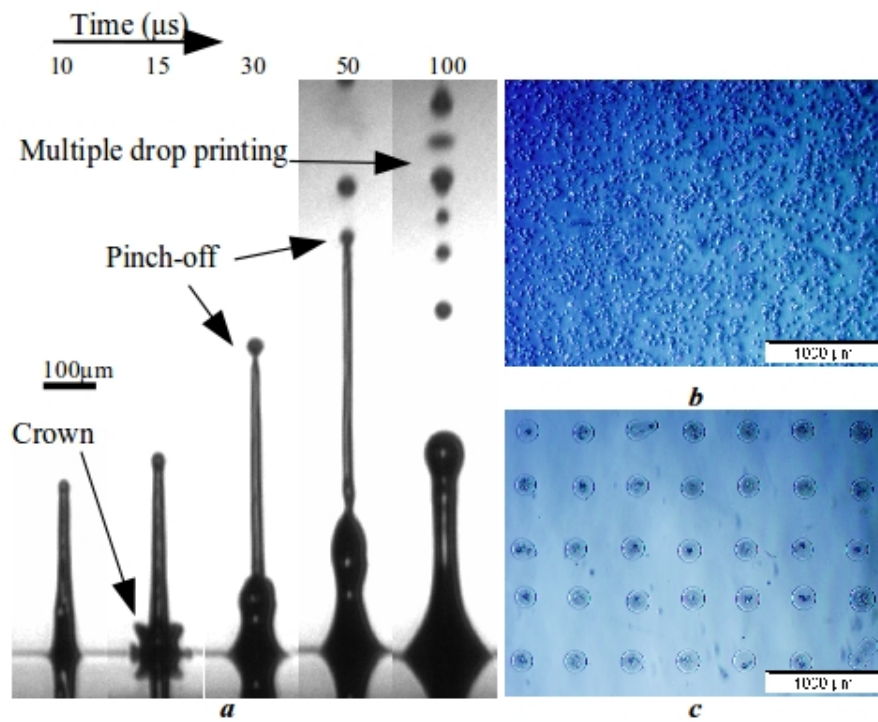


Figure 4.21: a) TRI of laminar jet of  $5 \times 10^6$  cells/mL with  $21 \mu\text{J}$ , b) Donor ( $5 \times 10^6$  cells/mL), c) Droplets obtained

Cell concentration is further increased to  $5 \times 10^6$  cells/mL. TRI (Fig. 4.21a) shows a uniform jet at  $10 \mu\text{s}$ . Slender jet with clear crown like structure across its base at  $15 \mu\text{s}$  can be observed. Tip of jet has grown into an almost spherical mass which will eventually detach as a droplet. At  $30 \mu\text{s}$ , first pinch off occurs. It gets thinner as it moves further. A fragmented

drop and second pinch off are observed at 50 $\mu$ s. The cells are printed by drop contact. At 100 $\mu$ s, it is evident that multiple droplets are landing on the receiver substrate. Jet is moving backward after fragmenting into droplets. The donor has uniform distribution of cells (Fig. 4.21b) and lot of corresponding prints (Fig. 4.21c) contain cells.

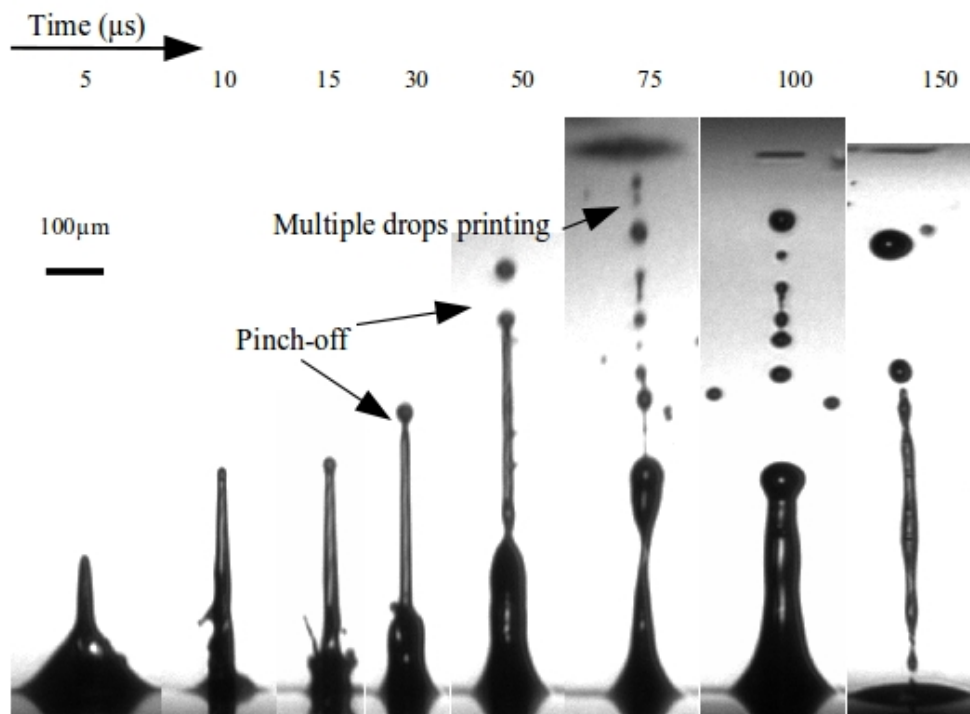


Figure 4.22: a) TRI of laminar jet of  $10 \times 10^6$  cells/mL with 21 $\mu$ J

With  $10 \times 10^6$  cells/mL (Fig. 4.22a) bioink yields slender and thinner jet. Crown structure across the base appears at 15 $\mu$ s. In subsequent progression at 30 $\mu$ s, jet has a profound droplet at its head. Second pinch-off occurs at 50 $\mu$ s. At 75 $\mu$ s the top fluid thread converts into connected droplets which is attributed to viscosity. Cells are printed with multiple drops. Fragmented droplets at 100 $\mu$ s and a thick jet which later becomes thinner at 150 $\mu$ s can be observed. The corresponding prints (Fig. 4.22c) contain cells.

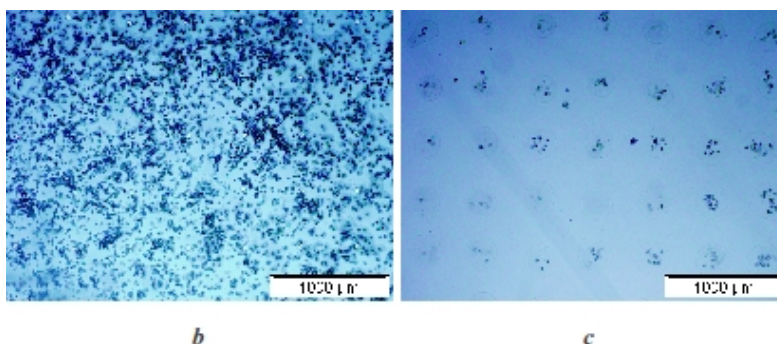


Figure 4.22: b) Donor of  $10 \times 10^6$  cells/mL, c) Corresponding droplets obtained on receiver



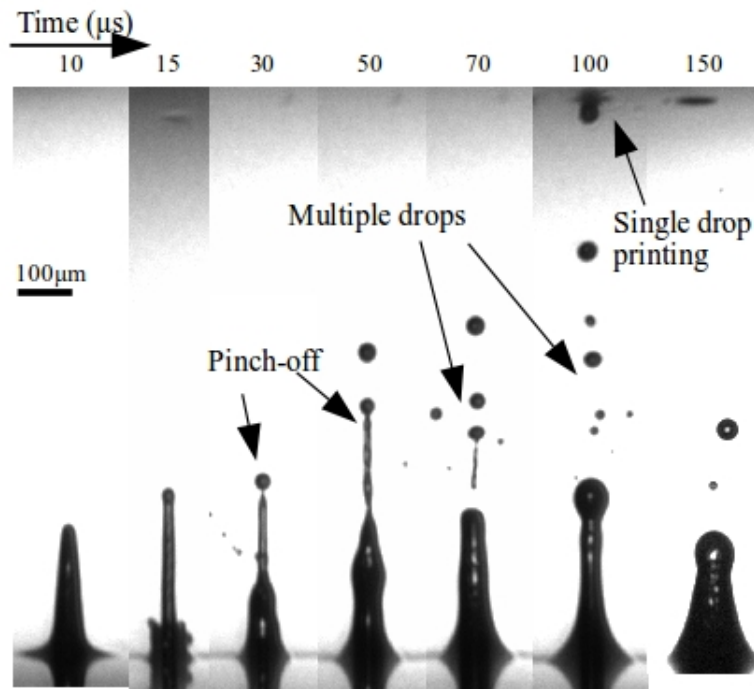


Figure 4.23: a) TRI of slow jet of  $50 \times 10^6$  cells/mL with  $21 \mu\text{J}$

From  $50 \times 10^6$  cells/mL bioink, we have a fully developed jet at  $10 \mu\text{s}$  (Fig. 4.23a). The jet moves further with significant reduction in its base width which generates crown around its base at  $15 \mu\text{s}$ . Later at  $30 \mu\text{s}$ , fully developed droplet at first pinch-off is prominent. As jet moves upward, a flying drop and second pinch-off is observed at  $50 \mu\text{s}$ . At  $70 \mu\text{s}$ , more than three droplets are visible. The flying drop is landing at substrate at  $100 \mu\text{s}$ . Later at  $150 \mu\text{s}$  jet is retreating back and just a single drop has been printed which is so-called single flying drop printing. All the printed droplets contain significant number of cells (Fig. 4.23c).

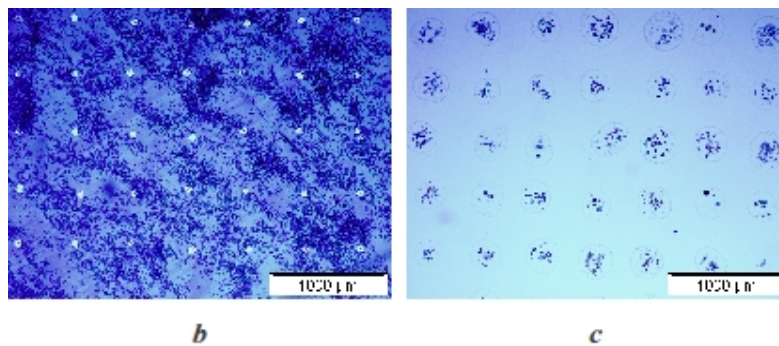


Figure 4.23: b) Donor of  $50 \times 10^6$  cells/mL, c) Corresponding prints on receiver

Formation of fully developed jet from  $100 \times 10^6$  cells/mL at  $15 \mu\text{s}$  is shown in Figure 4.24a. The jet moves further with significant reduction in its base width and has crown around its base at  $30 \mu\text{s}$  which persists till  $50 \mu\text{s}$ . At this stage, jet carries a droplet on its top. First pinch-off is observed at  $75 \mu\text{s}$ . At  $100 \mu\text{s}$ , the droplet detaches from the jet and lands on the

receiving substrate. The subsequent frame shows another droplet reaching to the receiver. Later, at 200 $\mu$ s the jet is moving back. All the printed droplets contain significant number of cells (Fig. 4.24c).

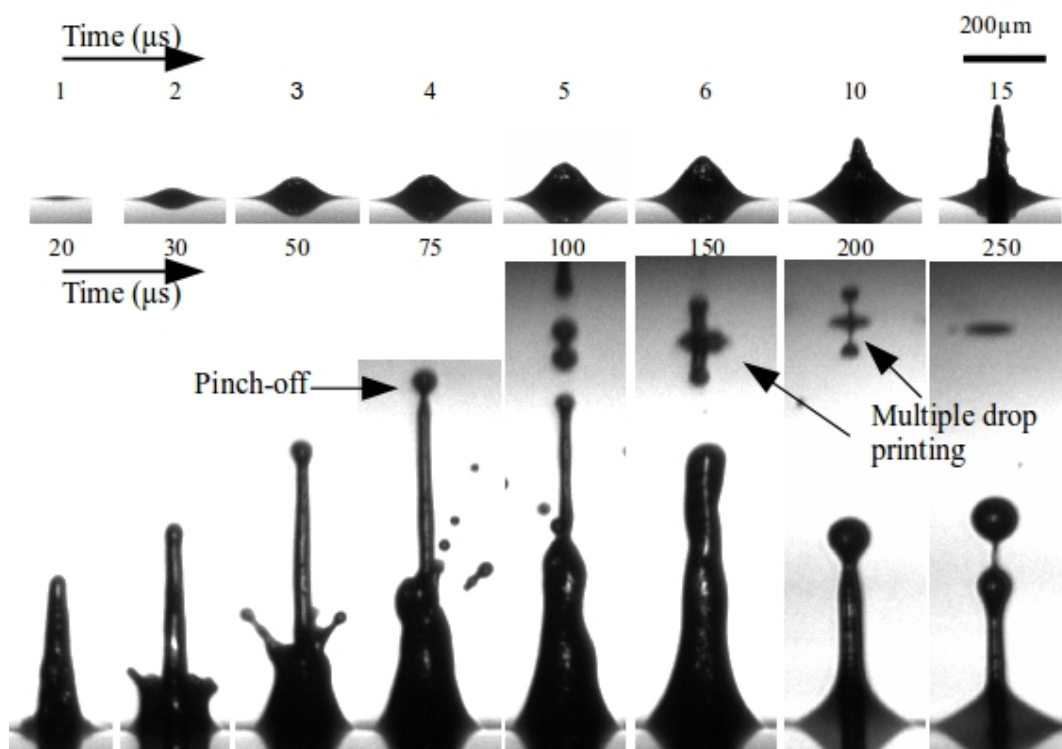


Figure 4.24: a) TRI of slow jet of  $100 \times 10^6$  cells/mL with 21  $\mu$ J

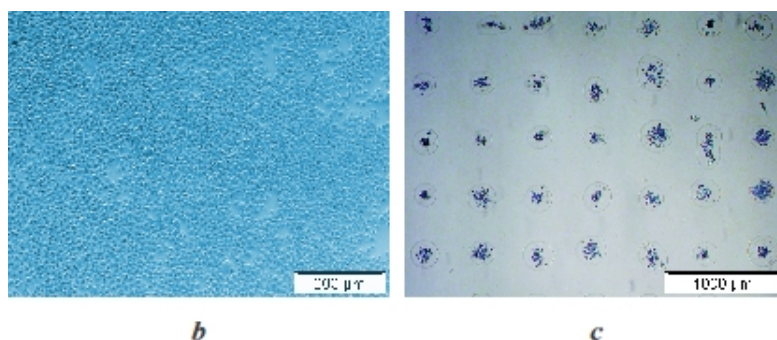


Figure 4.24: b) Donor of  $100 \times 10^6$  cells/mL, c) Corresponding droplets obtained on receiver

These results suggest that upward printing could be useful for cell printing. A single flying drop can print cells (significant numbers of cells per drop) while using  $50 \times 10^6$  cells/mL. Increasing cell concentration to  $100 \times 10^6$  cells/mL leads to multiple drops printing while low cell concentration such as  $10^6$  cells/mL demonstrates jet contact printing. Moreover low cell concentration may lead to prints without any cell. For the 50 and  $100 \times 10^6$  cells/mL every droplet has significant number of cells. The maximum velocity of the jets is 27m/s for  $10^6$

cells/mL bioink. The maximum velocity decreases with increasing cell concentration. It is reduced to 12m/s for jets of bioink with  $100 \times 10^6$  cells/mL.

#### 4.5.2 Cell printing

Based on TRI results mention in § 4.5.1 a bioink with  $100 \times 10^6$  cells/mL is selected for cell printing. An array (3x4) of cells separated by 1000 $\mu$ m (Fig. 4.25) is created as cell patterns using 3D translational stage of TRI setup. We used 50 $\mu$ m thickness of bioink and 21 $\mu$ J energy to print cells.

Printed patterns are observed under an optical microscope soon after printing. Regular prints of cells are obtained (Fig. 4.25). However their numbers were not uniform. This variation in the number of cells by spot may be attributed to the heterogeneity of cell distribution inside the bioink of the donor (Fig. 4.25).

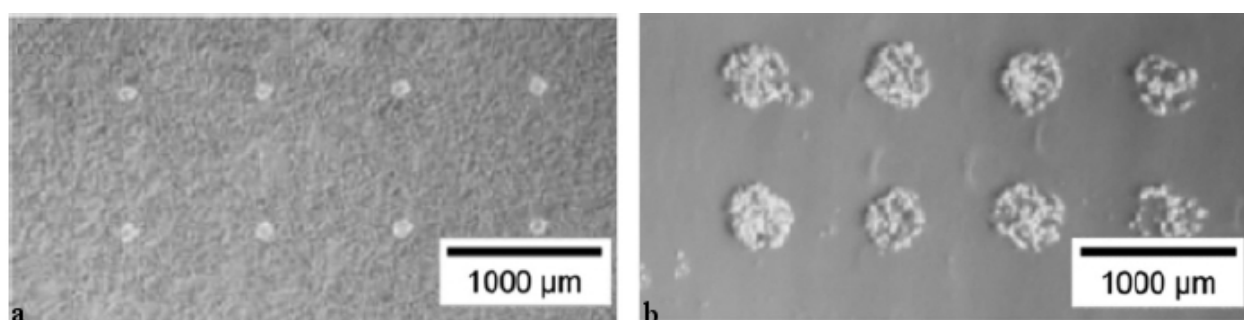


Figure 4.25: Observation of the bioink donor and the substrate after printing. (a) Impacts on the donor due to the gold vaporization after laser energy deposition, and (b) printed cells on the receiving substrate.

##### 4.5.2.1 Landing impact

Laminar jets used for cell printing produce good results. Just after the printing process, cells have a spherical shape (Figs. 4.25b, 4.26i); 24 hours after printing, cells are spreading on the collagen hydrogel (Fig. 4.26-i). The cleavage of Calcein-AM by esterases in living cells, leading to the cytoplasmic green fluorescence, reveals that the post printing viability of cells is close to 100% (Fig. 4.26-ii) (cells are not stained with EthD-1 suggesting that the cell membranes are not damaged).

These results suggest that slow jetting conditions can be used for cell printing. Higher viability is attributed to reduced landing impact caused by low velocity of the jets. Morphology (splashing and spreading phenomena) of printed drops depends on landing impact [184], viscosity [186] as well as K.E. of the droplet/jet hence velocity. Generally, low impact velocities lead to perfect drops while higher velocities initiate splashing. Pulse having energy slightly higher than threshold energy could provide optimal transfer condition to have



circular, uniform and reproducible drops without satellite droplets or splashes (Figs. 3.20b-i, 4.25b). The ejection speed of cells loaded droplet is important to determine cell viability during the landing process of the drop and it should be well controlled to minimize cell damage during the landing due to final impact on the receiver. In this context, Wang et al. [185] has shown (Fig. 4.27) that:

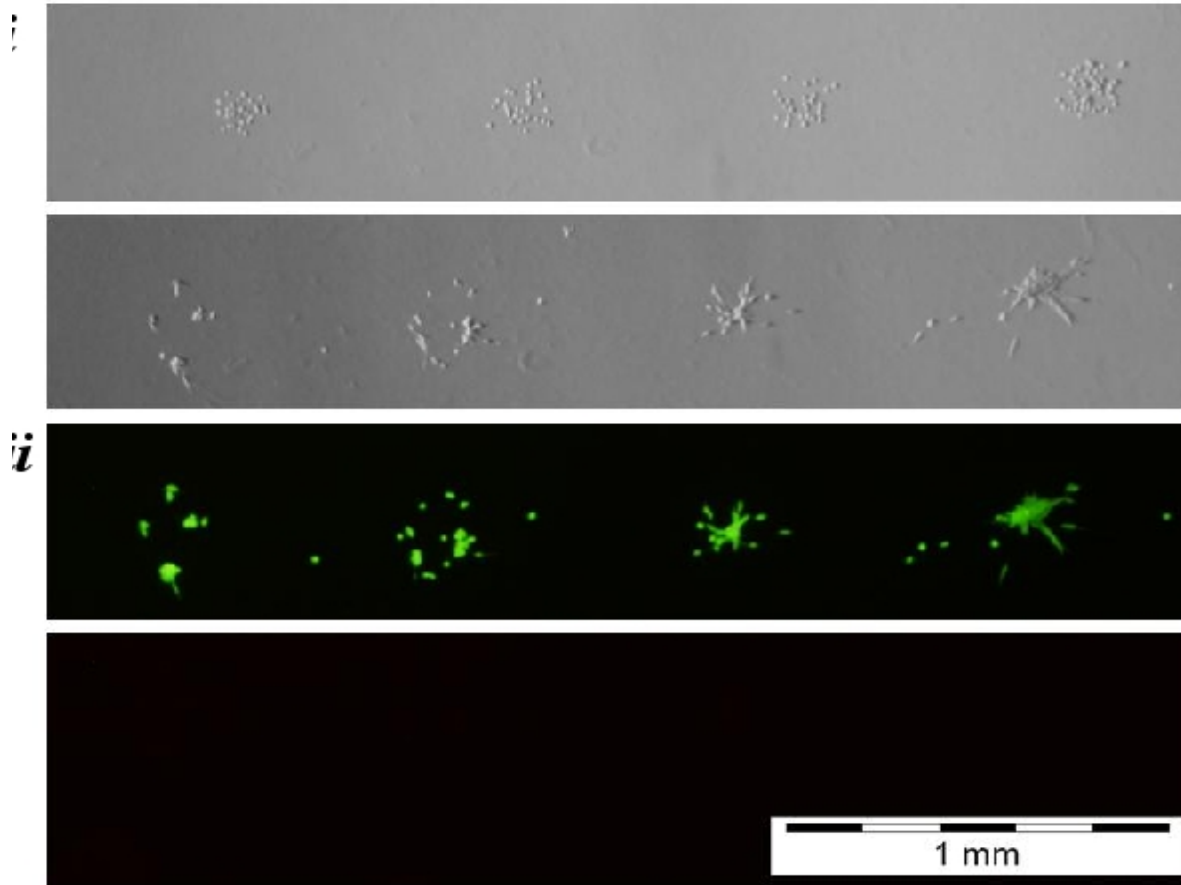


Figure 4.26: Viability of printed cells. i) Cells on collagen hydrogel just after the printing process and 24 hours later. ii) Live/dead assay 24 hours after printing. Scale bar = 1mm

1. The cell velocity (Fig. 4.27a) oscillates initially and then smooths out gradually with a constant ejection velocity. The cell can first accelerate as high as  $10^9 \text{ m/s}^2$  at the beginning and then quickly approaches zero in an oscillation manner (Fig. 4.27b); high acceleration lasts in a very short time of  $\sim 0.1 \text{ s}$ .
2. Initially, cells experience a very high pressure but this pressure also decreases rapidly to zero with an oscillatory pattern (Fig. 4.27c), like the evolution of the cell acceleration. Cell upper region undergoes the highest pressure level, followed by the bottom and then the central region.

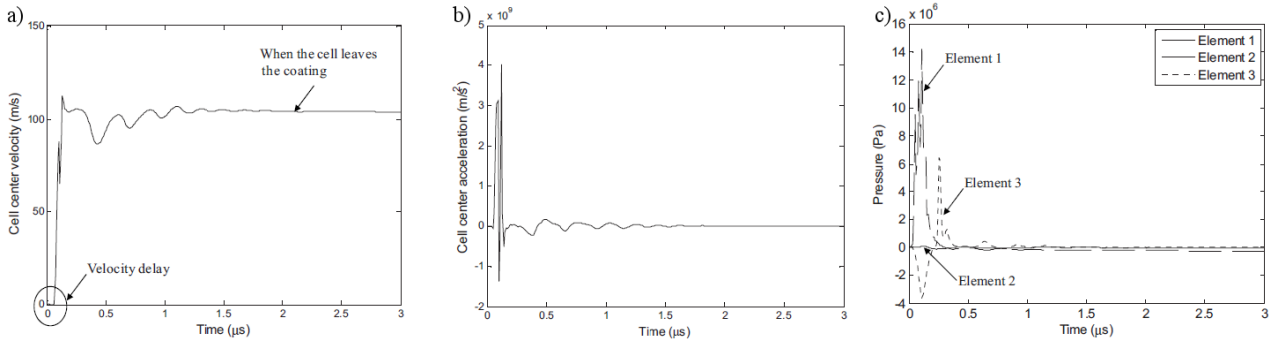


Figure 4.27: Evaluation of cell a) centre velocity, b): centre acceleration c): pressure at different internal regions

#### 4.6 LAB Mechanism: Schematic representation of LAB

Figure 4.28 provides schematic representation for whole printing mechanism of LAB. The mechanism of the LAB involves generation of a bubble due to laser-induced heating and evaporation (Fig. 4.28-ii). Our experimental conditions are bit different from the free bubble shown in the cavitation experiments. In our case, this bubble is trapped between donor slide and air. Donor slide inhibits spherical expansion of the bubble, whereas in the direction of the collector slide, the bioink-air interface shows lowest resistance against the vapour bubble enlargement. Due to this relative lower resistance the bubble causes deformation in thin veneer of liquid (separating the bubble and free surface). The bubble further expands toward the free surface (Fig. 4.28ii-v) and accelerates the liquid bubble in the upward direction. The bubble grows until all, or nearly all, K.E. has been imparted to the fluid by the time it reaches maximum volume. At this stage the angles between the local tangents to surface falls below the  $105^\circ$  (Fig. 4.28-iv), it is stipulated  $109^\circ$  by Longuet-Higgins. The expansion leads to drop the internal pressure and eventually the enclosed pressure inside the bubble ( $P_v$ ) becomes equal to the atmospheric pressure ( $P_{atm}$ ):  $P_v = P_{atm}$  (Fig. 4.28-iv). It is a transient equilibrium stage, later  $P_v < P_{atm}$  (Fig. 4.28-v) which decelerates bubble expansion and leads to bubble collapse [202], however the flowing liquid continues its fast movement under the influence of inertia towards the apex of the bubble (Fig. 4.28-v). The liquid aligns itself across bubble periphery to reach low pressure zone. The two streams of the liquid collide at the pole of bubble (Fig. 4.28-vi), consequently two liquid jets directed upward and downward (inside the bubble) are produced (Fig. 4.28-vii), similar to collapse of cavitation bubbles on a liquid-air interface [173,174,188].

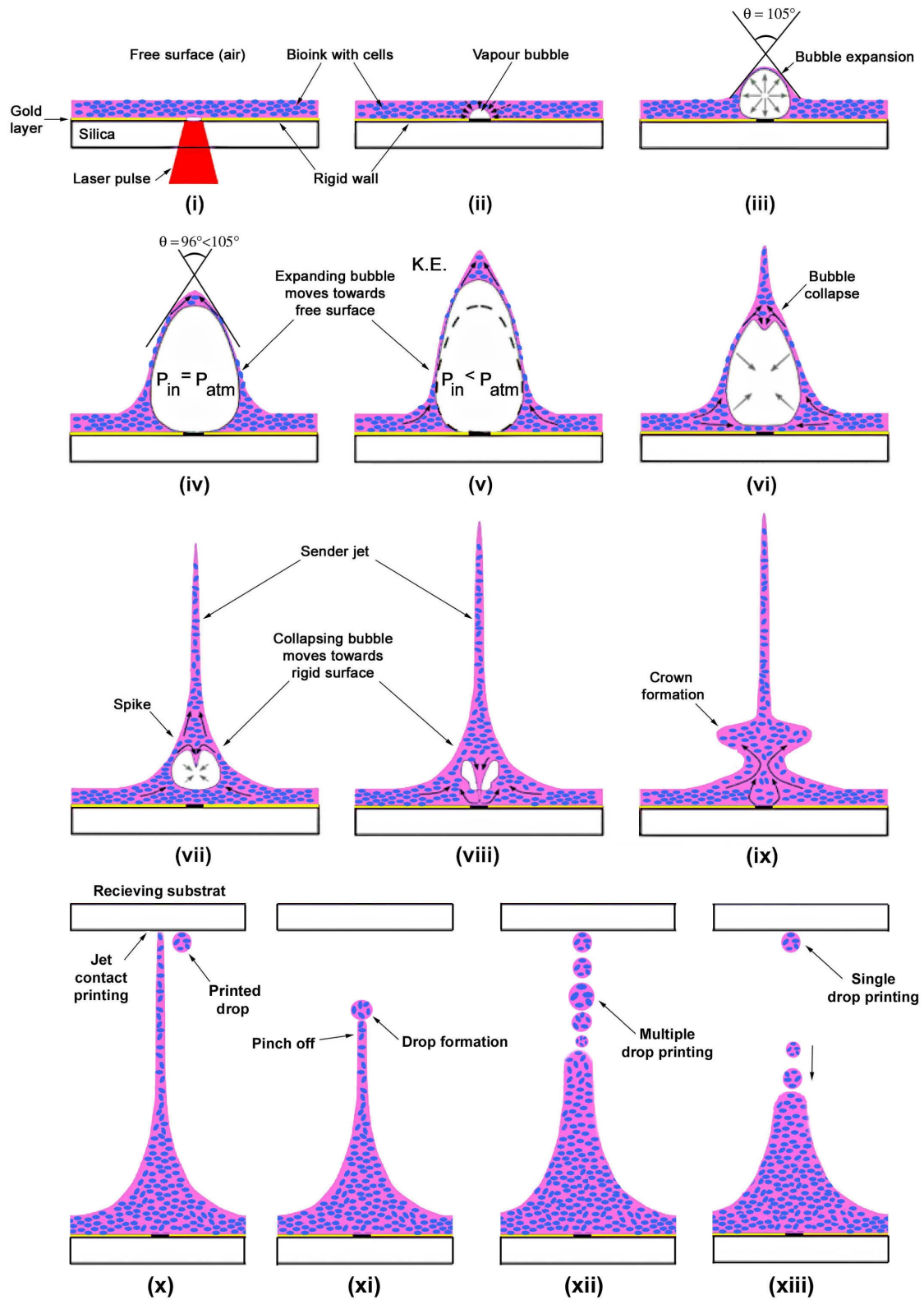


Figure: 4.28: Scheme of the bubble dynamics and jet formation for cell printing by LAB.

The observation of counter-jet is, however, more elusive (Fig. 4.5), and have only been reported in few studies [180,203]. It is the genesis of jet due to bubble collapse near free surface. The same have been reported in time-resolved imaging of LIFT experiments with

liquids [135,139,179–181,214,228,229] and modelling simulations [142,191,198,230]. Once the jet emerges the collapsing bubble is still there and moving toward (Fig. 4.28-viii) the donor (solid surface as explained in § 4.1.2.1). This downward motion of the collapsing drop displaces the surrounding liquid leading to surface sinking (surface depression). Eventually crown-like structure appears. Figure 4.28-ix can represent the scheme of crown phenomenon due to complex flow, where flow direction is given by arrows. The crown can not become a mature second jet due to low energy.

In LAB, jet is produced from thin film therefore viscous forces become relevant early in jetting process [180] contrary to formation of jets from free surface of semi-infinite domain [188,207,216]. The later stages of the jet are governed by the onset of Rayleigh–Plateau instabilities [231], which result in the progressive thinning of the jets until they finally break up from the base. This leads to the formation of long liquid-detached threads which move away from the free surface. Once jet is formed, its subsequent dynamics can be analysed on rheological parameters. Liquid jet involves complex fluid mechanics and dimensionless numbers like Reynolds ( $Re$ ), Weber ( $We$ ) and Ohnesorge ( $Oh$ ) are the most useful to characterize jet behaviour as described in §4.1.3. The analysis based on  $Re$  and  $We$  and  $Oh$  may determine the fate of the produced jet either in laminar flow domain and may print materials without satellites droplets or turbulent and not suitable for printing. For example jets with  $0.7 \leq Re \leq 20$ ,  $5 \leq We \leq 800$  could be in printable domain as determined by Derby [89] for inkjet printing (Fig. 4.9). The importance of the viscosity is characterized by Ohnesorge number. Viscosity can be neglected for small Ohnesorge numbers whereas long and thin threads are formed between droplet before breakup in case of jets with larger Ohnesorge numbers as observed in figure 4.16 [222]. Weber number determines the influence of surface tension on dynamic of liquid jet. Surface tension effects dominate overall jetting and pinch-off behaviour in case of the small dimensions (5–10  $\mu m$  in diameter) of the jets produced in LAB. Inertial forces dominate in case of large  $We$  (>1000 usually during initial stages of jetting). However, the Weber number rapidly decays as the jet velocity slows and surface tension begins to dominate.

Upon landing, the drop undergoes a significant deceleration and one or more impact between the cells and the receiving substrate [184,185] which may damage the cells. In this context, upward printing provides three different scenarios for cell transfer depending upon the velocity and rheological properties of the bioink. First of all, materials can be deposited on the substrate by jet contact (Fig. 4.28-x), however, the sessile drop will have feeding from the

contacting jet. Secondly, transfer can take place by multiple drops printing (Fig. 4.28-xii). At last, the best option which can be availed in upward printing configuration is the single drop printing in which just a single flying drop can reach to the receiving substrate (Fig. 4.28-xiii). So far at suitable printing parameters, no LAB-induced alteration of cell biology has been detected [137,232–234].

## CHAPTER 5

### 5 CONCLUSIONS & PERSPECTIVES

#### 5.1 Conclusions

Laser based technologies are renowned for precise deposition of materials while keeping their structural and functional properties intact. Such remarkable potentials exhorted their development and applications in tissue engineering (T.E.) for high resolution printing of viscous bioink. T.E. applications require a perfect control of jet and droplet formation to guaranty process robustness, hence reproducibility, up-scalability, printing resolution and cell viability. In this context, the global objective of this thesis work was to better understand the mechanism of Laser Assisted Bioprinting (LAB) and hence define printing conditions for cells with enhanced cell viability.

The following conclusions can be deduced from this thesis:

The studies in contexts of transition between sub-threshold and jetting regimes demonstrate that there exists a vertex angle for jet initiation in LAB process with a minimum value of  $105^\circ$ , which is corroborating to the findings of Blake & Gibson as  $104^\circ$ . Moreover, it is in qualitative agreement with  $109.5^\circ$  as modelled by Longuet-Higgins. Accordingly we can describe that any protrusion remains in *Sub-Threshold regime* till its vertex angle  $\geq \sim 105^\circ$  (*critical angle*) while once vertex angle drops below this critical value, deformation emerges as a jet (*Jetting regime*). This critical angle can be attributed as a geometrical parameter associated to transition between sub-threshold and jetting regimes regardless of setup.

Quantitative analyses of jet dynamics observed with different energies demonstrate a direct relation between energy and jet speed. We can demystify jetting regime as *slow*, *high-speed* and *turbulent* jets. Higher energies close to plume regime lead to supersonics but turbulent jets. Turbulent jets could not be an optimum choice for printing purpose. Energy slightly higher than threshold produces slow jet. Slow jets are unperturbed, more stable and could serve as an optimal transfer condition to have circular, uniform and reproducible drops without satellites or splashes, hence very much recommend for bioprinting. Slow jetting results in lesser landing impact on substrate. Moreover such printing conditions could reduce shear stress within the jet. As printing speed is also critical to minimise cell damage, in this context slow jetting may improve cell viability and help to slacken the applied stress to the materials (e.g. cells). The remarkable feature of high speed jets produced with LAB is the penetration through thick membrane of collagen. This indicates potential application of high-

speed jet as needle-free liquid injectors. Several methods of microjet generation suitable for this application have been proposed [235,236], but they all have several shortcomings: the production of each jet requires a significant amount of energy, the resulting shape of the ejected liquid mass tends to be diffuse rather than focused, the small size nozzles are easily clogged and others. In this context, the avoidance of very thin nozzles makes the systems less susceptible to clogging, thus it could improve the reliability and controllability.

In the experiments conducted in the conventional LAB setup, it is observed that the setup faces a major drawback of inhomogeneity of the liquid film (bioink). A uniform thickness with micron level accuracy all over the surface of the donor could not be possible in downward setup because donor needs to be fixed in inverted position. As the energy used for the jetting is slightly above threshold, sometimes it does not produce jet at one position of the donor slide and it works well for another position on the same donor slide. This difference is attributed to the local inhomogeneities present in the film thickness as rest of the parameters (pulse energy, focussing position) are controlled. Inhomogeneity of the liquid films results into formation of local areas with different thickness which seriously compromises the LAB process and leads to irreproducibility.

Time-resolved microscopy of slow jets in upward configuration has shown that ejection mechanism of LAB involves generation of the an expanding bubble due to laser-induced heating. The expanding bubble collapses at its apex which leads to jet formation, whatever the viscosity of the bioink. The propagation of the jet results in the progressive thinning of jet until it finally break up into droplets (so called Rayleigh-Plateau instability).

Morphological analyses of the drops collected on a receiver substrate conclude that circular drops from inks with wide range of viscosity (27-2618mPas) can be printed with well defined contours at larger separation distances through novel LAB configuration (upward printing). The diameter of microdrops increases with the laser energy and decreases with the increasing viscosity (i.e. sodium alginate concentration) and separation distance. Hence drop diameter is directly proportional to the energy and inversely related to viscosity and separation distance. Upward configuration can efficiently be used to print drops with significant accuracy at larger separation distances upto 10mm.

Temporal evolution of upward jets used for cell printing exhibits three different features. The printing could be through jet-contact, in which thin jet may reach to receiving substrate (if the substrate is close enough) and deposit material by contact. On the other hand

jet can be fragmented into drops. In this case multiple or single drops can reach to the substrate hence so-called multiple drops printing or signal flying drop printing respectively. Therefore deposit could be result of jet-contact, multiple drops and single drop printing.

Slow jetting condition in upward configuration of LAB can prints cells from bioinks with wide range of cell concentrations. Numbers of cell per printed drops may not be uniform. This variation in the number of cells by spot may be attributed to the heterogeneity of cell distribution inside the bioink of the donor. Cells demonstrate very high post printing viability ~100% without any damage to the cell membranes. The coherence of the jets, good reproducibility and controllability are the unique features of the upward printing configuration. It concludes that slow jetting conditions can be used for cell printing.

We conclude that upward printing could help to improve cell viability and reproducibility with high resolution.



## 5.2 Perspectives

There are numerous perspectives of this work. Modelling could be one of them. Previous modelling studies are more oriented towards ejection mechanism and the others describe landing process. So a comprehensive modelling study with complete description of the all the printing process as shown in Figure 4.27 is required to predict the results from predefined printing conditions. In this context, effect of surface tension of the bioink should be incorporated which is generally neglected. Secondly, temporal evaluation of the jet propagation with larger FOV could reveal required printing parameters for cell landing with minimum impacts on the receiver substrate (i.e. zero velocity). In this context time-resolved imaging (TRI) with novel configuration (upward printing) could help to create zero velocity landing. Such temporal evolutions could also be very useful in comparison study for the ejection mechanism and jet dynamics with femtosecond laser.

High-speed jets can be potentially used for therapeutic delivery. The penetration power of the high speed jet could be explored for needle-free liquid injectors. The insights gained through this research and the ability to generate focused, controllable, and high velocity microjets open new doors for the realization, among others, of reliable needle-free drug delivery systems. Moreover penetrating jet can also be used for microfluidic studied into pre-machined 3D structures made by micro-machining such as shown in Figure 5.1.

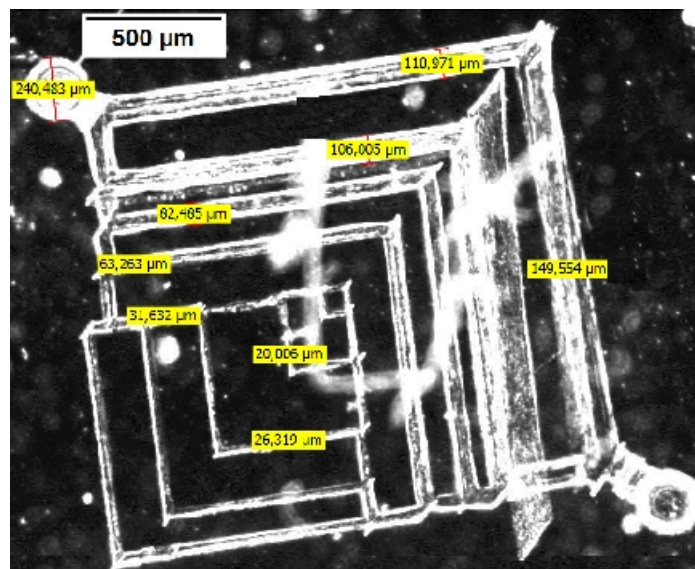


Figure 5.1: Micromachining with laser in Polyacrylamide sheet for microfluidic studies

Another variant of LIFT technique, developed by Brown et al., is named as blister-actuated LIFT [181] where metallic interlayer is substituted with polymer layer which deforms on absorbing laser energy. At moderate energies polymer layer is not fractured that

eliminates the direct laser/ink interaction, which also prevents the bioink from being contaminated with debris of the metallic layer. Comparison studies like cell printing using upward configurations in LAB and BA-LIFT cloud also describe printing conditions to improve cell viability.

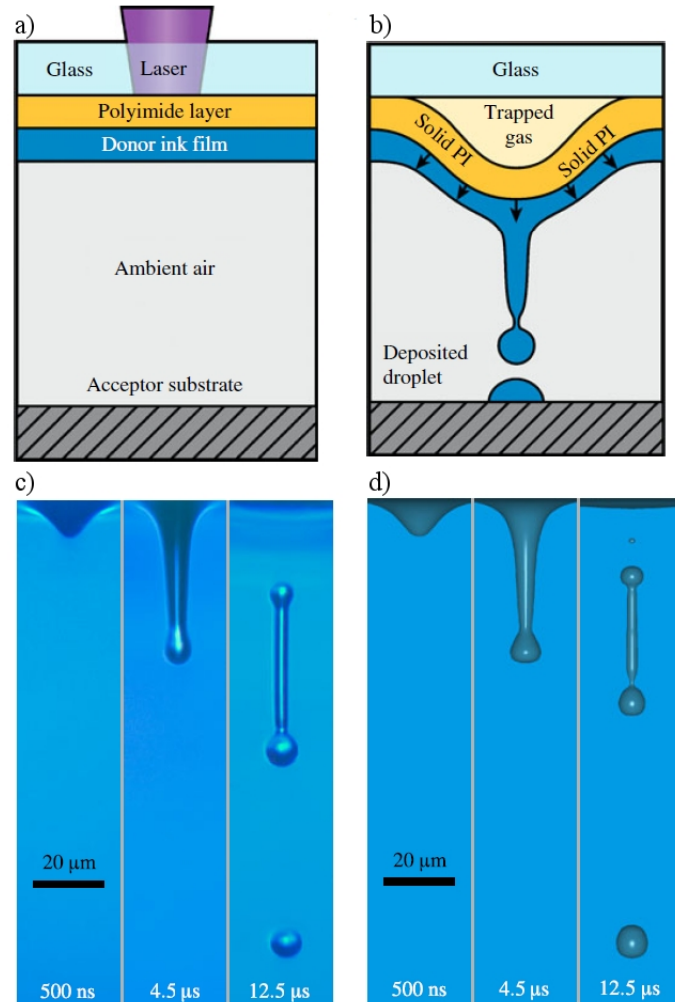


Figure 5.2: BA-LIFT, a) the laser is absorbed within a thin layer of the polymer film, b) deformation leads to jetting, c) TRI experimental images and b) computational results of fluid ejections [230]



## References

- [1] Woese C R 2004 A New Biology for a New Century *Microbiol. Mol. Biol. Rev.* **68** 173–86
- [2] Gordon J P, Zeiger H J and Townes C H 1954 Molecular Microwave Oscillator and New Hyperfine Structure in the Microwave Spectrum of  $\text{NH}_3$  *Phys. Rev.* **95** 282–4
- [3] Schawlow A L and Townes C H 1958 Infrared and Optical Masers *Phys. Rev.* **112** 1940–9
- [4] Maiman T H 1960 Optical and Microwave-Optical Experiments in Ruby *Phys. Rev. Lett.* **4** 564–6
- [5] Maiman T H 1960 Stimulated Optical Radiation in Ruby *Nature* **187** 493–4
- [6] Peng Q, Juzeniene A, Chen J, Svaasand L O, Warloe T, Giercksky K-E and Moan J 2008 Lasers in medicine *Rep. Prog. Phys.* **71** 056701
- [7] McGuff P E, Bushnell D, Soroff H S and Deterling R A Jr 1963 Studies of the surgical applications of laser (Light Amplification by Stimulated Emission of Radiation) *Surg Forum* **14** 143–5
- [8] McGuff P E, Deterling R A, Gottlieb L S, Fahimi H D, Bushnell D and Roeber F 1964 The Laser Treatment of Experimental Malignant Tumours *Can Med Assoc J* **91** 1089–95
- [9] Bradley P F 1997 A review of the use of the neodymium YAG laser in oral and maxillofacial surgery *Br J Oral Maxillofac Surg* **35** 26–35
- [10] Fankhauser F and Kwasniewska S 2003 Clinical effects of the Nd:YAG laser operating in the photodisruptive and thermal modes. A review *Ophthalmologica* **217** 1–16
- [11] Johnson L F 1963 Optical Maser Characteristics of Rare-Earth Ions in Crystals *Journal of Applied Physics* **34** 897–909
- [12] Myers T D and McDaniel J D 1991 The pulsed Nd:YAG dental laser: review of clinical applications *J Calif Dent Assoc* **19** 25–30
- [13] Nanni C A and Alster T S 1998 A practical review of laser-assisted hair removal using the Q-switched Nd:YAG, long-pulsed ruby, and long-pulsed alexandrite lasers *Dermatol Surg* **24** 1399–1405; discussion 1405
- [14] Desiate A 2009 980 nm diode lasers in oral and facial practice: current state of the science and art *International Journal of Medical Sciences* 358
- [15] Anderson R R and Parrish J A 1983 Selective photothermolysis: precise microsurgery by selective absorption of pulsed radiation *Science* **220** 524–7
- [16] Wheeland R G 1995 Clinical uses of lasers in dermatology *Lasers Surg Med* **16** 2–23
- [17] Peng Q, Warloe T, Berg K, Moan J, Kongshaug M, Giercksky K E and Nesland J M

- 1997 5-Aminolevulinic acid-based photodynamic therapy. Clinical research and future challenges *Cancer* **79** 2282–308
- [18] Burns T, Wilson M and Pearson G J 1993 Sensitisation of cariogenic bacteria to killing by light from a helium-neon laser *J. Med. Microbiol.* **38** 401–5
- [19] Burns T, Wilson M and Pearson G J 1994 Killing of cariogenic bacteria by light from a gallium aluminium arsenide diode laser *J Dent* **22** 273–8
- [20] Rovaldi C R, Pievsky A, Sole N A, Friden P M, Rothstein D M and Spacciapoli P 2000 Photoactive Porphyrin Derivative with Broad-Spectrum Activity against Oral Pathogens In Vitro *Antimicrob Agents Chemother* **44** 3364–7
- [21] Wilson M, Burns T, Pratten J and Pearson G J 1995 Bacteria in supragingival plaque samples can be killed by low-power laser light in the presence of a photosensitizer *J. Appl. Bacteriol.* **78** 569–74
- [22] Wilson M, Dobson J and Harvey W 1992 Sensitization of oral bacteria to killing by low-power laser radiation *Curr. Microbiol.* **25** 77–81
- [23] Wood S, Nattress B, Kirkham J, Shore R, Brookes S, Griffiths J and Robinson C 1999 An in vitro study of the use of photodynamic therapy for the treatment of natural oral plaque biofilms formed in vivo *J. Photochem. Photobiol. B, Biol.* **50** 1–7
- [24] Remacle M, Bodart E, Lawson G, Minet M and Mayné A 1996 Use of the CO<sub>2</sub>-laser micropoint micromanipulator for the treatment of laryngomalacia *Eur Arch Otorhinolaryngol* **253** 401–4
- [25] Remacle M, Lawson G, Degols J C, Evrard I and Jamart J 2000 Microsurgery of sulcus vergeture with carbon dioxide laser and injectable collagen *Ann. Otol. Rhinol. Laryngol.* **109** 141–8
- [26] Remacle M, Declaye X and Mayne A 1989 Subglottic haemangioma in the infant: contribution by CO<sub>2</sub> laser *J Laryngol Otol* **103** 930–4
- [27] Shapshay S M, Rebeiz E E, Bohigian R K and Hybels R L 1990 Benign lesions of the larynx: should the laser be used? *Laryngoscope* **100** 953–7
- [28] Bown S G 1991 Palliation of malignant dysphagia: surgery, radiotherapy, laser, intubation alone or in combination? *Gut* **32** 841–4
- [29] Fleischer D, Kessler F and Haye O 1982 Endoscopic Nd: YAG laser therapy for carcinoma of the esophagus: a new palliative approach *Am. J. Surg.* **143** 280–3
- [30] Nishioka N S 1995 Applications of lasers in gastroenterology *Lasers in Surgery and Medicine* **16** 205–14
- [31] Chan K F, Vassar G J, Pfefer T J, Teichman J M, Glickman R D, Weintraub S T and Welch A J 1999 Holmium:YAG laser lithotripsy: A dominant photothermal ablative mechanism with chemical decomposition of urinary calculi *Lasers Surg Med* **25** 22–37
- [32] Gupta N P, Ansari M S and Singh I 2001 Laser endoscopic incision: a viable

alternative to treat adult ureterocele *Int Urol Nephrol* **33** 325–8

- [33] Peng Q 2006 Editorial: photodynamic therapy and detection *J. Environ. Pathol. Toxicol. Oncol.* **25** 1–5
- [34] Campion M J and Singer A 1987 Vulval intraepithelial neoplasia: clinical review. *Genitourin Med* **63** 147–52
- [35] Jones R W and McLean M R 1986 Carcinoma in situ of the vulva: a review of 31 treated and five untreated cases *Obstet Gynecol* **68** 499–503
- [36] Reid R, Greenberg M D, Lörincz A T, Daoud Y, Pizzuti D and Stoler M 1990 Superficial laser vulvectomy. IV. Extended laser vaporization and adjunctive 5-fluorouracil therapy of human papillomavirus-associated vulvar disease *Obstet Gynecol* **76** 439–48
- [37] Bittl J A and Sanborn T A 1992 Excimer laser-facilitated coronary angioplasty. Relative risk analysis of acute and follow-up results in 200 patients *Circulation* **86** 71–80
- [38] LaMuraglia G M, Anderson R R, Parrish J A, Zhang D Y and Prince M R 1988 Selective laser ablation of venous thrombus: implications for a new approach in the treatment of pulmonary embolus *Lasers Surg Med* **8** 486–93
- [39] EARLE K M, CARPENTER S, ROESSMANN U, ROSS M A, HAYES J R and ZEITLER E 1965 CENTRAL NERVOUS SYSTEM EFFECTS OF LASER RADIATION *Fed. Proc.* **24** SUPPL 14:129+
- [40] Hüttmann G, Yao C and Endl E 2005 New concepts in laser medicine: Towards a laser surgery with cellular precision *Medical Laser Application* **20** 135–9
- [41] Shen N, Datta D, Schaffer C B, LeDuc P, Ingber D E and Mazur E 2005 Ablation of cytoskeletal filaments and mitochondria in live cells using a femtosecond laser nanoscissor *Mech Chem Biosyst* **2** 17–25
- [42] Tirlapur U K and König K 2002 Cell biology: Targeted transfection by femtosecond laser *Nature* **418** 290–1
- [43] Alfano R, Tata D, Cordero J, Tomashefsky P, Longo F and Alfano M 1984 Laser induced fluorescence spectroscopy from native cancerous and normal tissue *IEEE Journal of Quantum Electronics* **20** 1507–11
- [44] Dougherty T J, Gomer C J, Henderson B W, Jori G, Kessel D, Korbely M, Moan J and Peng Q 1998 Photodynamic therapy *J. Natl. Cancer Inst.* **90** 889–905
- [45] Nishioka N S 1994 Laser-induced fluorescence spectroscopy *Gastrointest. Endosc. Clin. N. Am.* **4** 313–26
- [46] Venter C and Cohen D 2004 The Century of Biology *New Perspectives Quarterly* **21** 73–7
- [47] Lalan S, Pomerantseva I and Vacanti J P 2001 Tissue engineering and its potential impact on surgery *World J Surg* **25** 1458–66

- [48] Langer R and Vacanti J 1993 Tissue engineering *Science* **260** 920–6
- [49] Bentley T S and Hanson S G 2011 *2011 U.S. organ and tissue transplant cost estimates and discussion* (Millima Research Report)
- [50] Lysaght M J, Jaklenec A and Deweerd E 2008 Great expectations: private sector activity in tissue engineering, regenerative medicine, and stem cell therapeutics *Tissue Eng Part A* **14** 305–15
- [51] Anon 2012 *Eurotransplant statistics report* ([www.statistics.eurotransplant.org](http://www.statistics.eurotransplant.org))
- [52] Gomes M E and Reis R L 2004 Tissue Engineering: Key Elements and Some Trends *Macromolecular Bioscience*
- [53] Griffith L G and Naughton G 2002 Tissue Engineering--Current Challenges and Expanding Opportunities *Science* **295** 1009–14
- [54] Nerem R M 2006 Tissue Engineering: The Hope, the Hype, and the Future *Tissue Engineering* **12** 1143–50
- [55] Olson J L, Atala A and Yoo J J 2011 Tissue engineering: current strategies and future directions *Chonnam Med J* **47** 1–13
- [56] Takebe T, Sekine K, Enomura M, Koike H, Kimura M, Ogaeri T, Zhang R-R, Ueno Y, Zheng Y-W, Koike N, Aoyama S, Adachi Y and Taniguchi H 2013 Vascularized and functional human liver from an iPSC-derived organ bud transplant *Nature* **advance online publication**
- [57] Blitterswijk C van, Thomsen P, Hubbell J, Cancedda R, Bruijn J de, Lindahl A, Sohier J and Williams D F 2008 *Tissue Engineering* (Academic Press)
- [58] MacArthur B D and Oreffo R O C 2005 Bridging the gap *Nature* **433** 19–19
- [59] Schulz J T 3rd, Tompkins R G and Burke J F 2000 Artificial skin *Annu. Rev. Med.* **51** 231–44
- [60] Schmidt A, Azevedo C F, Cheng A, Gupta S N, Bluemke D A, Foo T K, Gerstenblith G, Weiss R G, Marbán E, Tomaselli G F, Lima J A C and Wu K C 2007 Infarct tissue heterogeneity by magnetic resonance imaging identifies enhanced cardiac arrhythmia susceptibility in patients with left ventricular dysfunction *Circulation* **115** 2006–14
- [61] Hutmacher D W 2000 Scaffolds in tissue engineering bone and cartilage *Biomaterials* **21** 2529–43
- [62] Hutmacher D W, Loessner D, Rizzi S, Kaplan D L, Mooney D J and Clements J A 2010 Can tissue engineering concepts advance tumor biology research? *Trends in Biotechnology* **28** 125–33
- [63] Hutmacher D W, Schantz J T, Lam C X F, Tan K C and Lim T C 2007 State of the art and future directions of scaffold-based bone engineering from a biomaterials perspective *Journal of Tissue Engineering and Regenerative Medicine* **1** 245–60

- [64] Hutmacher D W, Sittinger M and Risbud M V 2004 Scaffold-based tissue engineering: rationale for computer-aided design and solid free-form fabrication systems *Trends Biotechnol* **22** 354–62
- [65] Hutmacher D W 2001 Scaffold design and fabrication technologies for engineering tissues--state of the art and future perspectives *J Biomater Sci Polym Ed* **12** 107–24
- [66] Hutmacher D W and Cool S 2007 Concepts of scaffold-based tissue engineering--the rationale to use solid free-form fabrication techniques *J. Cell. Mol. Med.* **11** 654–69
- [67] Place E S, Evans N D and Stevens M M 2009 Complexity in biomaterials for tissue engineering *Nat Mater* **8** 457–70
- [68] Atala A, Bauer S B, Soker S, Yoo J J and Retik A B 2006 Tissue-engineered autologous bladders for patients needing cystoplasty *Lancet* **367** 1241–6
- [69] Brauker J H, Carr-Brendel V E, Martinson L A, Crudele J, Johnston W D and Johnson R C 1995 Neovascularization of synthetic membranes directed by membrane microarchitecture *J. Biomed. Mater. Res.* **29** 1517–24
- [70] Wang N, Butler J P and Ingber D E 1993 Mechanotransduction across the cell surface and through the cytoskeleton *Science* **260** 1124–7
- [71] Lo H, Ponticciello M S and Leong K W 1995 Fabrication of controlled release biodegradable foams by phase separation *Tissue Eng.* **1** 15–28
- [72] Ma P X and Zhang R 1999 Synthetic nano-scale fibrous extracellular matrix *J. Biomed. Mater. Res.* **46** 60–72
- [73] Karageorgiou V and Kaplan D 2005 Porosity of 3D biomaterial scaffolds and osteogenesis *Biomaterials* **26** 5474–91
- [74] Chan B P and Leong K W 2008 Scaffolding in tissue engineering: general approaches and tissue-specific considerations *Eur Spine J* **17** 467–79
- [75] Guillemot F, Mironov V and Nakamura M 2010 Bioprinting is coming of age: report from the International Conference on Bioprinting and Biofabrication in Bordeaux (3B'09) *Biofabrication* **2** 010201
- [76] Mironov V, Boland T, Trusk T, Forgacs G and Markwald R R 2003 Organ printing: computer-aided jet-based 3D tissue engineering *Trens Biotechnol* **21** 157–61
- [77] Jakab K, Norotte C, Marga F, Murphy K, Vunjak-Novakovic G and Forgacs G 2010 Tissue engineering by self-assembly and bio-printing of living cells *Biofabrication* **2** 022001
- [78] Iwami K, Noda T, Ishida K, Morishima K, Nakamura M and Umeda N 2010 Bio rapid prototyping by extruding/aspirating/refilling thermoreversible hydrogel *Biofabrication* **2** 014108
- [79] Demirci U 2006 Acoustic picoliter droplets for emerging applications in semiconductor industry and biotechnology *Journal of Microelectromechanical Systems* **15**



- [80] Piqué A, Chrisey D B, Auyeung R C Y, Fitz-Gerald J, Wu H D, McGill R A, Lakeou S, Wu P K, Nguyen V and Duignan M 1999 A novel laser transfer process for direct writing of electronic and sensor materials *Appl. Phys. A* **69** 279–84
- [81] Lewis B R, Kinzel E C, Laurendeau N M, Lucht R P and Xu X 2006 Planar laser imaging and modeling of matrix-assisted pulsed-laser evaporation direct write in the bubble regime *J. Appl. Phys.* **100** 033107
- [82] Brisbane A D 1971 PATTERN DEPOSIT BY LASER -US Patents Office No. 3560258, Patented on Feb. 2, 1971
- [83] Claeysens F, Klini A, Mourka A and Fotakis C 2007 Laser patterning of Zn for ZnO nanostructure growth: Comparison between laser induced forward transfer in air and in vacuum *Thin Solid Films* **515** 8529–33
- [84] Bohandy J, Kim B F and Adrian F J Aug1986 Metal deposition from a supported metal film using an excimer laser *J Appl Phys* **60** 1538–9
- [85] Williams C Ink-jet printers go beyond paper *Physics world* **19** 24–9
- [86] Calvert P 2001 Inkjet Printing for Materials and Devices
- [87] De Gans B-J, Duineveld P C and Schubert U S 2004 Inkjet Printing of Polymers: State of the Art and Future Developments *Advanced Materials* **16** 203–13
- [88] Calvert P 2001 Inkjet Printing for Materials and Devices *Chem. Mater.* **13** 3299–305
- [89] Derby B 2010 Inkjet Printing of Functional and Structural Materials: Fluid Property Requirements, Feature Stability, and Resolution *Annual Review of Materials Research* **40** 395–414
- [90] Bharathan J and Yang Y 1998 Polymer electroluminescent devices processed by inkjet printing: I. Polymer light-emitting logo *Applied Physics Letters* **72** 2660–2
- [91] Sirringhaus H, Kawase T, Friend R H, Shimoda T, Inbasekaran M, Wu W and Woo E P 2000 High-Resolution Inkjet Printing of All-Polymer Transistor Circuits *Science* **290** 2123–6
- [92] Hayes D J, Wallace D B and Cox W R *MicroJet Printing of Solder and Polymers for Multi-Chip Modules and Chip-Scale Packages by*
- [93] Sachs E, Cima M and Cornie J 1990 Three-Dimensional Printing: Rapid Tooling and Prototypes Directly from a CAD Model *CIRP Annals - Manufacturing Technology* **39** 201–4
- [94] Seerden K A M, Reis N, Evans J R G, Grant P S, Halloran J W and Derby B 2001 Ink-Jet Printing of Wax-Based Alumina Suspensions *Journal of the American Ceramic Society* **84** 2514–20
- [95] Setti L, Fraleoni-Morgera A, Ballarin B, Filippini A, Frascaro D and Piana C 2005 An

amperometric glucose biosensor prototype fabricated by thermal inkjet printing *Biosens Bioelectron* **20** 2019–26

- [96] De Gans B-J and Schubert U S 2004 Inkjet Printing of Well-Defined Polymer Dots and Arrays *Langmuir* **20** 7789–93
- [97] Gamerith S, Klug A, Scheiber H, Scherf U, Moderegger E and List E J W 2007 Direct Ink-Jet Printing of Ag–Cu Nanoparticle and Ag-Precursor Based Electrodes for OFET Applications *Advanced Functional Materials* **17** 3111–8
- [98] Ko S H, Chung J, Pan H, Grigoropoulos C P and Poulidakos D 2007 Fabrication of multilayer passive and active electric components on polymer using inkjet printing and low temperature laser processing *Sensors and Actuators A: Physical* **134** 161–8
- [99] Plötner M, Wegener T, Richter S, Howitz S and Fischer W-J 2004 Investigation of ink-jet printing of poly-3-octylthiophene for organic field-effect transistors from different solutions *Synthetic Metals* **147** 299–303
- [100] Nakamura M, Kobayashi A, Takagi F, Watanabe A, Hiruma Y, Ohuchi K, Iwasaki Y, Horie M, Morita I and Takatani S 2005 Biocompatible inkjet printing technique for designed seeding of individual living cells *Tissue Eng* **11** 1658–66
- [101] Martin G D, Hoath S D and Hutchings I M 2008 Inkjet printing - the physics of manipulating liquid jets and drops *J. Phys.: Conf. Ser.* **105** 012001
- [102] Martin G D, Hoath S D and Hutchings I M 2008 Inkjet printing - the physics of manipulating liquid jets and drops *J. Phys.: Conf. Ser.* **105** 012001
- [103] Blazdell P. and Evans J R. 2000 Application of a continuous ink jet printer to solid freeforming of ceramics *Journal of Materials Processing Technology* **99** 94–102
- [104] Mei J, Lovell M R and Mickle M H 2005 Formulation and processing of novel conductive solution inks in continuous inkjet printing of 3-D electric circuits *IEEE Transactions on Electronics Packaging Manufacturing* **28** 265–73
- [105] Park J-U, Hardy M, Kang S J, Barton K, Adair K, Mukhopadhyay D kishore, Lee C Y, Strano M S, Alleyne A G, Georgiadis J G, Ferreira P M and Rogers J A 2007 High-resolution electrohydrodynamic jet printing *Nat Mater* **6** 782–9
- [106] Barron J A, Young H D, Dlott D D, Darfler M M, Krizman D B and Ringeisen B R 2005 Printing of protein microarrays via a capillary-free fluid jetting mechanism *Proteomics* **5** 4138–44
- [107] Sirringhaus H and Shimoda T 2003 Inkjet Printing of Functional Materials *MRS Bulletin* **28** 802–6
- [108] Boland T, Xu T, Damon B and Cui X 2006 Application of inkjet printing to tissue engineering *Biotechnol J* **1** 910–7
- [109] Antohe B V and Wallace D B 2002 Acoustic Phenomena in a Demand Mode Piezoelectric Ink jet Printer *Journal of Imaging Science and Technology* **46** 409–14

- [110] Reis N, Ainsley C and Derby B 2005 Ink-jet delivery of particle suspensions by piezoelectric droplet ejectors *Journal of Applied Physics* **97** 094903–094903–6
- [111] Klebe R J 1988 Cytoscribing: A method for micropositioning cells and the construction of two- and three-dimensional synthetic tissues *Experimental Cell Research* **179** 362–73
- [112] Saunders R E, Gough J E and Derby B 2008 Delivery of human fibroblast cells by piezoelectric drop-on-demand inkjet printing *Biomaterials* **29** 193–203
- [113] Xu T, Gregory C A, Molnar P, Cui X, Jalota S, Bhaduri S B and Boland T 2006 Viability and electrophysiology of neural cell structures generated by the inkjet printing method *Biomaterials* **27** 3580–8
- [114] Zhao W, Xu T, Aboushwareb T, Atala A and Yoo J 2010 In vivo generation of functional tissues using the inkjet printing technology for reconstructive surgery *Journal of the American College of Surgeons* **211** S87
- [115] Khatiwala C, Law R, Shepherd B, Dorfman S and Csete M 2012 3D CELL BIOPRINTING FOR REGENERATIVE MEDICINE RESEARCH AND THERAPIES *Gene Therapy and Regulation* **07** 1230004
- [116] Parsa S, Gupta M, Loizeau F and Cheung K C 2010 Effects of surfactant and gentle agitation on inkjet dispensing of living cells *Biofabrication* **2** 025003
- [117] Demirci U and Toner M 2006 Direct Etch Method for Microfluidic Channel and Nano-Height Post Fabrication by Picoliter Droplets *19th IEEE International Conference on Micro Electro Mechanical Systems, 2006. MEMS 2006 Istanbul* 19th IEEE International Conference on Micro Electro Mechanical Systems, 2006. MEMS 2006 Istanbul pp 326–9
- [118] Vozzi G, Flaim C, Ahluwalia A and Bhatia S 2003 Fabrication of PLGA scaffolds using soft lithography and microsyringe deposition *Biomaterials* **24** 2533–40
- [119] Fedorovich N E, De Wijn J R, Verbout A J, Alblas J and Dhert W J A 2008 Three-Dimensional Fiber Deposition of Cell-Laden, Viable, Patterned Constructs for Bone Tissue Printing *Tissue Eng* **14** 127–33
- [120] Tasoglu S and Demirci U 2013 Bioprinting for stem cell research *Trends Biotechnol.* **31** 10–9
- [121] Pirlo R K, Dean D M D, Knapp D R and Gao B Z 2006 Cell deposition system based on laser guidance *Biotechnol J* **1** 1007–13
- [122] Guillotin B, Souquet A, Catros S, Duocastella M, Pippenger B, Bellance S, Bareille R, Rémy M, Bordenave L, Amédée J and Guillemot F 2010 Laser assisted bioprinting of engineered tissue with high cell density and microscale organization *Biomaterials* **31** 7250–6
- [123] Odde D J and Renn M J 1999 Laser-guided direct writing for applications in biotechnology *Trends Biotechnol* **17** 385–9

- [124] Odde D J and Renn M J 2000 Laser-guided direct writing of living cells *Biotechnology and Bioengineering* **67** 312–8
- [125] Ashkin A 1970 Acceleration and Trapping of Particles by Radiation Pressure *Physical Review Letters* **24** 156–9
- [126] Guillotin B and Guillemot F 2011 Cell patterning technologies for organotypic tissue fabrication *Trends Biotechnol* **29** 183–90
- [127] Levene M L, Scott R D and Stryj B W 1970 Material Transfer Recording *Appl. Opt.* **9** 2260–5
- [128] Hon K, Li L and Hutchings I 2008 Direct writing technology—Advances and developments *CIRP Annals - Manufacturing Technology* **57** 601–20
- [129] A Piqué D W W 2002 Direct-write of sensor devices by a laser forward transfer technique *Proceedings of SPIE Proceedings of SPIE* 361–8
- [130] Kattamis N T, Purnick P E, Weiss R and Arnold C B 2007 Thick film laser induced forward transfer for deposition of thermally and mechanically sensitive materials *Appl. Phys. Lett.* **91** 171120–3
- [131] Mézel C, Souquet A, Hallo L and Guillemot F 2010 Bioprinting by laser-induced forward transfer for tissue engineering applications: jet formation modeling *Biofabrication* **2** 014103
- [132] Singh S C, Zeng H B, Guo C and Cai W 2012 *Nanomaterials* (John Wiley & Sons)
- [133] Mironov V, Trusk T, Kasyanov V, Little S, Swaja R and Markwald R 2009 Biofabrication: a 21st century manufacturing paradigm *Biofabrication* **1** 022001
- [134] Chrisey D B 2000 The Power of Direct Writing *Science* **289** 879 –881
- [135] Gruene M, Unger C, Koch L, Deiwick A and Chichkov B 2011 Dispensing pico to nanolitre of a natural hydrogel by laser-assisted bioprinting *Biomed Eng Online* **10** 19
- [136] Lin Y, Huang Y and Chrisey D B 2009 Droplet formation in matrix-assisted pulsed-laser evaporation direct writing of glycerol-water solution *J. Appl. Phys.* **105** 093111–6
- [137] Hopp B, Smausz T, Kresz N, Barna N, Bor Z, Kolozsvári L, Chrisey D B, Szabó A and Nógrádi A 2005 Survival and proliferative ability of various living cell types after laser-induced forward transfer *Tissue Engineering* **11** 1817–23
- [138] Koch L, Kuhn S, Sorg H, Gruene M, Schlie S, Gaebel R, Polchow B, Reimers K, Stoelting S, Ma N, Vogt P M, Steinhoff G and Chichkov B 2009 Laser Printing of Skin Cells and Human Stem Cells *Tissue Engineering Part C: Methods* 091221133515000
- [139] Duocastella M, Fernández-Pradas J M, Morenza J L and Serra P 2009 Time-resolved imaging of the laser forward transfer of liquids *J. Appl. Phys.* **106** 084907
- [140] Barron J A, Krizman D B and Ringeisen B R 2005 Laser printing of single cells: statistical analysis, cell viability, and stress *Ann Biomed Eng* **33** 121–30

- [141] Ringeisen B R, Othon C M, Barron J A, Young D and Spargo B J 2006 Jet-based methods to print living cells *Biotechnol J* **1** 930–48
- [142] Mezel C, Hallo L, Souquet A, Breil J, Hebert D and Guillemot F 2009 Self-consistent modeling of jet formation process in the nanosecond laser pulse regime *Phys. Plasmas* **16** 123112–12
- [143] Bohandy J, Kim B F, Adrian F J and Jette A N 1988 Metal deposition at 532 nm using a laser transfer technique *Journal of Applied Physics* **63** 1158–62
- [144] Yamada H, Sano T, Nakayama T and Miyamoto I 2002 Optimization of laser-induced forward transfer process of metal thin films *Applied Surface Science* **197** 411–5
- [145] Guillemot F, Souquet A, Catros S and Guillotin B 2010 Laser-assisted cell printing: principle, physical parameters versus cell fate and perspectives in tissue engineering *Nanomedicine* **5** 507–15
- [146] Baseman R J, Froberg N M, Andreshak J C and Schlesinger Z 1990 Minimum fluence for laser blow-off of thin gold films at 248 and 532 nm *Applied Physics Letters* **56** 1412–4
- [147] Schultze V 1991 Laser-induced forward transfer of aluminium *Applied Surface Science* **52** 303–9
- [148] Kántor Z, Tóth Z and Szörényi T 1992 Laser induced forward transfer: The effect of support-film interface and film-to-substrate distance on transfer *Appl. Phys. A* **54** 170–5
- [149] Tóth Z, Szörényi T and Tóth A L 1993 Ar<sup>+</sup> laser-induced forward transfer (LIFT): a novel method for micrometer-size surface patterning *Applied Surface Science* **69** 317–20
- [150] Kantor Z, Toth Z, Szorenyi T and Toth A L 1994 Deposition of micrometer sized tungsten patterns by laser transfer technique *Applied Physics Letters* **64** 3506–8
- [151] Kántor Z, Tóth Z and Szörényi T 1995 Metal pattern deposition by laser-induced forward transfer *Applied Surface Science* **86** 196–201
- [152] Kántor Z and Szörényi T 1995 Dynamics of long-pulse laser transfer of micrometer-sized metal patterns as followed by time-resolved measurements of reflectivity and transmittance *Journal of Applied Physics* **78** 2775–81
- [153] Zergioti I, Mailis S, Vainos N A, Papakonstantinou P, Kalpouzos C, Grigoropoulos C P and Fotakis C 1998 Microdeposition of metal and oxide structures using ultrashort laser pulses *Appl Phys A* **66** 579–82
- [154] Papakonstantinou P, Vainos N . and Fotakis C 1999 Microfabrication by UV femtosecond laser ablation of Pt, Cr and indium oxide thin films *Applied Surface Science* **151** 159–70
- [155] Sano T, Yamada H, Nakayama T and Miyamoto I 2002 Experimental investigation of laser induced forward transfer process of metal thin films *Applied Surface Science* **186** 221–6

- [156] Zergioti I, Papazoglou D., Karaiskou A, Vainos N. and Fotakis C 2002 Laser microprinting of InOx active optical structures and time resolved imaging of the transfer process *Applied Surface Science* **197–198** 868–72
- [157] Chakraborty S, Sakata H, Yokoyama E, Wakaki M and Chakravorty D 2007 Laser-induced forward transfer technique for maskless patterning of amorphous V2O5 thin film *Applied Surface Science* **254** 638–43
- [158] Arnold C B, Wartena R C, Swider-Lyons K E and Pique A 2003 Direct-Write Planar Microultracapacitors by Laser Engineering *J. Electrochem. Soc.* **150** A571–A575
- [159] C. B. Arnold et al 2004 Direct-write laser processing creates tiny electrochemical systems *Material Processing*
- [160] Arnold C B, Kim H and Piqué A 2004 Laser direct write of planar alkaline microbatteries *Appl Phys A* **79** 417–20
- [161] Kim H, Auyeung R C Y and Piqué A 2007 Laser-printed thick-film electrodes for solid-state rechargeable Li-ion microbatteries *Journal of Power Sources* **165** 413–9
- [162] Piqué A, Arnold C B, Kim H, Ollinger M and Sutto T E 2004 Rapid prototyping of micropower sources by laser direct-write *Appl Phys A* **79** 783–6
- [163] Boutopoulos C, Tsouti V, Goustouridis D, Chatzandroulis S and Zergioti I 2008 Liquid phase direct laser printing of polymers for chemical sensing applications *Applied Physics Letters* **93** 191109
- [164] Kim H, Auyeung R C Y, Lee S H, Huston A L and Piqué A 2009 Laser forward transfer of silver electrodes for organic thin-film transistors *Appl. Phys. A* **96** 441–5
- [165] Kim H, Auyeung R C Y, Lee S H, Huston A L and Piqué A 2010 Laser-printed interdigitated Ag electrodes for organic thin film transistors *J. Phys. D: Appl. Phys.* **43** 085101
- [166] Michael S, Sorg H, Peck C-T, Koch L, Deiwick A, Chichkov B, Vogt P M and Reimers K 2013 Tissue Engineered Skin Substitutes Created by Laser-Assisted Bioprinting Form Skin-Like Structures in the Dorsal Skin Fold Chamber in Mice *PLoS ONE* **8** e57741
- [167] Catros S, Fricain J-C, Guillotin B, Pippenger B, Bareille R, Remy M, Lebraud E, Desbat B, Amédée J and Guillemot F 2011 Laser-assisted bioprinting for creating on-demand patterns of human osteoprogenitor cells and nano-hydroxyapatite *Biofabrication* **3** 025001
- [168] Gruene M, Pflaum M, Deiwick A, Koch L, Schlie S, Unger C, Wilhelmi M, Haverich A and Chichkov B N 2011 Adipogenic differentiation of laser-printed 3D tissue grafts consisting of human adipose-derived stem cells *Biofabrication* **3** 015005
- [169] Koch L, Deiwick A, Schlie S, Michael S, Gruene M, Coger V, Zychlinski D, Schambach A, Reimers K, Vogt P M and Chichkov B 2012 Skin tissue generation by laser cell printing *Biotechnol. Bioeng.* **109** 1855–63

- [170] Young D, Auyeung R C Y, Piqué A, Chrisey D B and Dlott D D 2002 Plume and jetting regimes in a laser based forward transfer process as observed by time-resolved optical microscopy *Appl Surf Sci* **197-198** 181–7
- [171] Duocastella M, Fernández-Pradas J M, Serra P and Morenza J L 2008 Jet formation in the laser forward transfer of liquids *Appl. Phys. A* **93** 453–6
- [172] Duocastella M, Colina M, Fernandez-Pradas J M, Serra P and Morenza J L 2007 Study of the laser-induced forward transfer of liquids for laser bioprinting *Appl Surf Sci* **253** 7855–9
- [173] Pearson A, Cox E, Blake J R and Otto S R 2004 Bubble interactions near a free surface *Engineering Analysis with Boundary Elements* **28** 295–313
- [174] Robinson P B, Blake J R, Kodama T, Shima A and Tomita Y 2001 Interaction of cavitation bubbles with a free surface *J. Appl. Phys.* **89** 8225–37
- [175] Colina M, Serra P, Fernández-Pradas J M, Sevilla L and Morenza J L 2005 DNA deposition through laser induced forward transfer *Biosens Bioelectron* **20** 1638–42
- [176] Souquet A 2011 *Etude des processus physiques mis en jeu lors de la microimpression d'éléments biologiques assistée par laser* (Bordeaux 1)
- [177] Feinaeugle M, Alloncle A P, Delaporte P, Sones C L and Eason R W 2012 Time-resolved shadowgraph imaging of femtosecond laser-induced forward transfer of solid materials *Applied Surface Science* **258** 8475–83
- [178] Yu H, Dlott D D and Kearney F R 2006 Time-Resolved Microscopy Analysis of Laser Photothermal Imaging Media *J. Imaging Sci. Technol.* **50** 401
- [179] Unger C, Gruene M, Koch L, Koch J and Chichkov B N 2011 Time-resolved imaging of hydrogel printing via laser-induced forward transfer *Appl. Phys. A* **103** 271–7
- [180] Brown M S, Kattamis N T and Arnold C B 2011 Time-resolved dynamics of laser-induced micro-jets from thin liquid films *Microfluid Nanofluid* **11** 199–207
- [181] Brown M S, Kattamis N T and Arnold C B 2010 Time-resolved study of polyimide absorption layers for blister-actuated laser-induced forward transfer *J. Appl. Phys.* **107** 083103
- [182] Barron J A, Wu P, Ladouceur H D and Ringeisen B R 2004 Biological laser printing: a novel technique for creating heterogeneous 3-dimensional cell patterns *Biomed Microdevices* **6** 139–47
- [183] Barron J, Ringeisen B and Wu P 2004b Biological laser printing via indirect photonbiomaterial interactions, US Patent, WO/2004/108878
- [184] Wang W, Huang Y, Grujicic M and Chrisey D B 2008 Study of Impact-Induced Mechanical Effects in Cell Direct Writing Using Smooth Particle Hydrodynamic Method *J. Manuf. Sci. Eng.* **130** 021012–10
- [185] Wang W, Li G and Huang Y 2009 Modeling of Bubble Expansion-Induced Cell

- [186] Catros S, Guillotin B, Bacáková M, Fricain J-C and Guillemot F 2011 Effect of laser energy, substrate film thickness and bioink viscosity on viability of endothelial cells printed by Laser-Assisted Bioprinting *Appl Surf Sci* **257** 5142–7
- [187] Landau L D and Lifshitz E M 1975 *The Electrodynamics of Continuum Medium* (Pergamon Press, Oxford)
- [188] Blake J R and Gibson D C 1981 Growth and Collapse of a Vapour Cavity Near a Free Surface *Journal of Fluid Mechanics Digital Archive* **111** 123–40
- [189] Longuet-Higgins M S 1983 Bubbles, Breaking Waves and Hyperbolic Jets at a Free Surface *Journal of Fluid Mechanics Digital Archive* **127** 103–21
- [190] Guillemot F, Souquet A, Catros S, Guillotin B, Lopez J, Faucon M, Pippenger B, Bareille R, Rémy M, Bellance S, Chabassier P, Fricain J C and Amédée J 2010 High-throughput laser printing of cells and biomaterials for tissue engineering *Acta Biomater* **6** 2494–500
- [191] Mézel C, Souquet A, Hallo L and Guillemot F 2010 Bioprinting by laser-induced forward transfer for tissue engineering applications: jet formation modeling *Biofabrication* **2** 014103
- [192] Lin Y and Huang Y 2011 Laser-assisted fabrication of highly viscous alginate microsphere *Journal of Applied Physics* **109** 083107
- [193] Duocastella M, Fernández-Pradas J M and P. S, J. L. Morenza 2010 Sessile droplet formation in the laser-induced forward transfer of liquids: A time-resolved imaging study *Thin Solid Films* **518** 5321–5
- [194] Guillemot F, Guillotin B, Fontaine A, Ali M, Catros S, Kériquel V, Fricain J-C, Rémy M, Bareille R and Amédée-Vilamitjana J 2011 Laser-Assisted Bioprinting to Deal with Tissue Complexity in Regenerative Medicine *MRS Bulletin* **36** 1015–9
- [195] Guillemot F, Souquet A, Catros S, Guillotin B, Lopez J, Faucon M, Pippenger B, Bareille R, Rémy M, Bellance S, Chabassier P, Fricain J C and Amédée J 2010 High-throughput laser printing of cells and biomaterials for tissue engineering *Acta Biomater* **6** 2494–500
- [196] Xiu-Mei L, Jie H, Jian L and Xiao-Wu N 2008 Growth and collapse of laser-induced bubbles in glycerol–water mixtures *Chinese Physics B* **17** 2574–9
- [197] Prosperetti A 1982 A generalization of the Rayleigh–Plesset equation of bubble dynamics *Physics of Fluids (1958-1988)* **25** 409–10
- [198] Mezel C, Hallo L, Souquet A, Bourgeade A, Breil J, Hebert D, Guillemot F and Saut O 2010 Toward a new nanoLIFT transfer process ed A Gamucci, A Giulietti and L Labate *AIP Conf. Proc.* **1209** 67–70
- [199] Brennen C E 1995 *Cavitation and Bubble Dynamics*



- [200] Patrascioiu A, Fernández-Pradas J M, Palla-Papavlu A, Morenza J L and Serra P 2014 Laser-generated liquid microjets: correlation between bubble dynamics and liquid ejection *Microfluid Nanofluid* **16** 55–63
- [201] Brujan E-A, Nahen K, Schmidt P and Vogel A 2001 Dynamics of laser-induced cavitation bubbles near an elastic boundary *Journal of Fluid Mechanics* **433** 251–81
- [202] Franc J P 2004 Fundamentals of Cavitation
- [203] Gruene M, Unger C, Koch L, Deiwick A and Chichkov B 2011 Dispensing pico to nanolitre of a natural hydrogel by laser-assisted bioprinting *Biomedical engineering online* **10** 19
- [204] Duchemin L 2008 Self-focusing of thin liquid jets *Proceedings of the Royal Society A: Mathematical, Physical and Engineering Science* **464** 197–206
- [205] Petkovsek R and Gregorcic P 2007 A laser probe measurement of cavitation bubble dynamics improved by shock wave detection and compared to shadow photography *Journal of Applied Physics* **102** 044909–044909–9
- [206] Yu P-W, Ceccio S L and Tryggvason G 1995 The collapse of a cavitation bubble in shear flows—A numerical study *Physics of Fluids (1994-present)* **7** 2608–16
- [207] Duchemin L, Popinet S, Josserand C and Zaleski S 2002 Jet formation in bubbles bursting at a free surface *Physics of Fluids (1994-present)* **14** 3000–8
- [208] Baxter J and Mitragotri S 2005 Jet-induced skin puncture and its impact on needle-free jet injections: Experimental studies and a predictive model *Journal of Controlled Release* **106** 361–73
- [209] Mitragotri S 2006 Current status and future prospects of needle-free liquid jet injectors *Nat Rev Drug Discov* **5** 543–8
- [210] Chen R C C, Yu Y T, Su K W, Chen J F and Chen Y F 2013 Exploration of water jet generated by Q-switched laser induced water breakdown with different depths beneath a flat free surface *Opt Express* **21** 445–53
- [211] Thoroddsen S T, Takehara K, Etoh T G and Ohl C-D 2009 Spray and microjets produced by focusing a laser pulse into a hemispherical drop *Physics of Fluids* **21** 112101
- [212] Chahine G L 1977 Interaction Between an Oscillating Bubble and a Free Surface *J. Fluids Eng.* **99** 709–16
- [213] Pain A, Goh B H T, Klaseboer E, Ohl S-W and Khoo B C 2012 Jets in quiescent bubbles caused by a nearby oscillating bubble *Journal of Applied Physics* **111** 054912
- [214] Duocastella M, Patrascioiu A, Fernández-Pradas J M, Morenza J L and Serra P 2010 Film-free laser forward printing of transparent and weakly absorbing liquids *Opt Express* **18** 21815–25
- [215] Obreschkow D, Kobel P, Dorsaz N, De Bosset A, Nicollier C and Farhat M 2006 Cavitation Bubble Dynamics inside Liquid Drops in Microgravity *Phys. Rev. Lett.* **97**

- [216] Zeff B W, Kleber B, Fineberg J and Lathrop D P 2000 Singularity dynamics in curvature collapse and jet eruption on a fluid surface *Nature* **403** 401–4
- [217] Worthington A M and Cole R S 1900 Impact with a Liquid Surface Studied by the Aid of Instantaneous Photography. Paper II *Phil. Trans. R. Soc. Lond. A* **194** 175–99
- [218] Thoroddsen S T and Shen A Q 2001 Granular jets *Physics of Fluids (1994-present)* **13** 4–6
- [219] Boulton-Stone J M and Blake J R 1993 Gas bubbles bursting at a free surface *Journal of Fluid Mechanics* **254** 437
- [220] Changxue X, Zhengyi Z, Jianzhong F, Yong H and Roger R M 2013 *Time-Resolved Study of Droplet Formation Process During Inkjetting of Alginate Solution* (conference proceedings of SFF 2013, Austin, TX, pp:253-259)
- [221] Colina M, Duocastella M, Fernández-Pradas J M, Serra P and Morenza J L 2006 Laser-induced forward transfer of liquids: Study of the droplet ejection process *J. Appl. Phys.* **99** 084909
- [222] Eggers J and Villermaux E 2008 Physics of liquid jets *Rep. Prog. Phys.* **71** 036601
- [223] Kuznetsov A I, Unger C, Koch J and Chichkov B N 2012 Laser-induced jet formation and droplet ejection from thin metal films *Appl. Phys. A* **106** 479–87
- [224] Dinca V, Farsari M, Kafetzopoulos D, Popescu A, Dinescu M and Fotakis C 2008 Patterning parameters for biomolecules microarrays constructed with nanosecond and femtosecond UV lasers *Thin Solid Films* **516** 6504–11
- [225] Duocastella M, Fernández-Pradas J M, Serra P and Morenza J L 2008 Laser-induced Forward Transfer of Liquids for Miniaturized Biosensors Preparation *Journal of Laser Micro/Nanoengineering* **3** 1–4
- [226] Dinu C Z, Dinca V, Howard J and Chrisey D B 2007 Printing technologies for fabrication of bioactive and regular microarrays of streptavidin *Applied Surface Science* **253** 8119–24
- [227] Duocastella M, Fernández-Pradas J M, Morenza J L and Serra P 2011 Droplet printing through bubble contact in the laser forward transfer of liquids *Appl Surf Sci* **257** 2825–9
- [228] Lindinger A, Hagen J, Socaciu L D, Bernhardt T M, Wöste L, Duft D and Leisner T 2004 Time-Resolved Explosion Dynamics of H<sub>2</sub>O Droplets Induced by Femtosecond Laser Pulses *Appl. Opt.* **43** 5263–9
- [229] Serra P, Duocastella M, Fernandez-Pradas J M and Morenza J L 2009 Liquids microprinting through laser-induced forward transfer *Appl Surf Sci* **255**
- [230] Brown M S, Brasz C F, Ventikos Y and Arnold C B 2012 Impulsively actuated jets from thin liquid films for high-resolution printing applications *Journal of Fluid Mechanics* **709** 341–70

- [231] Eggers J 1997 Nonlinear dynamics and breakup of free-surface flows *Rev. Mod. Phys.* **69** 865–930
- [232] Gruene M, Deiwick A, Koch L, Schlie S, Unger C, Hofmann N, Bernemann I, Glasmacher B and Chichkov B 2010 Laser Printing of Stem Cells for Biofabrication of Scaffold-Free Autologous Grafts *Tissue Eng Part C* **17** 79–87
- [233] Raof N A, Schiele N R, Xie Y, Chrisey D B and Corr D T 2011 The maintenance of pluripotency following laser direct-write of mouse embryonic stem cells *Biomaterials* **32** 1802–8
- [234] Othon C M, Wu X, Anders J J and Ringeisen B R 2008 Single-cell printing to form three-dimensional lines of olfactory ensheathing cells *Biomedical Materials* **3** 034101
- [235] Han T and Yoh J J 2010 A laser based reusable microjet injector for transdermal drug delivery *Journal of Applied Physics* **107** 103110
- [236] Menezes V, Kumar S and Takayama K 2009 Shock wave driven liquid microjets for drug delivery *Journal of Applied Physics* **106** 086102
- [237] Chrisey D B 2002 Direct-write Technologies for Rapid Prototyping Applications
- [238] Wu P K, Ringeisen B R, Krizman D B, Frondoza C G, Brooks M, Bubb D M, Auyeung R C Y, Piqué A, Spargo B, McGill R A and Chrisey D B 2003 Laser transfer of biomaterials: Matrix-assisted pulsed laser evaporation (MAPLE) and MAPLE Direct Write *Review of Scientific Instruments* **74** 2546–57
- [239] Dinca V, Ranella A, Farsari M, Kafetzopoulos D, Dinescu M, Popescu A and Fotakis C 2008 Quantification of the activity of biomolecules in microarrays obtained by direct laser transfer *Biomed Microdevices* **10** 719–25
- [240] Dinca V, Kasotakis E, Mourka A, Ranella A, Farsari M, Mitraki A and Fotakis C 2008 Fabrication of amyloid peptide micro-arrays using laser-induced forward transfer and avidin-biotin mediated assembly *physica status solidi (c)* **5** 3576–9
- [241] Hopp B, Smausz T, Kresz N, Barna N, Bor Z, Kolozsvári L, Chrisey D B, Szabó A and Nógrádi A 2005 Survival and proliferative ability of various living cell types after laser-induced forward transfer *Tissue Eng.* **11** 1817–23
- [242] Ringeisen B R, Chrisey D B, Piqué A, Young H D, Jones-Meehan J, Modi R, Bucaro M and Spargo B J 2002 Generation of mesoscopic patterns of viable *Escherichia coli* by ambient laser transfer *Biomaterials* **23** 161–6
- [243] Zergioti I, Karaïskou A, Papazoglou D G, Fotakis C, Kapsetaki M and Kafetzopoulos D 2005 Femtosecond laser microprinting of biomaterials *Applied Physics Letters* **86** 163902
- [244] Boutopoulos C, Andreakou P, Kafetzopoulos D, Chatzandroulis S and Zergioti I 2008 Direct laser printing of biotin microarrays on low temperature oxide on Si substrates *physica status solidi (a)* **205** 2505–8
- [245] Chen C Y, Barron J A and Ringeisen B R 2006 Cell patterning without chemical

surface modification: Cell–cell interactions between printed bovine aortic endothelial cells (BAEC) on a homogeneous cell-adherent hydrogel *Appl Surf Sci* **252** 8641–5

- [246] Schiele N R, Koppes R A, Corr D T, Ellison K S, Thompson D M, Ligon L A, Lippert T K M and Chrisey D B 2009 Laser direct writing of combinatorial libraries of idealized cellular constructs: Biomedical applications *Appl Surf Sci* **255** 5444–7
- [247] Wu P ., Ringeisen B ., Callahan J, Brooks M, Bubbs D ., Wu H ., Piqué A, Spargo B, McGill R . and Chrisey D . 2001 The deposition, structure, pattern deposition, and activity of biomaterial thin-films by matrix-assisted pulsed-laser evaporation (MAPLE) and MAPLE direct write *Thin Solid Films* **398–399** 607–14
- [248] Barron J A, Rosen R, Jones-Meehan J, Spargo B J, Belkin S and Ringeisen B R 2004 Biological laser printing of genetically modified *Escherichia coli* for biosensor applications *Biosens Bioelectron* **20** 246–52
- [249] Hopp B, Smausz T, Antal Z, Kresz N, Bor Z and Chrisey D 2004 Absorbing film assisted laser induced forward transfer of fungi (*Trichoderma conidia*) *Journal of Applied Physics* **96** 3478–81
- [250] Serra P, Colina M, Fernández-Pradas J M, Sevilla L and Morenza J L 2004 Preparation of functional DNA microarrays through laser-induced forward transfer *Applied Physics Letters* **85** 1639–41
- [251] Chrisey D B, Piqué A, McGill R A, Horwitz J S, Ringeisen B R, Bubbs D M and Wu P K 2003 Laser deposition of polymer and biomaterial films *Chem. Rev.* **103** 553–76
- [252] Barron J A, Ringeisen B R, Kim H, Spargo B J and Chrisey D B 2004 Application of laser printing to mammalian cells *Thin Solid Films* **453–454** 383–7
- [253] Barron J A, Spargo B J and Ringeisen B R 2004 Biological laser printing of three dimensional cellular structures *Appl Phys A* **79** 1027–30
- [254] Lin Y, Huang G, Huang Y, Tzeng T-R J and Chrisey D 2010 Effect of laser fluence in laser assisted direct writing of human colon cancer cell *Rapid Prototyp J* **16** 202 – 208
- [255] Wu P K and Ringeisen B R 2010 Development of human umbilical vein endothelial cell (HUVEC) and human umbilical vein smooth muscle cell (HUVSMC) branch/stem structures on hydrogel layers via biological laser printing (BioLP) *Biofabrication* **2** 014111
- [256] Dinca V, Ranella A, Popescu A, Dinescu M, Farsari M and Fotakis C 2007 Parameters optimization for biological molecules patterning using 248-nm ultrafast lasers *Applied Surface Science* **254** 1164–8
- [257] Dinca V, Kasotakis E, Catherine J, Mourka A, Mitraki A, Popescu A, Dinescu M, Farsari M and Fotakis C 2007 Development of peptide-based patterns by laser transfer *Applied Surface Science* **254** 1160–3
- [258] Duocastella M, Fernández-Pradas J M, Domínguez J, Serra P and Morenza J L 2008 Printing biological solutions through laser-induced forward transfer *Appl. Phys. A* **93** 941–5

- [259] Doraiswamy A, Narayan R J, Lippert T, Urech L, Wokaun A, Nagel M, Hopp B, Dinescu M, Modi R, Auyeung R C Y and Chrisey D B 2006 Excimer laser forward transfer of mammalian cells using a novel triazene absorbing layer *Appl Surf Sci* **252** 4743–7
- [260] Serra P, Fernández-Pradas J M, Berthet F X, Colina M, Elvira J and Morenza J L 2004 Laser direct writing of biomolecule microarrays *Appl Phys A* **79** 949–52
- [261] Lin Y, Huang Y, Wang G, Tzeng T-R J and Chrisey D B 2009 Effect of laser fluence on yeast cell viability in laser-assisted cell transfer *J. Appl. Phys.* **106** 043106

## APPENDIX A

Already published applications of LAB for biological molecules or cells are listed in Table (No. A.1) in alphabetic order.

Name of Cell/Biomolecule	Laser Source	Substrates	Absorption Layer	Reference
Anti-BSA	ArF(193nm, 20ns)	Polystyrene plate, quartz plate, Digene silanated slide	Gelatin	[237,238]
Alkaline phosphate	KrF (248nm, 2.5ns)	Nitrocellulose coated glass slide	Gold (100nm), titanium (75), titanium oxide (85nm)	[106]
Avidin	KrF (248nm, 15ns-500fs)	Glass slides and nitrocellulose coated glass slides	Gold (10nm)	[239]
Amyloid peptide	KrF (248nm, 15ns)	ORMOCER coated glass slides	Gold (10nm)	[240]
Astroglial cells	KrF (248nm, 30ns)	Glass plate coated with a thin wet gelatin layer	Silver (100nm)	[241]
Bovine serum albumin (BSA)	ArF (193nm, 20ns)	Nitrocellulose coated glass slide	----	[242]
	Nd:YAG (266nm, 3-5ns), KrF (248nm, 2.5ns)	Matrigel coated slides, sinilated glass slides	Gold (35nm), titanium (75nm), titanium oxide (85nm)	[182]
	KrF (248nm, 2.5ns)	Nitrocellulose coated glass slide	Gold (100nm), titanium (75nm), titanium oxide (85nm)	[106]
	KrF (248nm, 500ns)	glass slide		[243]
Biotin	Nd:YAG (266nm, 4ns)	Si and Low temperature oxide on Si (LTO/Si)	Chromium (40nm)	[244]
	KrF (248nm, 15ns-500fs)	glass slide and Nitrocellulose coated glass slide	Gold (10nm)	[239]
Bovine aortic endothelial cells	KrF (248nm, 2.5ns)	Matrigel coated glass slide, cell media coated slide	Metal or metallic oxide (10-100nm)	[245]
Bovine embryonic stem cells	Nd:YVO <sub>4</sub> (355nm, 15ns)	Matrigel coated Petri dish	Polyimide (4μm)	[130]
Bovine pulmonary artery endothelial cells	ArF (193nm, 20ns)	Matrigel coated Petri dish		[246]
Chinese hamster ovaries	ArF (193nm, 20ns)	Quartz plate		[247]

Name of Cell/Biomolecule	Laser Source	Substrates	Absorption Layer	Reference
Endothelial cells Ea.hy926	Nd:YAG (1064nm, 30ns)	Matrige <sup>ITM</sup>	Gold (50 nm)	[186]
Enzyme horseradish peroxidase	KrF (248nm, 15ns-500fs)	Nitrocellulose coated glass slide	Gold (10nm)	[224]
Escherichia coli	ArF (193nm, 20ns)	Si glass slides, nutrient agar culture plates		[242]
	KrF (248nm, 2.5ns)	Agar-coated glass slide, solid LB Petri dish, microtiter plate	Gold (35nm), titanium (75nm)	[248]
Fungus (trichoerma conidia)	KrF (248nm, 30ns)	Cell media coated plate	Silver (50nm)	[249]
Glutathione s-transferase (GST)	KrF (248nm, 500fs)	Glass slides		[243]
Human cDNA	Nd:YAG (355nm, 10ns)	Poly-L-lysine coated slide	Titanium (50nm)	[175,250]
Human osteosarcoma cells	ArF (193nm, 20ns)	Ploystyrene plate, digene silanated slide	Gelatin	[251]
	ArF (193nm, 20ns)	Matrigel coated slides		[252]
	Nd:YAG (266nm, 5ns)	Matrigel coated slides	Titanium, titanium oxide (75-85)	[253]
	Nd:YAG (266nm, 3-5ns), KrF (248nm, 2.5ns)	Matrigel coated slides, silinated glass slides	Gold (35nm), titanium (75 nm), titanium oxide (85 nm)	[182]
	KrF (248nm, 2.5ns)	Matrigel coated slides	Gold (35nm), titanium (75 nm)	[140]
Human dermal fibroblasts	ArF (193nm, 20ns)	Matrigel coated petri dish		[246]
Human breast cancer cell	ArF (193nm, 20ns)	Matrigel coated petri dish		[246]
Human endothelial cells	Nd:YAG (1064nm, 30ns)	Quartz disc	Gold (20-30)	[195]
human colon cancer cells (HT-29)	193nm, 12nm			[254]
human osteoprogenitor cells	$\lambda=1064$ nm, 30 ns	quartz slide	Titanium (60 nm)	[167]
Human umbilical vein endothelial cell (HUVEC) and human umbilical vein smooth muscle cell (HUVSMC)	266nm, 5ns		Titanium, Gold	[255]
Human umbilical vein endothelial cell line Eahy926	$\lambda=1064$ nm, 30 ns	quartz slide	Titanium (50 nm)	[122]

Name of Cell/Biomolecule	Laser Source	Substrates	Absorption Layer	Reference
Lambda bacteriophage DNA	KrF (248nm, 500fs)	Glass slides		[243]
Mesenchymal stem cells (MSCs)	1064nm, 10ns		Gold	[232]
Mouse myoblasts	ArF (193nm, 20ns)	Matrigel coated petri dish		[246]
Polyphenol oxidase (PPO)	ArF (193nm, 20ns)	Pt microelectrode		[247]
	ArF (193nm, 20ns)	Polystyrene plate, quartz plate, digene silanated glass plate	Gelatin	[238,251]
Prostate tissue	ArF (193nm, 20ns)	Polystyrene plate, quartz plate, digene silanated glass plate	Gelatin	[238,251]
Photobiotin	KrF (248nm, 15ns-500fs)	Glass slides, nitrocellulose coated glass slides, agarose and ORMOCER treated glass slides	Gold (10nm)	[240,256]
Peptides (from the adenovirus fibre)	KrF (248nm, 15ns)	Gold coated glass slides	Gold (10nm)	[257]
Pig lens epithelial cells	KrF (248nm, 30ns)	Glass plates coated with a thin wet gelatin layer	Silver (100nm)	[137]
Rabbit antibody immunoglobulin G (IgG)	Nd:YAG (355-nm 10-ns)	poly-Llysine-coated glass slide	titanium film around 60-nm thick	[258]
Rabbit carcinoma cell line B16	$\lambda=1064$ nm, 30 ns	quartz slide	Titanium (50 nm)	[122]
Rat cardiac cells	ArF (193nm, 20ns)	Matrigel coated slides		[251] [252]
Rat Schwann cells	KrF (248nm, 30ns)	Glass plates coated with a thin wet gelatin layer	Silver (100nm)	[137]
Rat neuroblasts cells	ArF (193nm, 10ns)	Basement membrane (Matrigel) coated slides		[259]
Rat neural stem cells	ArF (193nm, 20ns)	Matrigel coated petri dish		[246]
Rat olfactory ensheathing cells	Nd:YAG (266nm, 5ns)	Cell culture chamber coated with poly(l-lysine) and filled with medium, Matrigel coated slides	Titanium, titanium oxide (30-40nm)	[234]
Skin cells and human stem cells.	1064 nm, 8ns		gold	[138]
Streptavidin	ArF (193nm, 30ns)	Glass slides		[226]
Treponema pallidum	Nd:YAG (355nm,	Nylon-coated glass	Titanium (60nm)	[260]



Name of Cell/Biomolecule	Laser Source	Substrates	Absorption Layer	Reference
17kDa antigen	10ns)	slide		
Tintin	KrF (248nm, 15ns-500fs)	Glass slides, nitrocellulose coated glass slides	Gold (10nm)	[239]
	KrF (248nm, 15ns-500fs)	Nitrocellulose coated glass slides	Gold (10nm)	[224]
Yeast cells Saccharomyces cerevisiae	ArF (193 nm, 12 ns)	Quartz glass		[261]

## APPENDIX B

### ALGINATE

Alginates are hydocolloids, water-soluble biopolymers extracted from brown seaweeds (Phaeophyceae, mainly *Laminaria*). It has remarkable properties like gelling, film-making, thickening and stabilizing characteristics. Such attributes lead to variety of applications for instance as gelling agent in the food industry.

#### Structural Unit

Alginic acid is a linear copolymer with homopolymeric blocks of (1-4)-linked  $\beta$ -D-mannuronate (M) and its C-5 epimer  $\alpha$ -L-guluronate (G) residues (Fig. A1), respectively, covalently linked together in different sequences or blocks.

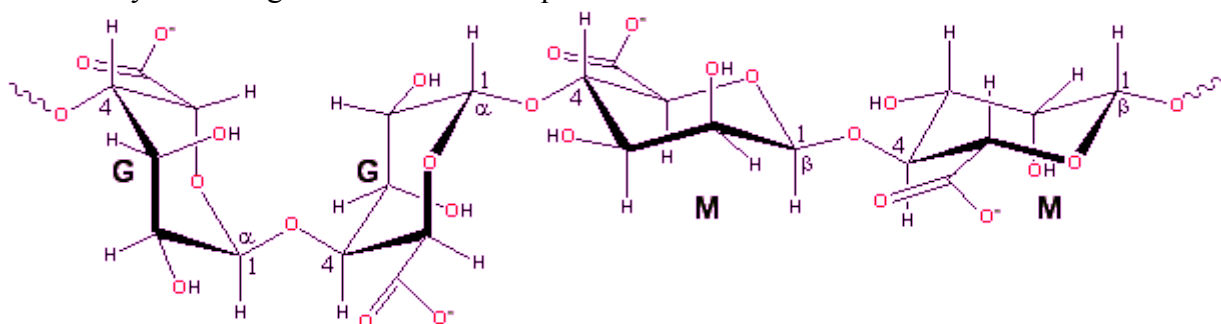


Figure A.1: Structural Unit of alginic acid

#### Molecular Structure

Alginates consist of blocks (Fig. A2) of similar and strictly alternating residues (that is, **MMMMMM**, **GGGGGG** and **GMGMGMGM**). G blocks provide gel-forming capacity, MM and MG units provide flexibility to the uronic acid chains, with flexibility increasing in the order  $GG < MM < MG$ . The proportion, distribution and length of these blocks determine the chemical and physical properties of the alginate molecules. The chemical composition of alginate varies according to seaweed species and structure. Alginates may be prepared with a wide range of average molecular weights (50 -100000 residues) to suit the application.

The viscosity of an alginate solution depends on the alginate concentration and length of the alginate molecules, or the number of monomer units in the chains (average molecular weight) with longer chains resulting to higher viscosities at similar concentrations. Aqueous solutions of alginate have shear-thinning characteristics, i.e. viscosity decreases with increasing shear rate. This property is known as pseudo-plasticity, or non-Newtonian flow. Temperature adversely influences the viscosity.

Alginates are refined from brown seaweeds. A wide variety of brown seaweeds of the phylum *Phaeophyceae* are harvested and converted into the raw material commonly known as

**sodium alginate.** **Sodium alginate** has a wide use across a wide variety of industries including food, textile printing and pharmaceutical. Dental impression material utilizes alginate as its means of gelling. Alginate is both food and skin safe. The chemical compound **sodium alginate** is the sodium salt of alginic acid. Its empirical formula is  $\text{NaC}_6\text{H}_7\text{O}_6$ . Sodium alginate is a gum, extracted from the cell walls of brown algae.

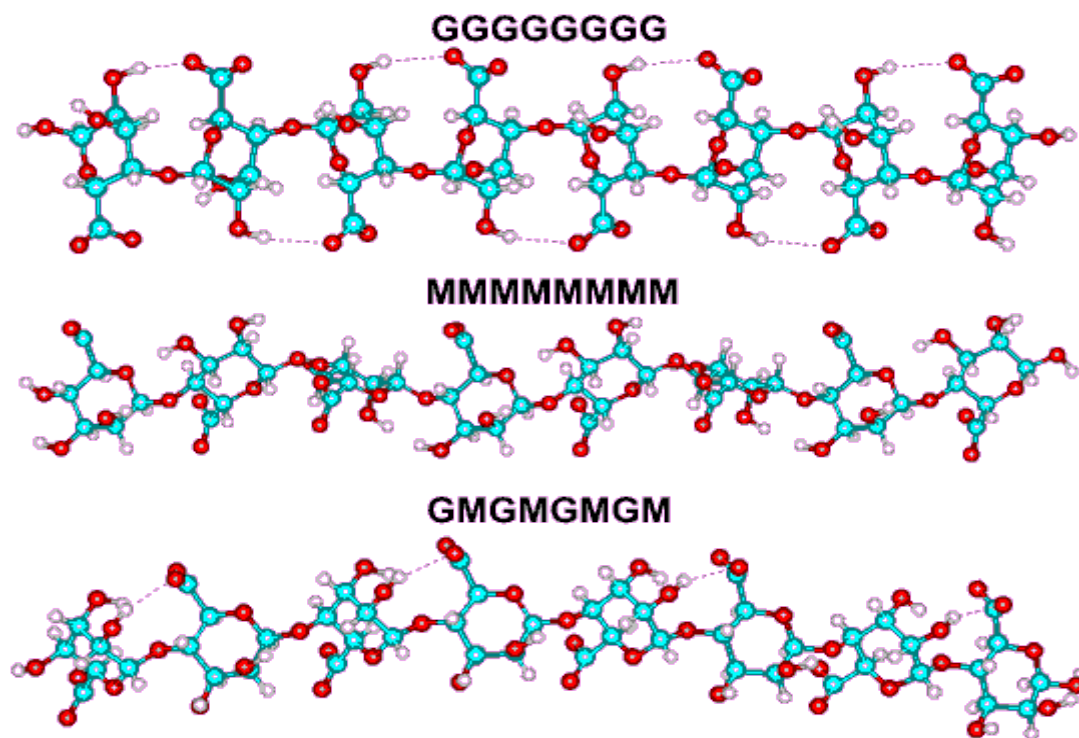


Figure A.2: Molecular structures of alginic acid

## APPENDIX C

### PROCESS ASTREE

ASTREE software (Fig. B1) for transfer station, developed by Novalase SA, can be used to create any pattern by selecting different parameters of choice.

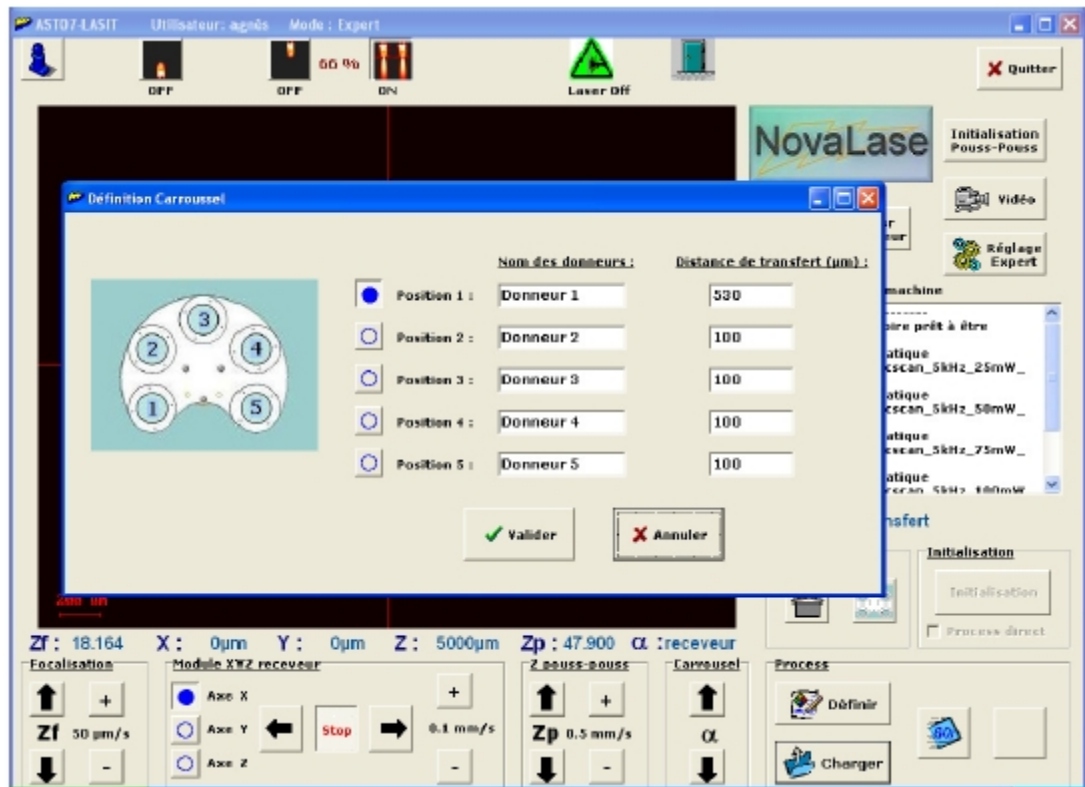


Figure B.1: Choice (of) donor (s) and printing distance (s)

During the creation of the process (Fig. B.2), printing parameters are fixed, namely:

- The scanning speed of scanners (up to 2000mm / s)
- The aperture (3 to 18 mm),
- The expander (1x to 3x)
- The defocus-if necessary
- The frequency of the laser,
- The power of the laser.

Once these parameters have entered, pattern is defined from five options:

- Arcs and circles
- Punch
- Right Segment
- Rectangle
- Image Bitmap

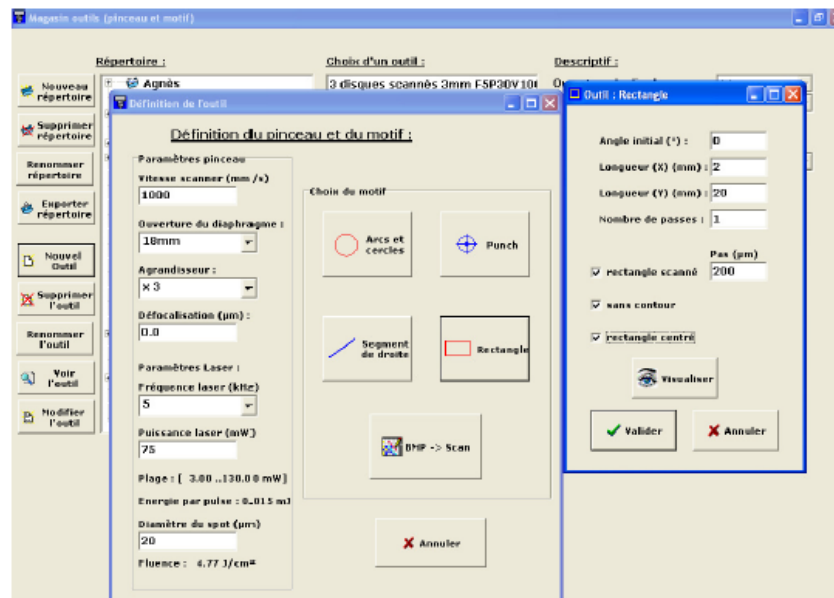


Figure B.2: Definition of a rectangle tool

Later, trajectory of the process is defined (fixed plate or sequential path) according to donor and receiver positions (Fig. B.3). By repeating the selection (or creating) a programmed parameters, a process is created. The Figure B.4 (a) shows the creation of a rectangle 2mm x 20mm and Figure B.4 (b) the process created by repeating the triangle for 5 times.

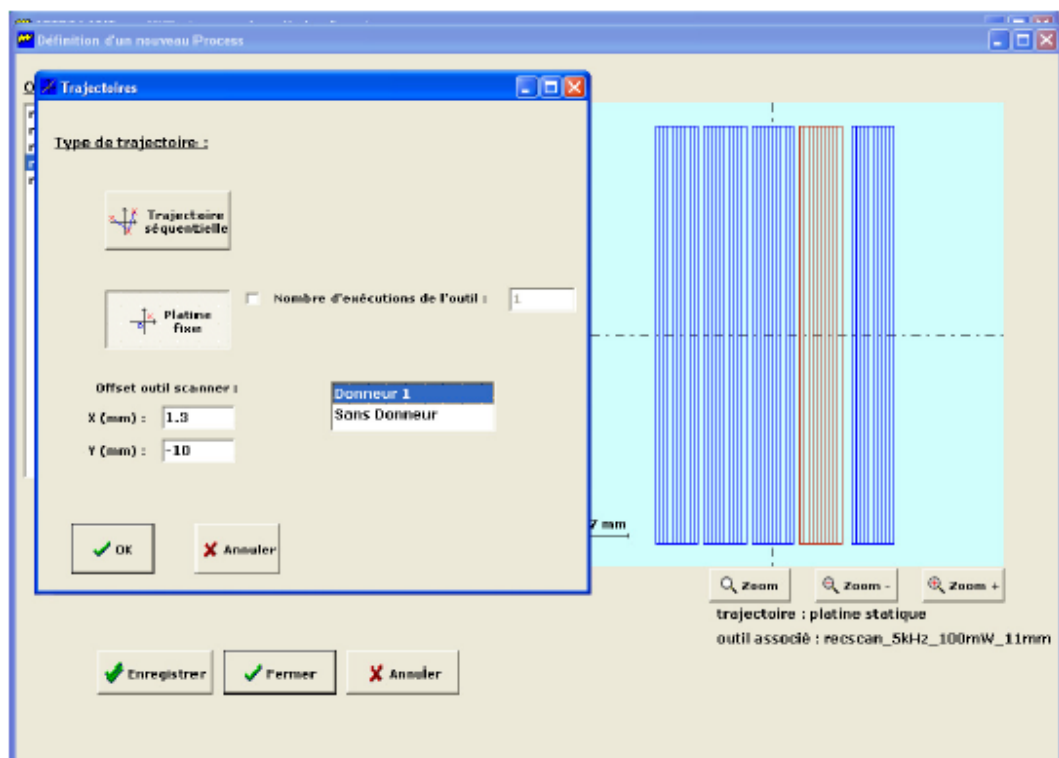
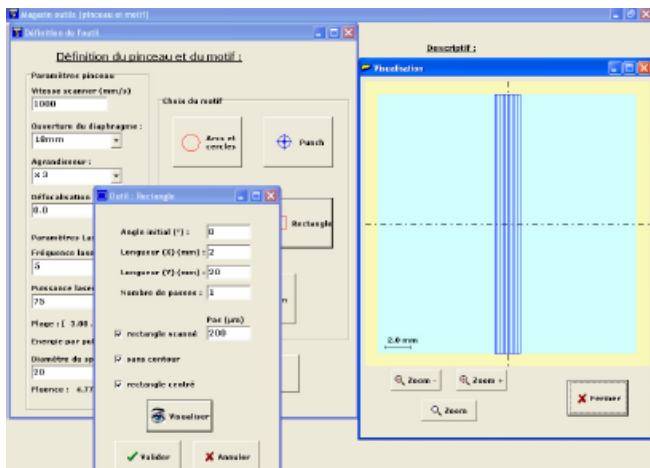
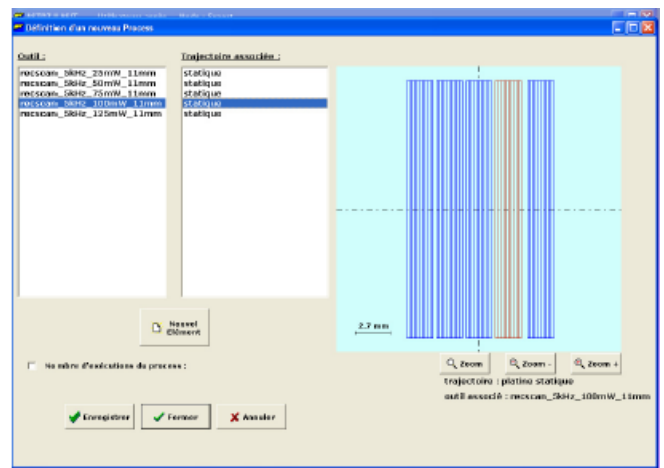


Figure B.3:Definition of the trajectory of a pattern



(a) Creation of a rectangle



(b) Process for five rectangles

Figure B.4: Creating a printing process with ASTREE



## APPENDIX D

### PROCEDURE ImageJ

ImageJ software is a processing and analysis written in Java images. Image processing such as the display allows the adjustment and the histogram of the gray levels, the illumination correction, edge detection etc. Image analysis allows to count particles, evaluate their aspect ratios to measure various quantities (distances, areas) and extract the coordinates of contours.

To determine the diameter of the drops from an image, five steps are required:

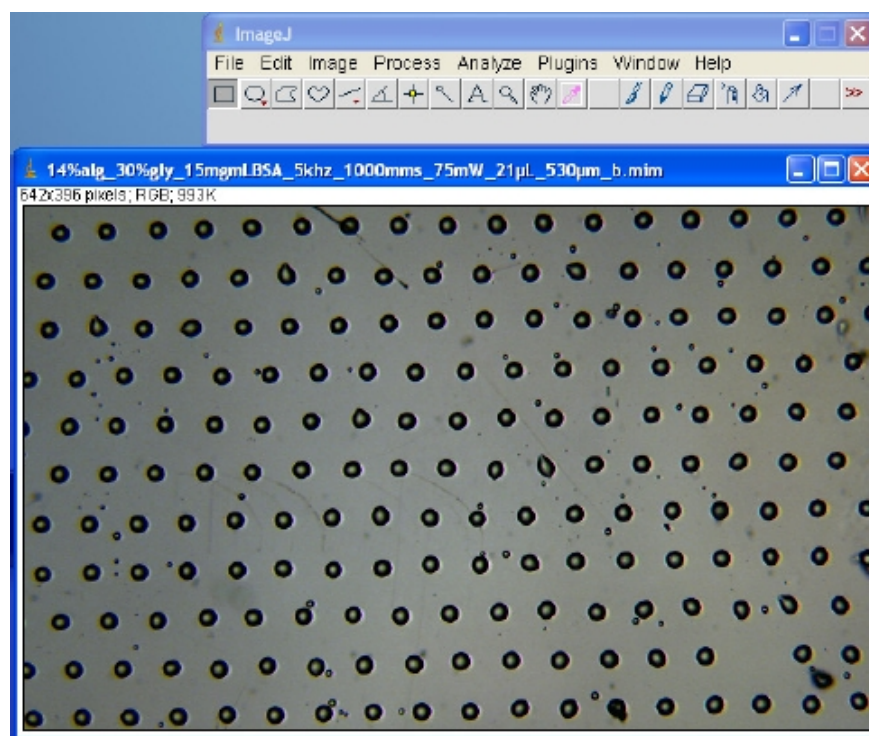
1. Set the scale,
2. Convert the image to 8-bit,
3. Convert image to binary
4. Detect edges,
5. Analyze the particles to count and measure their diameters.

An example of a macro used to determine the diameter of the droplets:

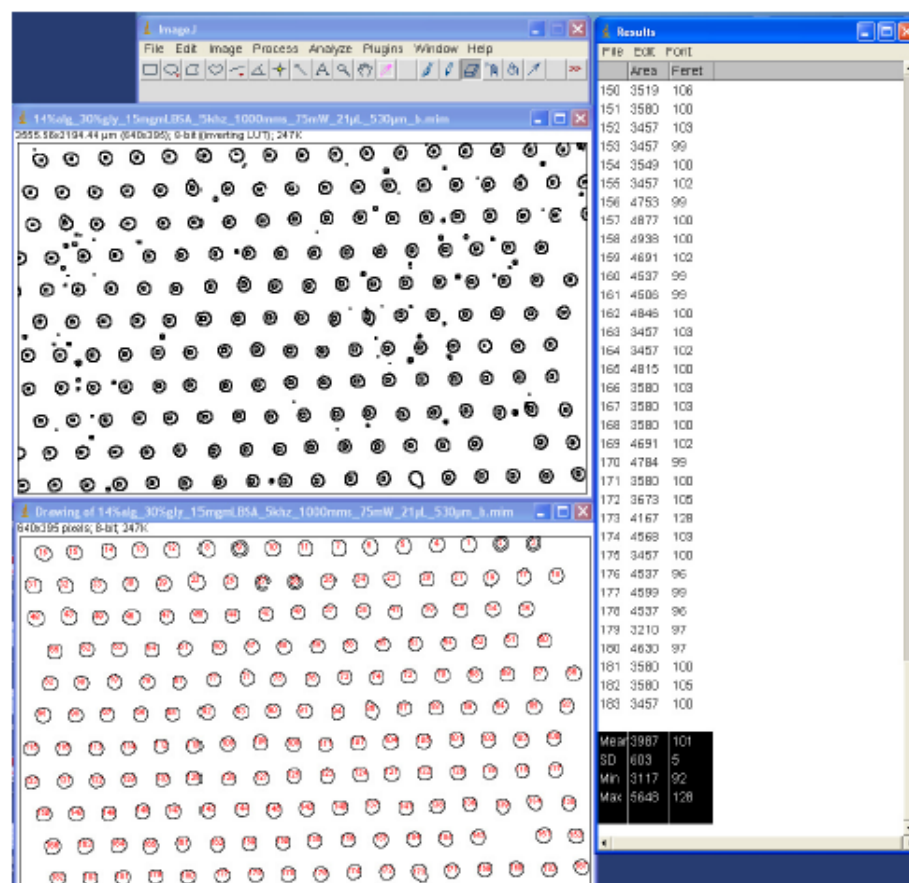
```
run("8-bit");  
run("Make Binary");  
run("Find Edges");  
run("Set Scale...", "distance=36 known=200 pixel=1 unit=m");  
run("Analyze Particles...", "size=3000-15000 circularity=0.00-1.00  
show=Outlines display clear");
```

The [figure C.1 \(a\)](#) shows an original image of drops transferred and Figure C.1 (b) the resultant image after treatment by the ImageJ macro.





(a) Original Image



(b) After treatment for measurements with ImageJ  
Figure C.1-ImageJ

## APPENDIX E

### High Speed Jets in Jetting Regime

This work was done in collaboration with Joy TELLOUCK and Antoine Robinet PERRIN in the frame work of their master training. Figure E.1 shows jet velocity versus time for 30 microns thick layer of riboflavin with increasing energies ranging from 30 $\mu$ J to 69.2 $\mu$ J. The velocity increases rapidly till 2 $\mu$ s before reaching the maximum for a given energy and finally it decreases. Growth phase of the bubble is dominant till 2 $\mu$ s later jetting starts. The speeds are ranging from 60 to 200m/s.

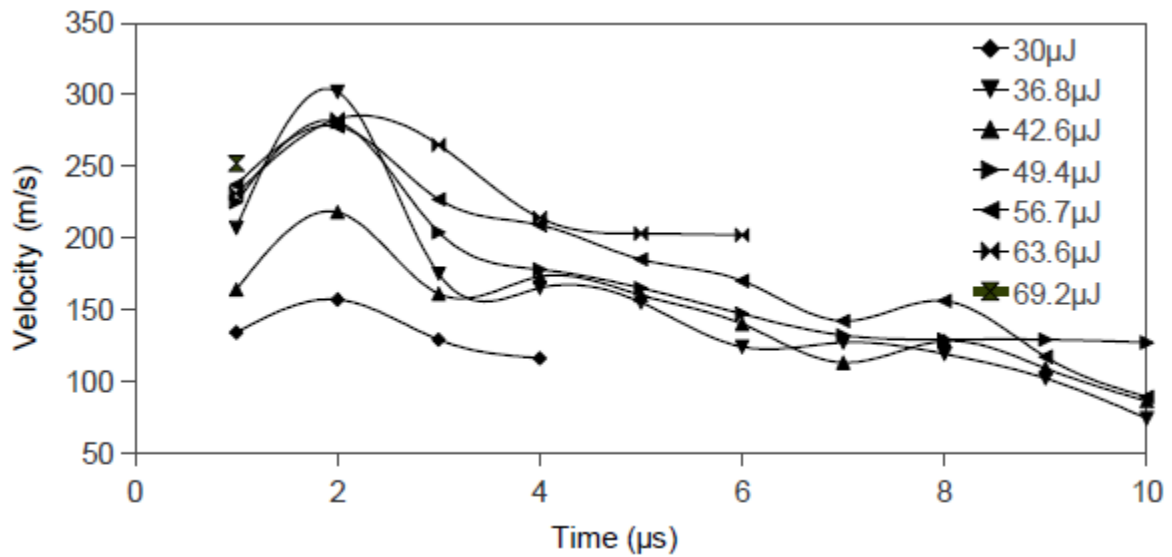


Figure E.1: Jet velocity as function of the time

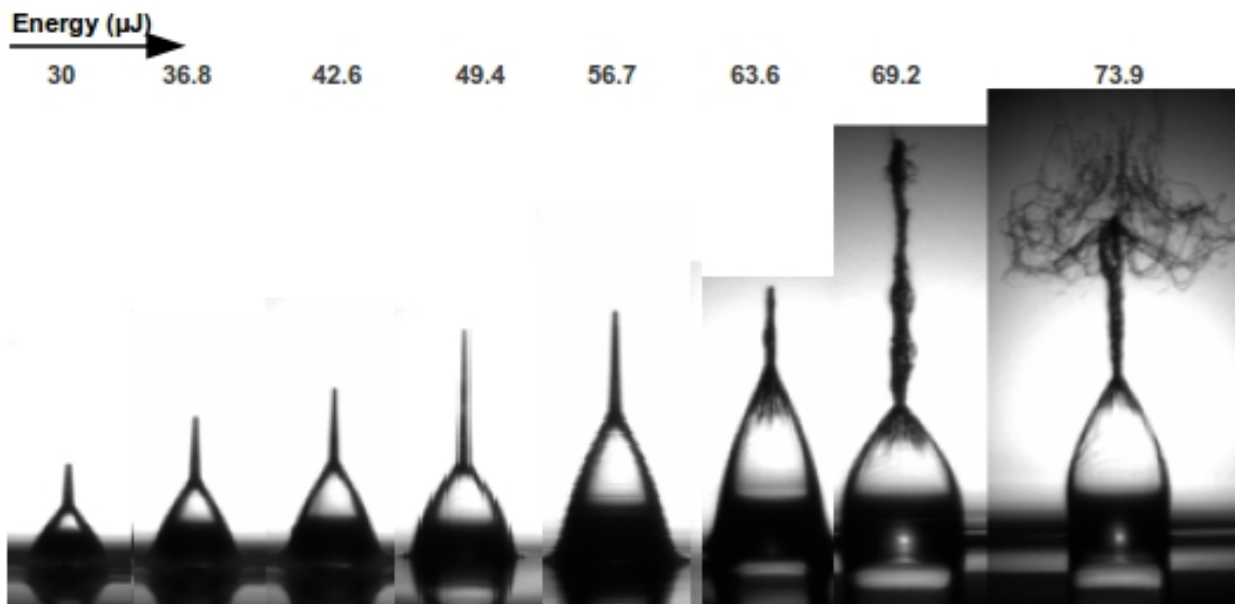


Figure E.2: TRI of the jets from 40 $\mu$ m thick riboflavin

Temporal profiles of the jet (Fig. E.2) produced from 40 $\mu$ m thickness with different

energies at 7 $\mu$ s show that jet became turbulent with increasing energy. Jet speed is plotted (Fig. E.3) against energy to determine relation between the jet speed and the energy at 7 $\mu$ s for different thicknesses of bioink i.e. 20, 30, 40 and 50 microns. Speed increases with laser energy for a given thickness. Jet speed is much higher for a thickness of 20 micron than one of 50 microns, for a given energy.

Jet velocity profile (Fig. E.3) for 40 $\mu$ m provides an upward trend where plume regime is observed with 73.9 $\mu$ J. Most of the jets have turbulence. For this reason we made other manipulations with additional experiments with 1/6 (Fig. E.4) and 1/3 times diluted solutions of riboflavin (Fig. E.5), where turbulence is more prominent even with lower energies. The jets produced with 1/3 times diluted solution present a less turbulent profile than that with the solution diluted to 1/6. As shown in figures (Fig. E.4-Fig. E.7), most of the jets are in a turbulent regime. Therefore we used pure riboflavin for further analysis of jetting dynamics to study penetration power of high-speed jets.

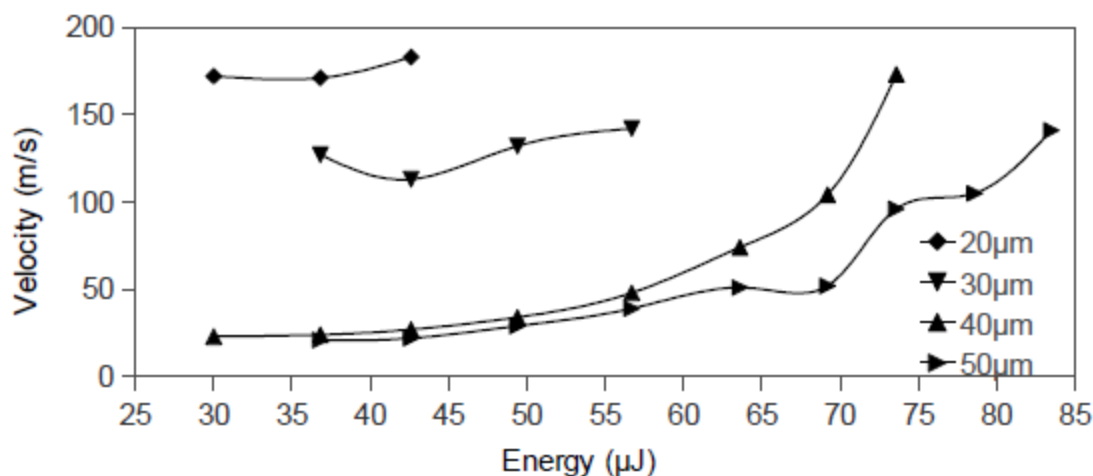


Figure E.3: Jet speed versus energy for different thicknesses

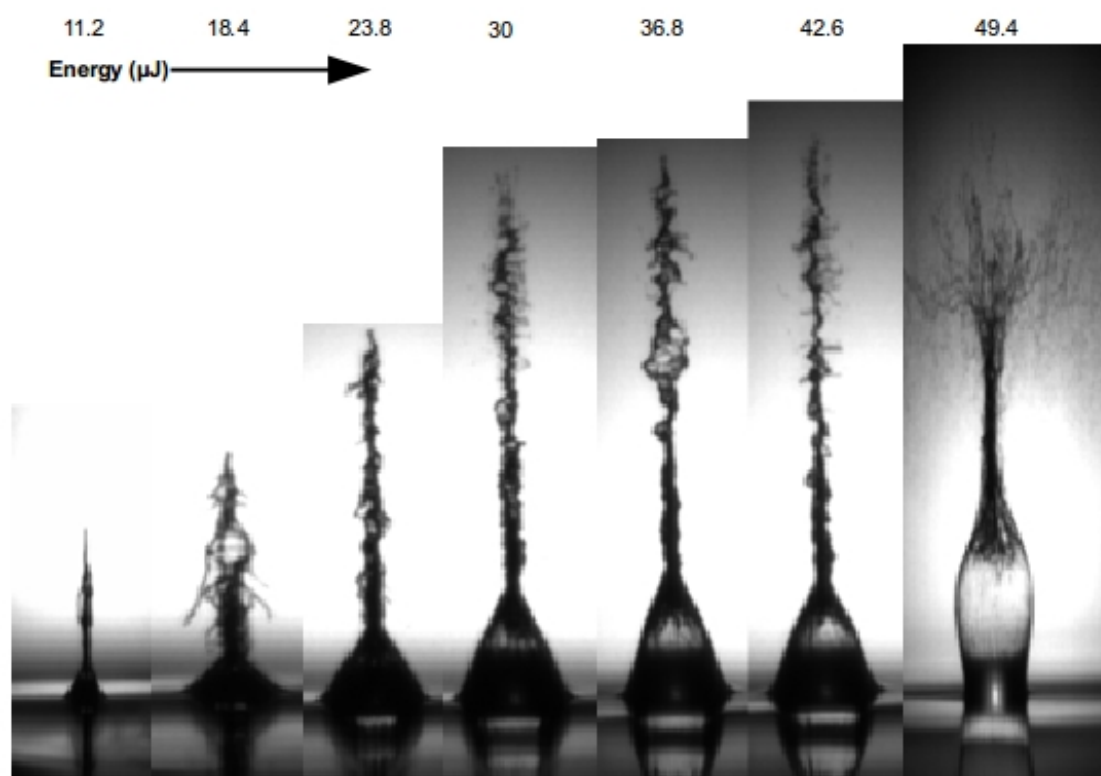


Figure E.4: TRI of jets at  $7\mu\text{s}$  for a  $40\mu\text{m}$  thickness of riboflavin solution diluted to  $1/6$

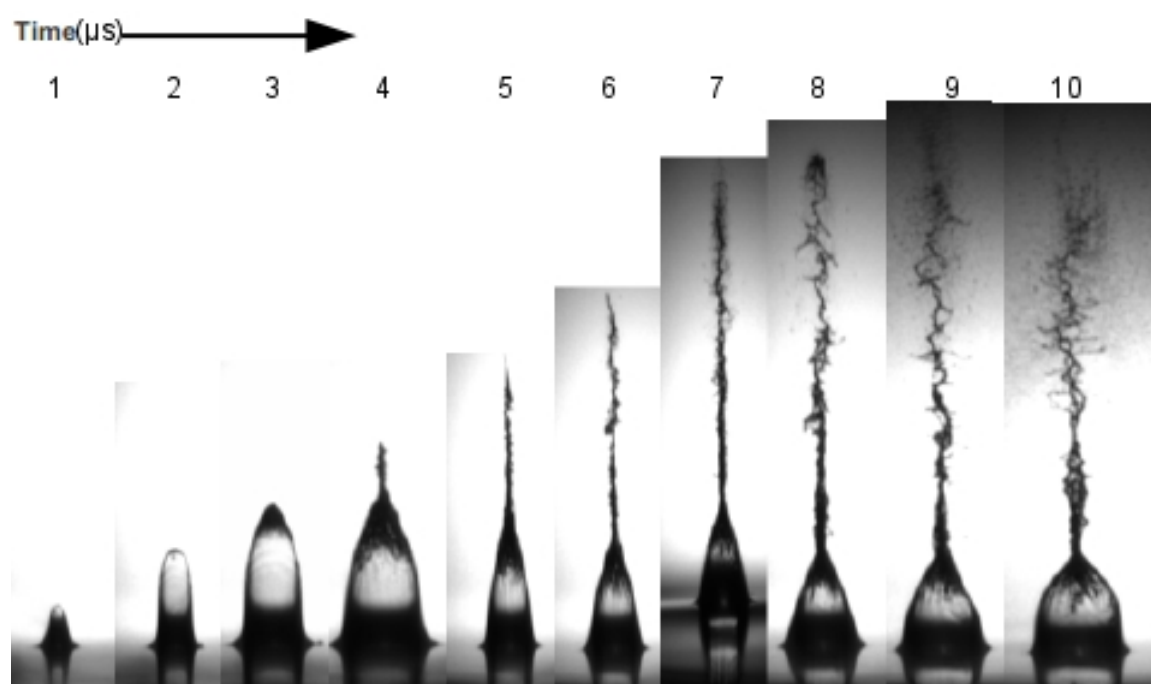


Figure E.5: TRI of the jet at  $36.8\mu\text{J}$  for a thickness of  $40\mu\text{m}$  of riboflavin solution diluted to  $1/3$

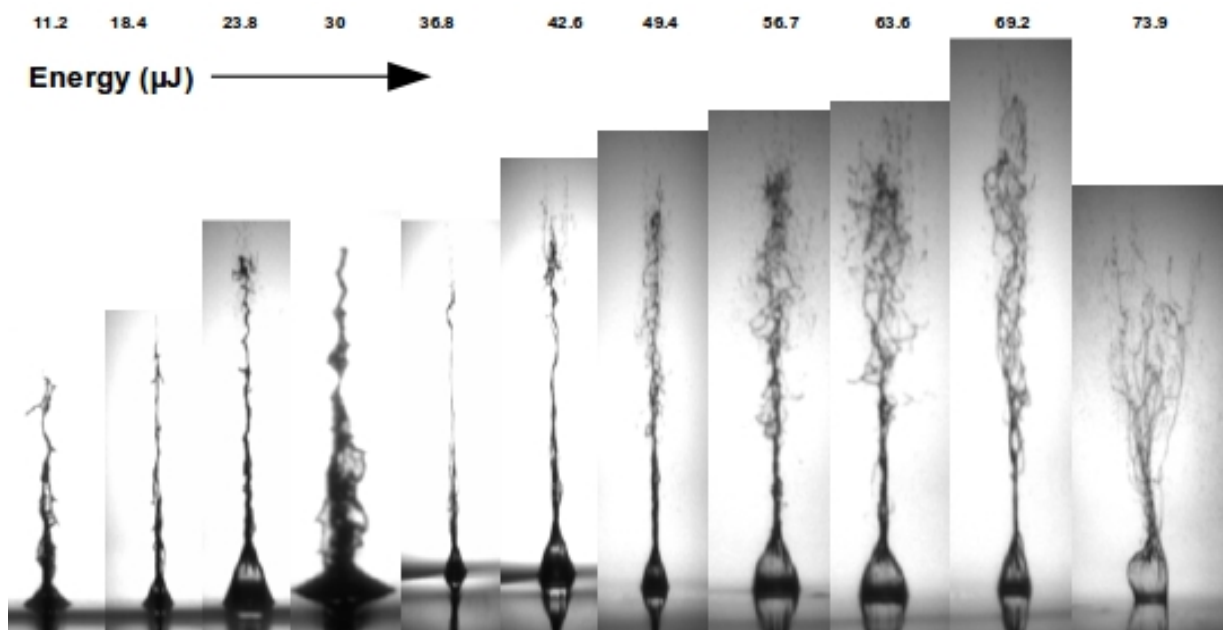


Figure E.6: Temporal images of the jet at 7 $\mu$ s from the solution diluted to 1/3 for a thickness of 40 $\mu$ m

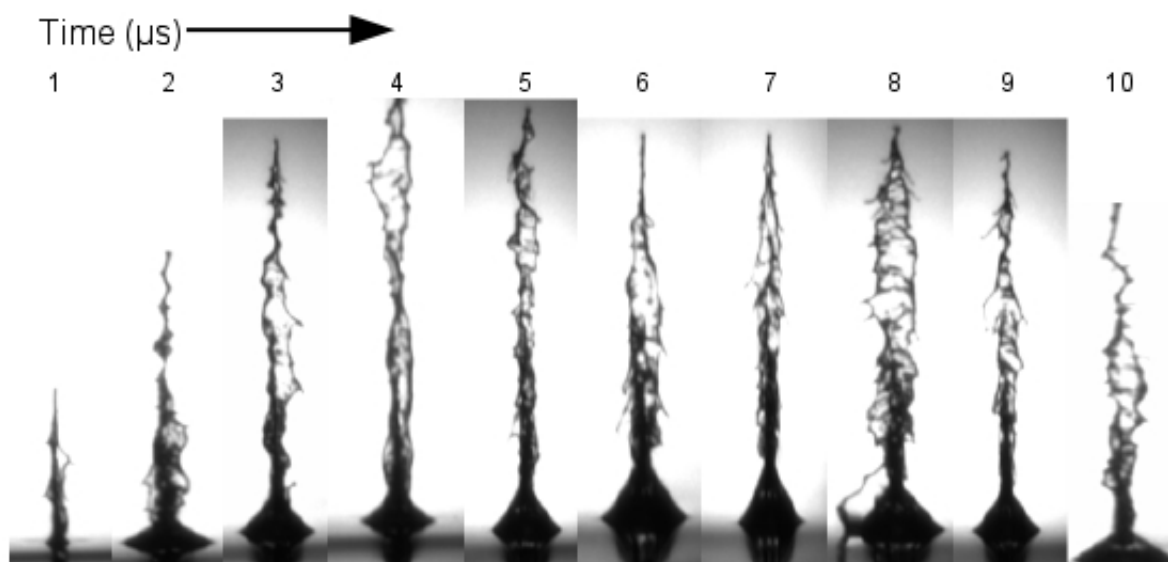


Figure E.7: TRI of the jet with 36.8 $\mu$ J laser energy and 40 $\mu$ m of thickness of the solution diluted to 1/6

Turbulence observed in high speed jets is attributed to high laser energy which produces high pressure vapour bubble. Speed (Fig. E.3) is directly proportional to the energy for a given thickness of the ink. Jet speeds are thus much larger for a thickness of 20 $\mu$ m than that of 50 $\mu$ m, for a given energy, which indicates an inverse relation between jet velocity and thickness of the bioink. For 20 $\mu$ m thickness, the jetting regime tends to shift to the plume regime for an energy of 49.4 $\mu$ J where as 73.9 $\mu$ J produces plume in 40 $\mu$ m thick bioink. Reducing viscosity of the bioink also leads to turbulence. This has been observed by dilution of the riboflavin by 1/3 and 1/6 times (Fig. E.4-E.7). This led us to use 40 $\mu$ m thick layer of riboflavin and 51 $\mu$ J energy to evaluate its penetration power through 150 $\mu$ m collagen membrane (Fig. 3.10).

## APPENDIX F

### PUBLICATIONS & COMMUNICATIONS

#### Journal Publications

**Laser-assisted bioprinting to deal with tissue complexity in regenerative medicine.**

Fabien Guillemot, Bertrand Guillotin, Aurélien Fontaine, Muhammad Ali, Sylvain Catros, Virginie Kériquel, Jean-Christophe Fricain, Murielle Rémy, Reine Bareille and Joëlle Amédée-Vilamitjana (2011). MRS Bulletin, **36** (12): 1015-1019.

**Controlling laser-induced jet formation for bioprinting mesenchymal stem cells with high viability and high resolution.**

Muhammad Ali; Emeline Pages; Alexandre Ducom; Aurélien Fontaine; Fabien Guillemot (2014). Biofabrication, BF-100112R1, Under review

#### Book's Chapters

**Laser-Assisted Bioprinting for Tissue Engineering.** Bertrand Guillotin, Muhammad Ali, Alexandre Ducom, Sylvain Catros, Virginie Kériquel, Agnes Souquet, Murielle Remy, Jean-Christophe Fricain, Fabien Guillemot. in **Biofabrication** Micro- and Nano-Fabrication, Printing, Patterning, and Assemblies Edited by: Gabor Forgacs and Wei Sun, William Andrew Applied Science Publisher USA, 1<sup>st</sup> Edition, April 2013.

**Cell Patterning by Laser-Assisted Bioprinting.** Raphael Devillard, Emeline Pages, Manuela Medina Correa, Virginie Kériquel, Murielle Remy, Jerome Kalisky, Muhammad Ali, Bertrand Guillotin and Fabien Guillemot. in **Micropatterning in Cell Biology Part A** (Methods in Cell Biology) Edited by Matthieu Piel and Manuel Théry, Burlington Academic Press, Vol. 119, January 2014.

#### Oral Communications

Seminars delivered in **instituto de engenharia biomédica (INEB)** Porto, Portugal meeting 2013 on research work of phd thesis

Seminars delivered in Tissue Engineering Assisted by Laser (TEAL) Meeting 2013 on experiment on distant droplet printing by laser.

Seminar delivered in INSERM U 1026 “Laboratoire Bioingénierie Tissulaire” 2012 meeting on research work of phd thesis.

Seminar on, “Micro-printing of Biological Elements by Laser” to mid-term thesis defence committee of doctoral school of Université de Bordeaux Segalen France 2012

Seminar delivered on experiment on micro-channel machining by laser in Tissue Engineering Assisted by Laser (TEAL) Meeting 2012

## Poster Presentations

**Time-Resolved Imaging Study of Laser Assisted Bioprinting.** Muhammad ALI, Raphael DEVILLARD, Emeline PAGES, Murielle REMY, Bertrand GUILLOTIN, Fabien GUILLEMOT. in scientific congress conducted by doctoral school of Université de Bordeaux Segalen France 2013

**Geometrical Parameters Associated with Laser Assisted Bioprinting (LAB),** Muhammad ALI, Aurélien FONTAINE, Agnès SOUQUET, Raphael DEVILLARD, Bertrand GUILLOTIN, Fabien GUILLEMOT in the International Conference on Biofabrication 2012, Manchester, UK October 29-31, 2012

**Geometrical Parameters to deal with Mechanism of Laser-Assisted Bioprinting,** Muhammad ALI, Aurelien FONTAINE, Agnès SOUQUET, Fabien GUILLEMOT. in E-MRS spring meeting, Strasbourg, France May 15-17, 2012.

**LASER ASSISTED MICRO-FABRICATION by Laser Induced Forward Transfer (LIFT),** Muhammad ALI, Florent DELOISON, Joelle AMEDEE, Fabien GUILLEMOT. in scientific congress conducted by doctoral school of Université de Bordeaux Segalen France 2012

## **APPENDIX G**

### **SCIENTIFIC PUBLICATIONS**

**F.1 MRS BULLETIN**

**F.2 BIOFABRICATION**

**F.3 BIOFABRICATION: MICRO- AND NANO-FABRICATION, PRINTING,  
PATTERNING AND ASSEMBLIES (MICRO AND NANO TECHNOLOGIES)**

**F.4 MICROPATTERNING IN CELL BIOLOGY PART A (METHODS IN CELL  
BIOLOGY)**





**Laser-assisted bioprinting to deal with tissue complexity in regenerative medicine**

**Abstract**

Laser-assisted bioprinting is one among several technologies that are being developed in the recent and growing field of bioprinting. Bioprinting is defined as the use of computer-aided transfer processes for patterning and assembling living and non-living materials with a prescribed 2D or 3D organization in order to produce bio-engineered structures serving in regenerative medicine, pharmacology, and basic cell biology studies. We describe the physical parameters that need to be tuned for laser-assisted bioprinting of materials and cells, with high throughput and controlled printing resolution. We present its applications for printing cells and tissue-relevant biomaterials, both *in vitro* and *in vivo*. Finally, we discuss how this technique may help in reproducing the local cell micro-environment and dealing with tissue complexity and heterogeneity for fabricating functional tissue-engineered 3D constructs.



F.2 BIOFARICATION BF-100112R1, Under review:

**Controlling laser-induced jet formation for bioprinting mesenchymal stem cells with high viability and high resolution.**

**ABSTRACT**

Laser-Assisted Bioprinting (LAB) is a versatile, non-contact, nozzle-free printing technique which has demonstrated high potential for cell printing with high resolution. Improving cell viability requires determining printing conditions which minimize shear stress for cells within the jet and cell impact at droplet landing. In this context, this study deals with laser-induced jet dynamics to determine conditions from which jets arise with minimum kinetic energies. The transition from sub-threshold regime to jetting regime has been associated with a geometrical parameter (vertex angle) which can be harnessed to print mesenchymal stem cells with high viability using slow jet conditions. Finally, hydrodynamic jet stability is also studied for higher laser pulse energies which give rise to supersonic but turbulent jets.

**Keywords**

Laser-Assisted Bioprinting

Time-resolved imaging

Liquid jet near free-surface

Jet formation by laser

Laser induced bubble



**Laser-Assisted Bioprinting for Tissue Engineering**

Laser-assisted bioprinting (LAB) is an emerging technology in the field of tissue engineering. Its physical mechanism makes it possible to print cells and liquid materials with a cell-level resolution. By giving tissue engineers control over cell density and organization of 3D tissue constructs, LAB holds much promise for fabricating living tissues with physiological functionality. After introducing the rationale of applying LAB to tissue engineering, we present exhaustively the physical parameters related to the laser-induced forward transfer technique (LIFT), which is implemented in LAB. These parameters are critical to controlling the cell printing process and must work together to print viable cell patterns with respect to cell-level histological organization and to high-throughput manufacturing. After describing the experimental requirements that should be considered to fabricate 3D tissues by LAB, we present some of the main breakthroughs, including multicomponent printing, 3D printing approaches, and bioprinting in vivo that may serve in tissue engineering and regenerative medicine.

**Keywords**

- Laser-assisted bioprinting;
- rapid prototyping;
- regenerative medicine;
- tissue engineering



## **F.4 MICROPATTERNING IN CELL BIOLOGY PART A (METHODS IN CELL BIOLOGY)**

### **Cell Patterning by Laser-Assisted Bioprinting**

The aim of tissue engineering is to produce functional three-dimensional (3D) tissue substitutes. Regarding native organ and tissue complexity, cell density and cell spatial 3D organization, which influence cell behavior and fate, are key parameters in tissue engineering. Laser-Assisted Bioprinting (LAB) allows one to print cells and liquid materials with a cell- or picoliter-level resolution. Thus, LAB seems to be an emerging and promising technology to fabricate tissue-like structures that have the physiological functionality of their native counterparts. This technology has additional advantages such as automation, reproducibility, and high throughput. It makes LAB compatible with the (industrial) fabrication of 3D constructs of physiologically relevant sizes.

Here we present exhaustively the numerous steps that allow printing of viable cells with a well-preserved micrometer pattern. To facilitate the understanding of the whole cell patterning experiment using LAB, it is discussed in two parts: (1) preprocessing: laser set-up, bio-ink cartridge and bio-paper preparation, and pattern design; and (2) processing: bio-ink printing on the bio-paper.